

**Relation at the Fluid-Structure Interface and Residuary Force in Flow Induced
Oscillations with Experimental Validation
(VIV & Galloping)**

by

James Kayode Ofuegbe

A dissertation submitted in partial fulfillment
of the requirements for the degree of
Doctor of Philosophy
(Naval Architecture and Marine Engineering)
in The University of Michigan
2021

Doctoral Committee:

Professor Michael M. Bernitsas, Chair
Professor Bogdan Epureanu
Assistant Professor Yulin Pan
Associate Professor Hai Sun
Professor Armin W. Troesch

James Kayode Ofuegbe

ofuegbej@umich.edu

ORCID iD: 0000-0002-7329-5327

© James Kayode Ofuegbe 2021

DEDICATION

To God the Father the source of all Wisdom, God the Son my Savior, and God the Holy Spirit
my ever-present Comforter.

For seeing me through this journey

To You belongs all the glory.

ACKNOWLEDGEMENT

I would like to express my profound gratitude to my advisor, Professor Michael M. Bernitsas for his tremendous contributions to the success of my PhD program. Time and again, he went the extra mile to ensure that I was able to solve the problems and overcome the obstacles I encountered all through the journey. I cannot thank you enough for the valuable suggestions you gave me, and for being so patient with me throughout my graduate program. I also want to express my appreciation to my committee members, Professor Bogdan Epureanu, Assistant Professor Yulin Pan, Professor Armin W Troesch and Associate Professor Hai Sun for their unique contributions (especially in the final state of the thesis) to the success of my PhD program. Their special contributions helped in improving the quality of my research and the dissertation. I appreciate that they took time out of their engaged schedules to give me timely and crucial input.

I am grateful to Associate Professor Hai Sun for taking me through the lab and teaching me how the equipment at the MRELab work at my early stages in the lab. I also want to thank him for being gracious as to allow me to use his experimental data in this research. I would like to thank Jau-Uei Chen and Andreas Mentzelopoulos for their help with the MATLAB coding aspect of this research and data post-processing.

My research has received financial support from the National University Commission (NUC) under Presidential Special Scholarship Scheme for Innovation and Development (PRESSID) and the Petroleum Technology Development Fund (PTDF) in Nigeria; and The University of Michigan, Ann Arbor. These sources of support are thankfully acknowledged.

Finally, I would like to express my appreciation to my family, friends and loved ones for their support, encouragement and prayers.

TABLE OF CONTENTS

DEDICATION.....	ii
ACKNOWLEDGEMENT.....	iii
LIST OF FIGURES	viii
LIST OF TABLES	xviii
LIST OF APPENDICES	xix
NOMENCLATURE.....	xx
ABSTRACT.....	xxiii
Chapter One	1
Introduction.....	1
1.1. Introduction	1
1.2. Vortex Induced Vibration (VIV).....	3
1.3. Galloping.....	5
1.4. Research Motivation, Goal, and Scope	6
1.5. Thesis Organization.....	7
Chapter Two.....	9
Literature Review	9
2.1. Previous Research work on VIV	9
2.2. Background on Mass-Damping Parameter ($m^*\zeta$).....	10
2.3. Background on Amplitude of Oscillation (A^*).....	12
2.4. Review on the VIVACE Converter.....	13
Chapter Three	16

Mathematical Framework.....	16
3.1. Introduction	16
3.2. Fluid Dynamics	16
3.2.1. Reynolds Number	17
3.2.2. Strouhal Number	17
3.3. Oscillator dynamics.....	21
3.3.1. Equations.....	21
3.3.2. Added Mass	22
3.3.3. Total force coefficient and phase	26
3.3.4. Velocity-force, coefficient, and phase	27
3.3.5. Mandatory resonance	28
3.3.6. Phase-lead ϕ_U	29
3.4. Eigen-relation at the FSI Interface	30
3.4.1. Eigen-relation.....	30
3.4.2. Use of the term eigen-relation in this thesis.....	32
3.4.3. The nature of eigen-relation (3A)	33
3.5. Force Coefficients	34
3.5.1. Added-mass force coefficient C_{A0}	35
3.5.2. In-phase-with-velocity force coefficient C_{U0}	36
3.5.3. Total force coefficient C_{T0}	37
3.6. Force Phases	38
3.7. Force Reconstruction.....	39

Chapter Four	41
Experimental Validation and Results	41
4.1. Introduction	41
4.2. Conclusions Based on the Theory and Data Analysis	42
4.2.1. Eigen-relation.....	42
4.2.2. Strouhal number St_n	43
4.2.3. Reynolds Number Re	43
4.2.4. FSI Interface.....	43
4.3. Comparison between Theory and Experiments for Cylinder with Turbulence Stimulation	44
4.4. Comparison between Theory and Experiments for Smooth Cylinder	56
Chapter Five	69
Discussion: VIV Facts – Old & New	69
5.1. Is VIV lock-in or resonance?	69
5.2. Is the mass-damping parameter $m^*\zeta$ relevant?.....	71
5.3. Is the reduced velocity U^* useful?	72
5.4. Is the mass-ratio m^* useful?.....	72
5.5. Effect of m^* on range of synchronization	72
5.6. Effect of m^* and k	74
5.7. Critical mass-ratio m^*	85
5.8. Is the Vortex Force Small?.....	88
5.9. How Do Vortices Affect the Interface?.....	89
5.10. Magnitude of Vortex Forces	94

Chapter Six	102
Discussion (Continued): Galloping Facts – Old & New	102
6.1. Introduction	102
6.2. Onset of galloping	103
6.3. Unifying onset of instabilities	103
6.4. How do vortices affect galloping?	103
Chapter Seven	105
Conclusions	105
7.1. Dissertation Summary	105
7.2. Closing remarks and Future Work	107
References	110
Appendix A	118
Post Processing Results for VIV of Smooth Cylinder	118
Appendix B	151
Post Processing Results for VIV and Galloping of Cylinder with Turbulence Stimulation.....	151

LIST OF FIGURES

Figure 3.1	Oscillator in steady uniform flow.....	18
Figure 3.2	Theoretical results for a cylinder in FIO	32
Figure 4.1	Theoretical and experimental comparison of FSI properties plotted vs f^* for a circular cylinder with turbulence stimulation $m^* = 1.685$, $K = 400N/m$, $\zeta_{vac} = 0.06$	48
Figure 4.2	Theoretical and experimental comparison of FSI properties plotted vs $U_{n,vac}^*$, for a circular cylinder with turbulence stimulation $m^* = 1.685$, $K = 400N/m$, $\zeta_{vac} = 0.06$	53
Figure 4.3	Theoretical and experimental comparison of FSI properties plotted vs f^* for a smooth cylinder $m^* = 1.595$, $K = 400N/m$, $\zeta_{vac} = 0.06$	59
Figure 4.4	Theoretical and experimental comparison of FSI properties plotted vs $U_{n,vac}^*$, for a smooth cylinder $m^* = 1.595$, $K = 400N/m$, $\zeta_{vac} = 0.06$	62
Figure 4.5	C_A/m^* vs. f^* [FSI eigen-relation eq. (3A)] for different (m^*, k) pairs. VIV and galloping of a circular cylinder with turbulence stimulation; $D=3.5"$, $L=35.5"$, total damping ratio in vacuo $\zeta_{vac} = 0.06$	65

Figure 4.6	C_A/m^* vs. f^* [FSI eigen-relation eq. (3A)] for different (m^*, k) pairs. VIV and galloping of a circular cylinder with turbulence stimulation; $D=3.5"$, $L=35.5"$, total damping ratio in vacuo $\zeta_{vac}=0.10$67
Figure 5.1	C_A/m^* vs. f^* [FSI eigen-relation eq. (3A)] for different (m^*, k) pairs. VIV and galloping of a circular cylinder with turbulence stimulation; $D=3.5"$, $L=35.5"$, total damping ratio in vacuo $\zeta_{vac}=0.06$77
Figure 5.2	C_A/m^* vs. f^* [FSI eigen-relation eq. (3A)] for different (m^*, k) pairs. VIV and galloping of a circular cylinder with turbulence stimulation; $D=3.5"$, $L=35.5"$, total damping ratio in vacuo $\zeta_{vac}=0.10$79
Figure 5.3	C_A/m^* vs. f^* [FSI eigen-relation eq. (3A)] for different (m^*, k) pairs. VIV and galloping of a circular cylinder with turbulence stimulation; $D=3.5"$, $L=35.5"$, total damping ratio in vacuo $\zeta_{vac}=0.22$81
Figure 5.4	C_A/m^* vs. f^* [FSI eigen-relation eq. (3A)] for different (m^*, k) pairs. VIV and galloping of a circular cylinder with turbulence stimulation; $D=3.5"$, $L=35.5"$, total damping ratio in vacuo $\zeta_{vac}=0.26$83
Figure 5.5a	C_A vs. f^* with parameter m^* as predicted by the eigen-relation eq. (3A).88
Figure 5.5b	C_A vs. f^* for $k=400N/m$, $\zeta_{vac}=0.06$, and parameter m^* as predicted by the eigen-relation eq. (3A).88

Figure 5.6	Theoretical and experimental comparison of C_A vs. $U_{n,vac}^*$, for a circular cylinder with turbulence stimulation: $D=3.5"$, $L=35.5"$, $m^*=1.685$, end-springs with total $k=400\text{N/m}$, damping ratio in vacuo $\zeta_{vac} \in [0.02-0.22]$91
Figure 5.7	Residuary force magnitude F_{Ro} as % of F_{To} for a circular cylinder with turbulence stimulation ; $D=3.5"$, $L=35.5"$, $m^*=1.685$, end-springs with $k \in [400-800\text{N/m}]$, total damping ratio in vacuo $\zeta_{vac}=0.06$92
Figure 5.8	Residuary force magnitude F_{Ro} as % of F_{To} for a circular cylinder with turbulence stimulation ; $D=3.5"$, $L=35.5"$, $m^*=1.685$, end-springs with $k=400\text{N/m}$; total damping ratio in vacuo $\zeta_{vac} \in [0.06-0.22]$92
Figure 5.9	Residuary force magnitude F_{Ro} as % of F_{To} for a circular cylinder with turbulence stimulation ; $D=3.5"$, $L=35.5"$, $m^* \in [1.007-1.890]$, end-springs with $k=400\text{N/m}$; total damping ratio in vacuo $\zeta_{vac}=0.06$93
Figure 5.10a	Time history of force components for a circular cylinder with turbulence stimulation $m^* = 1.685$, $k= 400\text{N/m}$ and $\zeta_{vac} = 0.06$ at $f^* = 0.5$96
Figure 5.10b	Magnified/zoomed time history of force components for a circular cylinder with turbulence stimulation $m^* = 1.685$, $k= 400\text{N/m}$ and $\zeta_{vac} = 0.06$ at $f^*= 0.5$97
Figure 5.10c	Kinematics components for a circular cylinder with turbulence stimulation $m^* = 1.685$, $k= 400\text{N/m}$ and $\zeta_{vac} = 0.06$ at $f^*=0.5$98
Figure 5.10d.	Magnified/zoom-in kinematics components for a circular cylinder with turbulence stimulation $m^* = 1.685$, $k= 400\text{N/m}$ and $\zeta_{vac} = 0.06$ at $f^*=0.5$99

Figure 5.11a	Magnified/zoomed Time history of force components for a circular cylinder with turbulence stimulation $m^* = 1.685, k = 400\text{N/m}$ and $\zeta_{vac} = 0.06$ at $f^* = 0.9$100
Figure 5.11b	Magnified/zoomed Kinematics of the Force components for a circular cylinder with turbulence stimulation $m^* = 1.685, k = 400\text{N/m}$ and $\zeta_{vac} = 0.06$ at $f^* = 0.9$101
Figure A1	Theoretical and experimental comparison of FSI properties plotted vs f^* for a smooth cylinder $m^* = 1.25, K = 400\text{N/m}, \zeta_{vac} = 0.06$119
Figure A2	Theoretical and experimental comparison of FSI properties plotted vs $U_{n,vac}^*$, for a smooth cylinder $m^* = 1.25, K = 400\text{N/m}, \zeta_{vac} = 0.06$121
Figure A3	Theoretical and experimental comparison of FSI properties plotted vs f^* for a smooth cylinder $m^* = 1.25, K = 400\text{N/m}, \zeta_{vac} = 0.10$123
Figure A4	Theoretical and experimental comparison of FSI properties plotted vs $U_{n,vac}^*$, for a smooth cylinder $m^* = 1.25, K = 400\text{N/m}, \zeta_{vac} = 0.10$125
Figure A5	Theoretical and experimental comparison of FSI properties plotted vs f^* for a smooth cylinder $m^* = 1.25, K = 800\text{N/m}, \zeta_{vac} = 0.06$127
Figure A6	Theoretical and experimental comparison of FSI properties plotted vs $U_{n,vac}^*$, for a smooth cylinder $m^* = 1.25, K = 800\text{N/m}, \zeta_{vac} = 0.06$129
Figure A7	Theoretical and experimental comparison of FSI properties plotted vs f^* for a smooth cylinder $m^* = 1.25, K = 800\text{N/m}, \zeta_{vac} = 0.10$131
Figure A8	Theoretical and experimental comparison of FSI properties plotted vs $U_{n,vac}^*$, for a smooth cylinder $m^* = 1.25, K = 800\text{N/m}, \zeta_{vac} = 0.10$133

Figure A9	Theoretical and experimental comparison of FSI properties plotted vs f^* for a smooth cylinder $m^* = 1.84$, $K = 400\text{N/m}$, $\zeta_{vac} = 0.06$	135
Figure A10	Theoretical and experimental comparison of FSI properties plotted vs $U_{n,vac}^*$, for a smooth cylinder $m^* = 1.84$, $K = 400\text{N/m}$, $\zeta_{vac} = 0.06$	137
Figure A11	Theoretical and experimental comparison of FSI properties plotted vs f^* for a smooth cylinder $m^* = 1.84$, $K = 400\text{N/m}$, $\zeta_{vac} = 0.10$	139
Figure A12	Theoretical and experimental comparison of FSI properties plotted vs $U_{n,vac}^*$, for a smooth cylinder $m^* = 1.84$, $K = 400\text{N/m}$, $\zeta_{vac} = 0.10$	141
Figure A13	Theoretical and experimental comparison of FSI properties plotted vs f^* for a smooth cylinder $m^* = 1.84$, $K = 800\text{N/m}$, $\zeta_{vac} = 0.06$	143
Figure A14	Theoretical and experimental comparison of FSI properties plotted vs $U_{n,vac}^*$, for a smooth cylinder $m^* = 1.84$, $K = 800\text{N/m}$, $\zeta_{vac} = 0.06$	145
Figure A15	Theoretical and experimental comparison of FSI properties plotted vs f^* for a smooth cylinder $m^* = 1.84$, $K = 800\text{N/m}$, $\zeta_{vac} = 0.10$	147
Figure A16	Theoretical and experimental comparison of FSI properties plotted vs $U_{n,vac}^*$, for a smooth cylinder $m^* = 1.84$, $K = 800\text{N/m}$, $\zeta_{vac} = 0.10$	149
Figure B1	Theoretical and experimental comparison of FSI properties plotted vs f^* for a circular cylinder with turbulence stimulation $m^* = 1.007$, $K = 400\text{N/m}$, $\zeta_{vac} = 0.06$	152

Figure B2	Theoretical and experimental comparison of FSI properties plotted vs $U_{n,vac}^*$, for a circular cylinder with turbulence stimulation $m^* = 1.007$, $K = 400N/m$, $\zeta_{vac} = 0.06$	154
Figure B3	Theoretical and experimental comparison of FSI properties plotted vs f^* for a circular cylinder with turbulence stimulation $m^* = 1.007$, $K = 400N/m$, $\zeta_{vac} = 0.10$	156
Figure B4	Theoretical and experimental comparison of FSI properties plotted vs $U_{n,vac}^*$, for a circular cylinder with turbulence stimulation $m^* = 1.007$, $K = 400N/m$, $\zeta_{vac} = 0.10$	158
Figure B5	Theoretical and experimental comparison of FSI properties plotted vs f^* for a circular cylinder with turbulence stimulation $m^* = 1.007$, $K = 800N/m$, $\zeta_{vac} = 0.06$	160
Figure B6	Theoretical and experimental comparison of FSI properties plotted vs $U_{n,vac}^*$, for a circular cylinder with turbulence stimulation $m^* = 1.007$, $K = 800N/m$, $\zeta_{vac} = 0.06$	162
Figure B7	Theoretical and experimental comparison of FSI properties plotted vs f^* for a circular cylinder with turbulence stimulation $m^* = 1.007$, $K = 800N/m$, $\zeta_{vac} = 0.10$	164
Figure B8	Theoretical and experimental comparison of FSI properties plotted vs $U_{n,vac}^*$, for a circular cylinder with turbulence stimulation $m^* = 1.007$, $K = 400N/m$, $\zeta_{vac} = 0.10$	166

Figure B9	Theoretical and experimental comparison of FSI properties plotted vs f^* for a circular cylinder with turbulence stimulation $m^* = 1.34$, $K = 400N/m$, $\zeta_{vac} = 0.06$	168
Figure B10	Theoretical and experimental comparison of FSI properties plotted vs $U_{n,vac}^*$, for a circular cylinder with turbulence stimulation $m^* = 1.34$, $K = 400N/m$, $\zeta_{vac} = 0.06$	170
Figure B11	Theoretical and experimental comparison of FSI properties plotted vs f^* for a circular cylinder with turbulence stimulation $m^* = 1.34$, $K = 400N/m$, $\zeta_{vac} = 0.10$	172
Figure B12	Theoretical and experimental comparison of FSI properties plotted vs $U_{n,vac}^*$, for a circular cylinder with turbulence stimulation $m^* = 1.34$, $K = 400N/m$, $\zeta_{vac} = 0.10$	174
Figure B13	Theoretical and experimental comparison of FSI properties plotted vs f^* for a circular cylinder with turbulence stimulation $m^* = 1.34$, $K = 800N/m$, $\zeta_{vac} = 0.06$	176
Figure B14	Theoretical and experimental comparison of FSI properties plotted vs $U_{n,vac}^*$, for a circular cylinder with turbulence stimulation $m^* = 1.34$, $K = 800N/m$, $\zeta_{vac} = 0.06$	178
Figure B15	Theoretical and experimental comparison of FSI properties plotted vs f^* for a circular cylinder with turbulence stimulation $m^* = 1.34$, $K = 800N/m$, $\zeta_{vac} = 0.10$	180

Figure B16	Theoretical and experimental comparison of FSI properties plotted vs $U_{n,vac}^*$, for a circular cylinder with turbulence stimulation $m^* = 1.34$, $K = 800N/m$, $\zeta_{vac} = 0.10$	182
Figure B17	Theoretical and experimental comparison of FSI properties plotted vs f^* for a circular cylinder with turbulence stimulation $m^* = 1.685$, $K = 400N/m$, $\zeta_{vac} = 0.06$	184
Figure B18	Theoretical and experimental comparison of FSI properties plotted vs $U_{n,vac}^*$, for a circular cylinder with turbulence stimulation $m^* = 1.685$, $K = 400N/m$, $\zeta_{vac} = 0.06$	186
Figure B19	Theoretical and experimental comparison of FSI properties plotted vs f^* for a circular cylinder with turbulence stimulation $m^* = 1.685$, $K = 400N/m$, $\zeta_{vac} = 0.10$	188
Figure B20	Theoretical and experimental comparison of FSI properties plotted vs $U_{n,vac}^*$, for a circular cylinder with turbulence stimulation $m^* = 1.685$, $K = 400N/m$, $\zeta_{vac} = 0.10$	190
Figure B21	Theoretical and experimental comparison of FSI properties plotted vs f^* for a circular cylinder with turbulence stimulation $m^* = 1.685$, $K = 800N/m$, $\zeta_{vac} = 0.06$	192
Figure B22	Theoretical and experimental comparison of FSI properties plotted vs $U_{n,vac}^*$, for a circular cylinder with turbulence stimulation $m^* = 1.685$, $K = 800N/m$, $\zeta_{vac} = 0.06$	194

Figure B23	Theoretical and experimental comparison of FSI properties plotted vs f^* for a circular cylinder with turbulence stimulation $m^* = 1.685$, $K = 800N/m$, $\zeta_{vac} = 0.10$	196
Figure B24	Theoretical and experimental comparison of FSI properties plotted vs $U_{n,vac}^*$, for a circular cylinder with turbulence stimulation $m^* = 1.685$, $K = 800N/m$, $\zeta_{vac} = 0.10$	198
Figure B25	Theoretical and experimental comparison of FSI properties plotted vs f^* for a circular cylinder with turbulence stimulation $m^* = 1.89$, $K = 400N/m$, $\zeta_{vac} = 0.06$	200
Figure B26	Theoretical and experimental comparison of FSI properties plotted vs $U_{n,vac}^*$, for a circular cylinder with turbulence stimulation $m^* = 1.89$, $K = 400N/m$, $\zeta_{vac} = 0.06$	202
Figure B27	Theoretical and experimental comparison of FSI properties plotted vs f^* for a circular cylinder with turbulence stimulation $m^* = 1.89$, $K = 400N/m$, $\zeta_{vac} = 0.10$	204
Figure B28	Theoretical and experimental comparison of FSI properties plotted vs $U_{n,vac}^*$, for a circular cylinder with turbulence stimulation $m^* = 1.89$, $K = 400N/m$, $\zeta_{vac} = 0.10$	206
Figure B29	Theoretical and experimental comparison of FSI properties plotted vs f^* for a circular cylinder with turbulence stimulation $m^* = 1.89$, $K = 800N/m$, $\zeta_{vac} = 0.06$	208

Figure B30	Theoretical and experimental comparison of FSI properties plotted vs $U_{n,vac}^*$, for a circular cylinder with turbulence stimulation $m^* = 1.89$, $K = 800N/m$, $\zeta_{vac} = 0.06$	210
Figure B31	Theoretical and experimental comparison of FSI properties plotted vs f^* for a circular cylinder with turbulence stimulation $m^* = 1.89$, $K = 800N/m$, $\zeta_{vac} = 0.10$	212
Figure B32	Theoretical and experimental comparison of FSI properties plotted vs $U_{n,vac}^*$, for a circular cylinder with turbulence stimulation $m^* = 1.89$, $K = 800N/m$, $\zeta_{vac} = 0.10$	214

LIST OF TABLES

Table 3A.	Eigen relation	32
Table 3B.	Force coefficients equations	38
Table 3C.	Force Phases	39
Table 3D.	Force Reconstruction	39

LIST OF APPENDICES

Appendix A Post Processing Results for VIV of Smooth Cylinder118

Appendix B Post Processing Results for VIV and Galloping of Cylinder with
Turbulence Stimulation151

NOMENCLATURE

A	$\sqrt{2}$ •RMS of measured displacement
A^*	A/D
c	is the total oscillator damping including bearing ($c_{bearing}$) and harness ($c_{harness}$)
C_A	Added mass coefficient
C_{To}	$=F_{To}/kA$; Coefficient of total force
C_{Ao}	$=F_{Ao}/kA$; Coefficient of force in phase with $\ddot{y}(t)$
C_{Uo}	$=F_{Uo}/kA$; Coefficient of force in phase with $\dot{y}(t)$
C_{Ro}	$=F_{Ro}/kA$; Coefficient of residuary force
D, L	Cylinder diameter and length, respectively
f^*	$f_{osc}/f_{n,vac}$
FIO	Flow-Induced Oscillation
FSI	Fluid-Structure Interaction
f_n^*	$f_{n,water}/f_{n,vac}$
$f_{n,vac}$	Natural frequency of oscillator in vacuum
$f_{n,water}$	Real (measured) natural frequency in water

f_{osc} Measured frequency of oscillation

$F_T(t)$ Total force on cylinder in the FIO direction

$F_A(t)$ Added-mass force in phase with $\dot{y}(t)$

$F_U(t)$ Velocity-force in phase with $\dot{y}(t)$

$F_R(t)$ Residuary force $F_R(t)=F_T(t)-F_A(t)-F_U(t)$; Measure of how closely assumptions in eqs. (3-10 to 3-14) are satisfied for a specific experiment.

$F_{To}, F_{Ao}, F_{Uo}, F_{Ro}$ Magnitude of force: Total, acceleration, velocity, residuary respectively.

k Total spring stiffness

LTFSW Low Turbulence Free Surface Water

MHK Marine Hydrokinetic

m_{osc} Total oscillating equivalent body mass without m_A

m_A Added mass

m_d Displaced fluid mass

$$m_d = \rho_{fluid}\pi D^2 L/4$$

m^* Dimensionless mass ratio

$$m^* = \frac{m_{osc}}{m_d}$$

SLT Steady Lift Technologies

St Strouhal number specifically used in VIV

St_n Generic Strouhal number in N-S equations

U Flow velocity

U^* Generic reduced velocity in literature

$U_{n,vac}^*$ Reduced velocity used in this research;

$$U_{n,vac}^* = \frac{U}{Df_{n,vac}}$$

VIV Vortex Induced Vibration

$y(t)$ Displacement time history

ζ_{vac} Damping ratio in vacuum

$$\zeta_{vac} = \frac{c}{2\sqrt{km_{osc}}}$$

ζ_{water} Damping ratio in water

$$\zeta_{water} = \frac{c}{2\sqrt{k(m_{osc} + m_A)}}$$

ϕ_A, ϕ_U, ϕ_T Force phases: Acceleration, velocity, total, respectively; eqs. (3C)

----	Theory using equations in Tables. (3A)-(3D)
Reconstructed based on theory and measured f^* (circles)	
oooo	Initial and upper VIV branches
oooo	Lower VIV branch and desynchronization
oooo	Transition VIV to galloping
oooo	Fully developed galloping
Measured experimentally (crosses)	
++++	Initial and upper VIV branches
++++	Lower VIV branch and desynchronization
++++	Transition VIV to galloping
++++	Fully developed galloping

ABSTRACT

Fluid-Structure Interaction (FSI) is a frequently occurring physical phenomenon in many applications and across various engineering disciplines including structural, offshore, aerospace, civil, mechanical and biomedical engineering. Suspension bridges, smoke-stacks, wind turbines, mooring lines, pipelines, heat exchangers, marine risers, and offshore platforms, are examples.

The problem for Flow Induced Oscillation (FIO) is studied using experimental data and a novel analytical method revealing an eigen-relation at the fluid-structure interface. That is a relation between excitation and a dynamical system that has to be satisfied for a non-trivial solution to exist. Consistent rather than heuristic nondimensionalization of the fluid and oscillator dynamics in fluid-structure interaction, leads to decoupling of amplitude from frequency response. Further, recognizing that the number of governing dimensionless parameters should decrease, rather than increase, due to the fluid-structure synergy at the interface, an eigen-relation is revealed for a cylinder in Flow Induced Oscillations (FIO). It shows that, for a given dimensionless oscillation frequency f^* , the ratio of real added-mass to oscillating-mass is fully defined. The primary assumption of this approach is that for the eigen-relation to hold, the FIO has to be monochromatic. This is a common assumption in VIV and galloping. For very low natural frequencies of the oscillator in vacuum this assumption does not hold.

Amplitude decoupling and the eigen-relation, lead to explicit expressions for coefficients, phases, and magnitudes of the total hydrodynamic force, the force in phase with the acceleration of the oscillator (added-mass), and the force in phase with the velocity of the oscillator. Those reveal their dependence on the generic Strouhal number, damping, and Reynolds. Heuristic dimensionless parameters, used in VIV data presentation are not needed. Theoretical derivations and force reconstruction match nearly perfectly with extensive experimental data collected over a decade in the Marine Renewable Energy Laboratory (MRELab) at the University of Michigan using four different oscillator test-models.

Further, based on the above derivations the following analyses are presented:

(a) Single-cylinder experimental data in FIO are analyzed using the eigen-relation and derived force expressions. The ranges of parameters are: mass ratio $m^* \in [1.007 \text{ to } 2.0]$, spring stiffness $k \in [400\text{N/m to } 1200\text{N/m}]$ and total system damping ratio $\in [0.02 \text{ to } 0.26]$

(b) Beyond the single frequency response model, the residuary force is derived by comparison to experiments. Using the theory, established facts regarding VIV and galloping and new important observations are readily explained:

- The effects of Strouhal, damping-ratio, mass-ratio, Reynolds, reduced velocity, and stagnation pressure.
- The cause of expansion/contraction of the VIV range of synchronization.
- The corresponding slope-change in oscillation frequency with respect to the Strouhal frequency of a stationary-cylinder.
- The critical mass-ratio implying perpetual VIV.
- The significance of the natural frequency of the oscillator in vacuum.
- The effect of vortices in VIV and galloping.
- The magnitude of vortex forces divided into direct and indirect forces.

(c) The derived eigen-relation is a first order solution to the VIV and galloping problems. The developed equations for the forces in-phase with the velocity and acceleration, when subtracted from the total force measured experimentally, yield a residuary force.

(d) Data obtained from the MRELab experimentally and with CFD are analyzed further to identify other force components likely related to vortex shedding directly. This is a step towards higher order theories for VIV and galloping beyond the eigen-relation.

Chapter One

Introduction

1.1. Introduction

According to the U.S Energy Information Administration EIA (2017) [32], the world energy consumption which currently stands at 140 QBTU (quadrillion British Thermal Units) will grow by 28% by 2040. Per the same report, renewable forms of energy are expected to be the fastest-growing energy sources, with utilization increasing by an average of 2.3% per year between 2015 and 2040. For the required world energy demand to be met and for the above projections to be accomplished, efforts must be channeled to utilizing renewable forms of energy. Deep-sea explorations, installations and productions of hydrocarbon energy via new technologies from the ocean should be considered as alternative source of energy on a large scale.

Renewable energy is energy that is derived from renewable resources, such as wind, sunlight, rain, tides and currents, waves, rivers, and geothermal heat. Over the years, solar energy has been one of the common renewable sources. However, it is expensive to achieve and implement on a large scale albeit the progress made in the last decade. Hydropower on the other hand is a relatively cheaper technology to implement compared to most renewable sources.

Hydrokinetic energy is defined as kinetic energy due to motion of the water body. The term marine renewable energy refers to energy generated by waves, tidal currents, open ocean currents, river currents, ocean thermal gradients, and salinity gradients. Hydrokinetic energy includes waves and

tides/currents/ivers. Technologies that make use of those renewable energy resources are known as Marine Hydrokinetic (MHK) energy technologies.

Hydrokinetic energy is defined as kinetic energy due to motion of the water body. The term marine renewable energy refers to energy generated by waves, tidal currents, open ocean currents, river currents, ocean thermal gradients, and salinity gradients. Hydrokinetic energy includes waves and tides/currents/ivers. Technologies that make use of those renewable energy resources are known as Marine Hydrokinetic (MHK) energy technologies. It could either be horizontal hydrokinetic energy referring to hydrokinetic energy in tidal, open-ocean, and river currents; or vertical hydrokinetic energy referring to hydrokinetic energy in waves, even though there is some vertical energy in the other sources of marine renewable energy. Ocean waves and currents, if adequately utilized, could be a major source of the world's energy generation. As indicated by the US EIA, the theoretical annual energy potential of waves off the coasts of the United States is estimated to be as much as 2.64 trillion kilowatt-hours, or the equivalent of about 64% of U.S. electricity generation in 2018. [31].

MHK energy can be harnessed by Steady Lift Technologies (SLT) like turbines or by Alternating Lift Technologies (ALT) Bernitsas (2016) [11]. Edmund and Bernitsas (2010) [18] also studied the effect of passive tails on harnessing hydrokinetic Energy. MHK is a vast source of energy that is worth investigating by the development and improvement of innovative technologies. In this research, we focus on harnessing horizontal hydrokinetic energy using an alternating lift technology (ALT) based on Flow Induced Oscillations (FIO's). This technology simply employs alternating lift occurring naturally in Fluid Structure Interaction (FSI). For instance, fish utilize alternating lift to propel efficiently in water. Lifting surfaces, such as fish-fins, are used primarily for steering rather than propulsion. Fins may contribute to propulsion as part of their entire body

motion, which is alternating. Bodies with either slender cross-sections like hydrofoils or bluff cross-sections like cylindrical pipelines are typically subjected to FSI phenomena.

1.2. Vortex Induced Vibration (VIV)

In the last few decades, Fluid-Structure Interaction (FSI) has been studied since it is a frequently occurring physical phenomenon in many applications and across various disciplines including structural, offshore, aerospace, civil, mechanical and biomedical engineering. In civil, mechanical and ocean engineering, applications include the design of suspension bridges, wind turbines, pipelines and piping systems, thermal and refrigeration systems, and offshore platforms, just to mention a few. Ocean structures such as drilling risers, mooring lines, cables, undersea piping and tension-leg platforms are often subjected to strong ocean currents and waves, therefore such structures are in high risk from Vortex-Induced Vibrations (VIV's), where vortex shedding of the flow interacts with the structural properties, leading to large amplitude vibrations in both in-line and cross-flow directions.

Vortex Induced Vibration (VIV) is a well-known phenomenon to both ocean and mechanical engineers. It occurs anytime a sufficiently bluff (non-streamlined) body is exposed to a fluid flow that produces vortex shedding at, or near, a structural natural frequency of the body. When this occurs, the alternating vortex shedding induces fluctuation of pressure on the surface of the cylinder. In turn, this pressure fluctuation results in hydrodynamic forces exerted by the formation of the vortices in the immediate wake of the body. These forces induce vibration/oscillation of the structure. Thus, hydrokinetic energy from the flowing fluid is converted to body kinetic energy. The kinetic energy in the oscillating body can be converted into electrical energy through a Power Take Off (PTO) system; Lee 2009 [38]. As far as VIV is concerned, the interaction between

structures and fluids is important in studying elongated structures with bluff cross-sectional geometry.

Ever since Leonardo da Vinci first observed VIV in 1504AD, in the form of “Aeolian Tones”, engineers have been trying to prevent or suppress VIV from damaging equipment and structures. Further, von Kármán (2005) [75] proved that the Tacoma Narrows bridge collapse in 1940 was due to the alternating nature of the vortex wake. He identified it as VIV; this was later labeled as flutter instability due to the slender cross-section of the bridge pavement and the two degrees of freedom of the bridge; rotational as well as translational. In fact, over the years, many experimental and numerical studies have been conducted to comprehend the underlying physical mechanisms. However, to date there is still limited theoretical understanding of the effect of oscillatory interactions between fluid flow and structural behavior though such interactions can cause large deformations. This research work contributes towards the understanding of the underlying phenomena.

Vortex-Induced Vibration (VIV) of cylindrical structures is a common phenomenon in many engineering applications. Due to its significance in ocean and marine engineering, VIV has been extensively studied over the past decades. Comprehensive reviews of various aspects of VIV can be found in the publications by Williamson and Govardhan (2004) [78], Sarpkaya (2004) [57], Gabbai and Benaroya (2005) [22], Assi et.al. (2010)[2], Bearman (2011) [5], Paidoussis et al. (2011) [48], and Triantafyllou et al. (2016) [69], just to mention a few. According to [22] and [57], VIV is a self-regulated nonlinear phenomenon with six degree of freedom vibration which often is reduced to one degree of freedom in the transverse direction to the flow. There are few theoretical developments in the literature for one and two dimensional problems looking into the theoretical nature of the underlying forces. Complete expressions for the added mass terms in a

six-degree of freedom body motion in a three-degree of freedom fluid motion have been derived by Foulhoux and Bernitsas (1993) [21].

Mostly, to study the dominant equation of structural oscillation, the stiffness and damping coefficients are assumed to be linear. There have been a few experimental studies in the MRELab at the University of Michigan studying nonlinear spring stiffness [12,43,66,79] and nonlinear damping [67].

1.3. Galloping

Another important phenomenon of Flow Induced Oscillation (FIO), which is relevant in ocean and marine engineering, is galloping. Galloping is a dynamic instability that can affect a slender structure subjected to a cross flow. It is a one degree of freedom instability, in transverse or torsional motion, for which the motion-induced fluid loading creates a negative added damping that triggers the instability beyond a critical velocity. Unlike VIV, where the amplitude is self-limiting, galloping is known to be a single degree of freedom, high amplitude, low frequency oscillation typically experienced by non-circular cross-sectional bodies (Alonso, 2009) [1]. Assi et.al. (2014) [3] discussed galloping of circular cylinders fitted with solid and slotted splitter plates.

Galloping is basically caused by induction of negative aerodynamic/hydrodynamic damping by which the total system damping falls below zero thereby generating motion-aiding forces destabilizing the system. The response would be motion in one direction if it were not for the elastic properties of the oscillator resulting in an oscillatory motion. The response of the oscillating body increases to very high amplitude motion as allowed by the frame of the oscillator.

The driving mechanisms in VIV and galloping are completely different. In VIV, the alternating vortex shedding creates alternating pressure variation, which synchronizes with the oscillator

motion. But in galloping, the driving mechanism is an instability in a steady direction. Oscillation occurs only because there is a spring or some other elastic constraint, which reverses the direction of the cylinder motion, at which point the instability initiates from the opposite side of the cylinder.

1.4. Research Motivation, Goal, and Scope

For over a hundred years, there have been a lot of experimental testing and numerical simulations performed by researchers to understand, properly model, and predict the phenomena of VIV and galloping of different bodies in fluid-flows as would be discussed in Chapter two. However, there has been little success in developing generic theoretical solutions, even of first order, for flow induced oscillation problems.

The main objective of the present research is to better understand the underlying concepts for VIV and galloping. The developed eigen-relation and the corresponding force expressions for transverse Flow Induced Oscillations contribute towards modeling and understanding these phenomena. The derived expressions are validated by experiments conducted in the MRELab (Marine Renewable Energy Laboratory) at the University of Michigan. This theoretical development can explain results obtained over the years by various researchers in the ocean engineering field on VIV and galloping over more than 70 years.

Furthermore, the VIVACE (Vortex Induced Vibrations Aquatic Clean Energy) Converter invented in the MRELab and patented through the University of Michigan is based on enhancing FIO and controlling the motion of the oscillating body to convert its energy to electricity [8-10,15]. VIVACE is used to harness horizontal MHK energy form tides/river/ocean currents.

This research work develops a first order rigorous mathematical framework to accurately predict VIV and galloping of a general elongated and elastic body with bluff cross-section like a cylinder.

While the FSI mechanism is a general process, this dissertation focuses on oscillatory interaction between moving structures and fluid flow in FIO. Such interactions cause large deformations and eventually failure. Alternatively, when FIO is controlled, it can generate energy as in the case of the VIVACE Converter.

To achieve the above goals, the following research tasks are undertaken:

- Derivation and development of the eigen-relation for linear oscillators with experimental confirmation using smooth cylinders and cylinders with passive turbulence stimulation.
- Processing experimental data for linear oscillators in VIV and galloping collected at the MRELab of the University of Michigan based on the developed eigen-relation and the corresponding force expressions.
- Validation of the eigen-relation and force expressions by comparing the theoretical results to the experimental ones for one-cylinder tests.
- Explain experimental observations for both VIV and galloping using the developed theory.
- Identifying limitations of the developed theory and verifying those experimentally.

1.5. Thesis Organization

This dissertation is arranged as follows. Chapter 1 is on the introduction of VIV and galloping, and the objective and motivation of this research. Chapter 2 provides a review of literature related to this research. In Chapter 3, the mathematical framework of this dissertation is developed and explained revealing an eigen-relation at the interface between fluid and structures as well as explicit expressions for the forces. Further it decouples the generic Strouhal number effects from the Reynolds effects. Chapter 4 shows some of the results obtained by

using the eigen-relation and the corresponding force relations derived in Chapter 3 to process experimental data obtained in the MRELab. The accuracy of the predictions when the assumptions are satisfied is nearly perfect. In addition, the residuary forces are from the experimental data and are shown to match the direct vortex forces. Based on the results in Chapter 4, more light is shed on as many experimental observations as we could find published in the VIV and galloping literature in Chapters 5 and 6, respectively. The conclusions of the dissertation and future research are presented in Chapter 7. Appendices A and B show more experimental results for smooth cylinder and cylinder with turbulence stimulation (PTC) compared to the derived eigen-relation and force expressions. Complete sets of data are presented in MRELab Report 13 [46]. Parametric presentation of the results for comparison are presented in Report 14 [47].

Chapter Two

Literature Review

2.1. Previous Research work on VIV

Vortex Induced Vibrations (VIV) for flow past slender structures with bluff cross-sections, which are immersed into the fluid flow has been studied extensively and observed over a century. First observed by Leonardo da Vinci in 1504, the problem of Vortex Induced Vibration is still being studied experimentally, numerically, and with mathematical models. Since the discovery of formation of vortices produced by translating rods through air by Strouhal (1878) [63] and the analysis of stability of vortex street configurations by von Kármán (1912, 1938) [73,74], the problem of VIV has been studied extensively and is still being studied by experiments, simulations, and field-tests and observations. Some of the important work done in the field of VIV on normal incident and inclined rigid cylinder with only one degree of freedom (crossflow) are discussed in this chapter.

Hartlen and Currie (1970) [30] provided a lift-oscillator model to approach the lock-in behavior of VIV when they studied structures and bodies such as a flexible cylinder in uniform flow.

For VIV under unsteady current, several experiments were carried out for structures under sinusoidal oscillatory flow or sinusoidal oscillating structures in still water. In order to properly

visualize the vortices pattern formed, Williamson (1985) [76], and Williamson and Roshko (1988) [77] used flow visualization techniques to capture the evolution of vortices in the wake of a structure. Keulegan and Carpenter (1958) [34], Feng (1968) [19], Sarpkaya (1976, 1986) [52,53,55,56] and Justesen (1989) [33] measured forces under oscillatory flow in the range of 1-30 for KC number. Sumer and Fredsoe (1988) [64] described transverse vibrations of an elastically mounted cylinder exposed to oscillatory flow.

For VIV of curved structures or inclined structures, some of the research that has been conducted up till now are described next. Bearman et al. (1984) [4] proposed a frequency varying forcing model for the harmonically oscillating flow. Triantafyllou (1991) [68] reported the dynamic response of flexible cable structures under added mass and drag force effects. Kozakiewicz et al. (1995) [37] studied the influence of oblique incidence of current flow. Ferrari and Bearman (2000) [20] modified the original model and carried out numerical simulations. Blevins (1990) [13] provided a thorough and compact resource for a variety of flow induced vibration topics.

2.2. Background on Mass-Damping Parameter ($m^*\zeta$)

Dimensionless parameters are needed to model and present experimental results. The mass-damping parameter has been used for about 70 years and is a controversial parameter in the VIV research field. Most researchers believe that it is an important parameter for modeling the flow induced oscillation (FIO) of the body under consideration. Recently, the value of this heuristic parameter has been questioned Zdravkovich (1982) [80], Vandiver (2012) [70].

First introduced by Scruton in 1955 [58], the mass-damping parameter was used for the purpose of characterization of flow induced vibration of cantilevered, flexible structures in wind. Not long after, many researchers adopted it and it was called the Scruton number. (Scruton, 1955, 1956, 1965, 1966) [58-61], (Vickery and Watkins,1964) [71], (Zdravkovich, 1982) [80]

$$S_c = 2m\delta/\rho D^2 = \pi^2 m^* \zeta \quad (2-1)$$

The Scruton number was shown to work perfectly in collapsing maximum response amplitude data for high mass ratio cantilevers to a single curve of A^*_{\max} versus S_c .

Later in 1973, Griffin and colleagues decided to expand this application of mass-damping to predict the maximum response amplitude of a wide variety of flexible structures, including cables in water. (Griffin et al., 1973 [27]; Griffin and Skop, 1976 [28]; Griffin and Koopman, 1977 [29]). They came up with a new parameter, from a wake oscillator model which at the time was referred to as K_s [28]. Also the Scruton number became the Skop-Griffin parameter (S_G) which is:

$$S_G = 2\pi St^2 (2m\delta/\rho D^2) = 2\pi^3 St^2 m^* \zeta \quad (2-2)$$

The symbol St is the Strouhal number for flow past a stationary cylinder and was intended by Griffin et al [28]. to be taken as a constant. Although, the Griffin plots showed general trends of agreement between maximum response amplitude and S_G , there was lots of scatter to the data. This was in part due to mixing data from structures with different mode shapes and also because the dependence on Reynolds number had not yet been appreciated.

By the late 1970s critics began to point out shortcomings of mass-damping parameters as predictors of VIV response amplitude, particularly at low mass ratios (Sarpkaya, 1979) [54]. Criticism continued to grow and increase, and in 1990 Zdravkovich recommended that mass-damping parameters be used only for very high mass ratio cylinders, such as structures in air (Zdravkovich, 1990) [81]. In 1997, the classical plot was updated by Skop & Balasubramanian (1997) [62]. Later on, Sarpkaya gave a detailed analysis of the deficiencies of mass-damping parameters in [57].

However, Khalak, Govardhan and Williamson in their studies brought up again the use of the mass damping parameter. Khalak and Williamson (1999) [35], Govardhan and Williamson (2006) [26]

made significant progress in reducing the scatter in the Griffin plots. However, Vandiver (2012) [70], claimed that none of the previous damping parameters proposed were useful in organizing response at reduced velocities away from the peak-in response. He proposed another mass damping parameter called c^* which may be used to characterize VIV at all reduced velocities in the lock-in range. Vandiver also claimed that the success of damping parameter(α) used by Govardhan and Williamson (2006) [26] was partly due to the way they eliminated the mode shape as a variable when the problem was simplified to that of understanding the Vortex induced vibration (VIV) of two dimensional spring-supported rigid cylinders in a uniform flow.

This research work seeks to answer and shed more light to this controversially used parameter as would be discussed in Chapter five.

2.3. Background on Amplitude of Oscillation (A^*)

The most important measurement in Flow Induced Oscillations (VIV and galloping) is the amplitude of cylinder oscillation $A^*=A/D$. Khalak and Williamson in their experiments [35], involving the transverse oscillations of an elastically mounted rigid cylinder at very low mass and damping claimed that A^* primarily depends on the mass ratio m^* . Also the regime of synchronization depends primarily on the mass ratio, m^* . According to Feng's experiment [19], where $m^* = 248$, $\zeta = 0.00103$, $m^*\zeta = 0.255$ and Re between 10^4 to 5×10^4 , he observed that there are two amplitude branches (the initial and the lower) in the response characteristics of a flexibly mounted circular cylinder in air. However, Khalak and Williamson (1999) [35] with a significantly smaller mass ratio ($m^*= 10$), the same damping ratio but lower Reynold's number ($Re = 3500-10000$) observed three amplitude branches (initial, upper and lower), a larger peak amplitude with broader range of synchronization for a flexibly mounted circular cylinder in water. Govardhan and

Williamson (2000) [24], indicated that it is principally the parameter ($m^*\zeta$) which influences whether the upper branch will appear or not.

According to (Williamson and Roshko 1988 [77]; Govardhan and Williamson 2000 [24]; Morse and Williamson 2008 [45]); A^* is closely related to the vortex- shedding mode of the cylinder. [77] described extensively terminologies for each mode that is encountered in VIV. Each periodic vortex wake pattern has single vortices(S) and vortex pairs(P). Shedding modes such as 2S, 2P, P+S, even 2P + 2S have been reported by researchers in the literature. Most of the previous studies report amplitude values up to 1.13 diameters (Williamson and Govardhan 2004 [78]). However, studies conducted at a higher Reynolds numbers (TrSL3 regime according to the classification of flow by Zdravkovich (1990) [81]; TrSL3 regime is a high-lift regime) have yielded much higher amplitudes of oscillation reaching $A^*=1.9$ (Raghavan (2007) [49]; Bernitsas et al. 2008 [6]). Hence whether the amplitude of oscillations is solely dependent on the mass ratio m^* or the Reynold's number or it indeed depends on some other parameters is yet to be fully understood and would be investigated using the eigen-relation that would be developed in this research work.

2.4. Review on the VIVACE Converter

Over the years, many attempts to utilize the ocean energy resources to generate power have been made. Vortex Induced Vibration for Aquatic Clean Energy Converter (VIVACE) is one of the promising concepts to generate clean renewable electricity from ocean currents without using blades and rotors (turbines). It is a hydrokinetic power generating device invented by Bernitsas and Raghavan in 2005 [6,9,10] and further developed by Bernitsas and his research group in the Marine Renewable Energy Laboratory (MRELab) of the University of Michigan (Bernitsas and Raghavan, 2009 [9]; Lee and Bernitsas, 2011 [40]; Lee et al., 2011 [41]; Raghavan and Bernitsas, 2010 [50]; Chang et al., 2011 [16], Chang and Bernitsas, 2011 [15]). It is a device developed to

harness energy from water current by utilizing Vortex Induced Vibrations (VIV) while satisfying the requiring standards of all clean renewable energy in the United States; most important being fish friendly. Lee (2010) [39] reported that a single cylinder (D=3.5", L=36") VIVACE Converter successfully generated hydrokinetic power from a current as slow as 0.4m/s and a maximum power of 15.85W at low speed of 1.11m/s. Moreover, Chang (2010) [14] was able to harness 49.35W at the low speed of 1.45 m/s. The power-to-volume ratio (power density) was $341\text{W}/\text{m}^3$ at the low speed of 1.45 m/s by utilizing Passive Turbulence Control (PTC) on the single cylinder VIVACE. In 2016, Lin Ding et al (2016) [42] further investigated using numerical simulations and concluded that for a single cylinder with Passive Turbulence control the energy conversion efficiency reaches 37% in simulations and 28% in experiments.

As the years went by, seeing the success and great prospect of the single cylinder VIVACE system, multi-cylinder VIVACE converters were developed. This is to enhance the cylinders to work synergistically thereby harnessing more power and increase the power density. Kim (2013) [36] in his dissertation explained extensively the various factors and parameters that could enhance the synergy of multiple cylinders in flow induced motion for hydrokinetic energy harnessing. Some of his conclusions are as follows:

- For multiple cylinders, there is increase in galloping, increased range of synchronization, and higher amplitude regardless of other parameters.
- For tandem center-to-center spacing of $1.43D$, FIM of two cylinders in tandem is distinct. He claimed that galloping starts earlier, and the amplitude of the 2nd cylinder is higher. The frequency of oscillation is lower for both cylinders and the energy conversion is 60% higher.

- Finally, he claimed that 2,3, and 4 cylinders synergistically operating in FIO can harness more marine hydro-kinetic energy than the same number of cylinders acting in isolation.

Chapter Three

Mathematical Framework

3.1. Introduction

The mathematical approach and models used in this research are derived in this chapter. The discussions are restricted to the mathematical equations in fluid dynamics that are relevant to this research. The basic Navier-Stokes equation is presented along with the oscillator dynamic model. From those, the relevant dimensionless groups are derived. In Section 3.3, the oscillator dynamics is studied. The combination of fluid dynamics and oscillator dynamics in Fluid Structure Interaction (FSI) leads to an eigen-relation of the transverse flow induced oscillations in Section 3.4. In the remaining of the chapter analytical force relations are derived.

3.2. Fluid Dynamics

Fluid Structure Interaction (FSI) problems are governed by the fluid dynamics equations and the oscillator equation. For fluid dynamics, satisfying continuity for an incompressible fluid does not provide any Π -group (dimensionless parameters). The Navier-Stokes equations in dimensionless vector form are:

$$\left[\frac{D}{TU_\infty} \right] \frac{\partial \vec{V}^*}{\partial t^*} + [1](\vec{V}^* \cdot \vec{\nabla}^*) \vec{V}^* = \left[\frac{gD}{U_\infty^2} \right] \vec{f}^* - \left[\frac{p_\infty}{\rho U_\infty^2} \right] \vec{\nabla}^* \cdot p^* + \left[\frac{\nu}{DU_\infty} \right] \Delta^* \vec{V}^* \quad (3-1)$$

where "*" indicates dimensionless quantity, D is diameter, T is relevant time scale, \vec{V}^* =velocity vector, U_∞ and p_∞ are velocity and pressure at infinity. There are four Π -groups in square brackets in eq. (3-1), which are well-known hydrodynamic dimensionless parameters. From left to right,

these Π -groups are the Strouhal number, the Froude number, Euler number and Reynolds' number, respectively. In the absence of free-surface and cavitation, Fr and Eu numbers can be neglected. That leaves the Reynolds and Strouhal numbers as the two important dimensionless numbers for Flow Induced Oscillations (FIO) analysis.

3.2.1. Reynolds Number

The Reynolds number (Re), is the ratio of inertia forces to viscous forces in the fluid and is of crucial importance for a real-fluid problem. For bluff bodies like a cylinder, the integral of the normal pressure forces represents about 95% of the forces compared to the integral of the shear forces producing the skin friction which accounts for the remaining 5%. The indirect effect of viscosity of course is more important as the separated flow region and dead flow in the immediate wake of the cylinder are affected by the shear layer roll-up, which is stronger and closer to the cylinder in the TrSL3 flow-regime than in TrSL2, resulting in much higher lift and amplitude response [6,7,50]. The shear layers in TrSL3 are fully turbulent [81].

3.2.2. Strouhal Number

The ratio of the local inertia to convective inertia terms in the N-S equation (3-1), is the Strouhal number (St_n) and is most important and needs to be defined carefully. The reduced velocity U^* and the Keulegan-Carpenter number KC are forms of Strouhal number. However, both are defined heuristically. The challenge here is due to the fact that FIO are typically studied in a steady uniform flow where no fluid reference acceleration (local or convective) is readily identifiable.

Fluid dynamics is governed by N-S eq. (3.1), which reveals the four familiar Π -groups, for which the, Fr and Eu numbers are not applicable here, but the Re number adequately models the viscosity effects. St_n though, requires a careful definition. $U_{n,vac}^*$ and KC , which are forms of St_n , are

heuristic and irrelevant, because they do not abide by the definition of the generic Strouhal number St_n as

$$St_n = \frac{Local_inertia}{Convective_Inertia} \quad (3-2)$$

Since a steady flow is characterized by constant velocity, U , to identify a reference acceleration, or some form of local and convective accelerations, one must look into the hydrodynamic forces exerted on the oscillator in greater details. Those can be found at the fluid-structure interface. Specifically, Foulhoux et.al (1993) [21] provides complete expressions for forces and moments on small bodies in six degree-of-freedom motion in a three-dimensional flow for an ideal fluid. In tensor notation, the two dimensional (x,y) force equations become (Fig 3.1),

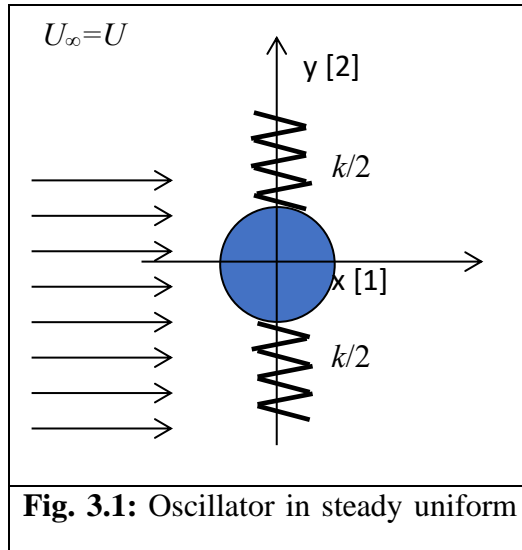


Fig. 3.1: Oscillator in steady uniform

$$\vec{F}_{inertia} = F_1 \hat{i} + F_2 \hat{j} \quad (3-3)$$

$$F_j = \rho V_B \left\{ \frac{\partial}{\partial t} U_j + (U_i - u_i) \frac{\partial U_j}{\partial x_i} \right\} + m_{jj} \left(\frac{\partial U_j}{\partial t} - \frac{du_j}{dt} \right) + m_{ii} (U_i - u_i) \frac{\partial U_j}{\partial x_i} \quad (3-4)$$

where U_j =fluid velocity, u_j =body velocity; m_{ij} =added mass; V_B =displaced fluid volume, and ρ =fluid density. For a circular cylinder $m_{ij}=m_{11}=m_{22}=m_A$. Expanding eq. (3-4), $j=1,2$, we have

$$F_1 = \rho V_B \left\{ \frac{\partial}{\partial t} U_1 + (U_1 - u_1) \frac{\partial U_1}{\partial x_1} + (U_2 - u_2) \frac{\partial U_1}{\partial x_2} \right\} + \left\{ m_A \left(\frac{\partial U_1}{\partial t} - \frac{du_1}{dt} \right) + (U_1 - u_1) \frac{\partial U_1}{\partial x_1} + (U_2 - u_2) \frac{\partial U_1}{\partial x_2} \right\} \quad (3-5)$$

$$F_2 = \rho V_B \left\{ \frac{\partial}{\partial t} U_2 + (U_1 - u_1) \frac{\partial U_2}{\partial x_1} + (U_2 - u_2) \frac{\partial U_2}{\partial x_2} \right\} + \left\{ m_A \left(\frac{\partial U_2}{\partial t} - \frac{du_2}{dt} \right) + (U_1 - u_1) \frac{\partial U_2}{\partial x_1} + (U_2 - u_2) \frac{\partial U_2}{\partial x_2} \right\} \quad (3-6)$$

For a cylinder in transverse FIO in steady flow, $U_1=U$, $U_2=0$; and $u_1=0$, $u_2=A\omega_{osc}\cos(\omega_{osc}t)$; where A and ω_{osc} are the amplitude and frequency of the cylinder oscillation. Eqs. (3-5) and (3-6) reduce to (3-7) and (3-8), respectively.

$$F_1 = 0 \quad (3-7)$$

$$F_2 = m_A A \omega_{osc}^2 \sin(\omega_{osc}t) \quad (3-8)$$

Thus, in the y-direction of the cylinder oscillation, the numerator of St_n in eq. (3-2) appears in eq. (3-8) while the denominator is not readily identifiable. This is so because eqs. (3-3) to (3-6) represent the far-field approximation of the forces, while the N-S eq. (3-1) is the exact flow momentum equation.

To identify a relevant convective inertia term to properly define St_n , we need to delve into the near-field flow particulars; without solving the N-S equation of course. Eqs. (3-5 to 3-6), albeit being a far-field force approximation, clearly show two groups of terms in brackets. One bracket is multiplied by the cylinder added mass, and the other by the displaced fluid mass. Within each

bracket, there are local accelerations, absolute and relative, and relative convective terms applied on absolute fluid velocities.

Since there is a fluid-structure interface and the body is subjected to an added mass force, it is clear that fluid in the vicinity of the body is accelerated due to the body motion. That is, the variables in eqs. (3-5) and (3-6), which are not in eqs. (3-7) and (3-8), exist due to the unknown, near-field, fluid acceleration. The convective terms are due to spatial changes of the flow, such as vortex shedding in the immediate cylinder wake. Thus, the next step is to look for the correct time-scale.

In this problem, there are two time-scales: One is D/U related to the x-direction of the flow as in the N-S eq. (3-1). This time-scale is actually irrelevant to the FIO study in spite of the fact that it is used in U^* . The other time-scale is in the y-direction of cylinder FIO and is defined as $T_{n,vac} = 2\pi/\omega_{n,vac} = 1/f_{n,vac}$, the natural period of the oscillator in vacuum. This is the only time-scale relevant to the FIO analysis, which, when coupled with eqs. (3-2) and (3-8), leads to the relevant *Strouhal number* as:

$$St_n = f_{osc}/f_{n,vac} = f^* \quad (3-9)$$

whose significance is solidified in the analysis presented in the rest of this chapter. The St_n is denoted by f^* and is used traditionally to present the dominant response-frequency in dimensionless form in the subsequent chapters. f^* which is the Strouhal number serves the purpose of eq (3-2) *making other forms of St_n questionable because they can be reproduced from St_n and Re .*

3.3. Oscillator dynamics

3.3.1. Equations

The FIO of a rigid cylinder on springs is basically monochromatic – single frequency sinusoidal – both in VIV and in galloping. The linear oscillator model with linear viscous damping typically used is

$$m_{osc}\ddot{y}(t) + c\dot{y}(t) + ky(t) = F_{Y,total}(t) \quad (3-10)$$

Where displacement y and force $F_{Y,Total}$ are perpendicular to the flow as shown in Fig. 3.1.

m_{osc} is the total oscillating mass including 1/3 of the spring mass and other components such as supporting struts, belts, and pulley equivalent masses;

$F_{Y,total}$ is total fluid force including potential and vortex forces exerted transversely to the direction of the flow, that is, in the direction of the oscillation of the cylinder; and

c is the total structural damping including bearing ($C_{bearing}$) and harness ($C_{harness}$)

k is the total spring stiffness

In steady-state,

$$y(t) = A \sin(\omega_{osc}t) \quad (3-11)$$

$$\dot{y}(t) = A\omega_{osc} \cos(\omega_{osc}t) \quad (3-12)$$

$$\ddot{y}(t) = -A\omega_{osc}^2 \sin(\omega_{osc}t) \quad (3-13)$$

$$F_{Y,total}(t) = F_{T0} \sin(\omega_{osc}t + \phi_T) \quad (3-14)$$

where $y(t)$ is the displacement of the cylinder motion, $\dot{y}(t)$ is the velocity, $\ddot{y}(t)$ is the acceleration and F_{T0} is the coefficient of the total force and ϕ_T is the phase angle between the force and the displacement.

3.3.2. Added Mass

Morison et.al (1950) [44] and Keulegan et.al (1958) [34] show that the force component in-phase with the cylinder acceleration (added-mass force) can be calculated from experimental force measurement or force reconstruction. Cunha et.al. (2006) [17] described the robustness of the added mass in VIV models. In order to best understand the added mass coefficient (C_A), we will calculate C_A using two different methods and show indeed that both C_A expressions are identical.

Vikestad (2000) [72] evaluated the added mass coefficient C_a through an experimental setup intended to investigate the Vortex Induced Vibrations (VIV) in a multiple frequency environment. He claimed that the excitation frequency components depend on the velocity profile and local cylinder motion. The local cylinder motion typically has many frequency components. He adopted the following procedure for calculating C_a .

Equation of dynamic equilibrium for the experimental setup is given by:

$$m\ddot{x} + c\dot{x} + k_{total}x = F_v(t) + k_2y(t) \quad (3-15)$$

where, m is the effective dry mass of the cylinder, c is the damping coefficient, k_{total} is the total stiffness of the system, k_2 is the stiffness of the oscillator support, y is the motion of the support system, x is the cylinder motion and F_v is the cross-flow component of the total hydrodynamic force. Assuming harmonic response, $x(t) = x_0 \sin(\omega_0 t)$ and $F_v(t) = F_{total} = F_0 \sin(\omega_0 t + \phi)$, where ω_0 represents the oscillation frequency. Substituting these expressions in eq. (3-15), we have

$$m(-\omega_0^2 x_0 \sin(\omega_0 t)) + c(\omega_0 x_0 \cos(\omega_0 t)) + k_{total}x = F_0(\sin(\omega_0 t) \cos\phi + \cos(\omega_0 t) \sin\phi) + k_2y(t) \quad (3-16)$$

Rearranging and separating the $\sin(\omega_0 t)$ from the $\cos(\omega_0 t)$ terms we have

$$(-m\omega_o^2 x_0 - F_0 \cos\phi) \sin(\omega_o t) + (c\omega_o x_0 - F_0 \sin\phi) \cos(\omega_o t) + k_{total} x = k_2 y(t)$$

Multiplying and dividing the first and second terms with \ddot{x} and \dot{x} respectively and rearranging the terms, we have

$$\left(m + \frac{F_0 \cos\phi}{\omega_o^2 x_0}\right) \ddot{x} + \left(c - \frac{F_0 \sin\phi}{\omega_o x_0}\right) \dot{x} + k_{total} x = k_2 y(t) \quad (3-17)$$

Next, we derive expressions for $F_v \dot{x}$ and $F_v \ddot{x}$ as shown below:

$$\begin{aligned} \lim_{T \rightarrow \infty} \frac{\int_t^{t+T} F_v \dot{x} dt}{T} &= \lim_{T \rightarrow \infty} \frac{1}{T} \int_t^{t+T} F_0 (\sin(\omega_o t) \cos\phi + \cos(\omega_o t) \sin\phi) * (\omega_o x_0 \cos(\omega_o t)) dt \\ &= \lim_{T \rightarrow \infty} \frac{1}{T} (F_0 \omega_o x_0) \int_t^{t+T} (\cos(\omega_o t) \sin(\omega_o t) \cos\phi + \cos^2(\omega_o t) \sin\phi) dt \\ &= \lim_{T \rightarrow \infty} \frac{1}{T} (F_0 \omega_o x_0) \left(\cos\phi \left[\frac{\sin^2(\omega_o t)}{2\omega_o} \right]_t^{t+T} + \sin\phi \left[\frac{t}{2} + \frac{\sin 2(\omega_o t)}{4\omega_o} \right]_t^{t+T} \right) \\ &= \lim_{T \rightarrow \infty} \frac{1}{T} (F_0 \omega_o x_0) \left(\cos\phi \left[\frac{\sin^2(\omega_o(t+T)) - \sin^2(\omega_o t)}{2\omega_o} \right] + \sin\phi \left[\frac{T}{2} + \frac{\sin 2(\omega_o(t+T)) - \sin 2(\omega_o t)}{4\omega_o} \right] \right) \\ &= \lim_{T \rightarrow \infty} \frac{1}{2} (F_0 \omega_o x_0) \sin\phi = \frac{1}{2} F_0 \omega_o x_0 \sin\phi \\ \text{i.e. } \lim_{T \rightarrow \infty} \frac{\int_t^{t+T} F_v \ddot{x} dt}{T} &= \frac{1}{2} F_0 \omega_o x_0 \sin\phi \end{aligned} \quad (3-18)$$

Similarly,

$$\begin{aligned} \lim_{T \rightarrow \infty} \frac{\int_t^{t+T} F_v \ddot{x} dt}{T} &= \lim_{T \rightarrow \infty} \frac{1}{T} \int_t^{t+T} F_0 (\sin(\omega_o t) \cos\phi + \cos(\omega_o t) \sin\phi) * (-\omega_o^2 x_0 \sin(\omega_o t)) dt \\ &= \lim_{T \rightarrow \infty} \frac{1}{T} (-F_0 \omega_o^2 x_0) \int_t^{t+T} (\sin^2(\omega_o t) \cos\phi + \cos(\omega_o t) \sin(\omega_o t) \sin\phi) dt \\ &= \lim_{T \rightarrow \infty} \frac{1}{T} (-F_0 \omega_o^2 x_0) \left(\cos\phi \left[\frac{t}{2} - \frac{\sin 2(\omega_o t)}{4\omega_o} \right]_t^{t+T} + \sin\phi \left[\frac{\sin^2(\omega_o t)}{2\omega_o} \right]_t^{t+T} \right) \\ &= \lim_{T \rightarrow \infty} \frac{1}{T} (-F_0 \omega_o^2 x_0) \left(\cos\phi \left[\frac{T}{2} - \frac{\sin 2(\omega_o(t+T)) - \sin 2(\omega_o t)}{4\omega_o} \right] + \sin\phi \left[\frac{\sin^2(\omega_o(t+T)) - \sin^2(\omega_o t)}{2\omega_o} \right] \right) \end{aligned}$$

$$= \lim_{T \rightarrow \infty} \frac{1}{2} (-F_0 \omega_o^2 x_0) \cos \phi = -\frac{1}{2} F_0 \omega_o^2 x_0 \cos \phi$$

$$\text{i.e.} \quad \lim_{T \rightarrow \infty} \frac{\int_t^{t+T} F_v \ddot{x} dt}{T} = -\frac{1}{2} F_0 \omega_o^2 x_0 \cos \phi \quad (3-19)$$

Substituting equations (3-18) and (3-19) into (3-17) gives,

$$(m - \lim_{T \rightarrow \infty} \frac{2}{T(\omega_o^2 x_0)^2} \int_t^{t+T} F_v \ddot{x} dt) \ddot{x} + (c - \lim_{T \rightarrow \infty} \frac{2}{T(\omega_o x_0)^2} \int_t^{t+T} \dot{x} dt) \dot{x} + k_{total} x = k_2 y(t) \quad (3-20)$$

Considering the inertia term in equation (3-20), it is evident that the added mass term is given by:

$$m_a = -\lim_{T \rightarrow \infty} \frac{2}{T(\omega_o^2 x_0)^2} \int_t^{t+T} F_v \ddot{x} dt \quad (3-21)$$

Integrating over n oscillation periods and over the length of the cylinder, the added mass coefficient can be calculated from experimental data as,

$$C_A = -\frac{1}{\frac{\rho \pi L D^2}{4}} * \frac{2}{nT(\omega_{osc}^2 A)^2} \int_t^{t+nT} F_v \ddot{y}(t) dt = -\frac{8}{nT \rho \pi L D^2 (\omega_{osc}^2 A)^2} \int_t^{t+nT} F_v \ddot{y}(t) dt \quad (3-22)$$

$$C_A = -\frac{8}{nT \rho \pi L D^2 (\omega_{osc}^2 A)^2} \int_0^{nT} F_{Y,Total} \ddot{y}(t) dt \quad (3-23)$$

Eq. (3-23) is the added mass calculated using Vikestad's method. On the other hand, [44] used the expression below for C_A

$$C_A = \frac{2U_m T}{\pi^3 D} \int_0^{2\pi} \frac{F}{\rho D U_m^2} \sin \theta d\theta \quad (3-24)$$

To show that (3-23) and (3-24) are identical, we work through the following mathematical manipulations.

Using the relations: $y(t) = A \sin \theta$, $U_m = A\omega_{osc}$ and $T = \frac{2\pi}{\omega}$, where $\theta = \omega_{osc}t$, and substituting into eqn. (3-22), we have

$$C_A = -\frac{2U_m T}{\rho D U_m^2 \pi^3 D} \int_0^T F \ddot{y} \left(\frac{2\pi}{T} \right) dt = -\frac{4}{\rho U_m \pi^2 D^2 (\omega_{osc}^2 A)} \int_0^T F \ddot{y}(t) dt = -\frac{4}{\rho \pi^2 D^2 (\omega_{osc}^3 A^2)} \int_0^t F \ddot{y}(t) dt$$

Multiplying and dividing by T, and by the relation $T = \frac{2\pi}{\omega_{osc}}$, we have

$$C_A = -\frac{8}{T \rho \pi D^2 (\omega_{osc}^2 A)^2} \int_0^T F \ddot{y}(t) dt \quad (3-25)$$

Integrating the above equation over the length of the cylinder and over n oscillation periods, gives,

$$C_A = -\frac{8}{n T \rho \pi L D^2 (\omega_{osc}^2 A)^2} \int_0^{nT} F \ddot{y}(t) dt \quad (3-26)$$

which indeed shows that the two equations (3-23) and (3-24) are identical.

Substituting eq. (3-11) to (3.14) into (3.10) yields,

$$\left[m_{osc} + \frac{F_{T0} \cos \phi_T}{A \omega_{osc}^2} \right] \ddot{y}(t) + \left[c - \frac{F_{T0} \sin \phi_T}{A \omega_{osc}} \right] \dot{y}(t) + ky(t) = 0 \quad (3-27)$$

yielding another equivalent expression for m_A [72]

$$m_A = m_d C_A = \frac{F_{T0} \cos \phi_T}{A \omega_{osc}^2} \quad (3-28)$$

Further manipulation of (3.27) yields

$$(-m_{osc} A \omega_{osc}^2 - F_{T0} \cos \phi_T + kA) \sin(\omega_{osc} t) + (cA \omega_{osc} - F_{T0} \sin \phi_T) \cos(\omega_{osc} t) = 0 \quad (3-29)$$

Comparing coefficients gives,

$$F_{T0} \cos \phi_T = kA - m_{osc} A \omega_{osc}^2 \quad (3-30)$$

$$F_{T0} \sin \phi_T = cA \omega_{osc} \quad (3-31)$$

3.3.3. Total force coefficient and phase

Substituting eq. (3-11) to (3.14) into (3.10) also yields,

$$-m_{osc} A \omega_{osc}^2 \sin(\omega_{osc} t) + cA \omega_{osc} \cos(\omega_{osc} t) + kA \sin(\omega_{osc} t) = F_{T0} \sin(\omega_{osc} t + \phi_T) \quad (3-32)$$

The critical step is to nondimensionalize eq. (3-32) consistently. This equation represents the balance of forces in the y-direction and consequently *the stagnation pressure force in the x-direction is irrelevant*. Mathematically, the relevant factor is obviously kA ; which is also the magnitude of the force as measured by the spring deformation. Thus, eq. (3.32) becomes

$$\left[-\frac{m_{osc} \omega_{osc}^2}{k} \sin(\omega_{osc} t) \right] + \frac{c \omega_{osc}}{k} \cos(\omega_{osc} t) + \sin(\omega_{osc} t) = \left[\frac{F_{T0}}{kA} \right] \sin(\omega_{osc} t + \phi_T) \quad (3-33)$$

Expanding the right side of eq. (3-33) yields

$$\left(1 - \frac{m_{osc} \omega_{osc}^2}{k} \right) \sin(\omega_{osc} t) + \frac{c \omega_{osc}}{k} \cos(\omega_{osc} t) = \left[\frac{F_{T0}}{kA} \right] \sin(\omega_{osc} t) \cos \phi_T + \sin \phi_T \cos(\omega_{osc} t) \quad (3-34)$$

Separating the terms yields:

$$C_{T0} \cos \phi_T = 1 - \left[\frac{m_{osc} \omega_{osc}^2}{k} \right] \quad (3-35)$$

and

$$C_{T0} \sin \phi_T = \left[\frac{c \omega_{osc}}{k} \right] \quad (3-36)$$

where the total force coefficient C_{T0} and phase ϕ_T are the unknowns and amplitude A has vanished from the input quantities on the right side of eq. (3.35) and (3.36).

3.3.4. Velocity-force, coefficient, and phase

Next, we split $F_{Y,Total}$ into added mass force and the remaining component $F_U(t)$.

$$F_T(t) = F_A(t) + F_U(t) \quad (3-37)$$

Combining it with eq. (3-10) it yields:

$$F_{T0} \sin(\omega_{osc}t + \phi_T) = -m_A \ddot{y}(t) + F_U(t) \quad (3-38)$$

Or

$$(m_{osc} + m_A) \ddot{y}(t) + c \dot{y}(t) + ky(t) = F_U(t) \quad (3-39)$$

It should be noted that under the ideal conditions where all eq. (3-10 to 3-14) hold - that is, the oscillator response in FIO is a perfect single-frequency sinusoid - force $F_U(t)$ is the force component of the total force $F_T(t)$ in phase with velocity $\dot{y}(t)$ as proven in the next section (3.3.5).

In the actual experimental data, the difference $F_T(t) - F_A(t) - F_U(t)$ will not be zero as in eq. (3-37), but $F_R(t)$ accounting for nonlinear effects – such as the direct vortex effect. In fact, this value is plotted in Figures (4.1.n,4.3.n) and is referred to as F_{R0} as will be seen in Chapter 4.

Using eq. (3-39) and repeating the steps in Section 3.3.3 we have

$$(m_{osc} + m_A) \ddot{y}(t) + c \dot{y}(t) + ky(t) = F_{U0} \sin(\omega_{osc}t + \phi_U) \quad (3-40)$$

$$\left[m_{osc} + m_A + \frac{F_{U0} \cos \phi_U}{A \omega_{osc}^2} \right] \ddot{y}(t) + \left[c - \frac{F_{U0} \sin \phi_U}{A \omega_{osc}} \right] \dot{y}(t) + ky(t) = 0 \quad (3-41)$$

$$F_{U0} \cos \phi_U = kA - (m_{osc} + m_A) A \omega_{osc}^2 \quad (3-42)$$

$$F_{Uo} \sin \phi_U = cA \omega_{osc} \quad (3-43)$$

Nondimensionalizing (3.41) by kA gives

$$\left[-\frac{(m_{osc} + m_A) \omega_{osc}^2}{k} \right] \sin(\omega_{osc} t) + \left[\frac{c \omega_{osc}}{k} \right] \cos(\omega_{osc} t) + \sin(\omega_{osc} t) = \left[\frac{F_{Uo}}{kA} \right] \sin(\omega_{osc} t + \phi_U) \quad (3-44)$$

Expanding and matching $\sin(\omega_{osc} t)$ and $\cos(\omega_{osc} t)$ terms yields

$$C_{Uo} \cos \phi_U = 1 - \left[\frac{(m_{osc} + m_A) \omega_{osc}^2}{k} \right] \quad (3-45)$$

$$C_{Uo} \sin \phi_U = \left[\frac{c \omega_{osc}}{k} \right] \quad (3-46)$$

From eq. (3-41), it is observed that c_{added} is

$$c_{added} = \frac{F_{Uo} \sin \phi_U}{A \omega_{osc}} = \frac{2}{n T_{osc} (A \omega_{osc})^2} \int_0^{n T_{osc}} F_{Y,total}(t) \dot{y}(t) dt \quad (3-47)$$

3.3.5. Mandatory resonance

Eq. (3-40) represents a dynamical system in steady state forced oscillation. Applying the well-known response equations we have:

- Natural frequency

$$f_{n,water} = \frac{1}{2\pi} \sqrt{\frac{k}{m_{osc} + m_A}} \quad (3-48)$$

Substituting eq. (3-28) into (3-48) gives

$$f_{n,water} = \frac{1}{2\pi} \sqrt{\frac{k}{m_{osc} + \frac{F_{T0} \cos \phi_T}{A \omega_{osc}^2}}} \quad (3-49)$$

Substituting eq. (3-30) into (3-49) gives

$$f_{n,water} = \frac{1}{2\pi} \sqrt{\frac{k}{m_{osc} + \frac{kA - m_{osc}A\omega_{osc}^2}{A\omega_{osc}^2}}} \quad (3-50)$$

$$f_{n,water} = \frac{1}{2\pi} \sqrt{\frac{k}{m_{osc} + \frac{kA}{A\omega_{osc}^2} - m_{osc}}}$$

$$f_{n,water} = \frac{1}{2\pi} \omega_{osc} = f_{osc} \quad (3-51)$$

From eq. (3-51) we can make an important inference. *This process proves that when a dynamical system is in forced monochromatic oscillations in water and follows eq. (3-11) to (3-14), such as systems in FIO (VIV or galloping), the frequency of oscillation is its undamped natural frequency in water.*

This conclusion agrees with the experiments by [72] and the extensive data analysis by Garcia and Bernitsas (2018) [23]. It is also intuitively correct in FIO and leads to the eigen-relation in Section 3.4.

3.3.6. Phase-lead ϕ_U

To confirm that eqs. (3-10) and (3-40) lead to mandatory resonance with variable added mass, when eqs. (3-11) to (3-14) are assumed, we must show that force $F_U(t)$ and $\dot{y}(t)$ velocity are in phase, that is $\phi_U = \pi/2$. Comparing eq. (3-41) to eqs. (3-27 & 3-28), shows $\cos\phi_U = 0$ or $\phi_U = \pi/2$.

Alternatively, the phase for the forced system modeled by eq. (3-40) is

$$\tan\phi_U = \frac{2\zeta\frac{\omega_{osc}}{\omega_n}}{1 - \frac{\omega_{osc}^2}{\omega_n^2}} = \frac{2\zeta_{n,water}\frac{\omega_{osc}}{\omega_{n,water}}}{1 - \frac{\omega_{osc}^2}{\omega_{n,water}^2}} \quad (3-52)$$

$$\tan\phi_U = \frac{2\frac{c}{\sqrt{k(m_{osc} + m_A)}\omega_{n,water}}}{1 - \frac{\omega_{n,water}^2}{\omega_{n,water}^2}} \quad (3-53)$$

$$\tan\phi_U = \frac{2 \frac{c}{\sqrt{k(m_{osc} + m_A)}} 1}{1 - 1}$$

$$\tan\phi_U = \infty \quad (3-54)$$

3.4. Eigen-relation at the FSI Interface

In this section, we derive the eigen-relation which is indeed the crux of the mathematical derivation for this thesis. According to Section 3.2, fluid dynamics analysis confirmed that St_n (eq. 3-9) and Re are the only nondimensional groups required for modeling. Oscillator dynamics analysis revealed that consistent force nondimensionalization for FIO, based on kA and not on $0.5\rho DLU^2$, results in decoupling A from the FIO problem leading to an eigen-relation. It is an eigen-relation as explained in Section 3.4.2. Further, equation (3-51) is an interface constraint that can be recast as the sought eigen-relation below.

3.4.1. Eigen-relation

Combining eqs. (3-9) and (3-51) yields

$$St_n = \frac{f_{osc}}{f_{n,vac}} = f^* = \frac{f_{n,water}}{f_{n,vac}} = St_{FSI} = f_n^* \quad (3-55)$$

We use the symbol f_n^* to indicate the ratio of the two natural frequencies in eq. (3-51). Using the definitions of $f_{n,vac}$ and $f_{n,water}$ (eq. 3-51), and substituting into eq. (3-55), we have

$$\frac{1}{f^{*2}} = \frac{f_{n,vac}^2}{f_{n,water}^2} = \frac{1/4\pi^2 (k/m_{osc})}{1/4\pi^2 (k/(m_{osc} + m_A))} \quad (3-56)$$

$$\frac{1}{f^{*2}} = \frac{m_{osc} + m_A}{m_{osc}} \quad (3-57)$$

Dividing the right side of eq. (3-57) throughout by m_{osc} gives

$$\frac{1}{f^{*2}} = 1 + \frac{m_A}{m_{osc}} \quad (3-58)$$

$$\frac{1}{f^{*2}} - 1 = \frac{m_A}{m_{osc}} \quad (3-59)$$

Recall

$$m^* = \frac{m_{osc}}{m_d}$$

Dividing the right side of eq. (3-57) throughout by m_d gives

$$\frac{1}{f^{*2}} = \frac{m_{osc}/m_d + m_A/m_d}{m_{osc}/m_d} = \frac{m^* + C_a}{m^*} \quad (3-60)$$

$$\frac{1}{f^{*2}} = 1 + \frac{C_a}{m^*} \quad (3-61)$$

$$\frac{1}{f^{*2}} - 1 = \frac{C_a}{m^*} \quad (3-62)$$

Equations (3-59) and (3-62) are equivalent. Combining both gives the eigen-relation as shown in eq. (3-63). In subsequent sections, the importance of eq. (3-63) is discussed.

$$\frac{m_A}{m_{osc}} = \frac{C_a}{m^*} = \frac{1}{f^{*2}} - 1 \quad (3-63)$$

In eq. (3-63), f^* is the nondimensional frequency of cylinder oscillation. The eigen-relation is the black line in Fig. 3.2 shown along with the force coefficients and phases derived in Section 3.5 below. Note that the eigen-relation is also *independent* of the system damping.

Table 3A. Eigen relation

$$\frac{m_A}{m_{osc}} = \frac{C_A}{m^*} = \frac{1}{f^{*2}} - 1$$

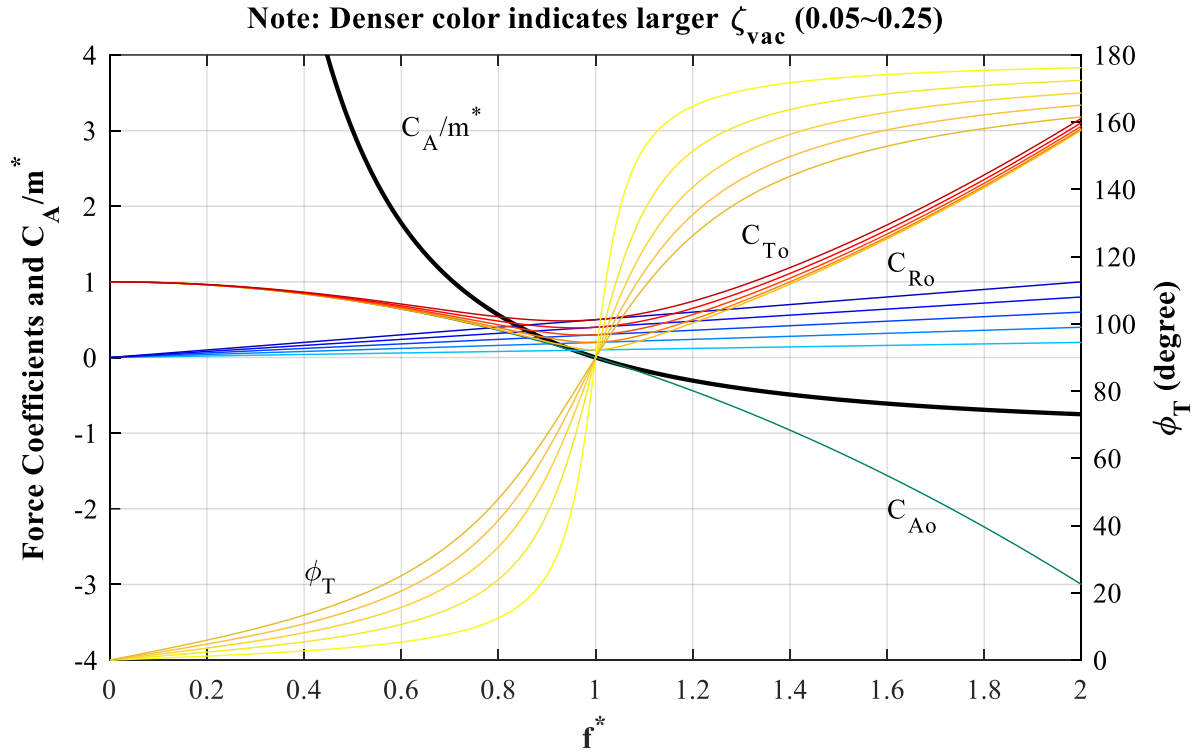


Fig. 3.2. Theoretical results for a cylinder (circular or not) in FIO (VIV, galloping). (a) Eigen-relation: C_A/m^* eq. (3-63). (b) Added mass force coefficient C_{Ao} eq. (3-71). (c) Total force coefficient C_{To} eq. (3-78). (d) Total force phase lead ϕ_T [degree] eq. (3-79). (e) Velocity-force coefficient C_{Uo} eq. (3-75).

3.4.2. Use of the term eigen-relation in this thesis

Conventionally, eigenvalue problems are defined as follows:

“Let $T:V \rightarrow V$ be a linear transformation from a vector space V to itself. We say that λ is an eigenvalue of T if there exists a nonzero vector $v \in V$ such that $T(v) = \lambda v$.”

A 1x1 scalar matrix consists of a single element, whose determinant is simply the value of that element - therefore, such a matrix is invertible unless it is equal to the 1x1 zero matrix. Eigen

relation (3-63) derived above is as one such 1x1 scalar matrix, which like all non-zero square matrices is invertible and has an eigenvalue.

In this research, the word “eigen-relation” is used in its generic form: It is a relation between forcing and system properties that has to hold for a nontrivial solution to exist. Such as the Euler linear buckling load equation, the dispersion relation in free surface linear wave theory, the natural frequency of a linear oscillator, etc. In the linear VIV and galloping oscillations eq. (3-63) is the eigen relation that has to hold for a single frequency response to exist.

Equation (3-63) serves as a “characteristic or benchmark” equation for the solution to exist and from there other response of the oscillator (forces) are derived. It is a characteristic equation for FSI problems in the sense that we can pick an f^* at any point of the oscillator and define the oscillator response at that point. The one response that cannot be defined – as in all linear eigen solutions – is the amplitude of oscillation. This would be discussed further in subsequent sections of this chapter.

In summary, the term “eigen-relation” is used in its generic form, which means that a specific relation has to hold for a nontrivial solution to exist.

3.4.3. The nature of eigen-relation (3A)

There are several features of eq. (3-63) that require discussion.

- For a given dimensionless frequency of oscillation f^* , a property of the oscillator at the interface is defined. That is, C_A/m^* is set for FSI to occur at f^* . *Its value is independent of the amplitude of oscillation.* The analogy of eq. (3-63) to the Eigen-relation of the free surface waves

$$\omega^2 = kg \tanh(kd) \tag{3-64}$$

where $k = 2\pi/\lambda$ is the wave number, λ is wavelength, and d is water depth, can help illustrate the use of eq. (3-63) In both cases, the frequency of the oscillator at the interface is selected resulting in unique properties of the oscillator; λ for waves and C_A/m^* for the FSI oscillator. That is, in both cases, oscillations of different frequencies are dispersed. A cannot be defined by either Eigen-relation. The linear wave-dispersion relation eq. (3-64) for waves (also valid to second order) does not include A .

- A can be defined by external factors related to entry energy-level and energy-capacity of the oscillator. For waves, as wind transfers energy into the water-air interface, a minimum level is needed to initiate a longer wave, and too much energy will result in wave breaking and energy transfer to longer waves. In the FSI oscillator, a minimum energy level is needed to overcome the Coulomb friction, opposing tip-effects, and other damping of the oscillator with the specific C_A/m^* value and to initiate FSI at a specific f^* . Excessive energy put into the oscillator will terminate the FSI as the vortex streets modify the driving force.

- A most important point in this discussion is the involvement of damping in the Eigen-relation. The system damping does not appear in the Eigen-relation. Damping will be involved in the onset and termination of FIO.

3.5. Force Coefficients

Based on Section 3.3, explicit force coefficient equations are derived. Those are independent of amplitude A due to the consistent nondimensionalization of force by kA . These force coefficients are derived as shown in this section and their formulae are tabulated in table (3B).

3.5.1. Added-mass force coefficient C_{Ao}

From eq. (3-38), we have

$$F_A(t) = -m_A \ddot{y}(t) = k A C_{Ao} \sin(\omega_{osc} t) \quad (3-65)$$

$$F_A(t) = -m_A \ddot{y}(t) = m_A A \omega_{osc}^2 \sin(\omega_{osc} t) = k A C_{Ao} \sin(\omega_{osc} t) \quad (3-66)$$

From eq. (3-65), using the eigen-relation (3-63), we have

$$C_{Ao} = \frac{m_A A \omega_{osc}^2}{k A} \quad (3-67)$$

Recall from eq. (3-51) that $\omega_{osc} = \omega_{n,water}$, hence

$$C_{Ao} = \frac{m_A A \omega_{n,water}^2}{k A} = \frac{m_A \omega_{n,water}^2}{k} \quad (3-68)$$

Substituting $\omega_{n,water}^2 = \frac{k}{m_{osc} + m_A}$ into eq. (3-68) yields

$$C_{Ao} = \frac{m_A}{m_{osc} + m_A} = \frac{m_A/m_d}{m_{osc}/m_d + m_A/m_d} = \frac{C_A}{C_A + m^*} \quad (3-69)$$

From the eigen relation in eq (3-63),

$$\frac{C_A}{m^*} = \frac{1 - f^{*2}}{f^{*2}} \quad (3-70)$$

Dividing eq (3-69) throughout by m^* and substituting (3-70) into the expression, we have

$$C_{Ao} = \frac{C_A/m^*}{C_A/m^* + m^*/m^*} = \frac{\frac{1 - f^{*2}}{f^{*2}}}{\frac{1 - f^{*2}}{f^{*2}} + 1} = \frac{1 - f^{*2}}{f^{*2}} \bigg/ \frac{1}{f^{*2}}$$

$$C_{Ao} = 1 - f^{*2} \quad (3-71)$$

C_{A0} (eq.3-71) is shown in Fig. 3.2 (green solid line) and is independent of damping like the FIO Eigen-relation relation. The added mass force is the dominant driver of FIO but not over the entire f^* range. As Fig.3.2 shows, in the vicinity of $f^*=1$ when the frequency of oscillation is near $f_{n,vac}$, the added mass force is nearly zero and the dominant force is the velocity-force. *The vortices, albeit applying small forces directly, modify the flow through the vortex street making the added mass force or the velocity-force dominant depending on f^* . Vortices are the dominant player in VIV by modifying the flow, not by direct force application.* We discuss this in greater details in chapter five where VIV and galloping characteristics are compared.

3.5.2. In-phase-with-velocity force coefficient C_{Uo}

From eq. (3-46), we derive C_{Uo} , which depends linearly on f^* and on damping ratio ζ_{vac} as shown by the blue lines in Fig. 3.2. As can be seen from eq. (3B) and fig 3.2, C_{Uo} is in general the smaller component of C_{To} except in the vicinity of ($C_A/m^*=0, f^*=1$).

From (3-46) we have,

$$C_{Uo} \sin\phi_U = \frac{c\omega_{osc}}{k}$$

Since the velocity force $F_u(t)$ is the force component of the total force in phase with the velocity, $\sin\phi_U = 1$, also recall from (3-50) that at resonance, $\omega_{osc} = \omega_{n,water}$ hence (3-46) becomes

$$C_{Uo} = \frac{c\omega_{osc}}{k} = \frac{c\omega_{n,water}}{k} \quad (3-72)$$

Substituting the expression for $\omega_{n,water}$ into (3-72) yields

$$C_{Uo} = \frac{c}{k} \sqrt{\frac{k}{m_{osc} + m_A}} = \frac{c}{\sqrt{k}\sqrt{k}} \frac{\sqrt{k}}{\sqrt{m_{osc} + m_A}}$$

$$C_{Uo} = \frac{c}{\sqrt{k(m_{osc}+m_A)}} = 2\zeta_{n,water} \quad (3-73)$$

Further manipulation of eq (3.73) gives,

$$C_{Uo} = \frac{c}{\sqrt{m_{osc}k}} \sqrt{\frac{m_{osc}}{(m_{osc}+m_A)}} \quad (3-74)$$

From eq. (3-57), $f^* = \sqrt{\frac{m_{osc}}{(m_{osc}+m_A)}}$ and Recall that $\zeta_{vac} = \frac{c}{2\sqrt{m_{osc}k}}$, Substituting these into eq (3.74) gives

$$C_{Uo} = 2\zeta_{vac}f^* \quad (3-75)$$

3.5.3. Total force coefficient C_{T_o}

From eq. (3-35) and (3-36), we derive C_{T_o} , which is a function of f^* and damping ratio ζ_{vac} . It is shown by the red lines in Fig. 3.2. As can be seen in equations in table (3B), depending on the value of ζ_{vac} , for $f^* \neq 0$, C_{A_o} is the dominant C_{T_o} component. Below is the derivation for the total force coefficient.

Squaring eq. (3-35) and (3-36) then adding them together gives

$$C_{T_o}^2 (\cos^2 \phi_T + \sin^2 \phi_T) = \left(1 - \left[\frac{m_{osc}\omega_{osc}^2}{k}\right]\right) \left(1 - \left[\frac{m_{osc}\omega_{osc}^2}{k}\right]\right) + \left(\left[\frac{c\omega_{osc}}{k}\right]\right) \left(\left[\frac{c\omega_{osc}}{k}\right]\right) \quad (3-76)$$

Recall that $(\cos^2 \phi_T + \sin^2 \phi_T) = 1$, hence eq (3-75) becomes

$$C_{T_o} = \sqrt{\left(1 - \left[\frac{m_{osc}\omega_{osc}^2}{k}\right]\right) \left(1 - \left[\frac{m_{osc}\omega_{osc}^2}{k}\right]\right) + \left(\left[\frac{c\omega_{osc}}{k}\right]\right) \left(\left[\frac{c\omega_{osc}}{k}\right]\right)} \quad (3-77)$$

Substituting eq. (3-71,3-72 and 3-73) into (3-77), we have

$$C_{T_o} = \left[(1 - f^{*2})^2 + (2\zeta_{vac}f^*)^2\right]^{0.5} \quad (3-78)$$

The force coefficients eqs. (3-71, 3-75, and 3-78) are summarized in table 3B below.

Table 3B. Force coefficients equations

Added-mass force coefficient	$C_{Ao} = 1 - f^{*2}$
In-phase-with-velocity force coefficient	$C_{Uo} = 2\zeta_{vac}f^*$
Total force coefficient	$C_{To} = [(1 - f^{*2})^2 + (2\zeta_{vac}f^*)^2]^{0.5}$

3.6. Force Phases

Based on eq. (3-66), $\phi_A = -\pi$. From eq. (3-54) $\phi_U = \pi/2$. From eqs. (3-35 and 3-36), we derive ϕ_T shown by the yellow lines in Fig 3.2 and equations in Table 3C. The derivation of ϕ_T is shown below.

Dividing eq. (3-35) by (3-36) gives

$$\frac{C_{To} \sin \phi_T}{C_{To} \cos \phi_T} = \frac{\left[\frac{c \omega_{osc}}{k} \right]}{1 - \left[\frac{m_{osc} \omega_{osc}^2}{k} \right]}$$

Recall that $\sin \phi_T / \cos \phi_T = \tan \phi_T$. Substituting this and eqs. (3-71, 3-72 and 3-75) into the above expression gives

$$\tan \phi_T = \frac{2\zeta_{vac}f^*}{1-f^{*2}} = \frac{C_{Uo}}{C_{Ao}} \quad (3-79)$$

Table 3C. Force Phases

Added-mass force phase	$\phi_A = -\pi$
In-phase-with-velocity force phase	$\phi_U = \pi/2$
Total force phase	$\tan\phi_T = \frac{2\zeta_{vac}f^*}{1-f^{*2}} = \frac{C_{Uo}}{C_{Ao}}$

3.7. Force Reconstruction

Based on the equations in Tables 3B and 3C, for a given amplitude of oscillation A , we can reconstruct the forces exerted on a cylinder in FIO as shown in Table 3D.

Table 3D. Force Reconstruction

Added-mass force	$F_A(t) = kAC_{Ao} \sin(\omega_{osc}t)$
In-phase-with-velocity force	$F_U(t) = kAC_{Uo} \cos(\omega_{osc}t)$
Total force	$F_T(t) = kAC_{To} \sin(\omega_{osc}t + \phi_T)$

The necessary steps involved in FIO calculations are summarized below:

- For a given oscillator, oscillating at f_{osc} , eq. in Table 3A provides the oscillator added mass coefficient C_A .
- The force coefficients can be calculated from eqs. in table (3B), which show their dependence on parameters eliminating speculations on forms of a mass-damping parameter.
- The force-phases are given by equations in Table 3C.
- The previous steps can be followed in Fig. 3.2.

- The amplitude A can be specified from measurement or for modeling. This depends on the oscillating body mechanics and energy transfer; e.g., different oscillators may have different Coulomb friction, different tip-flow effects affecting the lift vs. drag length of the cylinder, etc. As long as FIO is initiated by energy transfer, eqs. in Tables 3A - 3C hold.
- Finally, the forces are reconstructed using equations in Table 3D.

Chapter Four

Experimental Validation and Results

4.1. Introduction

This chapter validates the eigen-relation theory presented in Chapter three. Results from smooth cylinders and cylinders with passive turbulence stimulation are presented in this chapter in comparison to the theory presented in Chapter 3.

In Section 4.2, some inferences were discussed based on the theory developed in Chapter three and the experimental data analyzed.

Section 4.3 shows the results obtained experimentally for a PTC (Passive Turbulence Control) cylinder. One data set is presented in Section 4.3. More data are presented in Appendix B and the complete set of experiments are published in MRELab Report #13 and #14 [46,47].

Section 4.4 shows the results obtained for a smooth cylinder experimentally. One data set is presented here. More data are presented in Appendix A and the complete set of experiments are published in the MRELab Report #13 [46].

The results presented in this chapter demonstrate experimentally that an eigen-relation exists for transverse flow induced oscillations at the fluid structure interface. Furthermore, as seen in the results presented in Sections 4.3 and 4.4, these solutions are truly in alignment with experimental results for both VIV and galloping.

The theoretical formulas developed in Chapter 3, predict very accurately experimental results for FIO of a single cylinder on elastic supports. Both smooth cylinders and cylinders with turbulence stimulation (in the form of PTC) have been tested showing that the theoretical formulas collapse the VIV and galloping experimental results well. The theory developed in Chapter three, as validated by the experimental data in this chapter, is a totally novel approach to FIO and (a) explains all observations made experimentally on VIV and several on galloping, and (b) enables pursuing higher order terms in FIO which is briefly addressed in Section 5.10 but is beyond the scope of this thesis.

The theory is proven to be accurate in the results shown in Sections 4.3, 4.4 and in the two appendices for Single Cylinders (Smooth and PTC). Several different sets of experimental results for linear oscillators are analyzed using the developed theory. Data sets for both smooth cylinder and cylinders with passive turbulence stimulation, with system damping ratio ranging from 0.02 to 0.26, mass ratio from 1.007 to 1.984 and stiffness ranging from 400 to 1200N/m in the TrSL3 flow regime, where the lift coefficient is high due to fully turbulent shear layers are analyzed for theory validation.

4.2. Conclusions Based on the Theory and Data Analysis

4.2.1. Eigen-relation

Equation in Table (3A) has been verified based on the data collected in the MRELab under the assumptions of the theory. It is valid for any form of FIO as long as there is a predominant f_{osc} . This is clear in VIV and galloping (Figs. 4.3 and 4.4). It is also clear in transition from VIV to galloping because in this dataset the onset of galloping occurs before the lower VIV branch and desynchronization are reached. Figures 4.1 and 4.2 show that for a cylinder which is smooth and consequently does not undergo galloping, the eigen-relation holds down to the last VIV oscillation.

4.2.2. Strouhal number St_n

The equation in Table (3A) depends only on the generic and relevant St_n , which is equal to f^* .

Eq. (3-63) is independent of the response amplitude A and determines the ratio of the added mass coefficient to mass-ratio (C_A/m^*), which defines the oscillator properties. That is, the oscillator properties are decoupled from the response amplitude. Also, Re does not appear to define the oscillator in any way; it defines the energy into the oscillator as discussed next.

4.2.3. Reynolds Number Re

Along with the generic Strouhal number St_n , Reynold's number Re fully defines the FIO. Re is not involved in the oscillator definition. It is obvious that it is coupled with A . Re , being proportional to velocity and body-size, defines the energy that can be transmitted from fluid to body, while amplitude defines the energy that can be absorbed by the oscillator at a given frequency. Indeed, as the fluid velocity increases and shear layers become fully turbulent (from TrSL2 to TrSL3 flow regime) the peak amplitude of oscillation A in VIV increases from about 1 to about 2, [50]. The lower branch gradually disappears; it is very broad in TrSL2 Govardhan, R.N., Williamson, C.H.K., (2006), Williamson, C.H.K., Govardhan,R,(2004) [26,78]; and it is barely noticeable in TrSL3 [6,7,11,16,40,65].

4.2.4. FSI Interface

The oscillator is the common boundary between the structure and the fluid. The boundary condition is the oscillator dynamics providing the eigen-relation to the FSI problem. The solution was revealed by consistent nondimensionalization of the oscillator dynamics by force kA rather than the irrelevant stagnation pressure force ($0.5\rho DLU^2$). In the VIV/transition/galloping problem, the eigen-solution is eq. (3A). Figs. 4.1d, 4.3d, and all graphs in Figs. 4.3-4.6 confirm it by comparison to experiments.

In the next chapter (five) of this thesis, several facts on VIV and galloping, that have been observed and established since the 1960's, will be properly discussed and explained based on the developed theory.

4.3. Comparison between Theory and Experiments for Cylinder with Turbulence

Stimulation

Figures 4.1 and 4.2 below show the results obtained by employing the eigen-relation discussed in Chapter 3 and the ensuing force expressions to analyze one set of experimental data on cylinders with passive turbulence stimulation.

Corresponding to Fig. 4.1 are Figures B1, B3, B5, ... B31 in Appendix B and Figures 4 in Report #13 [46].

Corresponding to Fig. 4.2 are Figures B2, B4, B6, ... B32 in Appendix B and Figures 5 in Report #13 [46].

The mass ratio m^* for Figs 4.1 and 4.2 is 1.685 with stiffness of 400N/m. The theoretical results are marked as “-----”; the values calculated by theoretically at points where experimental data is available by “oooo”; and the corresponding experimental value by “++++”. The different colors in the figures show the different stages of FIO. These stages are consistent with the way they have been defined in the literature over the years. For instance, in Feng (1968) [19], there were two amplitude branches, the ‘initial’ branch and the ‘lower’ branch. Later in 1999, Khalak and Williamson defined another branch, between the previous two branches called the ‘upper response branch’. Williamson and Govardhan (2004) [78] showed in their work the initial excitation stage, the upper branch, the lower branch, and the desynchronization region.

All the figures in this thesis with the exception of those in chapter 3 use circles for theoretical predictions and crosses for experimental measurements and different colors (see Nomenclature)

for different response branches to facilitate understanding the differences and limits between VIV, transition from VIV to galloping, and fully developed galloping stage. The blue colored points are the initial and upper VIV branches, the red colored points are the lower VIV branch and desynchronization region, the green colored points falls in the transition region between VIV and galloping, at this point the flow is partly turbulent and finally the black colored points are the fully developed galloping phase. The highest amplitude occurs in this region.

Fig. 4.1 presents VIV and galloping data for a circular cylinder with turbulence stimulation. The time history of displacement $y(t)$ is the only direct experimental measurement. Derived from $y(t)$ are the dominant frequency f_{osc}^* and the reconstructed total force $F_T(t)$.

In Fig. 4.1, the important response properties of the oscillator are plotted versus f^* or $U_{n,vac}^*/U/Re$ as follows:

- Fig. 4.1.a: Amplitude ratio A^* vs. $U_{n,vac}^*/U/Re$. The various VIV branches, transition from VIV to galloping, and galloping are clearly visible. In transition, both mechanisms of VIV and galloping coexist and contribute to the fast increase in amplitude. In fully developed galloping vortex shedding desynchronizes and acts out of phase with the galloping mechanism – sometimes enhancing and sometimes opposing galloping. In fully developed galloping, the amplitude exhibits a plateau due to the limits of the facility. If the length of the oscillator rails was unlimited the amplitude would increase till a stop or spring were hit.
- Fig. 4.1.b: f^* vs. $U_{n,vac}^*/U/Re$. It shows the relation between the two variables which are used as independent variables for presenting the results.
- Fig. 4.1.c: Amplitude ratio A^* vs. f^* . It shows how data collapse differently from Fig. 4.1.a. Particularly the data in the galloping region, collapse on a single f^* point regardless of the flow velocity U .

- Fig. 4.1.d: Ratio of added mass coefficient and mass ratio vs f^* . It shows the eigen relation eq. 3A. The graph shows how closely the experimental results follow the eigen relation and that the ratio $C_A/m^*=m_A/m_d$ is constant.
- Fig. 4.1.e: Added mass coefficient vs f^* . This is a figure derived directly from the eigen-relation after multiplying C_A/m^* in Fig. 4.1.d by m^* . It shows the dependence of C_A on f^* . From the beginning of VIV, C_A starts decreasing in order to maintain the nonlinear resonance. At the end of synchronization, as the galloping mechanism starts becoming stronger, C_A returns to non-VIV values and reaches a constant value of 0.8 in fully developed galloping. That value stays constant in galloping.
- Fig. 4.1.f: Theoretical added mass coefficient C_{Ao} vs f^* . The next value to be calculated is that of the added mass force coefficient. The experimental values fall exactly inside the circles on the theoretical line.
- Fig. 4.1.g: Added mass force magnitude F_{Ao} vs. f^* . This shows the theoretical force in phase with the acceleration. As expected, following Fig. 4.1.f for C_{Ao} , F_{Ao} in Fig. 4.1.g also shows the experimental values falling exactly inside the circles on the theoretical line.
- Fig. 4.1.h: Total force coefficient C_{To} vs. f^* . The total force coefficient is calculated from eq (3B)
- Fig. 4.1.i: Total force phase ϕ_T vs. f^* . It shows the phase angle between the total force and the displacement $y(t)$.
- Fig. 4.1.j: Total force magnitude F_{To} vs. f^* . Here is where we would expect some differences accounting for the higher order terms. That is, F_{To} contains the two first order terms in phase with the velocity F_{Uo} and the acceleration F_{Ao} plus the higher order terms or F_{Ro} .

- Fig. 4.1.k: Coefficient C_{Uo} of force in-phase with velocity vs. f^* . This also exhibits excellent agreement between theory and experiments.
- Fig. 4.1.l: Force in-phase with velocity F_{Uo} vs. f^* . This also exhibits excellent agreement between theory and experiments as expected following the agreement of C_{Uo} with experiments.
- Fig. 4.1.m: Residuary force coefficient C_{Ro} vs. f^*
- Fig. 4.1.n: Residuary force F_{Ro} vs. f^*
- Fig. 4.1.o: Ratio F_{Ro}/F_{To} [%] of vs. f^*

The last three figures include all the nonlinear terms which are beyond the eigen-relation and linear theory. This information is used to discuss the magnitude of the vortex force in Section 5.10.

Figure 4.1. Circular cylinder with turbulence stimulation, $m^*=1.685$, $k=400\text{N/m}$, $\zeta_{vac}=0.06$; $D=8.89\text{cm}$ (3.5"), $L=90.17\text{cm}$ (35.5") Theoretical and experimental comparison of FSI (VIV) properties plotted vs. f^*
 (a) ---- Theory using eqs. (3A)-(3D). (b) $\circ\circ\circ\circ$ Reconstructed based on theory and measured f^* . (c) $++++$ Measured experimentally

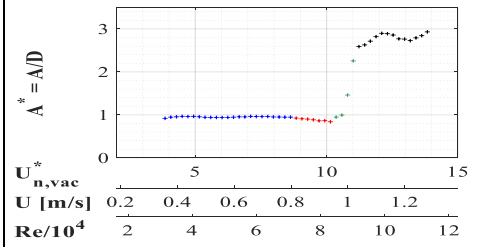


Fig. 4.1.a. Amplitude ratio $A^*=A/D$

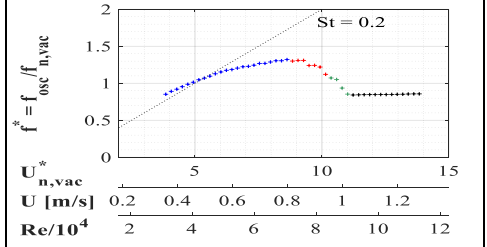


Fig. 4.1.b. $f^*=f_{osc}/f_{n,vac}$

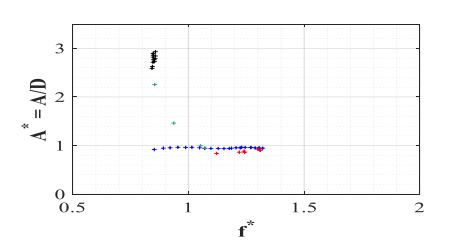


Fig. 4.1.c. $A^*=A/D$ vs. f^*

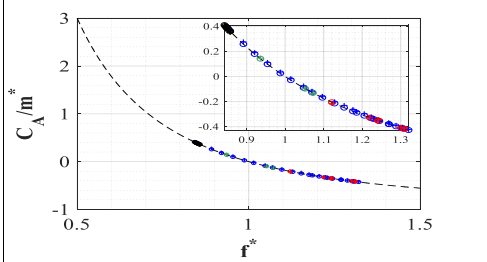


Fig. 4.1.d. Eigen-relation C_A/m^* ; ---Theory using eq. (3A).

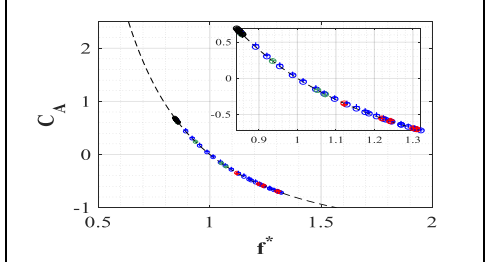


Fig. 4.1.e. Added mass coefficient C_A vs. f^* ; ---Theory using eq. (3A) and m^*

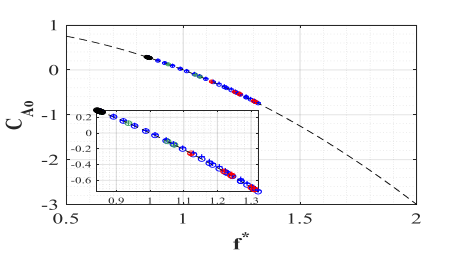


Fig. 4.1.f. Added-mass force coefficient C_{A0} ; ---Theory using eqs. (3B)

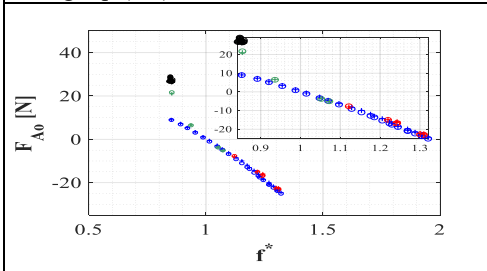


Fig. 4.1.g. Added mass force F_{A0} vs. f^*

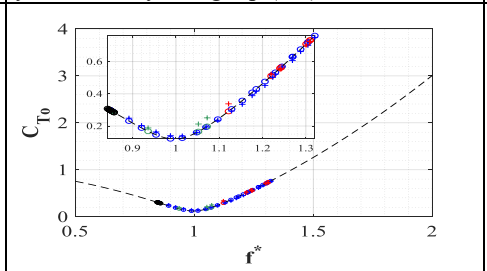


Fig. 4.1.h. Total force coefficient C_{T0} vs. f^*

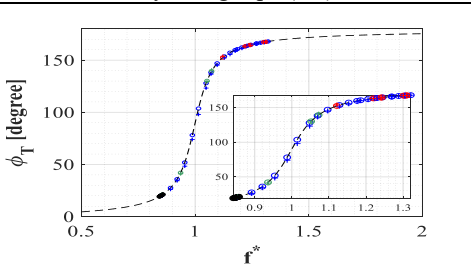
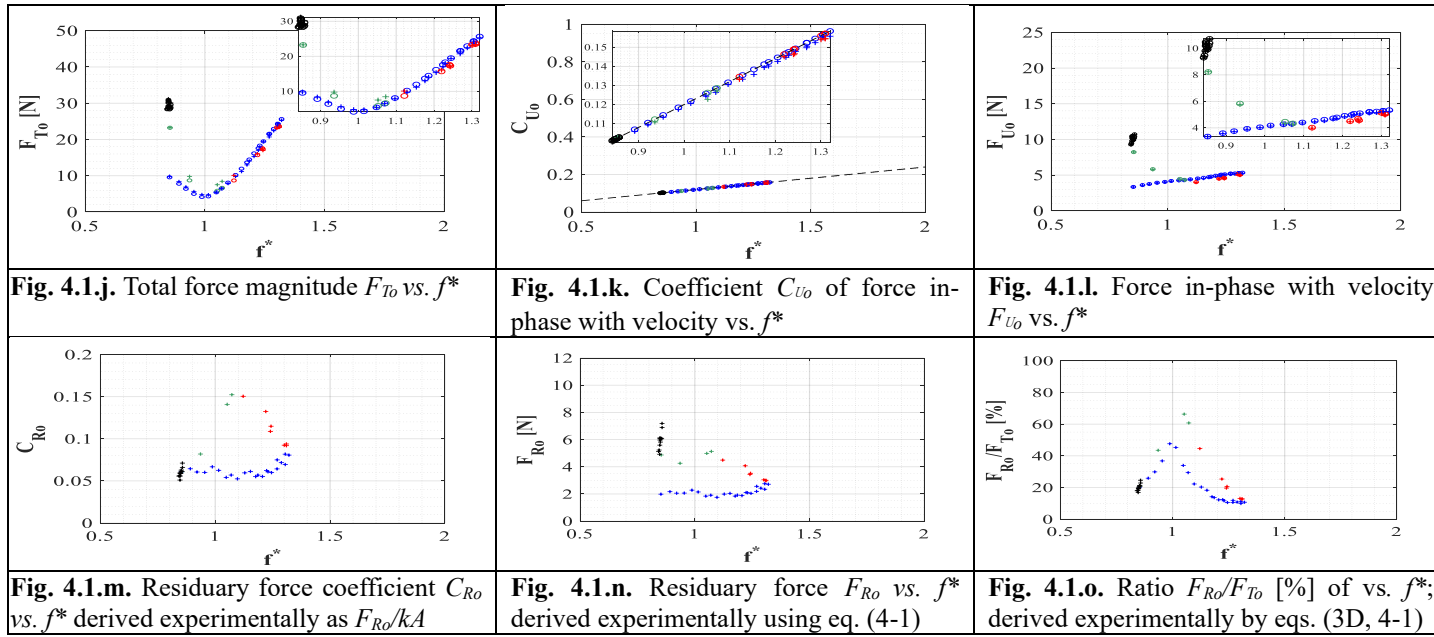


Fig. 4.1.i. Total force phase ϕ_T vs. f^*



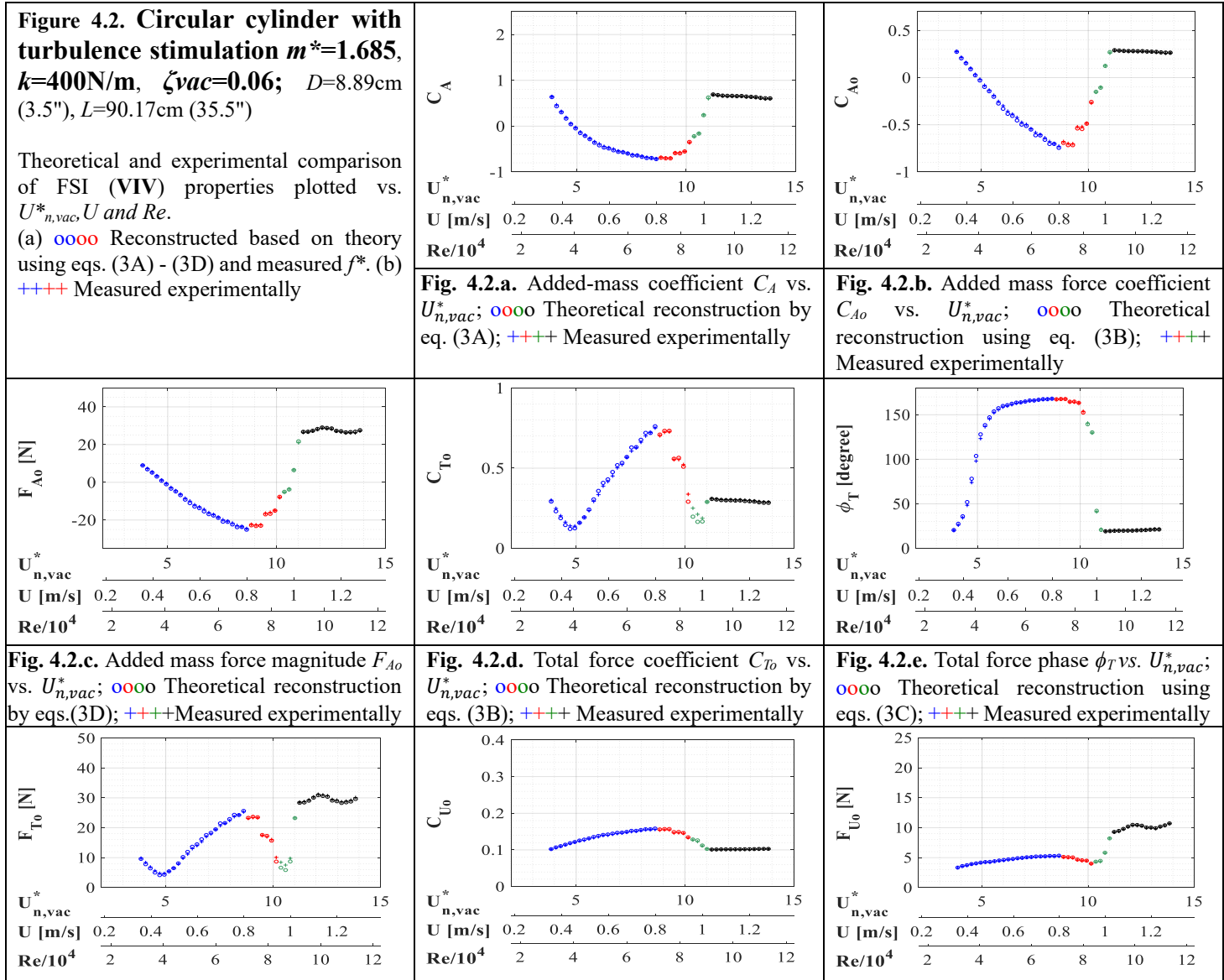
A few more observations on the figures in Fig. 4.1. follow. The figures in the first row (Figs 4.1.a-c) of fig 4.1 describe some interesting facts about the amplitude ratio A^* in details. A closer look at them show that they are closely related. The maximum amplitude occurs at the last point as expected because at this point galloping is fully developed and flow is fully turbulent. A^* is approximately 3.0 at this point (Fig 4.1a), and f^* is approximately 0.85 (Fig 4.1b). Also, from Fig 4.1b, it is interesting to note that f^* increases steadily up to the final point of the initial and upper branch of VIV at which point its value is about 1.32. From lower branch, the value of f^* starts decreasing steadily up until the point where galloping starts. f^* remains constant at galloping region and it has approximately the same value as it does at the beginning of initial VIV excitation. This observation is more pronounced in fig 4.1c as all the black points falls on the same point on the f^* axis. The question of f^* value ($f^*=0.85$) being the same at the onset of VIV and fully developed galloping would be discussed further in chapter 6. All the above observations described for the amplitude of oscillation can be verified as seen in the first row of all the odd numbered figures in Appendix B(for instance B1.a-c, B3.a-c,B5.a-c) and also in MRELab report #13 [46]. The same results hold even at higher damping values and higher stiffness.

Figures in the next row 4.1d-f show the added mass coefficients. Fig 4.1f is directly derived from eq. (3-71). It shows the theoretical and derived added mass coefficient. Which is one of the variables used to derive the theoretical added mass force shown in fig 4.1g. Lastly, the residuary force F_R derived experimentally is obtained as shown in eq. (4-1). Figs 4.1m and 4.1o show the residuary force coefficient and residuary force respectively.

Oscillator properties plotted in Fig 4.1 are replotted in Fig. 4.2 vs. $U_{n,vac}^*$, U , Re since readers are more familiar with $U_{n,vac}^*$ as the independent variable. It should be reminded though that neither $U_{n,vac}^*$ nor KC are the primary Strouhal number St_n related to FIO which has been shown in chapter 3.

- Fig. 4.2.a: Added mass coefficient C_A vs $U_{n,vac}^*/U/Re$.
- Fig. 4.2.b: Theoretical added mass coefficient C_{Ao} vs $U_{n,vac}^*/U/Re$.
- Fig. 4.2.c: Added mass force magnitude F_{Ao} vs. $U_{n,vac}^*/U/Re$. This shows the theoretical force in phase with the acceleration.
- Fig. 4.2.d: Total force coefficient C_{To} vs. $U_{n,vac}^*/U/Re$.
- Fig. 4.2.e: Total force phase ϕ_T vs. $U_{n,vac}^*/U/Re$. It shows the phase angle between the total force and the displacement $y(t)$.
- Fig. 4.2.f: Total force magnitude F_{To} vs. $U_{n,vac}^*/U/Re$. As discussed for Fig 4.1.j, we expect some slight differences between the theory and experiments here because higher order terms are being accounted for. That is, F_{To} contains the two first order terms in phase with the velocity F_{Uo} and the acceleration F_{Ao} plus the higher order terms or F_{Ro} .
- Fig. 4.2.g: Coefficient C_{Uo} of force in-phase with velocity vs. $U_{n,vac}^*/U/Re$. Theoretical C_{Uo} Obtained from eq. (3B), this exhibits excellent agreement between theory and experiments.
- Fig. 4.2.h: Force in-phase with velocity F_{Uo} vs. $U_{n,vac}^*/U/Re$. This also shows excellent agreement between theory and experiments as expected following the agreement of C_{Uo} with experiments.
- Fig. 4.2.i: Residuary force coefficient C_{Ro} vs. $U_{n,vac}^*/U/Re$.
- Fig. 4.2.j: Residuary force F_{Ro} vs. $U_{n,vac}^*/U/Re$.
- Fig. 4.2.k: Ratio F_{Ro}/F_{To} [%] of vs. $U_{n,vac}^*/U/Re$.

As mentioned earlier, the last three figures include all the nonlinear terms which are beyond the eigen-relation and linear theory. This information is used to discuss the magnitude of the vortex force in Section 5.10.



<p>Fig. 4.2.f. Total force magnitude F_{To} vs. $U_{n,vac}^*$; $\circ\circ\circ$ Theoretical reconstruction by eqs. (3D); $++++$ Measured experimentally</p>	<p>Fig. 4.2.g. Coefficient C_{ν_0} of force in-phase with velocity vs. $U_{n,vac}^*$; $\circ\circ\circ$ Theoretical reconstruction by eqs. (3B); $++++$ Measured experimentally</p>	<p>Fig. 4.2.h. Force in-phase with velocity F_{ν_0} vs. $U_{n,vac}^*$; $\circ\circ\circ$ Theoretical reconstruction by eqs.(3D); $++++$ Measured experimentally</p>
<p>Fig. 4.2.i. Residuary force coefficient C_{Ro} vs. $U_{n,vac}^*$ derived experimentally as F_{Ro}/kA</p>	<p>Fig. 4.2.j. Residuary force magnitude F_{Ro} vs. $U_{n,vac}^*$ derived experimentally by eq. (4-1)</p>	<p>Fig. 4.2.k. Ratio F_{Ro}/F_{To} [%] of vs. $U_{n,vac}^*$; derived experimentally by eqs. (3D, 4-1)</p>

Fig. 4.2 clearly show the reduced velocities at which the different stages of FIO begin and terminates.

From fig 4.2a, we can infer that galloping starts at a reduced velocity of about 11. This is not always the case as seen for the same stiffness and damping ratio but different mass ratio. for $m^* = 1.007$ (Fig. B2.a) galloping starts at about reduced velocity of 7.5. For $m^* = 1.34$ (Fig B10.a), it starts at 10, while for $m^* = 1.89$ (Fig B26.a) it starts at 12. Hence, we conclude that the higher the mass ratio m^* , the later the reduced velocity at which initiation of galloping starts. More discussion on this in chapters 5 and 6.

Both Fig 4.2a and Fig 4.2b show the calculated added mass. The difference though is that 4.2b is the theoretical calculated added mass derived directly from the formula. Eq (3-71) while 4.2a is derived as shown in Section 3.3.2. It is interesting to note that they both have the same trajectory despite the way they are calculated.

Fig 4.2e shows the phase of the total force with the displacement. Looking closely, we see that the phase angle gets to about 170 degree at the upper VIV branch after which it starts to drop.

According to eq. (3-37), the vector sum of the added mass force (Fig 4.2c) and force in phase with the velocity (Fig 4.2h) gives the total force F_{T0} (Fig 4.2f). Note that even though some of the values in the added mass force fig 4.2c are negative, the added mass force phase is negative as shown in table 3C and hence when combined vectorially with Fig 4.2h, gives the total force as shown in Fig 4.2f. This is in agreement with Fig 4.2f and fig 4.1j which shows that maximum total force (About 32N) occurs at the galloping region.

Finally, for Fig 4.2, just as we discussed for Fig 4.1, the residuary force is calculated experimentally and derived as shown in eq. (4-1). 4.2k shows the ratio of the residuary force compared to the total force. This would be discussed further when discussing direct vortex forces in Chapter 5.

4.4 Comparison between Theory and Experiments for Smooth Cylinder

Fig. 4.3 is the counterpart of Fig. 4.1 for a smooth circular cylinder, which unlike Fig 4.1, exhibits only VIV, not galloping. The figures below show the results obtained by analyzing one set of smooth cylinder experimental data. In the figures presented below, the mass ratio m^* is 1.595, stiffness $k=400\text{N/m}$ and damping ratio is 0.06. All the figures show that the eigen relation matches the experimental results. Even the phase angle results (4.3.i) collapse well.

Corresponding to Fig. 4.3 are Figures A1, A3, A5, ... A15 in Appendix A and Figures 6 in Report #13 [46].

Corresponding to Fig. 4.4 are Figures A, A4, A6, ... A16 in Appendix A and Figures 7 in Report #13 [46].

As established in Chapter three, f^* is an important dimensionless parameter, hence the oscillator properties are plotted versus f^* or $U^*_{n,vac}/U/Re$ as follows:

- Fig. 4.3.a: Amplitude ratio A^* vs. $U^*_{n,vac}/U/Re$. This figure shows that there are only two stages of FIO here compared to the four in Figs 4.1 and 4.2. As expected, galloping does not occur here since it is a smooth cylinder test result.
- Fig. 4.3.b: f^* vs. $U^*_{n,vac}/U/Re$ to show the relation between the two variables which are used as independent variables for presenting the results.
- Fig. 4.3.c: Amplitude ratio A^* vs. f^* . It shows how data collapse differently from Fig. 4.3.a.

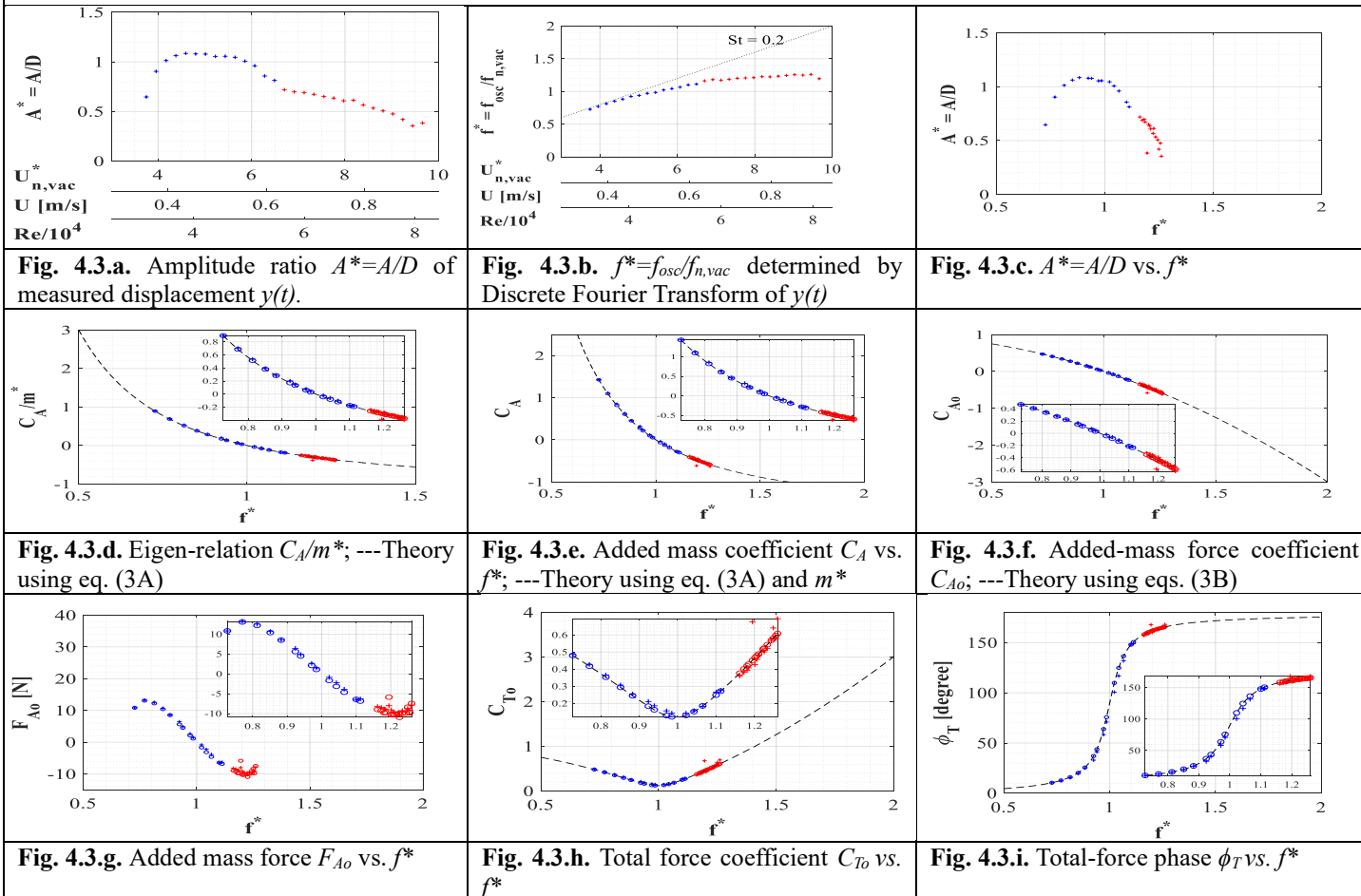
- Fig. 4.3.d: Ratio of added mass coefficient and mass ratio vs f^* . It shows the eigen relation eq. 3A. The graph shows how closely the experimental results follow the eigen relation and that the ratio $C_A/m^*=m_A/m_d$ is constant.
- Fig. 4.3.e: Added mass coefficient vs f^* .
- Fig. 4.3.f: Theoretical added mass coefficient C_{Ao} vs f^* . The next value to be calculated is that of the added mass force coefficient. The experimental values fall exactly inside the circles on the theoretical line.
- Fig. 4.3.g: Added mass force magnitude F_{Ao} vs. f^* . This shows the theoretical force in phase with the acceleration. As expected, following Fig. 4.3.f for C_{Ao} , F_{Ao} in Fig. 4.3.g also shows the experimental values falling exactly inside the circles on the theoretical line.
- Fig. 4.3.h: Total force coefficient C_{To} vs. f^* .
- Fig. 4.3.i: Total force phase ϕ_T vs. f^* . It shows the phase angle between the total force and the displacement $y(t)$.
- Fig. 4.3.j: Total force magnitude F_{To} vs. f^* . Total force magnitude F_{To} vs. f^* . Here is where we would expect some differences accounting for the higher order terms. That is, F_{To} contains the two first order terms in phase with the velocity F_{Uo} and the acceleration F_{Ao} plus the higher order terms or F_{Ro} .
- Fig. 4.3.k: Coefficient C_{Uo} of force in-phase with velocity vs. f^* . This exhibits excellent agreement between theory and experiments.
- Fig. 4.3.l: Force in-phase with velocity F_{Uo} vs. f^* . This also exhibits excellent agreement between theory and experiments as expected following the agreement of C_{Uo} with experiments.
- Fig. 4.3.m: Residuary force coefficient C_{Ro} vs. f^*
- Fig. 4.3.n: Residuary force F_{Ro} vs. f^*

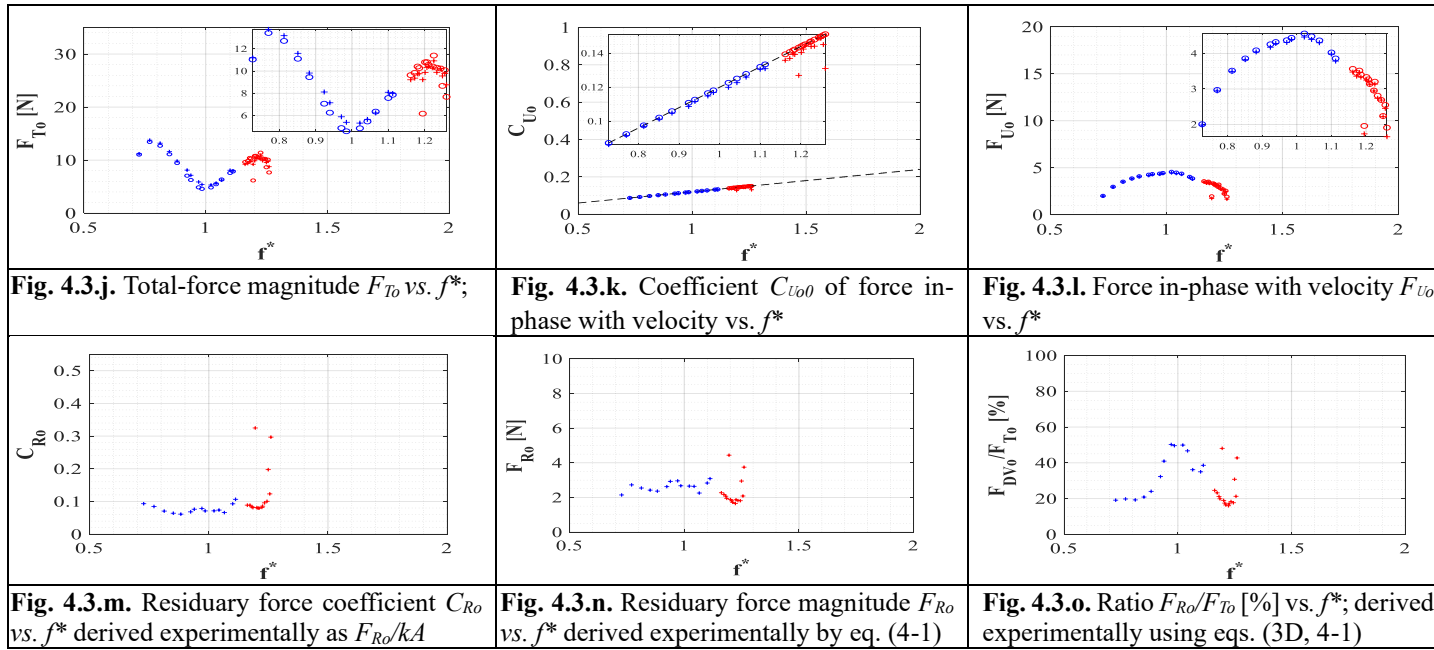
- Fig. 4.3.o: Ratio F_{Ro}/F_{To} [%] of vs. f^*

Figs 4.3.m – 4.3.o derived from eqs. (3D and 4-1), include all the nonlinear terms which are beyond the eigen-relation and linear theory. This information is used to discuss the magnitude of the vortex force in Section 5.10.

Lastly, as discussed in the previous section, the first row of Fig 4.3 shows some interesting things about the amplitude ratio A^* in details. As Fig 4.3b shows, f^* increases steadily from the first point of VIV initiation up to the last point of the lower branch. In fact, this same trend holds irrespective of the mass ratio, stiffness and damping ratio as seen from results in Appendix A. (Figs A1.b, A3.b, A5.b, and so on). On the other hand, Fig 4.3a shows that amplitude ratio A^* increases from VIV initiation till a point where the reduced velocity is 5 after which it starts decreasing steadily up until the last point of lower branch.

Figure 4.3. Theoretical and experimental comparison of FSI (VIV) properties plotted vs. f^* , for a smooth circular cylinder: $D=3.5''$, $L=35.5''$, $m^*=1.595$, end-springs with $k=400\text{N/m}$, total damping-ratio in vacuo $\zeta_{\text{vac}}=0.06$
 (a) ---- Theory using eqs. (3A)-(3D). (b) $\circ\circ\circ$ Reconstructed based on theory and measured f^* . (c) $++++$ Measured experimentally





Oscillator properties plotted in Fig 4.3 are replotted in Fig. 4.4 vs. $U^*_{n,vac}$, U , Re since readers are more familiar with $U^*_{n,vac}$ as the independent variable. Fig. 4.4 is the counterparts of fig. 4.2 for a smooth circular cylinder, which unlike Figs 4.2, exhibits only VIV, not galloping.

- Fig. 4.4.a: Added mass coefficient C_A vs $U^*_{n,vac}/U/Re$.
- Fig. 4.4.b: Theoretical added mass coefficient C_{Ao} vs $U^*_{n,vac}/U/Re$.
- Fig. 4.4.c: Added mass force magnitude F_{Ao} vs. $U^*_{n,vac}/U/Re$. This shows the theoretical force in phase with the acceleration.
- Fig. 4.4.d: Total force coefficient C_{To} vs. $U^*_{n,vac}/U/Re$.
- Fig. 4.4.e: Total force phase ϕ_T vs. $U^*_{n,vac}/U/Re$. It shows the phase angle between the total force and the displacement $y(t)$.
- Fig. 4.4.f: Total force magnitude F_{To} vs. $U^*_{n,vac}/U/Re$. As discussed for Fig 4.3.j, we expect some slight differences between the theory and experiments here because higher order terms are being accounted for. That is, F_{To} contains the two first order terms in phase with the velocity F_{Uo} and the acceleration F_{Ao} plus the higher order terms or F_{Ro} .
- Fig. 4.4.g: Coefficient C_{Uo} of force in-phase with velocity vs. $U^*_{n,vac}/U/Re$. Theoretical C_{Uo} Obtained from eq. (3B), this exhibits excellent agreement between theory and experiments.
- Fig. 4.4.h: Force in-phase with velocity F_{Uo} vs. $U^*_{n,vac}/U/Re$. This also shows excellent agreement between theory and experiments as expected following the agreement of C_{Uo} with experiments.
- Fig. 4.4.i: Residuary force coefficient C_{Ro} vs. $U^*_{n,vac}/U/Re$.
- Fig. 4.4.j: Residuary force F_{Ro} vs. $U^*_{n,vac}/U/Re$.
- Fig. 4.4.k: Ratio F_{Ro}/F_{To} [%] of vs. $U^*_{n,vac}/U/Re$.

Figure 4.4. Theoretical and experimental comparison of FSI (VIV) properties plotted vs. f^* , for a **smooth circular cylinder**: $D=3.5"$, $L=35.5"$, $m^*=1.595$, end-springs with $k=400\text{N/m}$, total damping-ratio in vacuo $\zeta_{vac}=0.06$
 (a) $\circ\circ\circ\circ$ Reconstructed based on theory using eqs. (3A)-(3D) and measured f^* .
 (b) $++++$ Measured experimentally

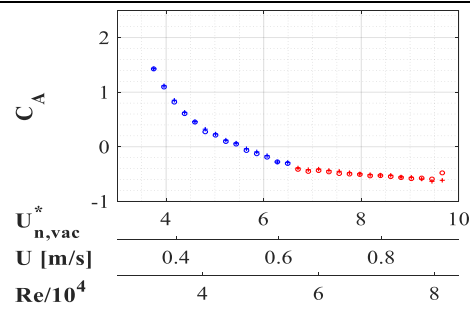


Fig. 4.4.a. Added-mass coefficient C_A vs. $U_{n,vac}^*$; $\circ\circ\circ\circ$ Theoretical reconstruction by eq. (3A); $++++$ Measured experimentally

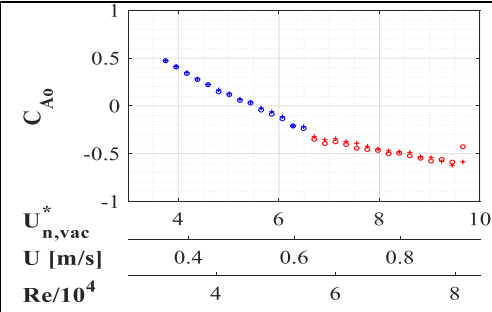


Fig. 4.4.b. Added-mass force coefficient C_{Ao} vs. $U_{n,vac}^*$; $\circ\circ\circ\circ$ Theoretical reconstruction by eqs.(3B); $++++$ Measured experimentally.

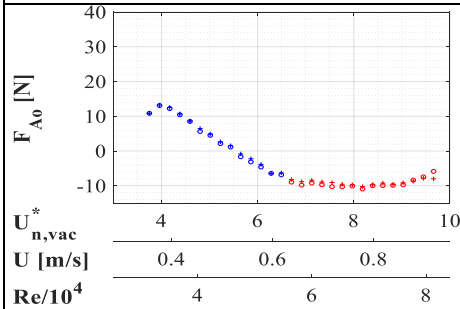


Fig. 4.4.c. Added-mass force magnitude F_{Ao} vs. $U_{n,vac}^*$; $\circ\circ\circ\circ$ Theoretical reconstruction by eqs. (3D); $++++$ Measured experimentally

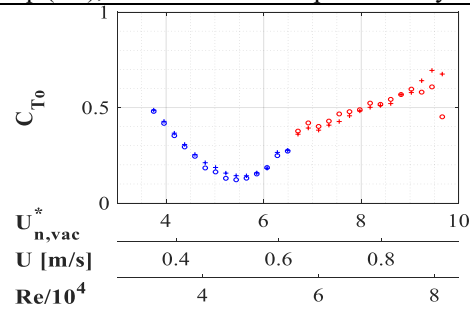


Fig. 4.4.d. Total-force coefficient C_{T0} vs. $U_{n,vac}^*$; $\circ\circ\circ\circ$ Theoretical reconstruction by eqs. (3B); $++++$ Measured experimentally

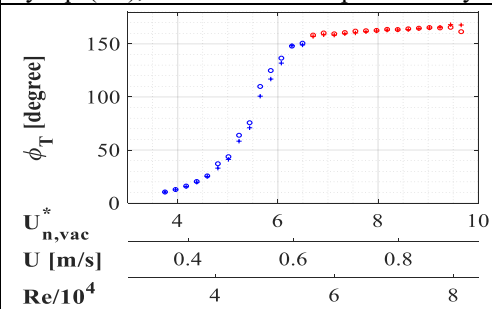
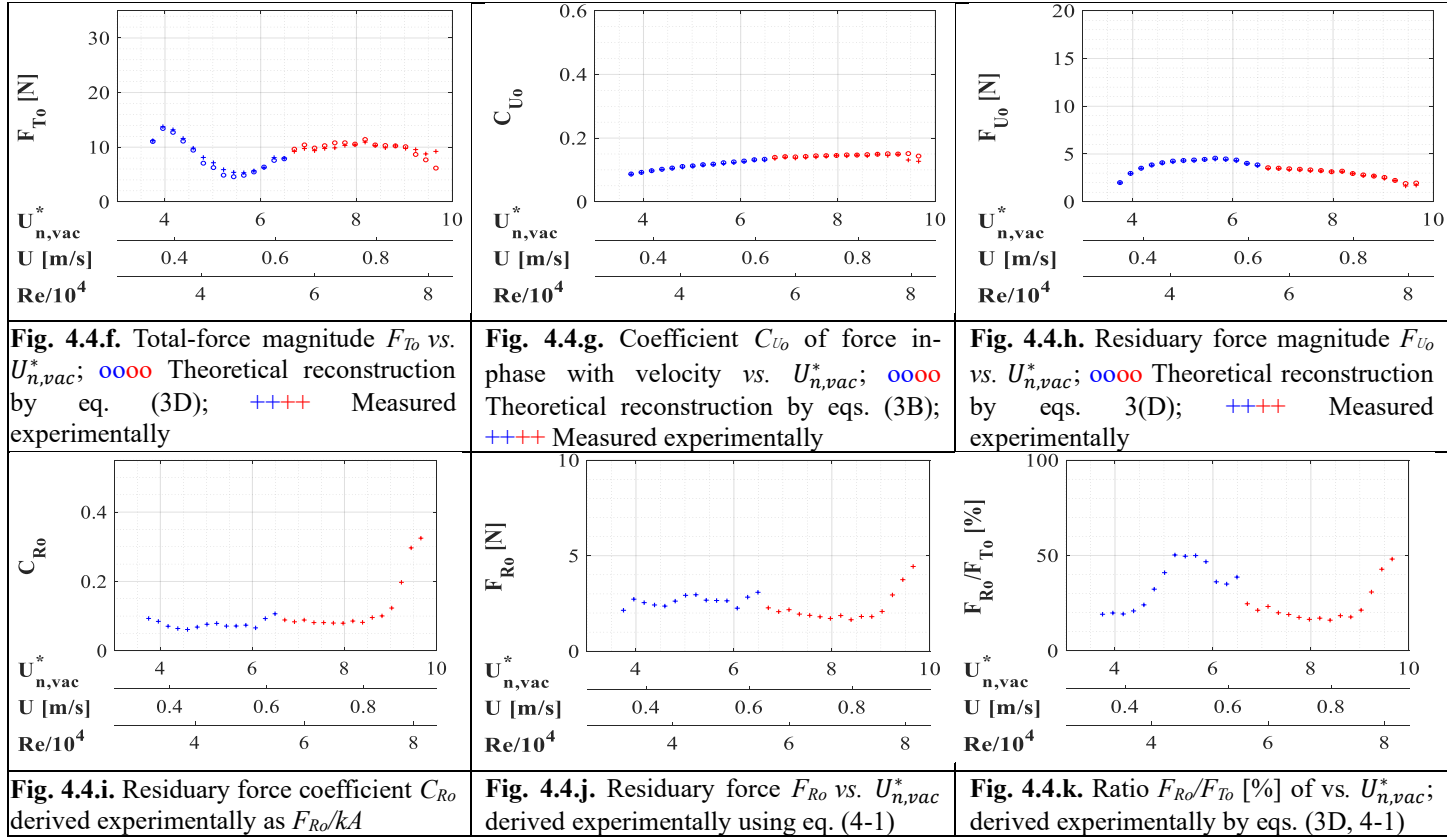


Fig. 4.4.e. Total-force phase ϕ_T vs. $U_{n,vac}^*$; $\circ\circ\circ\circ$ Theoretical reconstruction by eqs. (3C); $++++$ Measured experimentally

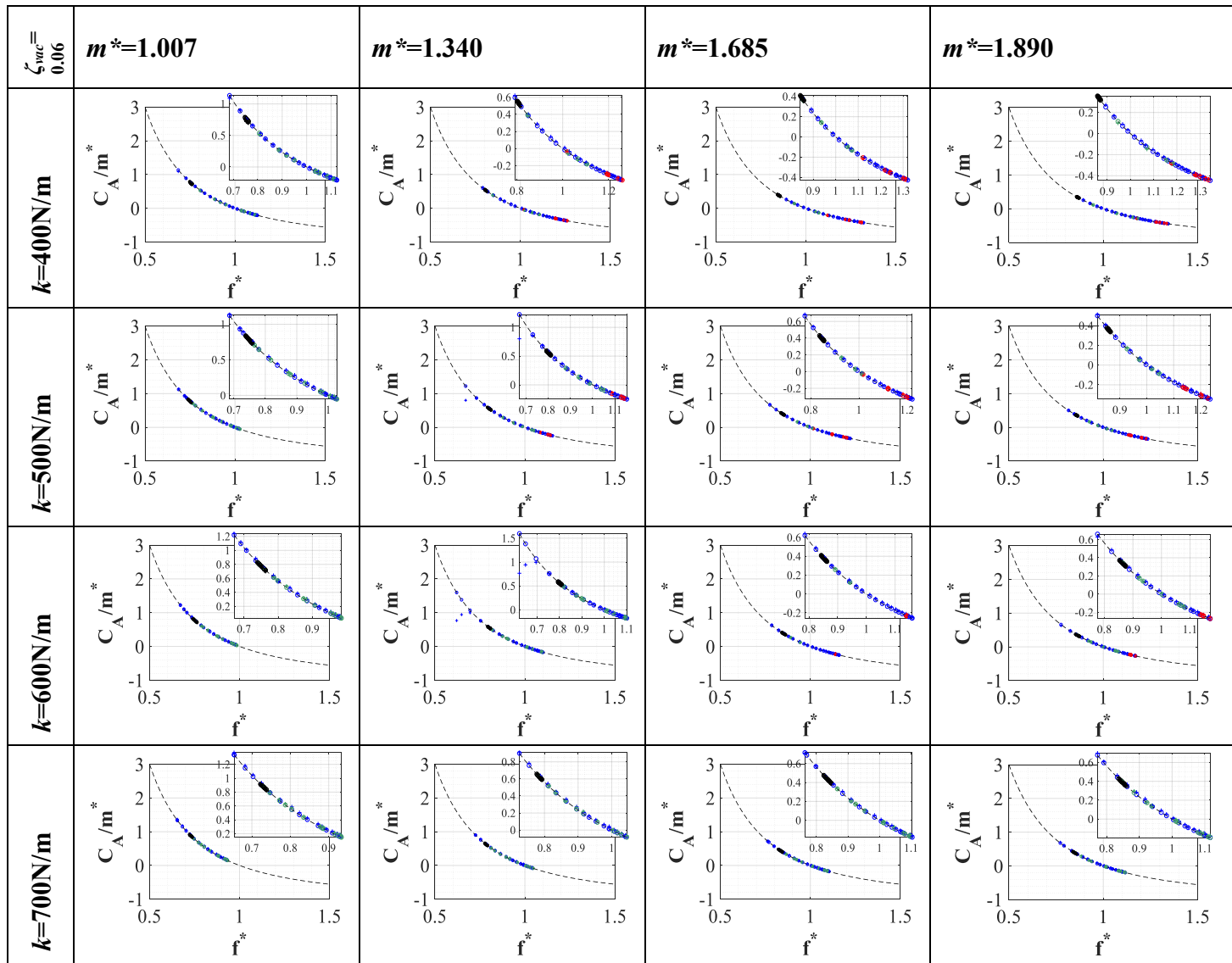


Figs. 4.5 and 4.6 show the effect of m^* and k on f^* and ranges of synchronization in VIV and galloping. Both are discussed extensively in Section 5.7.

To conclude this Chapter, it has been shown that the agreement between theory and experimental measurements is excellent for C_A/m^* , C_A ; C_{Ao} , ϕ_A , F_{Ao} ; C_{To} , ϕ_T , F_{To} ; and C_{Uo} , ϕ_U , F_{Uo} . The residuary force from the experiments is

$$F_R(t) = F_T(t) - F_A(t) - F_U(t) \quad (4-1)$$

calculated as the difference between experimental measurements and the single-frequency-response equations (3D). The results, constituting mostly the direct vortex force (further discussed in Section 5.8-5.10), are shown in Figs. 4.1.m-o; 4.2i-k; 4.3m-o; 4.4i-k.



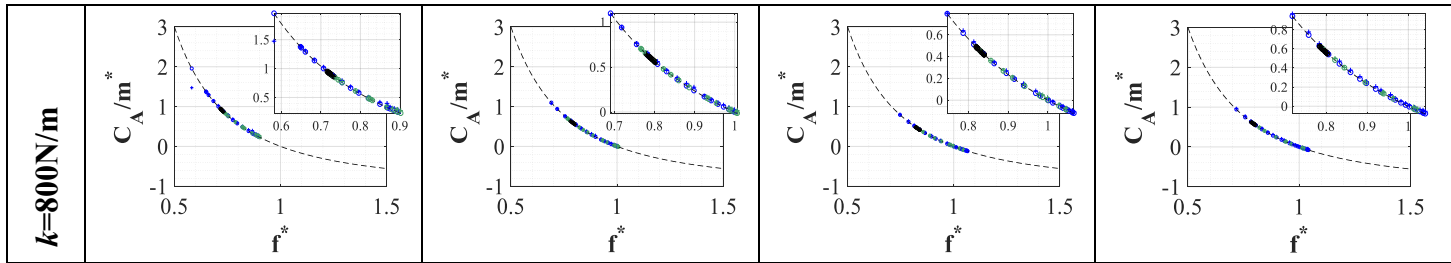
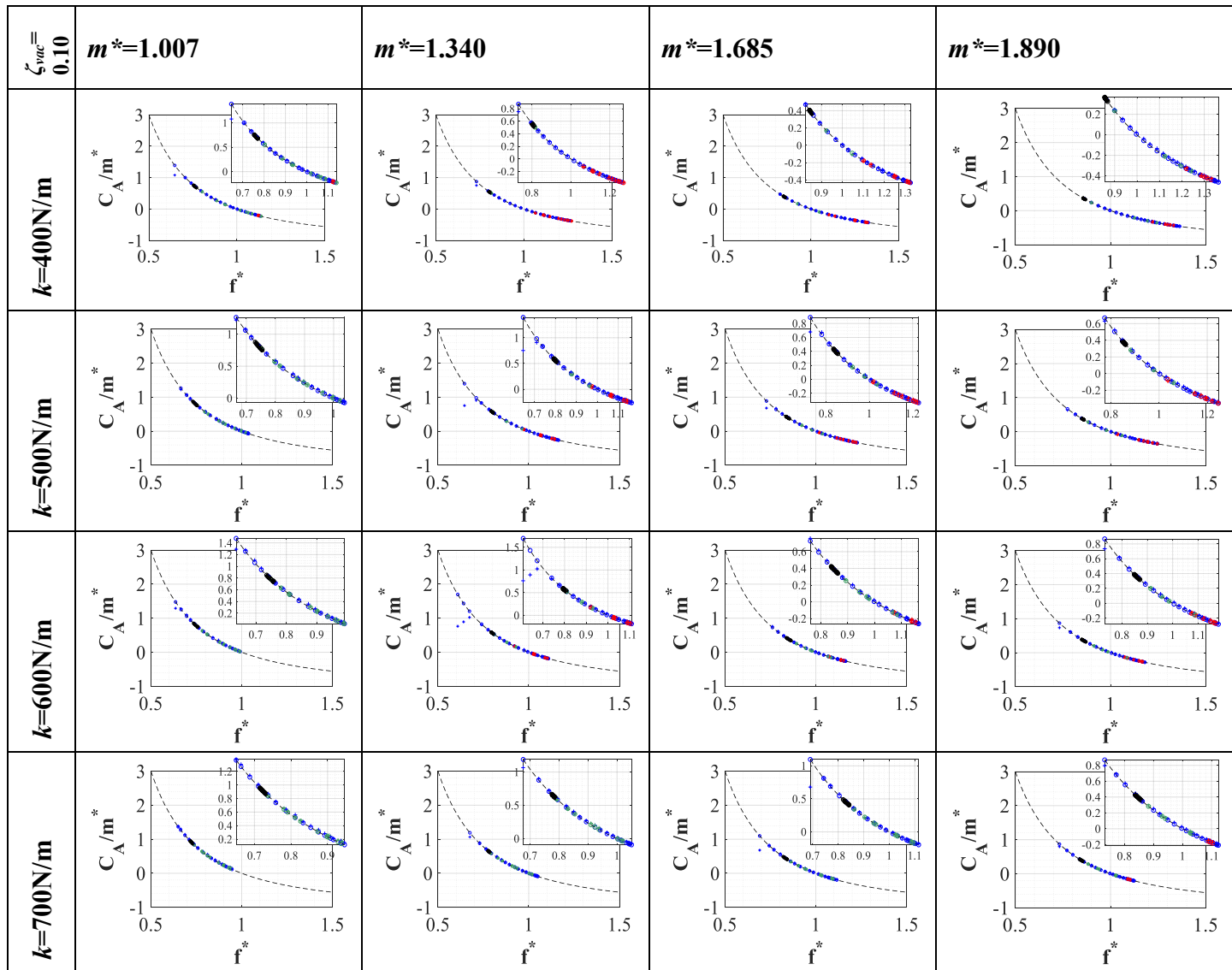


Fig. 4.5. C_A/m^* vs. f^* [FSI eigen-relation eq. (3A)] for different (m^*, k) pairs. (a) ---- Theory using eq. (3A). (b) $\circ\circ\circ$ Reconstructed based on theory and measured f^* . (c) $+++$ Measured experimentally
VIV and galloping of a circular cylinder with **turbulence stimulation**; $D=3.5"$, $L=35.5"$, total damping ratio in vacuo $\zeta_{vac}=0.06$



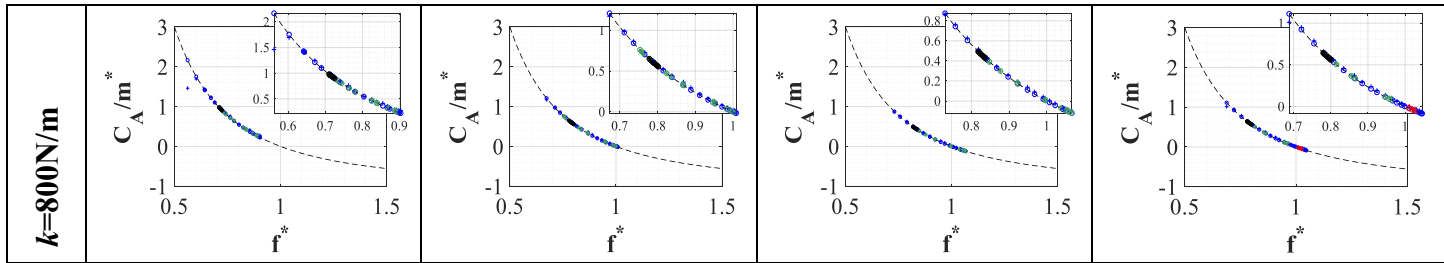


Fig. 4.6. C_A/m^* vs. f^* [FSI eigen-relation eq. (3A)] for different (m^*, k) pairs. (a) ---- Theory using eqs. (3A). (b) $\circ\circ\circ$ Reconstructed based on theory and measured f^* . (c) $++++$ Measured experimentally
VIV and galloping of a circular cylinder with turbulence stimulation; $D=3.5"$, $L=35.5"$, total damping ratio in vacuo $\zeta_{vac}=0.10$

Chapter Five

Discussion: VIV Facts – Old & New

The theory developed in Chapter 3 was compared to the extensive experimental data collected in the MRELab over a decade. Since the first models of VIV by Strouhal (1878) [63] and Rayleigh Lord (1896) [51] were developed, thousands of papers have been published and experiments have been conducted. Over the years, those studies have established numerous experimental observations on VIV, which are studied in this Chapter. They are all explained based on the derived theory and some are corrected and interpreted properly.

5.1. Is VIV lock-in or resonance?

The lock-in phenomenon initiates when the frequency of vortex shedding is close to the natural frequency of the oscillating/vibrating structure. When this occurs, it can lead to a large and destructive oscillation/vibration causing the structure to fail. The lock-in phenomenon for the case of flexibly-mounted, rigid cylinders in uniform flow has been extensively studied and reviewed by Bearman, 1984 [4]; Sarpkaya, 2004 [57]; Williamson and Govardhan, 2004 [78].

There is a long-standing argument among researchers of VIV whether VIV is a lock-in phenomenon [57] or a nonlinear resonance with variable added mass [78]. To answer this research question, let us go back to the basics by considering the modeling equations. The flow is in the x -direction. The motion of the cylinder in the y -direction is modeled by equation (3-10).

As eqs. (3-51) and (3-54) prove, the two are equivalent. A cylinder in VIV is under excitation due to the synchronization between body motion and vortex shedding. Even as Re increases and

vortex patterns change from 2S to 2P [69,78] and beyond [11], resulting in higher vortex shedding frequency, the wake frequency (groups of vortices) remains equal to the oscillator frequency. Per eq. (3-51), the oscillation frequency is equal to the *undamped* natural frequency of the oscillator in water with variable added mass as defined by the eigen-relation. Also, per eq. (3-54), the force is in phase with the oscillator velocity $\dot{y}(t)$. That is, eqs. (3-51 and 3-54) proved that the basic modeling eqs. (3-10 to 3-14) lead to mandatory resonance.

From the explanations above we can see that this controversy is unnecessary as both are simple modeling methods that cannot account for the range of synchronization of VIV or the self-limiting nature of the amplitude of oscillation. Both approaches model the response of the cylinder in FIM for a specific flow velocity and a given experiment. On the other hand, both approaches are useful in post-processing data and understanding the VIV phenomenon better.

For better understanding of the complexity of the added mass expression in forces and moments on a small body moving in a 3-D unsteady flow, the reader is referred to the detailed analysis and derivation in [21]. The dependence of the inertia terms on absolute and/or relative velocity as well as the form of convective terms is explained thoroughly putting into perspective the simplistic nature of the inertia term used in Morison's equation.

In conclusion, the eigen-equation shows mandatory response in FIO. Eq. (3-51) proves that f_{osc} is equal to the *undamped* natural frequency in water. That is, it is not affected by the system damping, which is an energy exchange mechanism at the interface between flow and oscillator. *If it were a pure nonlinear resonance issue, the measured frequency of oscillation would match the damped natural frequency; not the undamped one.* Figs. 5.1 and 5.2 show that oscillations occur on the eigen-relation regardless of damping ζ_{vac} . Furthermore, the eigen-relation holds for both FSI

phenomena considered in this work, VIV and galloping, in spite of the fact that their driving mechanisms are fundamentally different.

5.2. Is the mass-damping parameter $m^*\zeta$ relevant?

As discussed in Chapter two, the mass damping parameter is an important and controversial parameter in VIV research field. This parameter has been used by many researchers for different purposes over the years. For instance, Scruton in 1955 used it to characterize flow induced vibration of cantilevered flexible structures in wind [58]; Griffin 1973 [27]; Griffin and Koopman, 1977 [29]. By the late 1970s to 1980s, critics started highlighting some failures of the mass-damping parameters; Sarpkaya, 1979 [54]. This made some researchers doubt the usefulness of this parameter, Khalak, Govardhan and Williamson underlined the use of this parameter again in 1999, [35]. Later on, in [70] Vandiver pointed out that none of the previous damping parameters proposed were useful at organizing response at reduced velocities away from the peak-in response so he came in with another parameter, called c^* , which does not depend on the mass-damping parameter.

$$c^* = \frac{2c\omega}{\rho U^2} \quad (5 - 1)$$

Where c is the structural system damping, ω is response or excitation frequency, ρ is the fluid density and U is the flow speed.

As we see from the mathematical equations derived in Chapter 3, we have explicit expressions for coefficients, phases, and forces, showing their explicit dependence on each parameter including m^* and ζ , not on the product ($m^*\zeta$). The mass damping parameter $m^*\zeta$ was derived heuristically and we can conclude it's of no relevance in accurately predicting VIV and galloping responses as some researchers believed. Hence, *VIV and galloping results should not be presented or modeled in terms of any $m^*\zeta$ form.* Instead the exact expressions derived in Chapter 3 should be used.

5.3. Is the reduced velocity U^* useful?

The reduced velocity U^* is a form of the generic Strouhal number St_n , nondimensionalized by a different time scale and, consequently, is redundant. Its use is limited to our familiarity with the onset and termination of VIV defined by U^* between about 5 and 10 for $m^*=O(1)$. We know though, that this range changes with several parameters such as m^* and k as we will see in the sections below. That is, the notion that VIV initiates when the oscillator's natural frequency in quiescent (ideal) water is nearly equal to the Strouhal frequency f_s , for a stationary cylinder, translates to U^* between 5 and 10 only for m^* on the order of $O(1)$. As Figs. 5.1-5.5 show, the projection of the eigen-relation on the f^* -axis changes with m^* and k . Dependence of VIV on k and m^* is discussed further in Section 5.6.

5.4. Is the mass-ratio m^* useful?

This is also a heuristically derived parameter and it is not a governing hydrodynamic parameter; it is just a design parameter. Thus, m^* is a useful parameter, but now its role is linked to C_A by the eigen-relation (3A) and can be easily explained. It is also linked to k through $f_{n,vac}$ in the denominator of f^* . It is discussed further in the next four subsections (5.5-5.8)

5.5. Effect of m^* on range of synchronization

In 2000, Govardhan and Williamson [24] concluded that the mass ratio m^* is the main parameter that predicts the range of synchronization. They also inferred the peak amplitude is primarily controlled by the mass damping parameter. Moreover, [25] established that once the mass ratio becomes less than a critical value of 0.54 (called critical mass), the VIV range of synchronization becomes infinite and referred to it as “resonance forever”. This means the oscillator will initiate resonance (initial VIV branch) near its natural frequency and never get out of resonance as the

flow velocity increases. This conclusion however was derived experimentally for the case of $k=0\text{N/m}$. The explanation and generalization of this phenomenon is provided in Section 5.7. They concluded that there is an infinitely wide regime of resonance and due to this, the cylinder resonates forever. This subsection of the discussion sheds light on the effect of m^* on the range of VIV synchronization.

Fig. 5.5a shows the effect m^* has on C_A through the eigen-relation. For high m^* , the possible range of VIV, as projected on the f^* -axis, is very narrow. The range is nearly as narrow as the bandwidth of linear resonance in air as Feng's results showed in 1968 [19]. Also, a wider f^* range of synchronization would require drastic change in C_A . For low m^* , the eigen-relation becomes nearly parallel to the f^* -axis amplifying projection of a given ΔC_A segment on the f^* -axis. By a small change in C_A , which means little change in the real natural frequency in water, f^* can change dramatically expanding the synchronization range as shown experimentally in [25].

There is more to it though. Figure 5.5b shows experimental results on theoretical predictions for four m^* values. The theoretical lines pivot around the $(C_A=0, f^*=1)$ point, where the frequency of oscillation is equal to $f_{n,vac}$. The experimental results move towards the steeper slope of f^* (higher C_A values) as m^* decreases. Thus, we conclude that there are two counteracting ways in which m^* affects the range of VIV synchronization:

- (a) Decrease in m^* pivots the theoretical line towards paralleling the f^* -axis expanding projection of a given ΔC_A on the f^* -axis and, thus, the synchronization range.
- (b) On the other hand, decrease in m^* pushes the VIV synchronization range towards the lower f^* (= higher C_A) values narrowing down the ΔC_A projection the f^* -axis. This is due to the fact that m^*

is in the denominator of $f_{n,vac}$, which is in the denominator of f^* ; it is also confirmed by the experiments in Fig. 5.5b.

In fact, the above conclusions have been proven to be true as can be seen in figures 5.1-5.4 and in the numerous experimental results processed shown in Appendices A and B.

5.6. Effect of m^* and k

In this section, the importance of the mass ratio m^* and spring stiffness k on the performance of the oscillator are investigated. Experimental results and the analytical expressions derived in Chapter 3 are compared and discussed.

The following important observations are made related to m^* and k :

- For both smooth cylinders and cylinders with passive turbulence stimulation, A^* increases as m^* increases (Appendices A & B).
- For the same mass ratio m^* , maximum amplitude A^* occurs at the highest stiffness (Appendices A & B).
- For a constant spring stiffness k , amplitude A^* increases with increasing mass ratio m^* . Although this increment is more pronounced for the lower spring stiffness values k (Appendices A & B).
- For a constant value of m^* , the amplitude A^* decreases with increasing stiffness k (Appendices A & B).
- The range of synchronization and transitioning from VIV to galloping becomes shorter as the stiffness k increases for a constant mass ratio m^* (i.e the figures shrink and moves to the left) as shown in [47]

- As the mass ratio m^* increases, galloping starts at a higher reduced velocity. It starts around $U^*=8$ for the lowest mass ratio of 1.007 (Appendix B) and around $U^*=12$ for the highest mass ratio of about 1.9 (Appendix B). For the same mass ratio though, galloping starts earlier as the stiffness increases. In fact, for the lowest mass ratio m^* and highest stiffness k , galloping starts at $U^*=6$.

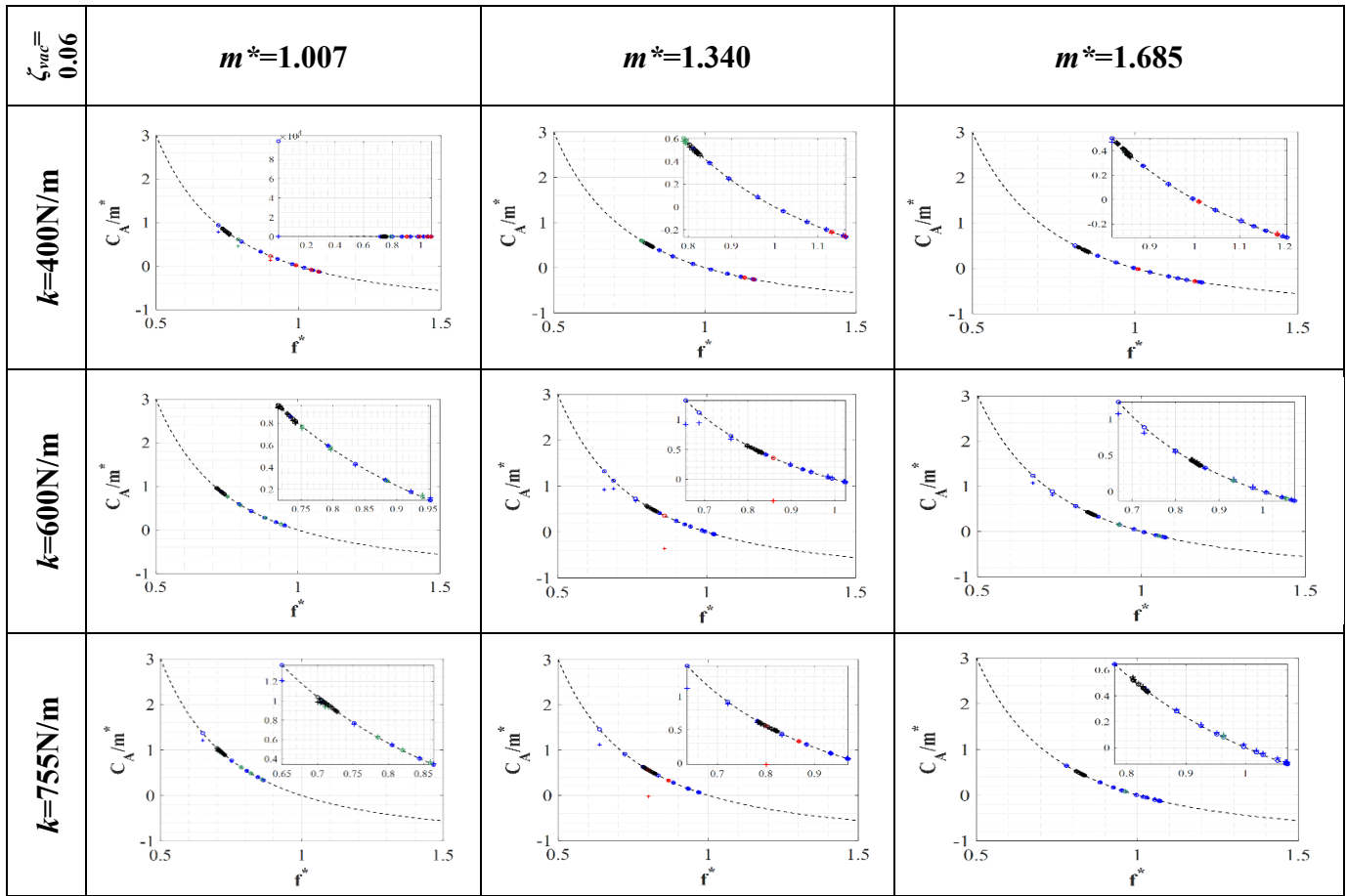
Based on the above highlighted observations, we say it is more appropriate to consider the effect of the combination of mass ratio m^* and spring stiffness k as it appears in $f_{n,vac}$ in eq. (5-2)

$$f_{n,vac} = \frac{1}{2\pi} \sqrt{\frac{k}{m_{osc}}} \quad (5 - 2)$$

since $f_{n,vac}$ is in the denominator of f^* . Fig. (5.1) shows experimental results for constant $\zeta_{vac}=0.06$ as they fall along the theoretical eigen-relation. Fifteen sets of tests (three m^* by five k values) are used. Figure (5.2) shows the corresponding data for $\zeta_{vac}=0.10$. Clearly, high k and low m^* , resulting in high $f_{n,vac}$, push the range of synchronization to low f^* - high C_A/m^* . Corresponding conclusion can be drawn for low k and high m^* , resulting in low $f_{n,vac}$, pushing the range of synchronization to high f^* - low C_A/m^* – because $f_{n,vac}$ is in the denominator of f^* .

Thus, *low mass may result in narrower VIV synchronization range* as explained also in Section (5.5). This conclusion appears to contradict the perpetual VIV observation in [25]. Actually, the observation was most likely correct but the interpretation that it is due to low m^* is not necessarily correct. The observation was made under the limiting condition of $k=0$, which makes $f_{n,vac}=0$ regardless of the m^* value. This pushes the synchronization range to the section of the eigen-relation which is nearly parallel to the f^* -axis, amplifying projection of a given ΔC_A segment on

the f^* -axis. Figures (5.1) and (5.2) show that increasing (not decreasing) m^* results in expansion of the projection of a VIV range of synchronization. Both, eigen-relation (3A) and the experimental results in Figs. (5.1) to (5.4), show that decreasing k has the same effect as increasing m^* ; both compress the range of synchronization (projection on the f^* -axis) pushing it in the high f^* end of eq. (3A) even at higher damping as seen in figs (5.3 and 5.4).



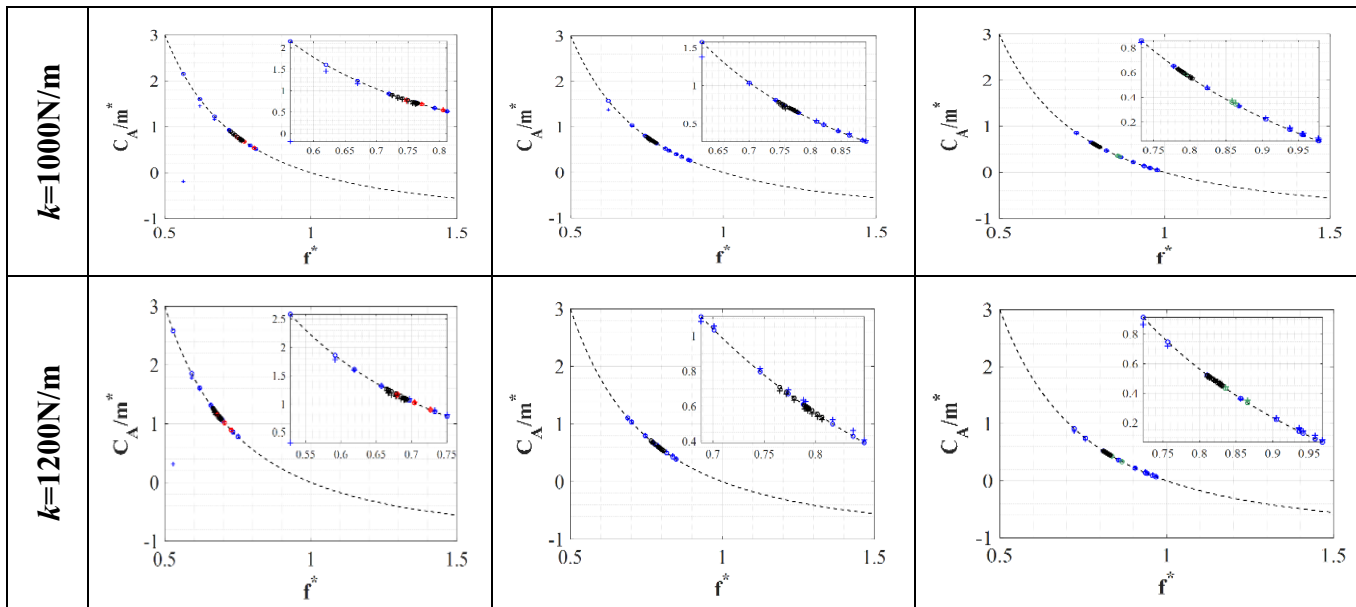
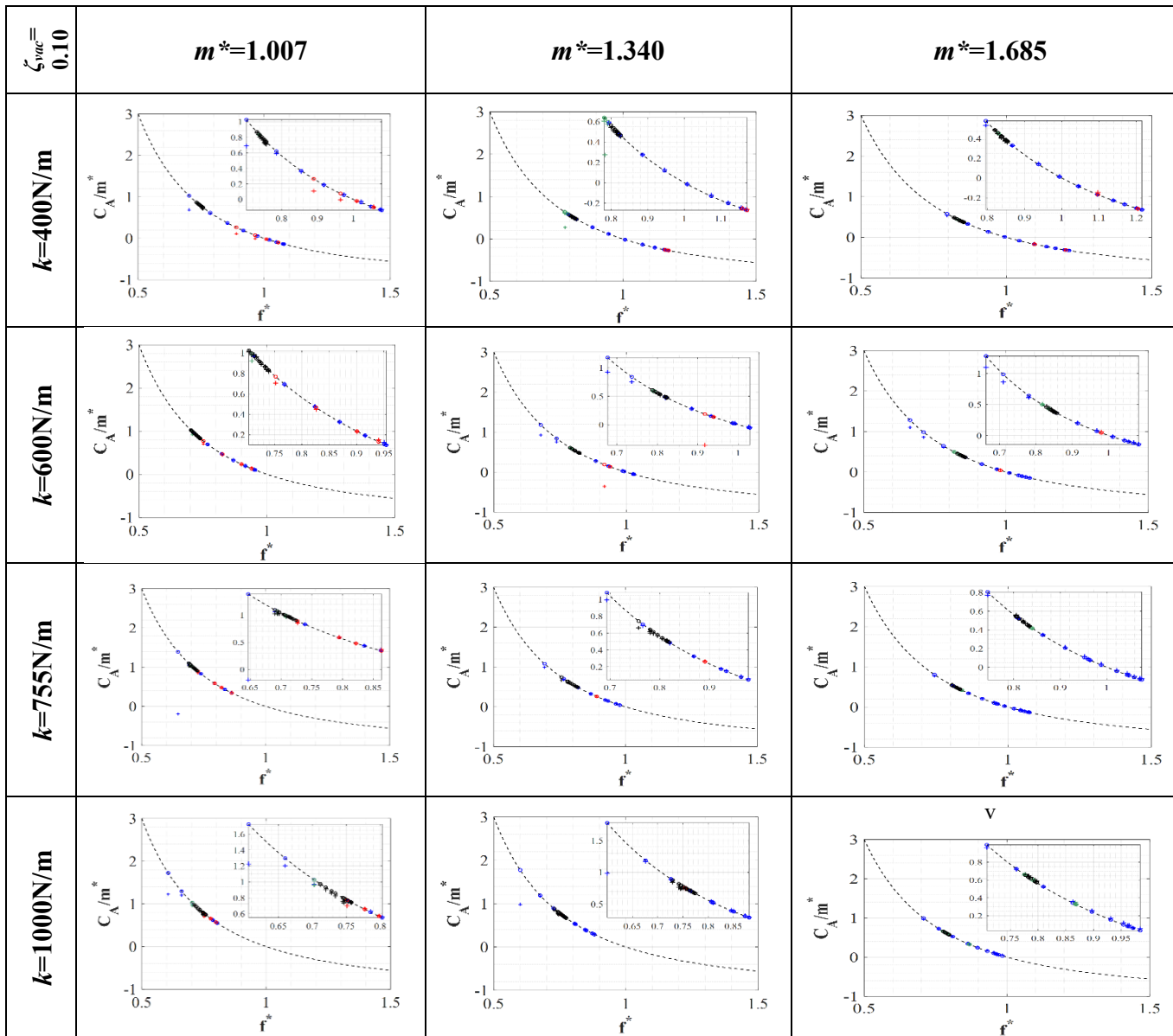
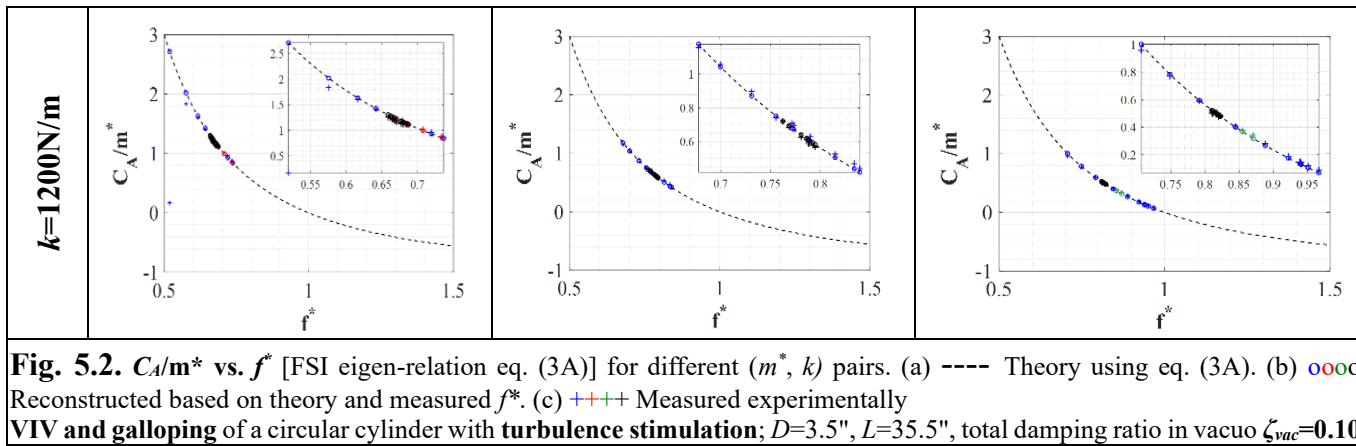
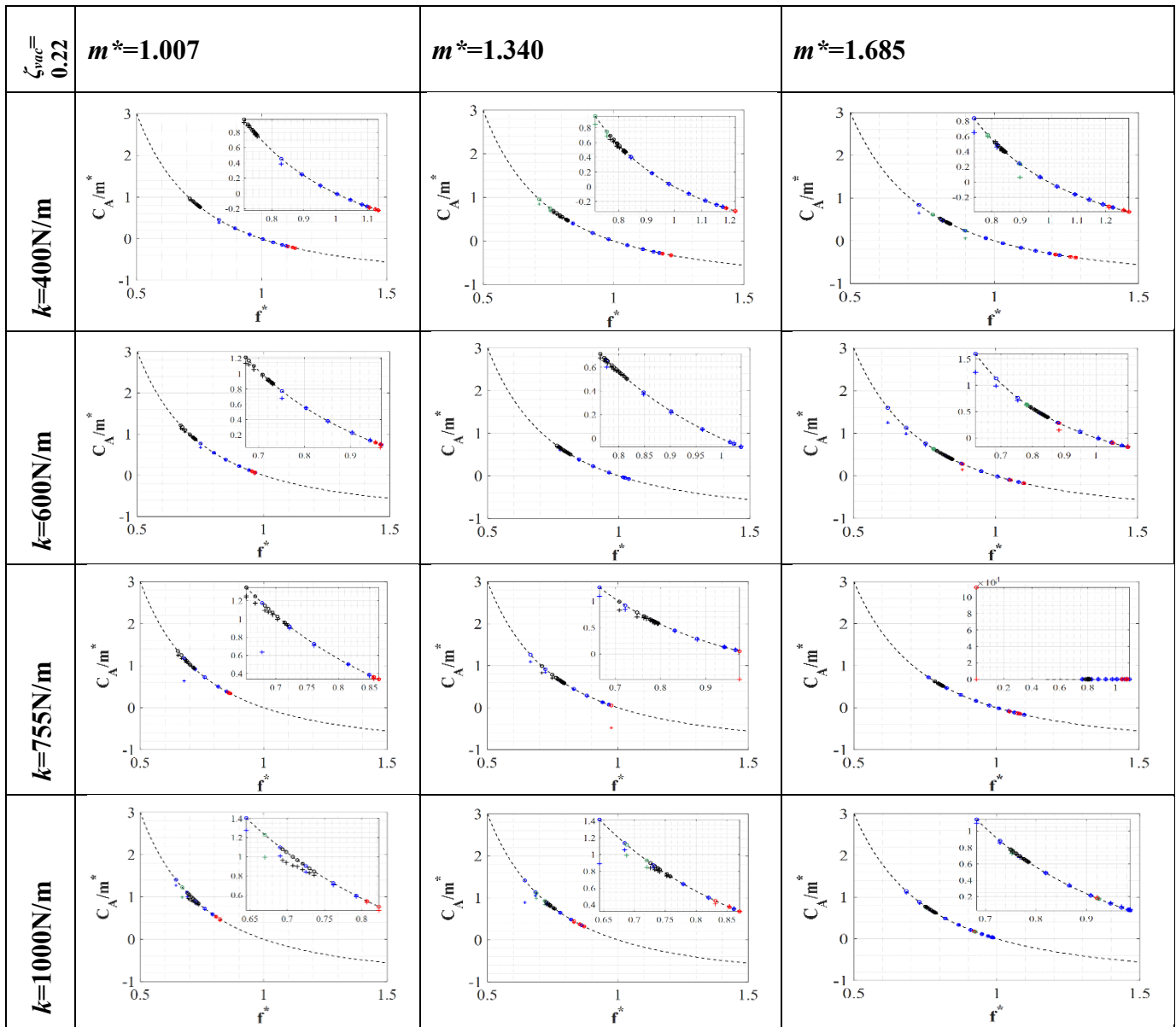


Fig. 5.1. C_A/m^* vs. f^* [FSI eigen-relation eq. (3A)] for different (m^*, k) pairs. (a) ---- Theory using eq. (3A). (b) oooo Reconstructed based on theory and measured f^* . (c) ++++ Measured experimentally
VIV and galloping of a circular cylinder with turbulence stimulation; $D=3.5''$, $L=35.5''$, total damping ratio in vacuo $\zeta_{vac}=0.06$







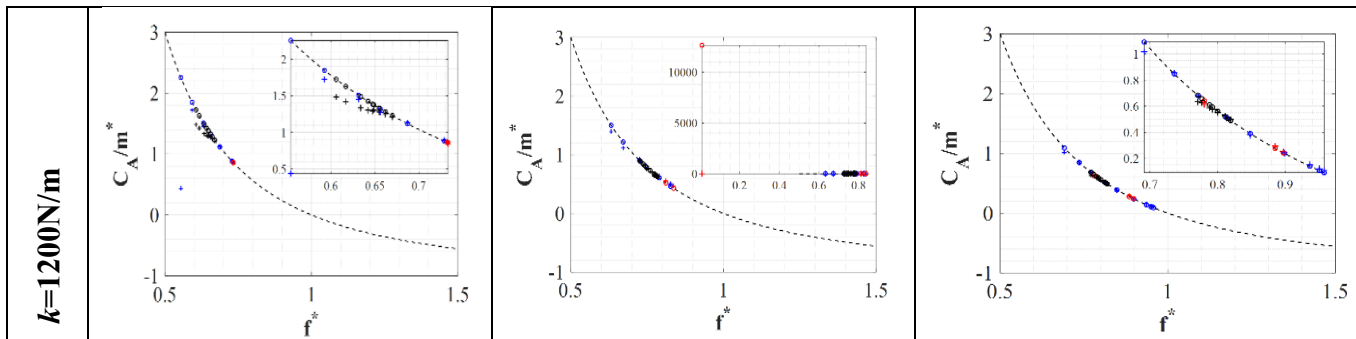
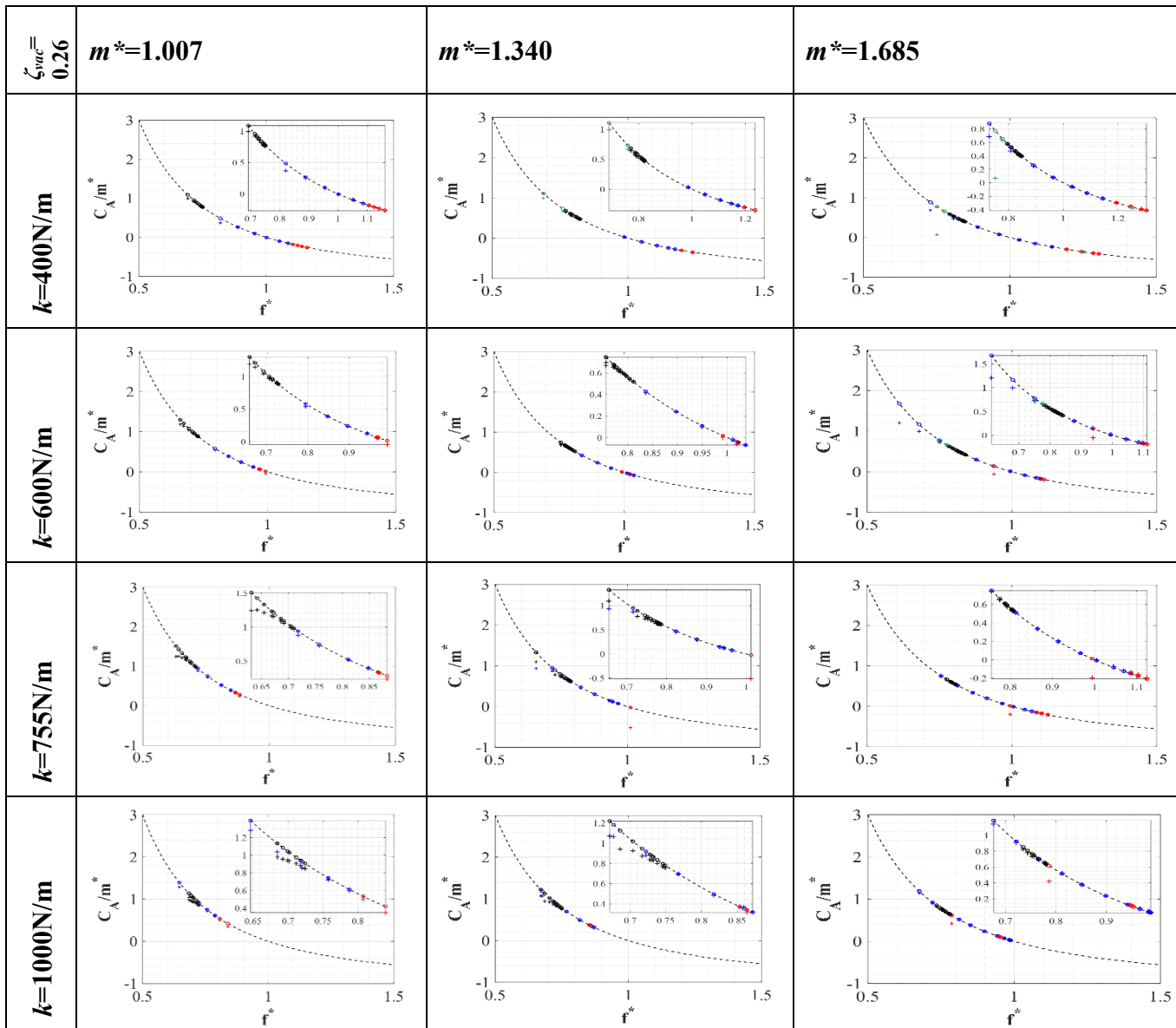
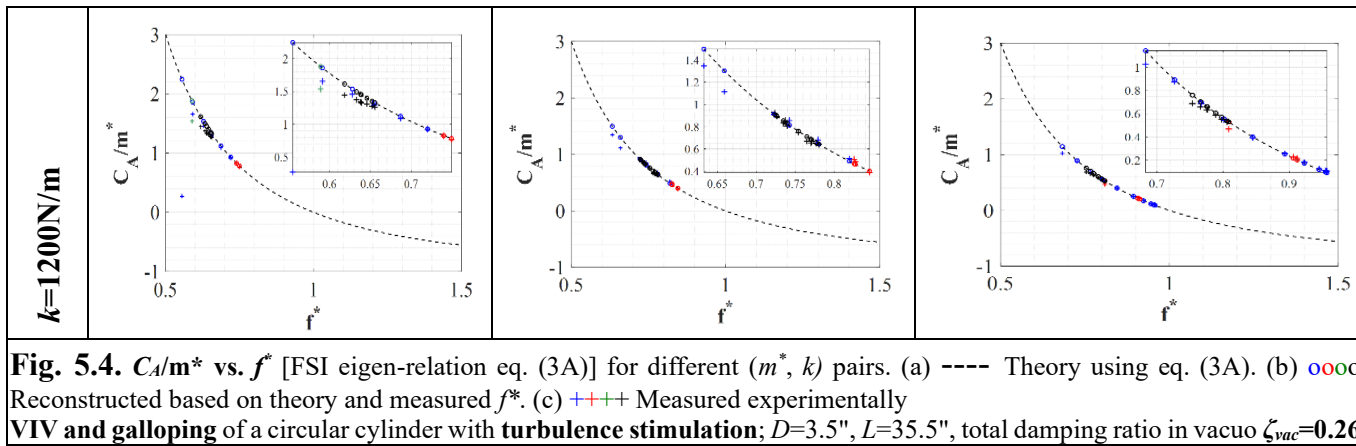


Fig. 5.3. C_A/m^* vs. f^* [FSI eigen-relation eq. (3A)] for different (m^*, k) pairs. (a) ---- Theory using eq. (3A). (b) $\circ\circ\circ\circ$ Reconstructed based on theory and measured f^* . (c) $++++$ Measured experimentally
VIV and galloping of a circular cylinder with **turbulence stimulation**; $D=3.5"$, $L=35.5"$, total damping ratio in vacuo $\zeta_{vac}=0.22$





5.7. Critical mass-ratio m^*

In [25], Govardhan and Williamson reported that an $m^* \cong 0.52-0.54$ exists, below which the end of the upper branch cannot be reached resulting in perpetual VIV. They measured this value experimentally for $k=0\text{N/m}$. They determined the end of the upper branch to be at $f_{osc}=f_{n,vac}$. Indeed, Figs. (5.1) and (5.2) show that for high k and low m^* , $f^*=1$ ($f_{osc}=f_{n,vac}$) is not reached. Results show smaller range of synchronization because it is actually located to the left of $f^*=1$; not to the right where expanded synchronization occurs.

In the absence of restoring force ($k=0\text{N/m}$), the cylinder will move with $f_{osc}=f_s$ the Strouhal vortex frequency, thus, following the Strouhal curve (Figs. 4.1.b, 4.3.b).

$$f^* = \frac{f_{osc}}{f_{n,vac}} = \frac{f_s}{f_{n,vac}} = \frac{0.2U}{D \frac{1}{2\pi} \sqrt{\frac{k}{m_{osc}}}} \rightarrow \infty \quad \text{For } St = 0.2 \text{ as } k \rightarrow 0 \quad (5-3)$$

This is the case when f^* goes to infinity as the eigen-relation (3A) in Fig. 3-2 and Fig. 5.5a show. This occurs when $C_A+m^*=0$ or $C_A/m^*=-1$. That is, there is a critical point with coordinates $(C_A/m^*=-1, f^*=\infty)$ where perpetual VIV occurs. That does not imply low m^* since $k=0$, as discussed in Section 5.6 above. From eq. (5-3) we have

$$\begin{aligned} f^* &= \frac{f_{osc}}{f_{n,vac}} = \frac{f_s}{f_{n,vac}} = \frac{0.2U}{D \frac{1}{2\pi} \sqrt{\frac{k}{m_{osc}}}} = \frac{0.2U}{D f_{n,vac}} = 0.2U_{n,vac}^* \rightarrow \infty && \text{For } st \\ &= 0.2 \text{ as } k \rightarrow 0 && (5-4) \end{aligned}$$

Perpetual oscillation is apparent in terms of $U_{n,vac}^*$, but not true in terms of absolute velocity U , as the nondimensionalization in $U_{n,vac}^*$ includes $f_{n,vac}$ in the denominator expanding the $U_{n,vac}^*$ range for low k and/or high m^* values.

That is, the criterion for expanded synchronization range is $C_A+m^=0$ and would occur for low $f_{n,vac}$, that is, low k and/or high m^* ; not only for $k=0$ at low m^* .*

This can easily be verified by looking at the oscillator eqn. (3-39). We can rewrite that equation as

$$(m_{osc} + m_A)\ddot{y}(t) + c\dot{y}(t) + ky(t) = F_U(t)\sim\sin(2\pi f_s t) \quad (5-5)$$

Next, $C_A+m^*=0$ means $(m_A+m_{osc})/m_d=0$, resulting in eqn. (5-6)

$$c\dot{y}(t) + ky(t)\sim\sin(2\pi f_s t) \quad (5-6)$$

Eqn. (5-6) is a first order linear equation whose solution shows that the oscillator oscillates at the frequency of vortex shedding.

To solve eq. (5-6), we proceed by using the integrating factor method as shown

$$\dot{y}(t) + \frac{k}{c}y(t) = \frac{1}{c}\sin(2\pi f_s t) \quad (5-7)$$

Next, we find the integrating factor $\mu(t)$

$$\mu(t) = \exp\left(\int \frac{k}{c} dt\right) = \exp\left(\frac{kt}{c}\right) \quad (5-8)$$

Multiplying eq. (5-7) throughout by the integrating factor gives

$$\exp\left(\frac{kt}{c}\right)\dot{y}(t) + \frac{k}{c}\exp\left(\frac{kt}{c}\right)y(t) = \frac{1}{c}\exp\left(\frac{kt}{c}\right)\sin(2\pi f_s t) \quad (5-9)$$

$$\left(\exp\left(\frac{kt}{c}\right) y(t) \right)' = \frac{1}{c} \exp\left(\frac{kt}{c}\right) \sin(2\pi f_s t) \quad (5-10)$$

Integrating both sides of eq. (5-10) with respect to t gives

$$\left(\exp\left(\frac{kt}{c}\right) y(t) \right) = \frac{1}{c} \int \exp\left(\frac{kt}{c}\right) \sin(2\pi f_s t) dt + a1 \quad (5-11)$$

$$\text{Recall that } \int \exp(ax) \sin(bx) dx = \frac{\exp(ax)}{a^2+b^2} [a \sin(bx) - b \cos(bx)] \quad (5-12)$$

where $a = \frac{k}{c}$ and $b = 2\pi f_s$, substituting these values into eq. (5-12) gives the right side of eq. (5-

11)

$$\frac{1}{c} \left\{ \left[\frac{\exp\left(\frac{kt}{c}\right)}{k^2/c^2 + 4\pi^2 f_s^2} \right] \left[\frac{k}{c} \sin(2\pi f_s t) - 2\pi f_s \cos(2\pi f_s t) \right] + a2 \right\}$$

$$\frac{\exp\left(\frac{kt}{c}\right)}{c} \left\{ \left[\frac{c^2}{k^2 + 4\pi^2 c^2 f_s^2} \right] \left[\frac{k}{c} \sin(2\pi f_s t) - 2\pi f_s \cos(2\pi f_s t) \right] + a2 \right\}$$

$$\exp\left(\frac{kt}{c}\right) \left\{ \left[\frac{1}{k^2 + 4\pi^2 c^2 f_s^2} \right] [k \sin(2\pi f_s t) - 2\pi c f_s \cos(2\pi f_s t)] + a2 \right\}$$

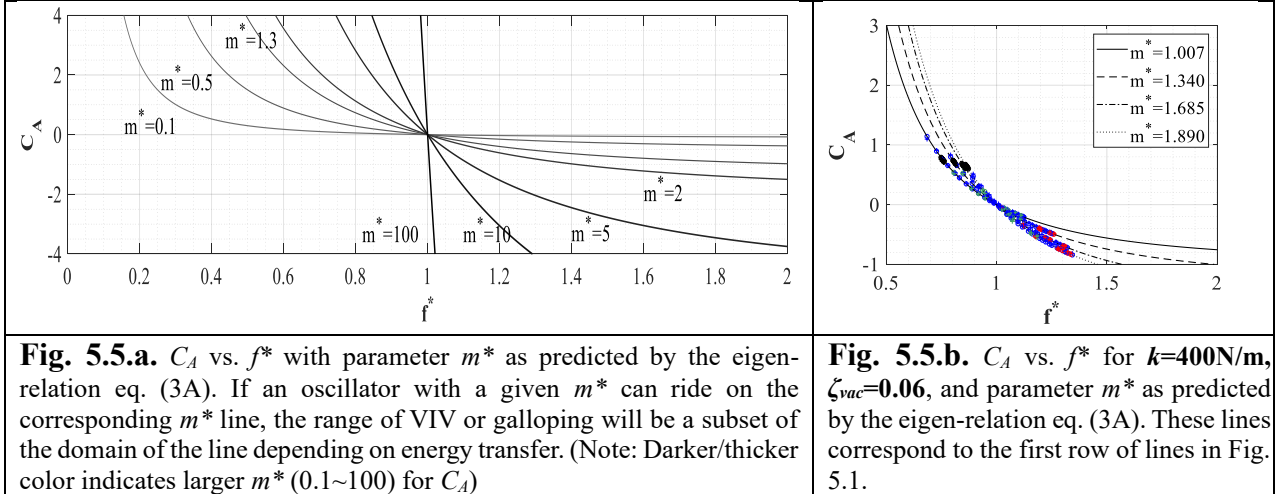
Finally,

$$y(t) = \left\{ \left[\frac{1}{k^2 + 4\pi^2 c^2 f_s^2} \right] [k \sin(2\pi f_s t) - 2\pi c f_s \cos(2\pi f_s t)] + a2 \right\} \quad (5-13)$$

$$y(t) = \left\{ \left[\frac{1}{k^2 + (2\pi c f_s)^2} \right] [k \sin(2\pi f_s t) - 2\pi c f_s \cos(2\pi f_s t)] \right\} + a3 \quad (5-14)$$

a1, a2, and a3 are constants of integration.

This proves that the oscillator oscillates at the Strouhal frequency of vortex shedding.



5.8. Is the Vortex Force Small?

Feng [19] first reported that the vortex forces are small [57]. Several papers reported that the vortex force is the residuary force [78] under the assumption that the theoretical added-mass ($C_A=1$ for a circular cylinder) can be separated from the total hydrodynamic force. Vortices shed nearly in synchronization with the force applied on the cylinder as they shed near the maximum displacement points, where the cylinder velocity is zero and the acceleration is maximum. *That is, the vortex force is nearly in synchronization with the acceleration $\ddot{y}(t)$ rather than the velocity $\dot{y}(t)$.* Thus, the residuary force under this definition cannot be the vortex force. Further, in the single-frequency model, after subtracting the force in phase with the acceleration $\ddot{y}(t)$ (added mass force) from the total force, the remaining force, $F_U(t)=F_T(t)-F_A(t)$, is in phase with the cylinder velocity $\dot{y}(t)$, as eq. (3D) shows.

A related question that we have been asked numerous times is: “How can the small vortex forces generate so much energy for harnessing by the VIVACE Converter?” Equivalently, “If the vortex force is not large how does it affect so strongly the oscillator dynamics?” To answer these questions we need to:

- (a) Clarify the vortex effects on the fluid-structure interface.
- (b) Calculate the relative magnitude of the vortex force compared to the other force components.
- (c) Identify the parameter ranges where vortex effects are strong or weak.

Based on the derived force expressions in equations in Table (3D) and the available experimental data in Figs. 5.7-5.9, these questions are addressed in the next two sections.

5.9. How Do Vortices Affect the Interface?

We propose that we classify vortex effects as *indirect* and *direct* and quantify them.

The indirect vortex effect would be that of modifying the flow in the cylinder vicinity, thus, affecting the force $F_A(t)$ in phase with $\ddot{y}(t)$ and $F_U(t)$ in phase with $\dot{y}(t)$. That can be clarified by comparison between VIV and galloping looking at the eigen-relation in Fig. 4.3.d. Specifically, galloping values are clustered around one f^* point, which just in this case coincides with the onset of VIV. This is further observable in Figs. 4.3.b, 4.3.e, 4.4a and 5.6. That is, prior to the full formation of the von Kármán street and after the end of it in fully developed galloping, the added mass coefficient is nearly constant around 0.8. This is not a general conclusion. In these figures, during VIV and transition from VIV to galloping, C_A varies between about +1 and -1. In other sets of data, C_A reaches higher values up to 3 or 4 at the onset of VIV (Garcia & Bernitsas (2018) [23]. Indirect vortex effects are nearly perfectly captured by the single-frequency response model of eqs. (3-10 to 3-14) as shown in all the experimental results for the entire range of VIV, transition to galloping, and galloping.

The direct vortex effect would be found in the residuary force $F_R(t)$ defined by eq. (4-1) as the difference between experiments and the remarkably accurate single-frequency response model as

a consequence of the eigen-relation derivation. In that case, $F_R(t)$ is primarily the “direct vortex force”. That is the vortex force exerted on the body at the moment of shedding. $F_R(t)$ is shown in Figs. 4.1.m-o, 4.2.i-k and Figs. 5.7-5.9

Figure 5.6. C_A at onset of VIV and galloping is nearly the same. Theoretical and experimental comparison of C_A vs. $U_{n,vac}^*$ for a circular cylinder with turbulence stimulation: $D=3.5''$, $L=35.5''$, $m^*=1.685$, end-springs with total $k=400\text{N/m}$, damping ratio in vacuo $\zeta_{vac} \in [0.02-0.22]$: (a) $\circ\circ\circ$ Reconstructed based on theory using eqs. (3A)-(3D) and measured f^* . (b) $++++$ Measured experimentally.

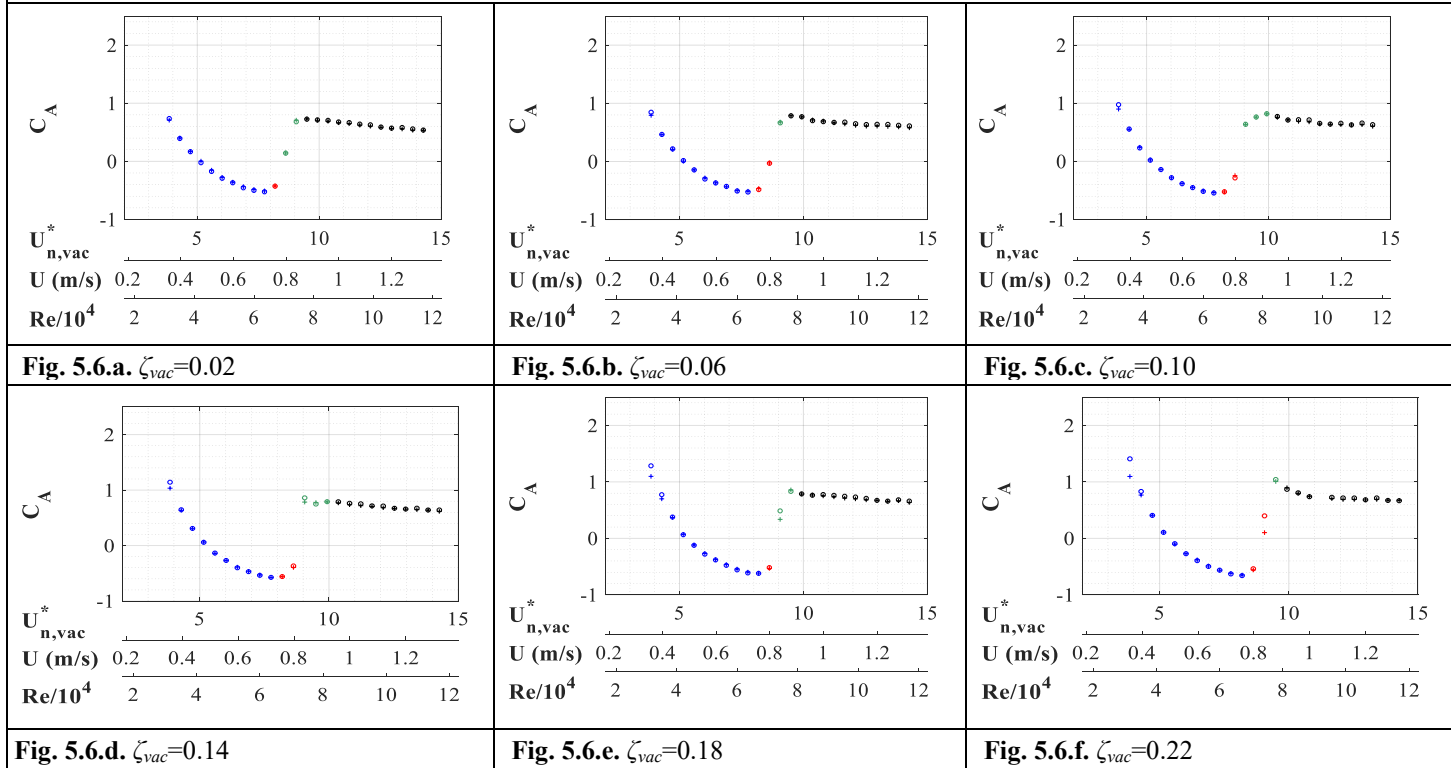


Figure 5.7. Residuary force magnitude F_{Ro} as % of F_{To} for a circular cylinder with **turbulence stimulation**; $D=3.5"$, $L=35.5"$, $m^*=1.685$, end-springs with $k \in [400-800 \text{N/m}]$, total damping ratio in vacuo $\zeta_{vac}=0.06$. +++ Measured experimentally

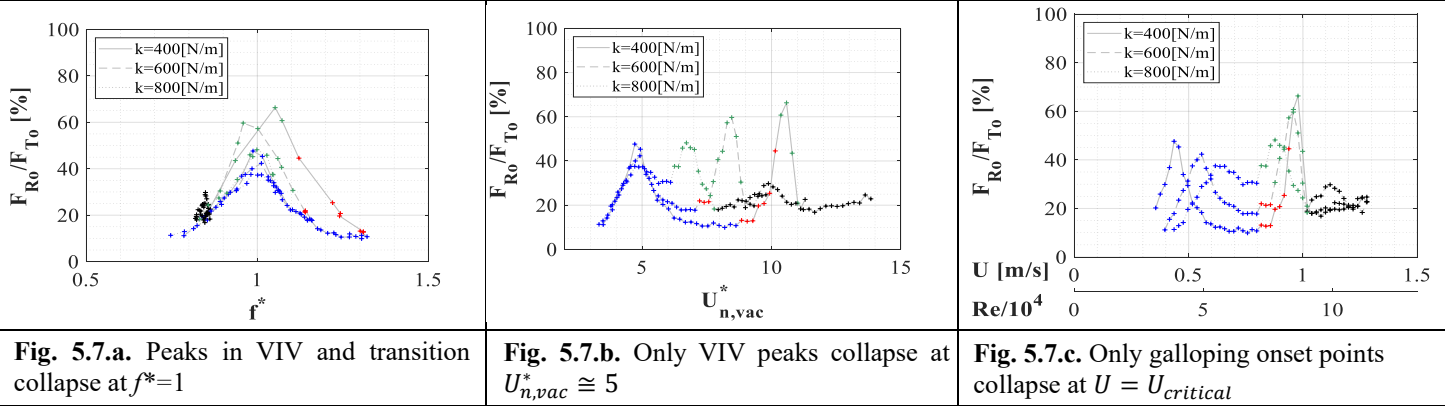


Figure 5.8. Residuary force magnitude F_{Ro} as % of F_{To} for a circular cylinder with **turbulence stimulation**; $D=3.5"$, $L=35.5"$, $m^*=1.685$, end-springs with $k=400 \text{N/m}$; total damping ratio in vacuo $\zeta_{vac} \in [0.06-0.22]$. +++ Measured experimentally.

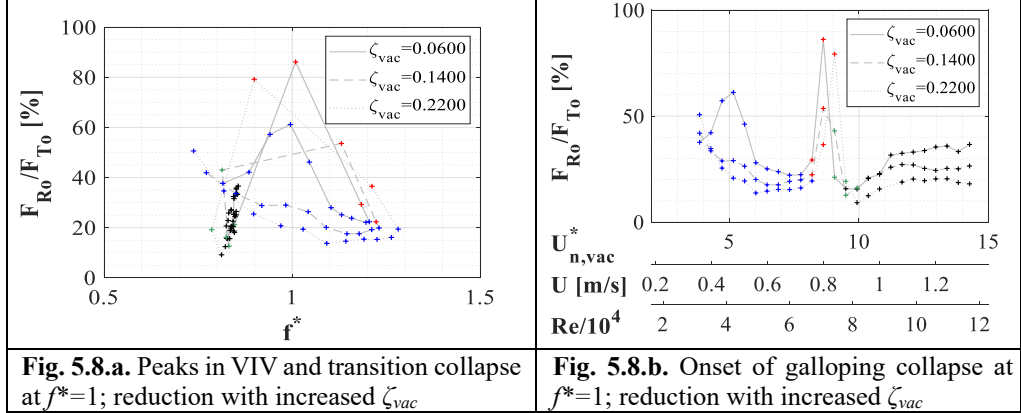
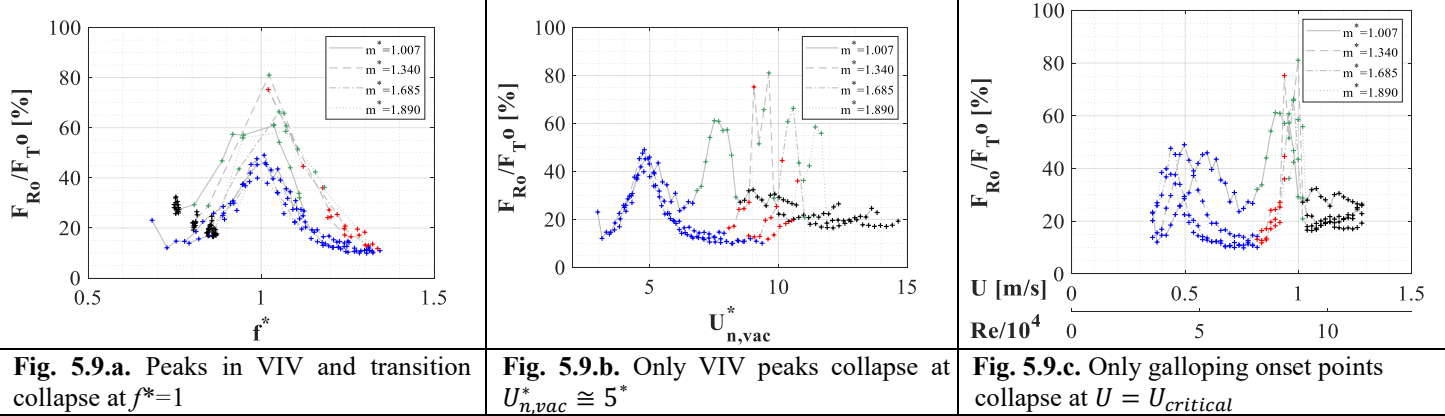


Figure 5.9. Residuary force magnitude F_{R0} as % of F_{T0} for a circular cylinder with **turbulence stimulation**; $D=3.5''$, $L=35.5''$, $m^* \in [1.007-1.890]$, end-springs with $k=400\text{N/m}$; total damping ratio in vacuo $\zeta_{vac}=0.06$. +++ Measured experimentally.



5.10. Magnitude of Vortex Forces

As discussed in Section 5.9, vortex effects are omnipresent. Their indirect effect on C_{Ao} (Fig. 4.4.b) and C_{Uo} (Fig. 4.4.g) can be seen by comparison between VIV and galloping over a wide range of ζ_{vac} . Their direct effect on C_{Ro} can be seen in Figs. 4.3.m-o, 4.4.i-k.

Cumulatively, Figs. 5.7, 5.8, 5.9 show the relative magnitude of the residuary forces with parameter k , ζ_{vac} , m^* , respectively. In each figure, the ratio F_{Ro}/F_{To} is plotted vs. f^* and the traditional $U^*_{n,vac}$. The latter shows collapse of data peaks in VIV but does not reveal the nature of the peaks in transition from VIV to galloping. On the contrary, *plotting F_{Ro}/F_{To} vs. f^* with respect to all three parameters shows consistent collapse of all peaks, at $f^*=1$, regardless of the hydrodynamic range. That is at $C_A=0$.*

Based on Figs. 3.2, 5.7a, 5.8a, and 5.9a, we can draw the following conclusion:

In general, vortex effects are omnipresent both directly and indirectly affecting the flow by changing it drastically. It would not be correct to state that vortex forces are small. It could possibly be stated that the direct vortex effect as measured in F_{Ro} may be small compared to the maximum total force. Relatively to F_{To} , though, F_{Ro} reaches around 50%, at ($f^*=1$, $C_A=0$), that is at $f_{osc}=f_{n,vac}$, where F_{To} is minimum. Again, helpful is comparison to galloping, where vortices do not shed in synchronization with the cylinder motion; the direct vortex effect is about 20% and $C_A \cong 0.8$.

The following two figures help shed light into the concept of direct and indirect vortex forces by looking at the time history of the forces in two specific cases: one close and one away from $f^*=1$.

5.10.a: For the case of $f^*=0.5$, the difference between the experimental/CFD results and the theoretical predictions are small and plotted in the last figure of the force cluster.

The peaks in the F_R force coincide with the vortex shedding moments. Those show the magnitude of the direct vortex force in Fig. 5-10a and clearer in the magnified Fig. 5-10b. The direct vortex force is relatively small because the test point is located away from $f^*=1$ where F_A would be zero.

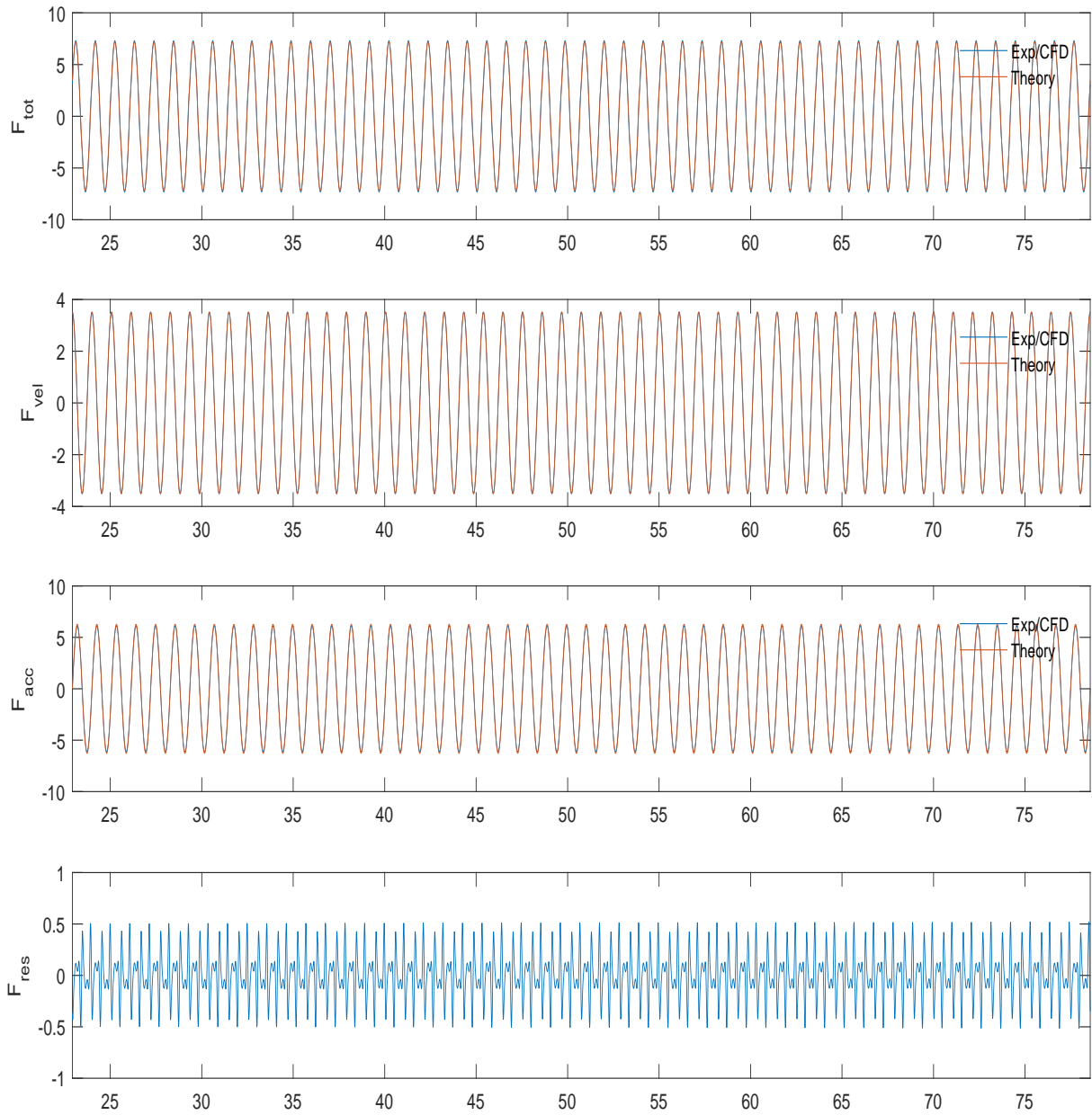


Figure 5.10a. Time history of force components for a circular cylinder with turbulence stimulation

$m^* = 1.685$, $k = 400\text{N/m}$ and $\zeta_{vac} = 0.06$ at $f^* = 0.5$

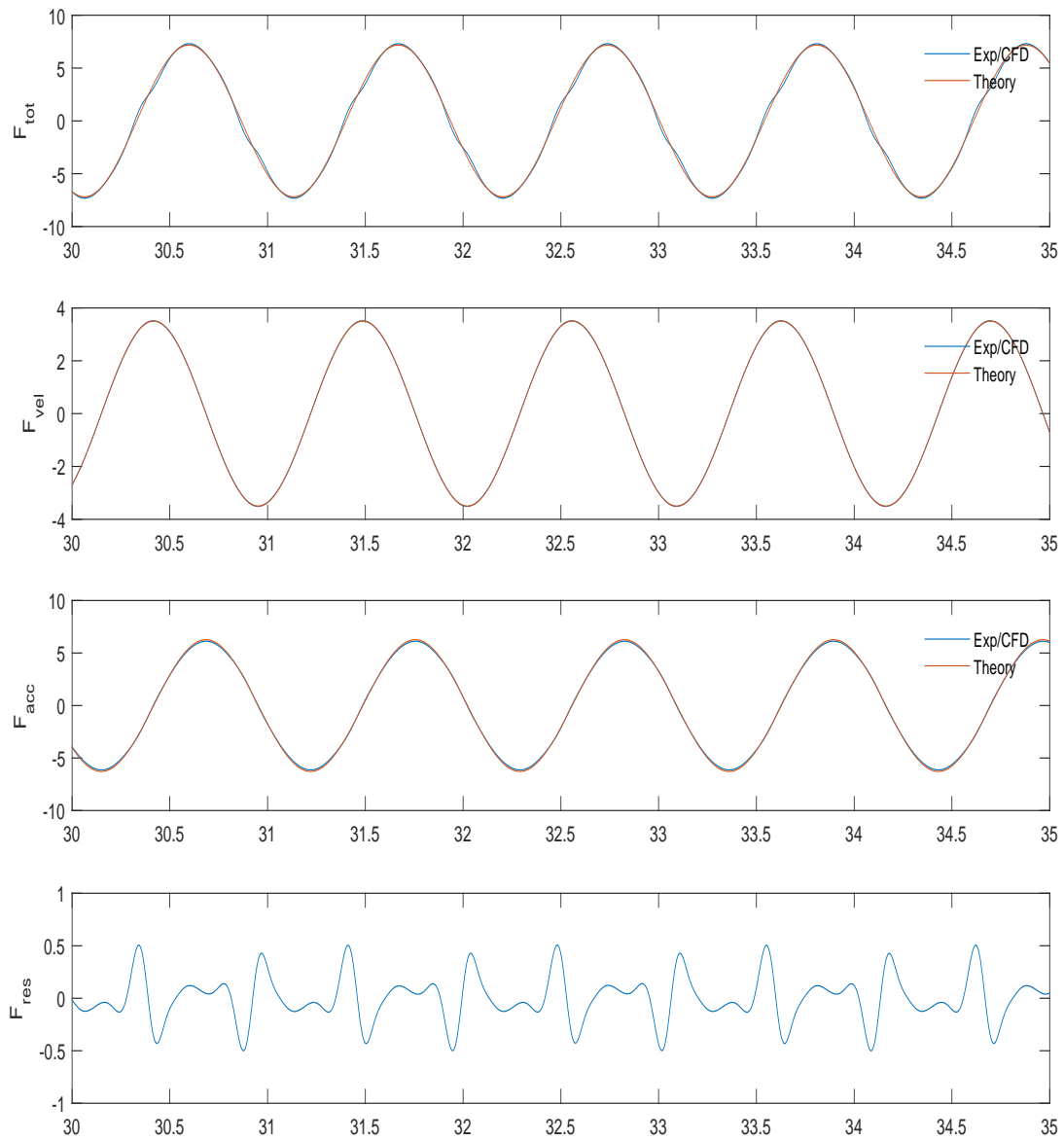


Figure 5.10b Magnified/zoomed time history of force components for a circular cylinder with turbulence stimulation $m^* = 1.685$, $k = 400\text{N/m}$ and $\zeta_{vac} = 0.06$ at $f^* = 0.5$

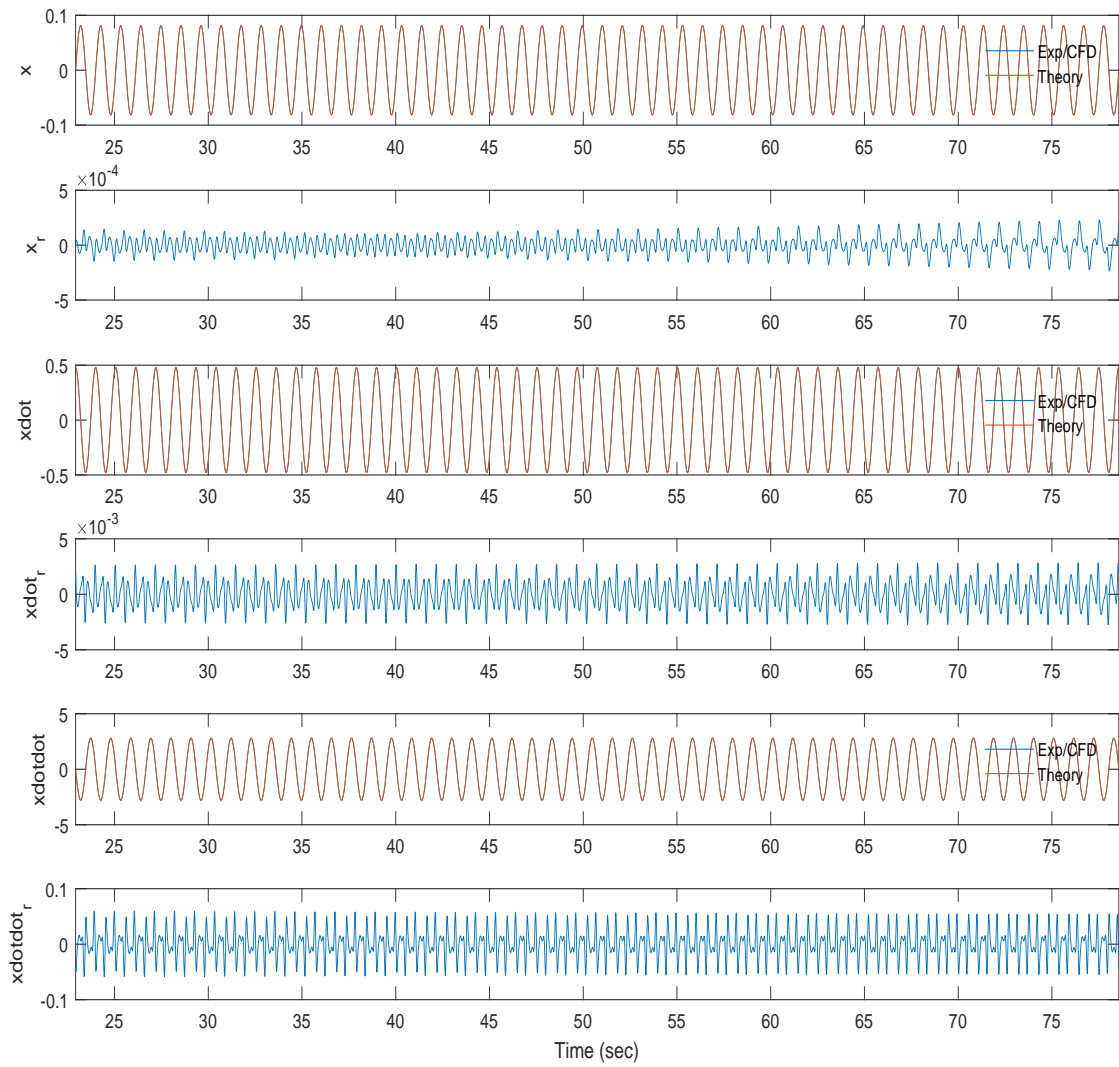


Figure 5.10c Kinematics components for a circular cylinder with turbulence stimulation $m^* = 1.685$, $k = 400\text{N/m}$ and $\zeta_{vac} = 0.06$ at $f^* = 0.5$

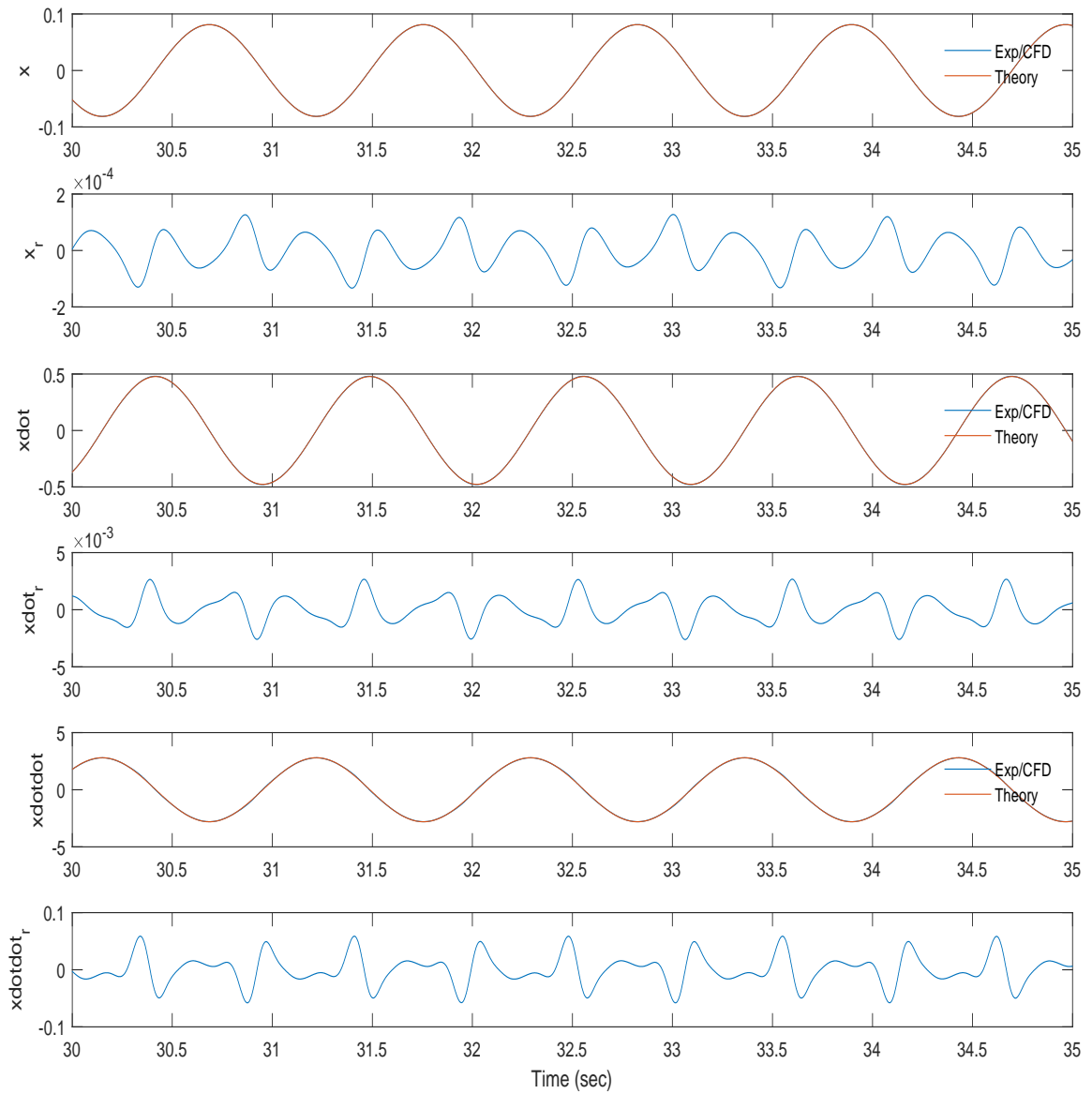


Figure 5.10d. Magnified/zoom-in kinematics components for a circular cylinder with turbulence stimulation $m^* = 1.685$, $k = 400\text{N/m}$ and $\zeta_{vac} = 0.06$ at $f^* = 0.5$

5.10.b: For the case of $f^*=0.9$, which is closer to $f^*=1$, where the added mass force would be nearly zero, the direct vortex force is by comparison large.

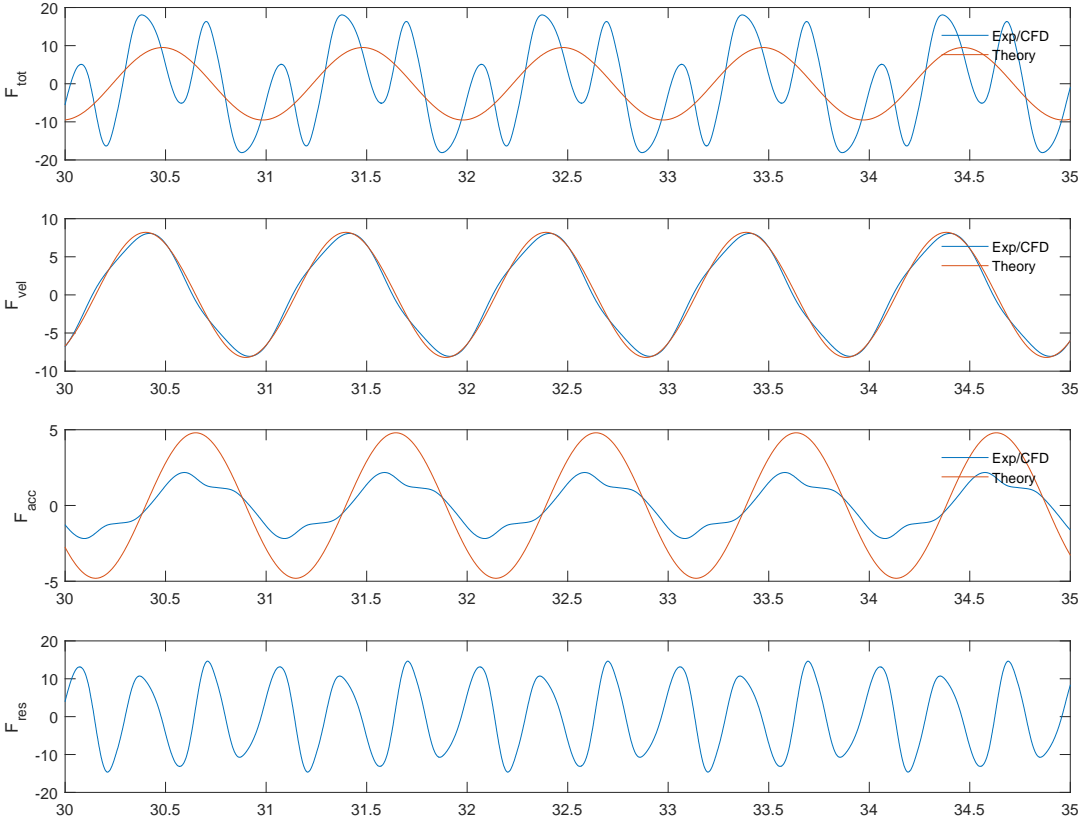


Figure 5.11a Magnified/zoomed Time history of force components for a circular cylinder with turbulence stimulation $m^* = 1.685$, $k = 400\text{N/m}$ and $\zeta_{vac} = 0.06$ at $f^* = 0.9$

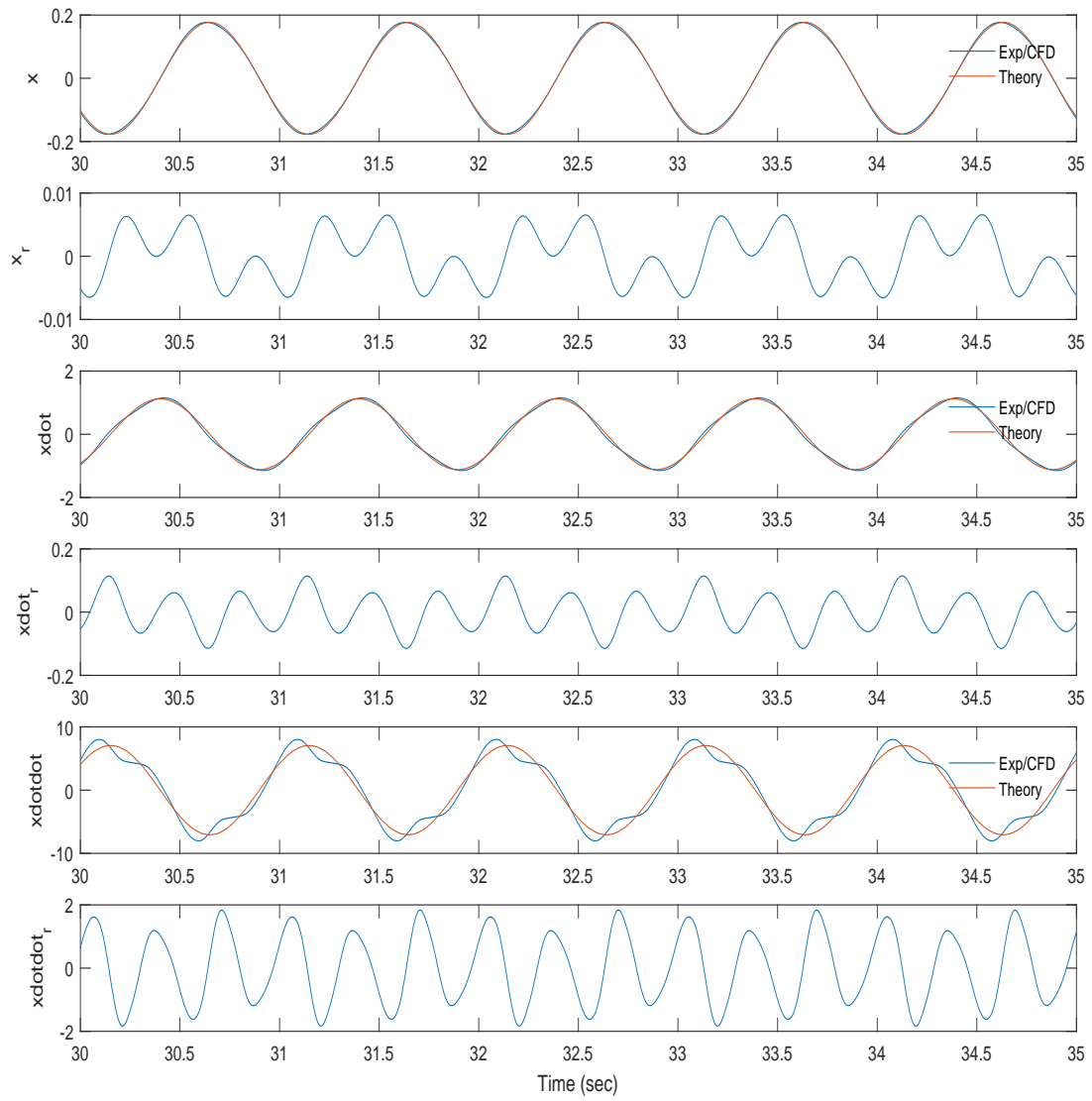


Figure 5.11b Magnified/zoomed Kinematics of the Force components for a circular cylinder with turbulence stimulation $m^* = 1.685$, $k = 400\text{N/m}$ and $\zeta_{vac} = 0.06$ at $f^* = 0.9$

Chapter Six

Discussion (Continued): Galloping Facts – Old & New

6.1. Introduction

The driving mechanisms in VIV and galloping are different. In VIV, the alternating vortex shedding creates alternating pressure variation, which synchronizes with the oscillator, which then follows the eigen-relation (eq. 3A). VIV may occur even with $k=0$. Typically, $k \neq 0$ and the springs provide a restoring force. That is, there are two mechanisms that contribute to VIV; a hydrodynamic excitation and a mechanical restoring force.

In galloping, the driving mechanism is an instability in a steady direction. Oscillation occurs only because there is a spring, or some other elastic constraint, which reverses the direction of the cylinder motion. At that point, the instability initiates from the opposite side of the cylinder. In our experiments, we use symmetric turbulence stimulation in the form of PTC. There is basically only a mechanical component that defines the natural frequency not a hydrodynamic one. Shedding vortices may be in-phase or out-of-phase with the galloping motion. In the former case they would enhance galloping; when vortex shedding is out-of-phase with the galloping motion it would oppose the galloping motion. Thus, the cylinder with turbulence stimulation oscillates below and near its $f_{n,vac}$ for all damping values. The value of the added mass remains about constant (Figs. 4.1.e, 4.2.a, 5.6).

The eigen-relation eq. (3A) holds in both phenomena, VIV and galloping, as is well verified by the experiments as shown in (Figs. 4.1.d, 4.5, 4.6). Also, all forces follow equations in Tables.

(3B-3D). Figs. 4.1, 4.2 and Appendix B show in different color the areas of VIV, transition between VIV and galloping, and fully developed galloping.

6.2. Onset of galloping

The onset of galloping is established in [11]. Since galloping follows eigen-relation eq. (3A), though, we may look at its onset from the point of view of f^* vs. C_A/m^* . Galloping response is at a nearly constant f^* a little below its $f_{n,vac}$, indicating a nearly constant C_A/m^* . Comparing C_A between VIV and galloping (Fig. 4.2.a) one can surmise the impact of vortex shedding on VIV. The vortex force is not everywhere small and particularly near $f^*=1$ as discussed in section 5.8-5.10.

6.3. Unifying onset of instabilities

Figs. 4.1b shows that VIV and galloping onsets occur experimentally nearly at the same f^* resulting in nearly the same C_A value (Fig. 4.2.a). Fig. 5.6 confirms this observation for damping values $\zeta_{vac} \in [0.02-0.22]$. The logical explanation is that at the very moment of initiation of the VIV instability the wake due to lock-in has not fully developed. Thus, the motion is instability-driven and vortices had not had the time to modify the flow for the transverse $F_A(t)$ to dominate the total force (Fig. 3.2). Quickly, this situation changes in the VIV range with increasing f^* and decreasing C_A .

6.4. How do vortices affect galloping?

We know that galloping is instability driven in one direction and vortices do not affect the motion. They may actually oppose motion depending on their shedding phase. As a result, the mechanism

of instability does not change and f^* and C_A remain nearly constant. Further, transition between VIV and galloping provides an interesting perspective. In transition, in tests where the end of VIV and the onset of galloping overlap as in Figs. 4.1.a and 4.1.b, both driving mechanisms coexist. As amplitude increases due to galloping the VIV synchronization ends and galloping takes over. That is, the vortices, albeit present and in increased numbers, and F_{Ro} being about 20% do not affect the added mass and galloping.

This issue requires further research for two reasons:

- The galloping response has reached the limit of the Low Turbulence Free Surface Water (LTFSW) Channel of the MRELab by approaching the free surface at about $A^*=3$;
- The onset of VIV should be defined more accurately accounting for the Coulomb static friction.

Chapter Seven

Conclusions

7.1. Dissertation Summary

Flow Induced Oscillations (FIO) is an important phenomenon in several engineering disciplines. In this dissertation, consistent rather than heuristic nondimensionalization of the fluid and oscillator dynamics in fluid-structure interaction, led to decoupling of amplitude from frequency response. Further, recognizing that the number of governing dimensionless parameters should decrease, rather than increase, due to the fluid-structure synergy at the interface, an eigen-relation is revealed for a cylinder in (FIO), including VIV and galloping: $m_A/m_{bod} = C_A/m^* = 1/f^{*2} - 1$. Here the term “eigen-relation” stands for a relation between excitation and system properties that has to hold for a solution to exist. It was shown that, for a given dimensionless oscillation frequency f^* , the ratio of real added-mass to oscillating-mass is fully defined. Amplitude decoupling and the eigen-relation, led to explicit expressions for coefficients, phases, and magnitudes of total, added-mass, and in-phase-with-velocity forces; revealing their dependence on the generic Strouhal number ($St_n = f_n^* = f_{osc}/f_{n,vacuo}$), damping, and Reynolds number. Heuristic dimensionless parameters, (mass-damping, reduced velocity, mass-ratio, force coefficients) used in VIV data presentation are not needed. Theoretical derivations and force reconstruction match nearly

perfectly with extensive experimental data collected over a decade in the Marine Renewable Energy Laboratory (MRELab) at the University of Michigan using four different oscillator test-models.

In this thesis:

- (a) Single-cylinder experimental data in FIO with mass ratio in the range [1.34 to 2.0], spring stiffness [400N/m to 1200N/m], and total system damping [0.02 to 0.26] are analyzed using the derived eigen-relation and force expressions.
- (b) The developed theory is used to explain some age-long experimental observations and potentially controversial questions in VIV and galloping among researchers in this field. Beyond the single frequency response model, the residuary force is derived by subtracting the single frequency response from the experimental data. Established facts regarding VIV and galloping and new important observations some of which are listed below are readily explained:
 - The effects of Strouhal, damping-ratio, mass-ratio, Reynolds, reduced velocity, and stagnation pressure.
 - The cause of expansion/contraction of the VIV range of synchronization.
 - The corresponding slope-change in oscillation frequency with respect to the Strouhal frequency of a stationary-cylinder vs. reduced velocity.
 - The critical mass-ratio m^* once considered to imply perpetual VIV.
 - The significance of the natural frequency of the oscillator in vacuo.

- The effect of vortices on VIV and galloping.
- The magnitude of vortex forces.
- The indirect and direct vortex effects.

(c) The derived eigen-relation is a first order solution to the VIV and galloping problems.

The developed equations for the forces in-phase with the velocity and acceleration, when subtracted from the total force measured experimentally, yields a residuary force.

(d) Data obtained from the MRELab experimentally and with CFD are analyzed further to identify other force components likely related to vortex shedding directly. This is a step towards higher order theories for VIV and galloping beyond the eigen-relation.

7.2. Closing remarks and Future Work

An eigen-relation, Table. (3A), was revealed at the fluid-structure interface in Flow Induced Oscillations based on the single-frequency response model. This resulted in change in the interpretation and modeling of VIV and galloping. Based on consistent nondimensionalization, the problem was reduced to two governing hydrodynamic parameters the generic Strouhal and Reynolds numbers. Proper interpretation of the interface between fluid and structure revealed a constraint, which led to the eigen-relation. Frequency response was linked to Strouhal only and amplitude was decoupled from Strouhal and linked to Reynolds only. Explicit dependence of forces and phases on parameters were derived, Table. (3B-3D), showing that heuristic parameters, like mass-damping and reduced velocity, may be of little relevance to FIO. Agreement with extensive experimental data is exceptional, proving equations in tables. (3A-3D).

The residuary force $F_R(t)$, being primarily the direct vortex force, is derived from the experimental data after subtracting the forces in phase with velocity and acceleration. Development beyond the single-frequency response model using perturbation would apply on $F_R(t)$. Direct vortex force is defined as the force exerted on the body at the moment of vortex shedding. This is not the force due to the vortex mass attached to the oscillating body which directly affects the added mass.

The developed methodology provides direct and simple interpretation of experimentally established facts on VIV and galloping. Thirteen observations were discussed showing consistency fully supported by theory and experiments.

Several research issues can be pursued immediately. More experimental observations can be verified and explained:

- (1) In the near future, more complex oscillators with nonlinear restoring forces and damping models already tested in the MRELab as shown in some papers [12,43,66] can be analyzed with the developed eigen-relation and force equations. Giving a further thought, the theoretical power harnessed by an oscillator in FIO can be calculated based on the force expressions developed in this research.
- (2) The developed methodology is general enough to be valid for: (a) FIO of any other shape – not just circular cylinders. (b) Other FSI phenomena, such as fluttering instabilities of foils, to reveal similar eigen-relations at the fluid-structure interface. (c) Two-dimensional cylinder and cable/pipeline FIO, where the modes can be defined for nondimensionalization.
- (3) The issue of energy transfer from fluid to structure can be addressed easier – albeit not easy – by relating energy transfer between fluid and structure to the interface conditions (eigen-relation and the selected amplitude A).

(4) The approach developed by Zueck (2019) [82] can show the energy that the structure can absorb satisfying the interface conditions, while energy transfer from fluid can be related to Reynolds without delving into small turbulence scales.

References

- [1] Alonso G., Valero E., Meseguer J., 2009. An analysis on the dependence on cross section geometry of galloping instability of two-dimensional bodies having either biconvex or rhomboidal cross sections. *European Journal of Mechanics B/Fluids* 28, 328-334.
- [2] Assi, G.R.S., Bearman, P.W., Meneghini, J., 2010. On the wake-induced vibration of tandem circular cylinders: The vortex interaction excitation mechanism, *Journal of Fluid Mechanics*. 661, 365-401.
- [3] Assi, G.R.S., Bearman, P.W., 2014. Transverse galloping of circular cylinders fitted with solid and slotted splitter plates. *Journal of Fluids and structures*. 54(2015) 263-280.
- [4] Bearman, P.W., 1984. Vortex shedding from oscillating bluff bodies. *Annual Review of Fluid Mechanics* 16, 195–222.
- [5] Bearman, P.W., 2011. Circular cylinder wakes and vortex-induced vibrations. *Journal of Fluid Mechanics* 27, 648–658.
- [6] Bernitsas M.M., Ben-Simon Y., Raghavan K., Garcia E. M. H., (2008), “The VIVACE Converter: Model Tests at Reynolds Numbers Around 10^5 ”, OMAE 2006; and *Journal of Offshore Mechanics and Arctic Engineering, ASME Trans.*, Feb. 2009, V.131(1), pp. 1-13.
- [7] Bernitsas, M.M., Raghavan, K., Duchene, G., 2006. Induced Separation and Vorticity Using Roughness in VIV of Circular Cylinders at $8 \times 10^3 < Re < 1.5 \times 10^5$. In: Proceedings of International Conference of Offshore Mechanics and Arctic Engineering, Estoril, Portugal, June 15
- [8] Bernitsas, M. M., Raghavan, K., Ben-Simon, Y. and Garcia, E. M. H., (2008), “VIVACE (Vortex Induced Vibration Aquatic Clean Energy): A new concept in generation of clean and renewable energy from fluid flow”, *Journal of Offshore*

- Mechanics and Arctic Engineering-Trans. of the ASME*, 130(4), No. 041101; OMAE2006.
- [9] Bernitsas, M.M., Raghavan, K., 2009. Fluid motion energy converter. United States Patent and Trademark Office Patent #7, 493, 759 B2 issued on February 24, 2009.
- [10] Bernitsas, M. M. and Raghavan, K., “Enhancement of Vortex Induced Forces & Motion through Surface Roughness Control” United States Patent and Trademark Office, Patent# 8,047,232 B2, issued on November 1, 2011.
- [11] Bernitsas, M.M. (2016), “Harvesting Energy by Flow Included Motions”, Chapter 47, Springer Handbook of Ocean Engineering. Springer, Heidelberg, Germany.
- [12] Bernitsas M.M, H. Sun (2018), “Hydrokinetic Energy Conversion Using A Single-Cylinder Nonlinear Oscillator In Flow Induced Oscillations”, Proceedings IUTAM Symposium on *Critical flow dynamics involving moving/deformable structures with design applications*, June 18-22, Santorini, Greece.
- [13] Blevins, R.D., 1990. Flow-Induced Vibration, 2nd Edition. Van Nostrand Reinhold, New York, USA.
- [14] Chang, C. C., 2010. Hydrokinetic Energy Harnessing by Enhancement of Flow Induced Motion Using Passive Turbulence Control. Ph.D. Thesis, Dept. of Naval Architecture & Marine Engineering, University of Michigan.
- [15] Chang C.C., Bernitsas M.M., 2011. Hydrokinetic energy harnessing using the VIVACE converter with passive turbulence control, Proceedings of the 30th OMAE 2011 Conf., Paper #50290, Rotterdam, The Netherlands, June 19-24, 2011.
- [16] Chang, C. C., Kumar, R.A., Bernitsas, M.M., 2011. VIV and galloping of single circular cylinder with surface roughness at $30,000 \leq Re \leq 120,000$. *Ocean Engineering* 38, 1713-1732.
- [17] Cunha, L.D., Pesce, C.P., Wanderley, J., Fajarra, A.L.C., 2006. “The Robustness of the Added Mass in VIV Models”, Proceedings of 25th OMAE 2006, Hamburg, Germany, June 04-09.
- [18] Edmund, D., Amanda D., Bernitsas, M. M. (2010), “First Study on the Effect of Passive Tails on Harnessing Hydrokinetic Energy using the VIVACE Converter”, Report Marine Renewable Energy Laboratory, January 2010.

- [19] Feng, C.-C., 1968. The measurement of vortex induced effects in flow past stationary and oscillating circular and d-section cylinders. Master's Thesis, Department of Mechanical Engineering, the University of British Columbia, Canada.
- [20] Ferrari, J.A. and Bearman, P.W (2000) A Three-Dimensional Model for Wave and Vortex-Induced Vibration of Deepwater Riser Pipes. *Flow-Induced Vibrations*, 3-10.
- [21] Foulhoux, L. and M.M. Bernitsas, (1993), "Forces and Moments on a Small Body Moving in a 3-D Unsteady Flow," *Journal of Offshore Mechanics and Arctic Engineering, ASME Trans.*, V.115, No.2, May, pp. 91-104.
- [22] Gabbai, R. D., and Benaroya, H., (2005) "An Overview of Modeling and Experiments of Vortex-induced Vibrations of Circular Cylinders", *Journal of Sound and Vibration*, Vol. 282, pp. 575-616.
- [23] Garcia, E.M.H., Bernitsas, M. M., (2018) "Effect of Damping on Variable Added Mass and Lift of Circular Cylinders in Vortex-Induced Vibrations", *Journal of Fluids and Structures*, 80 451–472
- [24] Govardhan, R., Williamson, C.H.K., 2000. "Modes of vortex formation and frequency response of a freely vibrating cylinder." *Journal of Fluid Mechanics* 420, 85–130.
- [25] Govardhan, R., Williamson, C.H.K., (2002), "Resonance forever: existence of a critical mass and an infinite regime of resonance in vortex-induced vibration" *J. Fluid Mech.* Vol. 473, pp. 147–166.
- [26] Govardhan, R.N., Williamson, C.H.K., 2006. Defining the "modified griffin plot" in vortex-induced vibration: revealing the effect of Reynolds number using controlled damping. *Journal of Fluid Mechanics* 561, 147–180.
- [27] Griffin, O.M., Skop, R.A., Koopman, G.H., 1973. "The vortex-excited resonant vibrations of circular cylinders." *Journal of Sound and Vibration* 31, 235–249.
- [28] Griffin, O.M., Skop, R.A., Ramberg, S.E., 1976. Modeling of the vortex-induced oscillations of cables and bluff structures. Society for Experimental Stress Analysis Spring Meeting, 9–14 May, Silver Spring, MD, USA.
- [29] Griffin, O.M., Koopmann, G.H., 1977. "The vortex-excited lift and reaction forces on resonantly vibrating cylinders." *Journal of Sound Vibration* 54, 435–448.
- [30] Hartlen, R.T., Currie, I.G., 1970. Lift oscillation model for vortex-induced vibration. *ASCE Journal of Engineering Mechanics Division* 96, 577–591.

- [31] <https://www.eia.gov/energyexplained/hydropower/wave-power.php>
- [32] <https://www.eia.gov/todayinenergy/detail.php?id=32912>
- [33] Justesen, P., 1989. Hydrodynamic forces on large cylinders in oscillatory flow, *Journal of Waterway, Port, Coastal and Ocean Engineering*, 115(4), 497-514.
- [34] Keulegan, G.H., and Carpenter, L.H., (1958), “Forces on cylinders and plates in an oscillating fluid,” *Journal of Research of the National Bureau of Standards*, V.60, No.5.
- [35] Khalak, A., Williamson, C.H.K., 1999. Motions, forces and mode transitions in vortex-induced vibrations at low mass-damping. *Journal of Fluids and Structures* 13, 813–851.
- [36] Kim, E.S. 2013. Synergy Of Multiple Cylinders In Flow Induced Motion For Hydrokinetic Energy Harnessing. Ph.D. Thesis, Dept. of Naval Architecture & Marine Engineering, University of Michigan.
- [37] Kozakiewicz, A., Fredsøe, J. and Sumer, B., 1995. Forces on Pipelines in Oblique Attack: Steady Current and Waves, Vol. II. The Hague, Netherlands, 174–183.
- [38] Lee J.H., Chang C. C., Xiros N., and Bernitsas M. M. (2009), “Integrated Power Take Off and Virtual Oscillator System for the VIVACE Converter: Vck System Identification”, Proceedings of the 2009 ASME International Engineering Congress and Exposition, Paper #, IMECE2009-11430, Lake Buena Vista, FL, Nov. 13-19, 2009.
- [39] Lee, J.H., 2010. Hydrokinetic Power Harnessing Utilizing Vortex Induced Vibrations through a Virtual c-k VIVACE Model. Ph.D. Thesis, Dept. of Naval Architecture & Marine Engineering, University of Michigan.
- [40] Lee, J.H., Bernitsas, M.M., 2011. High-damping, high-Reynolds VIV tests for energy harnessing using the VIVACE converter. *Ocean Engineering* 38, 1697-1712.
- [41] Lee, J.H., Xiros, N., Bernitsas, M.M., 2011. Virtual damper-spring system for VIV experiments and hydrokinetic energy conversion. *Ocean Engineering* 38, 732-747.
- [42] Lin Ding, Li Zhang, Michael M. Bernitsas, Che-Chun Chang, 2016. Numerical simulation and experimental validation for energy harvesting of single-cylinder VIVACE converter with passive turbulence control. *Renewable Energy* 85(2016) 1246-1259.
- [43] Ma, C., Sun, H., Bernitsas, Marinos M., “Nonlinear Piecewise Restoring Force in Hydrokinetic Power Conversion Using Flow Induced Motions of Two Tandem Cylinders”, Proceedings of the 36th OMAE 2017 Conf., Paper #61544, Trondheim,

- Norway, June 25-30, 2017; *Journal of Offshore Mechanics and Arctic Engineering*, ASME Transactions, (Jan. 2018) DOI: 10.1115/1.4038584; 140(4), 041901
- [44] Morison, J.R., O'Brian, M.P., Johnson, J.W., Schaaf, S.A., (1950), "The Force Exerted by Surface Waves on Piles", *Petroleum Trans. AIME*, TP 2846, V.189, pp. 149-157.
- [45] Morse, T. L., Govardhan, R., Williamson, C. H. K., 2008. The effect of end conditions on the vortex-induced vibration of cylinders, *Journal of Fluids and Structures* 24, 1227-1239.
- [46] Ofuegbe, J., Sun, H., Chen, J.-U., Bernitsas, M.M., "Experimental Data Analysis of Single Cylinder in Flow Induced Oscillations (VIV & Galloping): Processed by the Eigen-Relation Solution", Report #013; Marine Renewable Energy Laboratory, University of Michigan, May 2020.
- [47] Ofuegbe, J., Sun, H., Chen, J.-U., Bernitsas, M.M., "Experimental Data Analysis of Single Cylinder in Flow Induced Oscillations (VIV & Galloping): Graphs of Parametric Dependence", Report #014; Marine Renewable Energy Laboratory, University of Michigan, June 2020.
- [48] Paidoussis M.P, Price S.J, E. de Langre, (2011). *Fluid-Structure Interactions*, Cambridge Univ. Pres.
- [49] Raghavan, K., 2007. Energy extraction from a steady flow using vortex induced vibration. Ph.D. University of Michigan. M.M. Bernitsas (supervisor).
- [50] Raghavan, K., Bernitsas, M. M. (2010), "Experimental Investigation of Reynolds Number Effect on Vortex Induced Vibration of Rigid Cylinder on Elastic Supports," *Ocean Engineering*, Vol.38, No.5-6, April, pp.719-731.
- [51] Rayleigh Lord, 1896. *Theory of sound*, second ed. Macmillan, London.
- [52] Sarpkaya, T., 1976a. Vortex shedding and resistance in harmonic flow about smooth and rough circular cylinders at high Reynolds numbers. Technical Report No: NPS-59SL76021, Naval Postgraduate School, Monterey, CA, USA.
- [53] Sarpkaya, T., 1976b. In-line and transverse forces on smooth and sand-roughened cylinders in oscillatory flow at high Reynolds number. Naval Postgraduate School Technical Report No: NPS-69L76062, Monterey, CA, USA.
- [54] Sarpkaya, T., 1979. Vortex-induced oscillations: selective review. *Journal of Applied Mechanics* 46.

- [55] Sarpkaya, T., 1986a. In-line transverse forces on smooth and rough cylinder in oscillatory flow at high Reynolds numbers. Technical Report No. NPS-69-86-003, Naval Postgraduate School, Monterey, CA, USA.
- [56] Sarpkaya, T., 1986b. Force on a circular cylinder in viscous oscillatory flow at low Keulegan-Carpenter numbers. *Journal of Fluid Mechanics* 165, 61–71.
- [57] Sarpkaya, T., 2004. "A Critical Review of the Intrinsic Nature of Vortex-induced Vibrations", *Journal of Fluids and Structures*, Vol. 19, pp. 389–447.
- [58] Scruton, C., 1955. Wind-excited oscillations of tall stacks. *Engineer* 199, 806–808.
- [59] Scruton, C., 1956. Note on the Aerodynamic Stability of Truncated Circular Cones and Tapered Stacks. National Physical Laboratory, Teddington, UK.
- [60] Scruton, C., 1965. On the Wind-Excited Oscillations of Stacks, Towers, and Masts, In: Conference Proceedings of 1963 National Physical Laboratory, Teddington, UK.
- [61] Scruton, C., 1966. Brief review of wind effects on buildings and structures. *Royal Aeronautical Society Journal* 70, 553–560.
- [62] Skop, R.A., Balasubramanian, S., 1997. A new twist on an old model for vortex-excited vibrations. *Journal of Fluid and Structures* 11, 395–412.
- [63] Strouhal, 1878. V. Übereine besondere Art der Tonerregung. *Annalen der Physik* 1878;241(10):216-51.
- [64] Sumer, B. M., Fredsøe, J., 1988. Transverse vibrations of an elastically mounted cylinder exposed to an oscillating flow. *Journal of Offshore Mechanics and Arctic Engineering* 110, 387-394.
- [65] Sun, H., Bernitsas, M. P., Kim, E. S., Bernitsas, M. M., (2015), "Virtual Spring-Damping System for Fluid Induced Motion Experiments", *Journal of Offshore Mechanics and Arctic Eng., ASME Trans.*, V. 137, No. 1, 061801, Dec.
- [66] Sun Hai, Chunhui Ma, Michael M. Bernitsas, (2018), "Hydrokinetic Power Conversion using Flow Induced Vibrations with Nonlinear (adaptive piecewise-linear) Springs", *Energy*, 143, 1085-1106.
- [67] Sun Hai, Marinos M. Bernitsas, Mert Turkol (2020), "Adaptive Harnessing Damping in Hydrokinetic Energy Conversion by two Rough Tandem-Cylinders using Flow-Induced Vibrations", *Renewable Energy*, Volume 149, April 2020, pp. 828-860.

- [68] Triantafyllou, M. S. (1991). “Dynamics of cables, towing cables and mooring systems.” *Shock Vib. Digest*, 23(7), 3-8.
- [69] Triantafyllou, M.S., Bourguet, R., Dahl, J., Modarres-Sadeghi, Y. (2016), Chapter 36, “Harvesting Energy by Flow Included Motions”, Springer Handbook of Ocean Engineering. Springer, Heidelberg, Germany.
- [70] Vandiver, J.K., 2012, “Damping parameters for flow-induced vibration” *Journal of Fluids and Structures* Vol 35 (2012) 105-119
- [71] Vickery, B.J., Watkins, R.D., 1964. Flow-induced vibrations of cylindrical structures. In: Silvester, R. (Ed.), Proceedings of the First Australasian Hydraulics and Fluid Mechanics Conference, hosted by: University of Western Australia, Crawley, Australia, 1962, Pergamon Press, New York, pp. 213–241
- [72] Vikestad, K., Vandiver, J.K., Larson, C.M., (2000), “Added mass and oscillation frequency for a circular cylinder subjected to vortex-induced vibrations and external disturbance,” *J. of Fluids and Structures*, V.14, 1071-1088.
- [73] Von Karman, T., Rubach, H., 1912. The mechanism of the fluid and air- resistance. *Phys Z* 13, 49-59.
- [74] Von Kármán, T.W.R.S., 1938. Airfoil theory for non-uniform motion. *Journal of the Aeronautical Science* 5, 379-390.
- [75] Von Kármán, T. Reson (2005) 10: 97. Collapse of the Tacoma narrows bridge. Volume 10, Issue 8, pp 97–102. <https://doi.org/10.1007/BF02866750>.
- [76] Williamson, C.H.K., 1985, “Evolution of a single wake behind a pair of bluff bodies”, *J. Fluid Mech.*, Vol. 159, pp. 1-18.
- [77] Williamson, C.H.K., Roshko, A., 1988. Vortex formation in the wake of an oscillating cylinder. *Journal of Fluids and Structures* 2, 355–381.
- [78] Williamson, C.H.K., Govardhan, R., 2004. Vortex-induced vibrations. In: Lumley, J.L., Davis, S.H., Moin, P. (Eds.), Annual Review of Fluid Mechanics, Annual Reviews, Palo Alto, pp. 413–455.
- [79] Yanfang Lv, Liping Sun, Michael M. Bernitsas, Hai Sun, “A Comprehensive Review of Nonlinear Oscillators in Hydrokinetic Energy Harnessing using Flow-Induced Vibrations”. *Renewable & Sustainable Energy Reviews*.

- [80] Zdravkovich, M.M., 1982. Scruton number: a proposal. *Journal of Wind Engineering and Industrial Aerodynamics* 10, 263–265.
- [81] Zdravkovich, M.M., 1990. On origins of hysteretic responses of a circular cylinder induced by vortex shedding. *Zeitschrift fur Flugwissenschaften und Weltraumforschung (Journal of Flight Sciences and Space Research)* 14, 47–58. Springer-Verlag.
- [82] Zueck, R. F., (2019), “The Evolutionary Geometric Physics of Vortex Induced Vibrations”, Proceedings of 38th OMAE 2019, Glasgow, Scotland, June 9-14.

Appendix A

Post Processing Results for VIV of Smooth Cylinder

The figures in the next 16 pages show some of the results for data post-processing for a smooth cylinder in VIV for mass ratio ranging from 1.25 to 1.84. These results show how consistent the eigen relation theory is with the experimental data just as it was shown in Sections 4.3 and 5.6.

For clarity and proper understanding of this appendix, the results are arranged in increasing stiffness, damping ratio, and mass ratio.

The arrangement is as follows:

$m^* = 1.25$ - pages 2-9 of this appendix

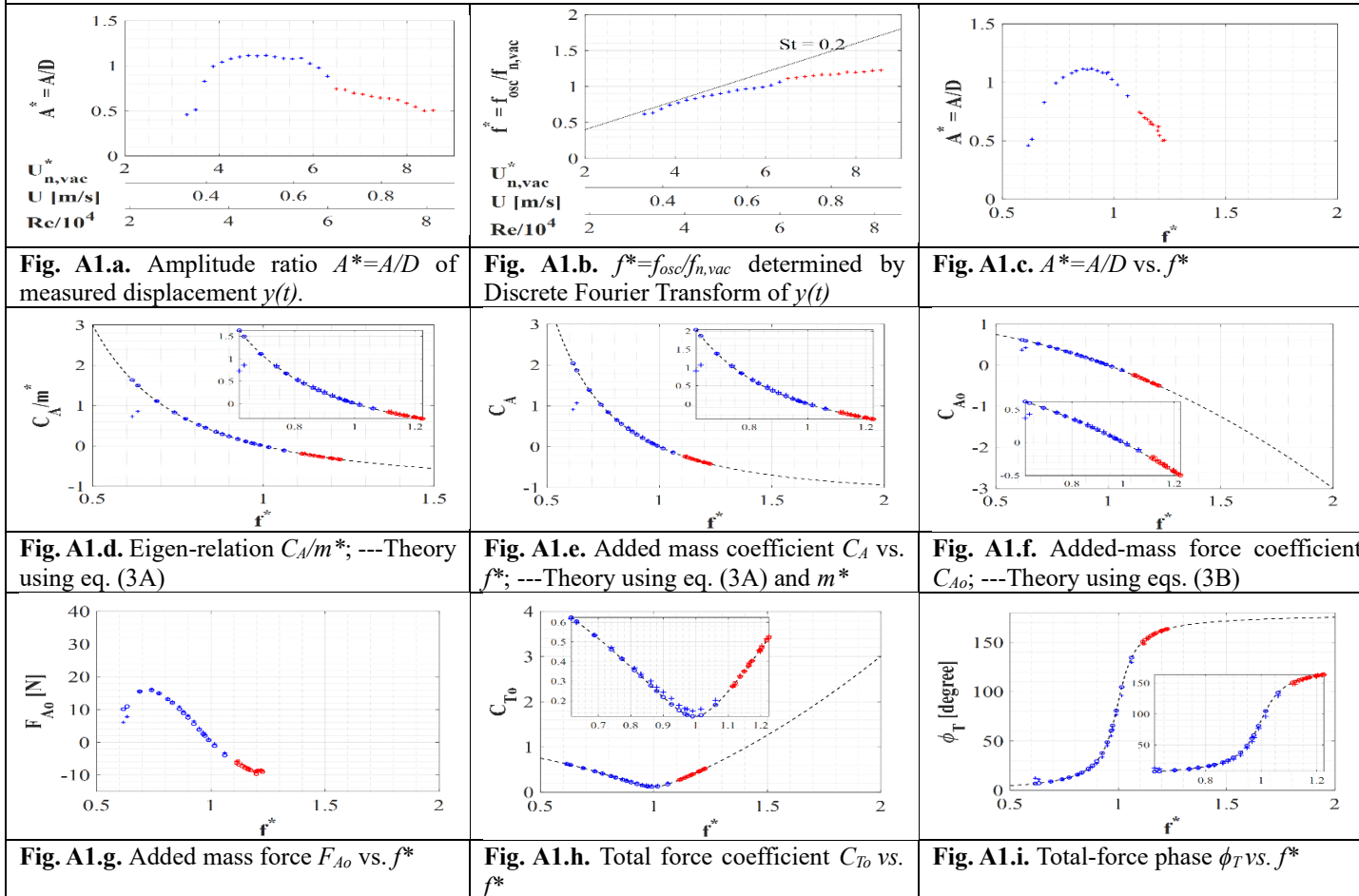
$m^* = 1.84$ - pages 10-17 of this appendix

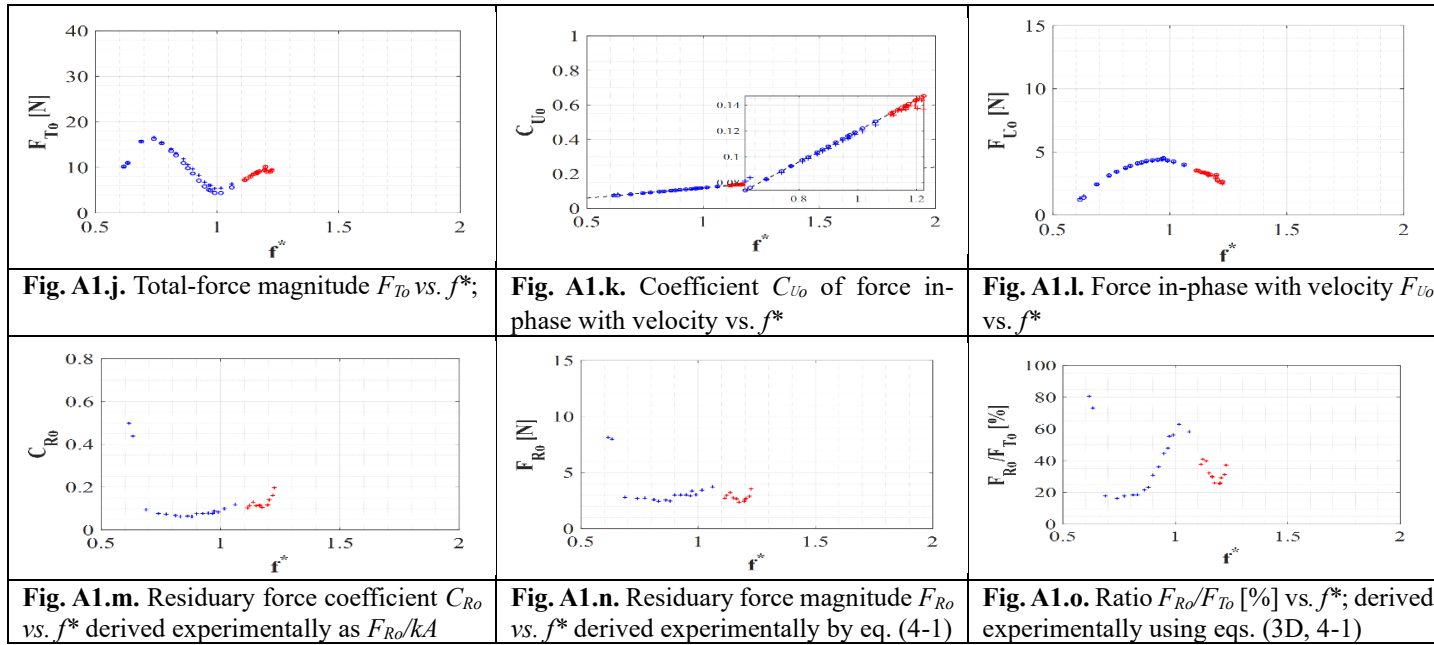
Results in this appendix buttress further the claims in results presented in Sections 4.4 and 5.6.

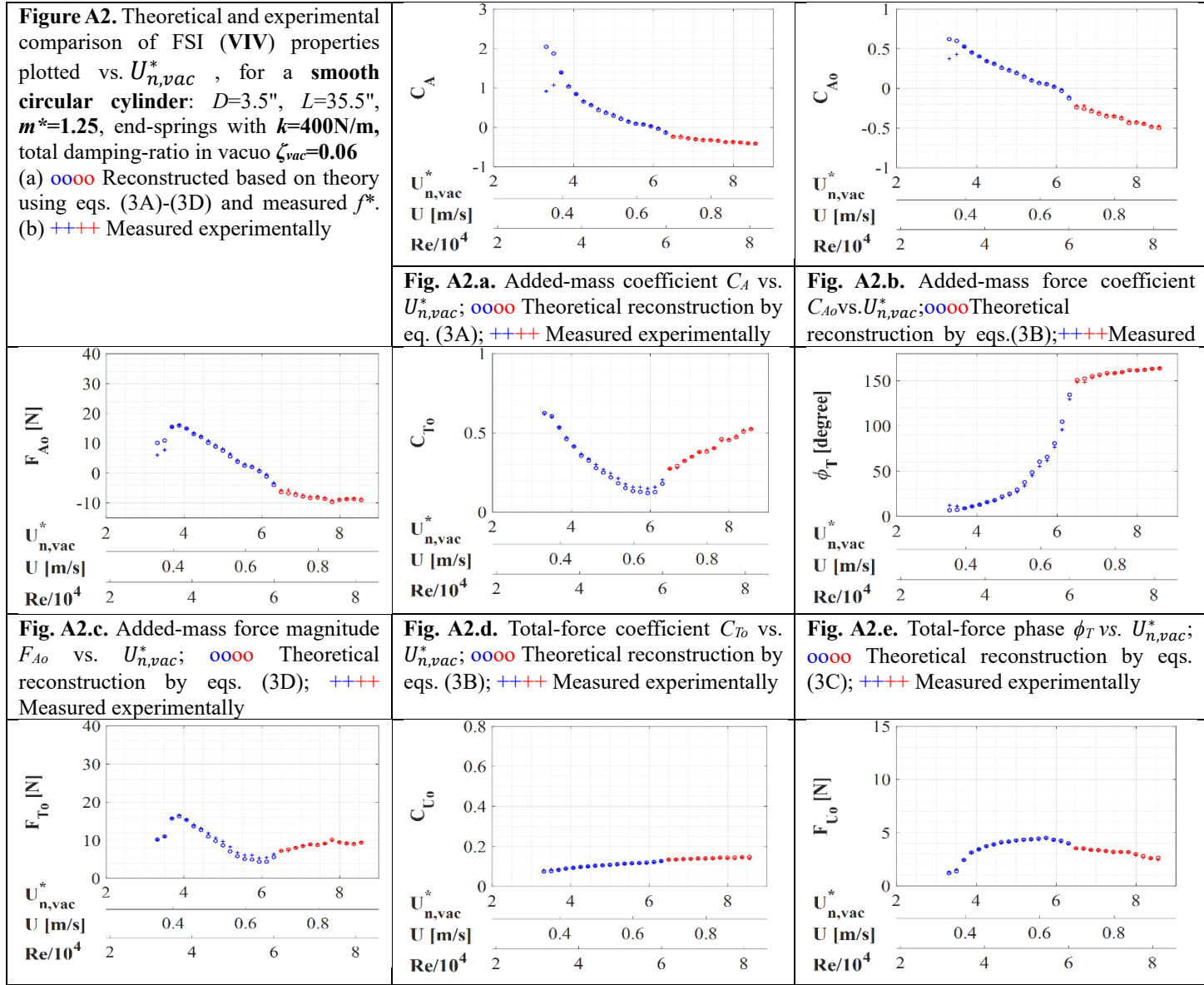
Results for stiffnesses ($k = 400\text{N/m}$ and 800N/m), and mass ratio ($m^* = 1.25$ and 1.84) are presented here in order to conserve space.

Complete sets of results are presented in the MRELab Report #13 and #14 [46,47] which has over 300 pages of figures.

Figure A1. Theoretical and experimental comparison of FSI (VIV) properties plotted vs. f^* , for a smooth circular cylinder: $D=3.5''$, $L=35.5''$, $m^*=1.25$, end-springs with $k=400\text{N/m}$, total damping-ratio in vacuo $\zeta_{\text{vac}}=0.06$
 (a) ---- Theory using eqs. (3A)-(3D). (b) $\circ\circ\circ$ Reconstructed based on theory and measured f^* . (c) $+++$ Measured experimentally







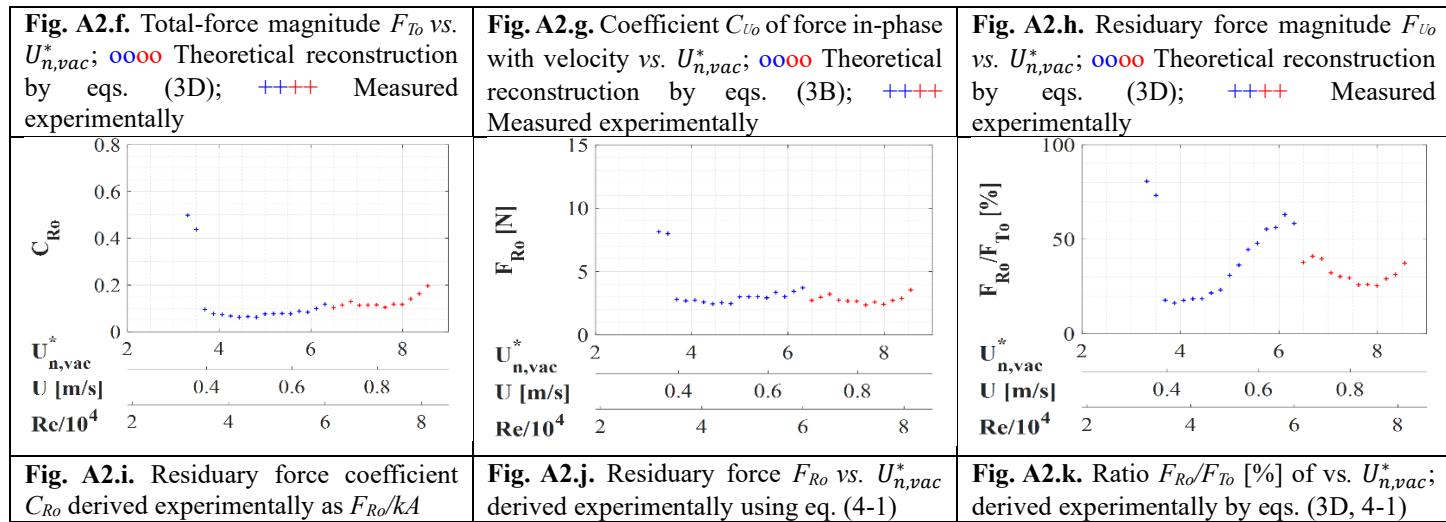
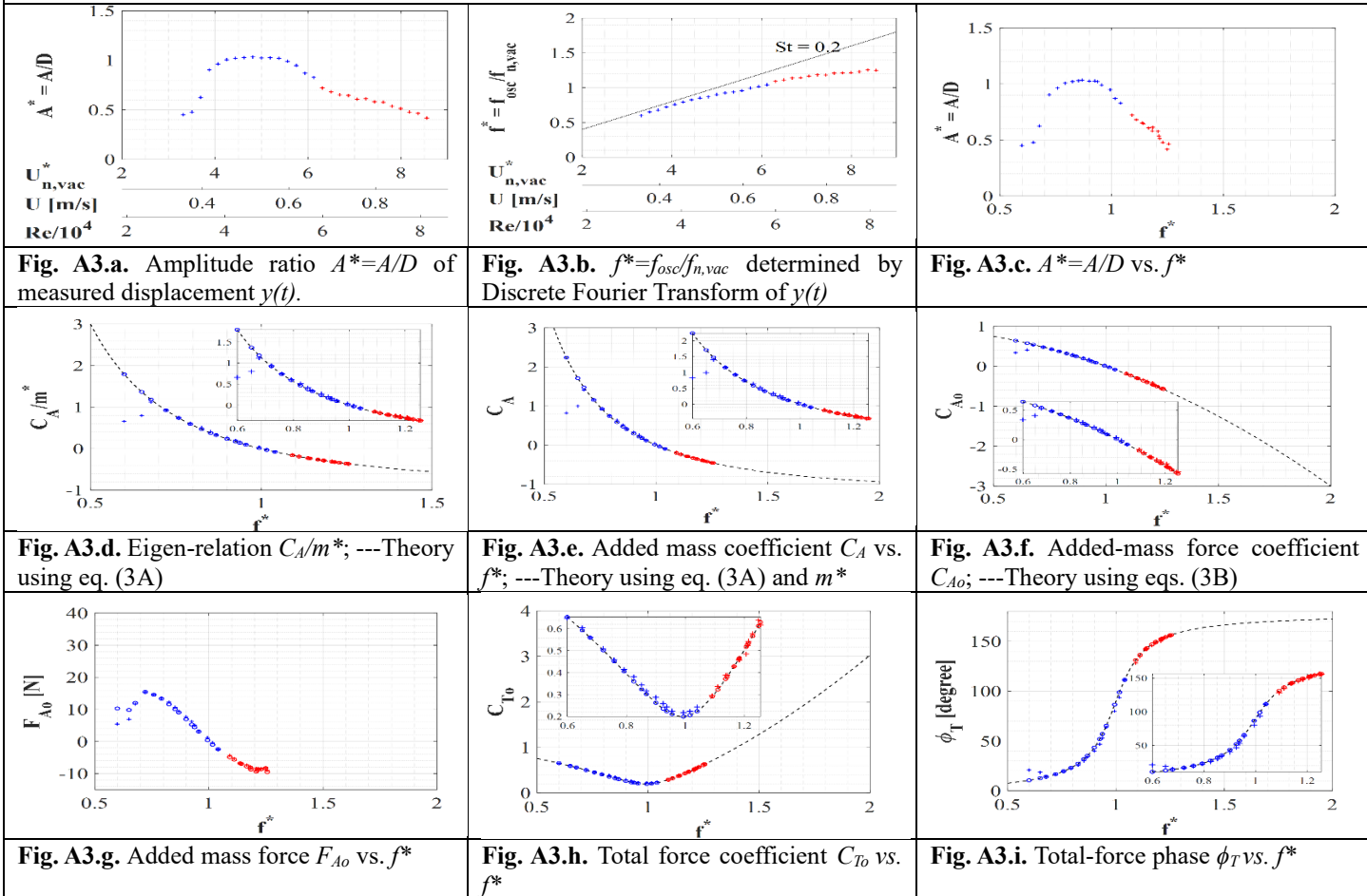
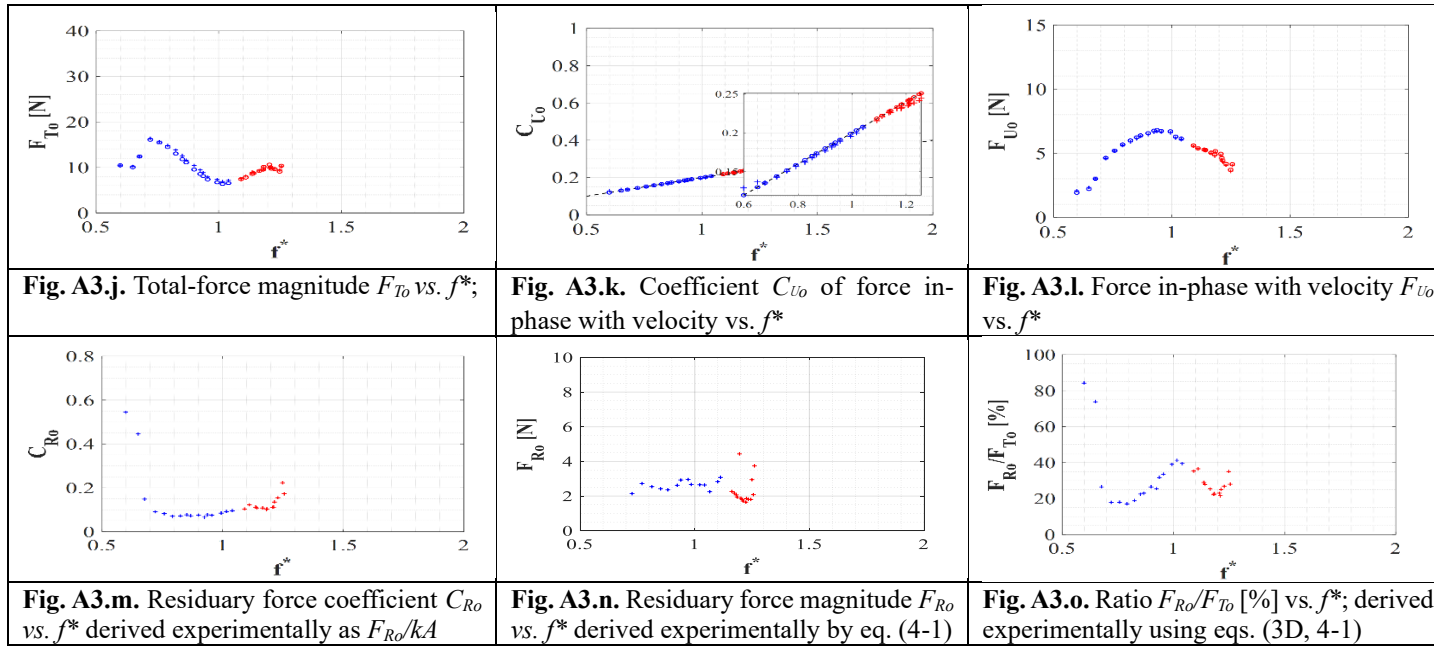
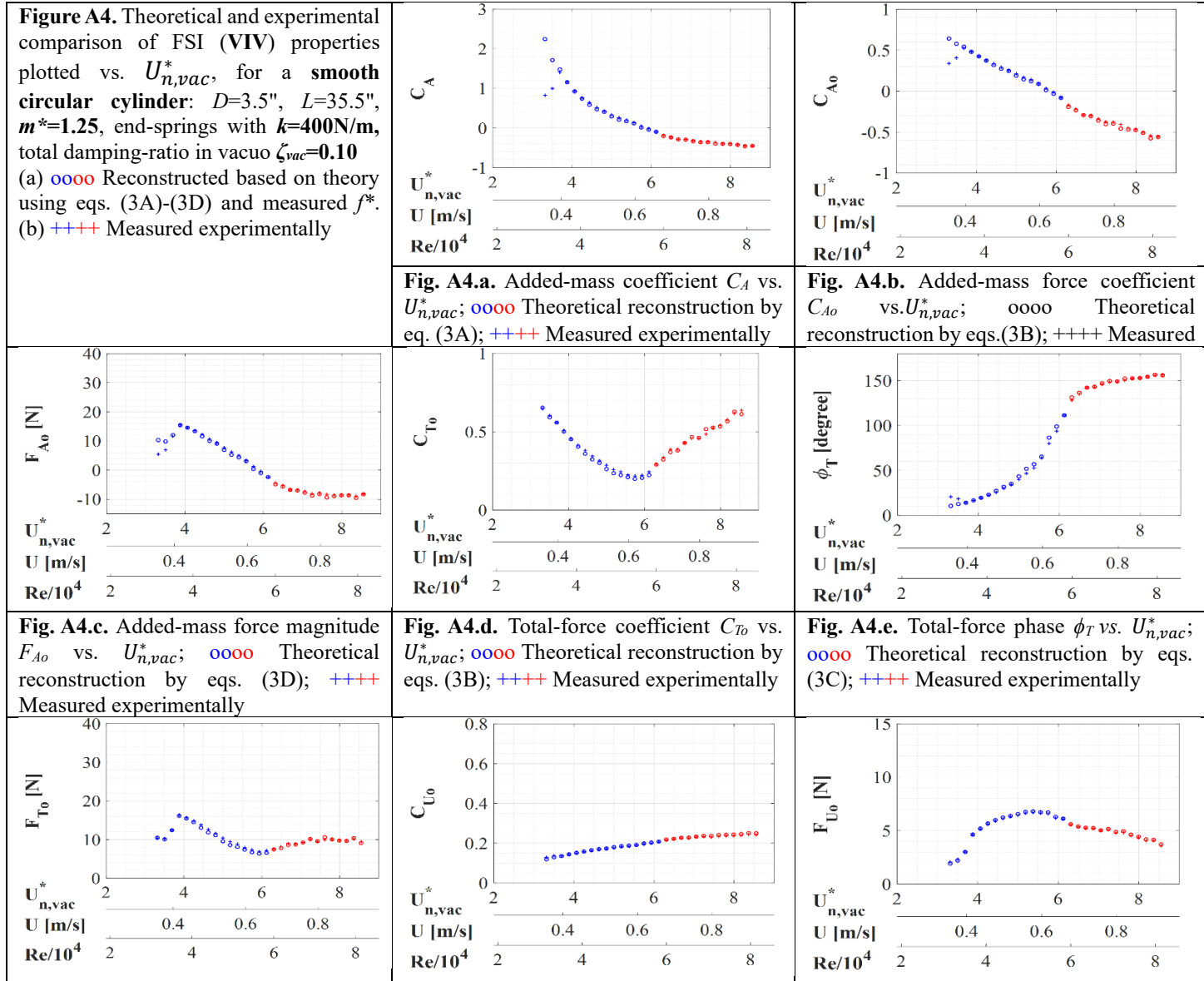


Figure A3. Theoretical and experimental comparison of FSI (VIV) properties plotted vs. f^* , for a smooth circular cylinder: $D=3.5''$, $L=35.5''$, $m^*=1.25$, end-springs with $k=400\text{N/m}$, total damping-ratio in vacuo $\zeta_{\text{vac}}=0.10$
 (a) ---- Theory using eqs. (3A)-(3D). (b) $\circ\circ\circ$ Reconstructed based on theory and measured f^* . (c) $+++$ Measured experimentally







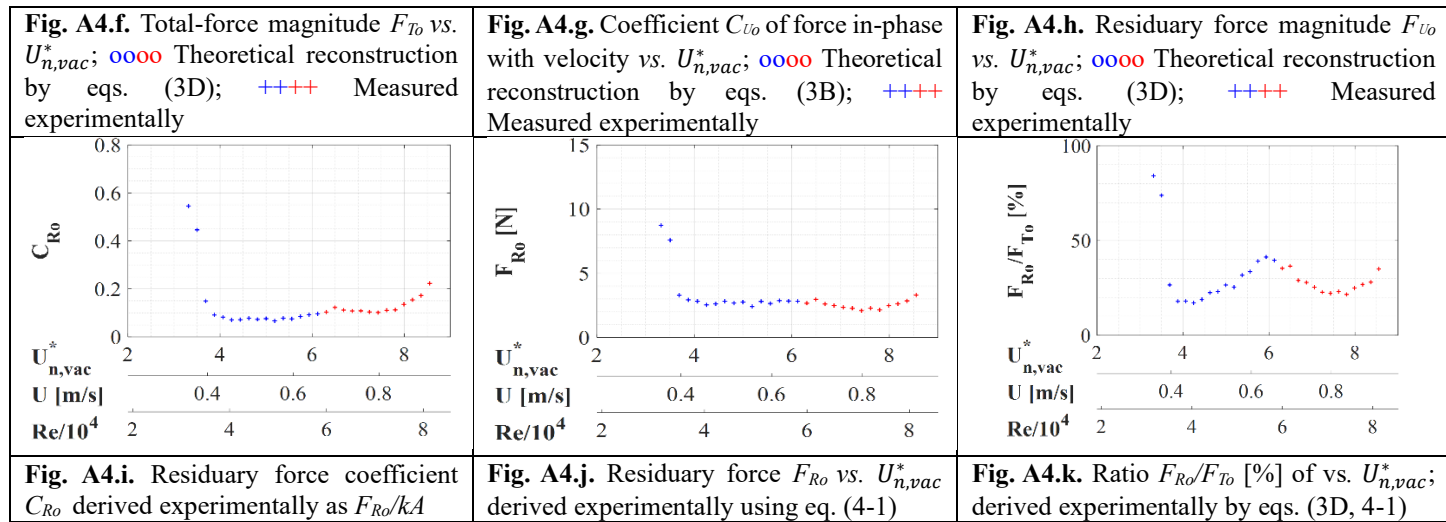


Figure A5. Theoretical and experimental comparison of FSI (VIV) properties plotted vs. f^* , for a smooth circular cylinder: $D=3.5''$, $L=35.5''$, $m^*=1.25$, end-springs with $k=800\text{N/m}$, total damping-ratio in vacuo $\zeta_{\text{vac}}=0.06$
 (a) ---- Theory using eqs. (3A)-(3D). (b) $\circ\circ\circ$ Reconstructed based on theory and measured f^* . (c) $+++$ Measured experimentally

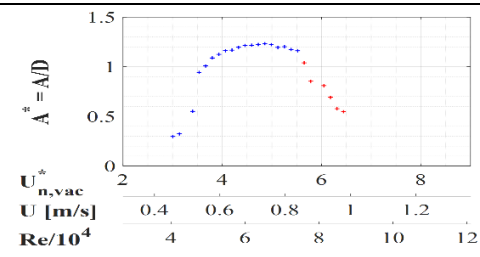


Fig. A5.a. Amplitude ratio $A^*=A/D$ of measured displacement $y(t)$.

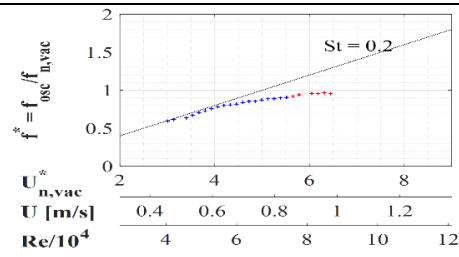


Fig. A5.b. $f^*=f_{\text{osc}}/f_{n,\text{vac}}$ determined by Discrete Fourier Transform of $y(t)$

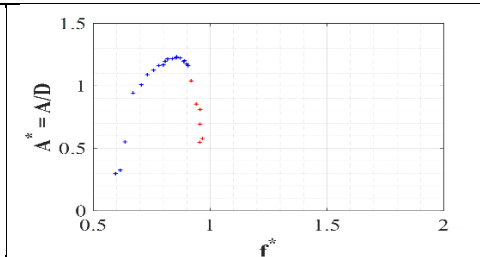


Fig. A5.c. $A^*=A/D$ vs. f^*

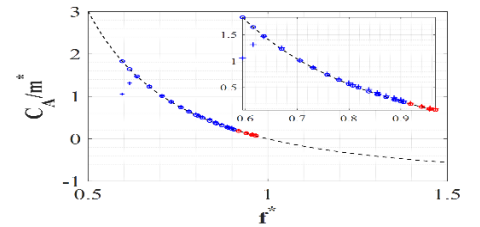


Fig. A5.d. Eigen-relation C_A/m^* ; ---Theory using eq. (A)

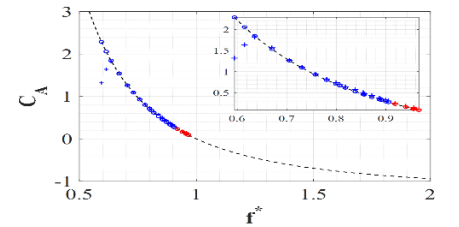


Fig. A5.e. Added mass coefficient C_A vs. f^* ; ---Theory using eq. (3A) and m^*

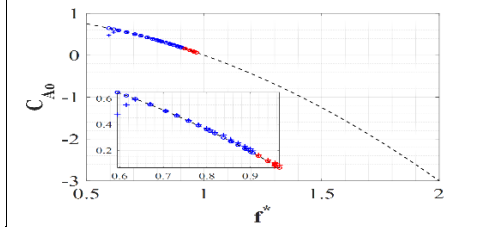


Fig. A5.f. Added-mass force coefficient C_{A0} ; ---Theory using eqs. (3B)

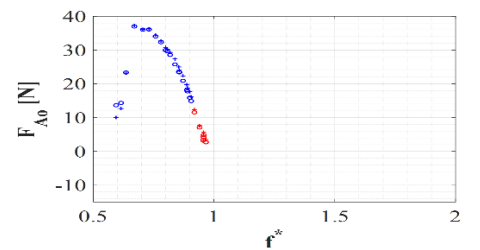


Fig. A5.g. Added mass force F_{A0} vs. f^*

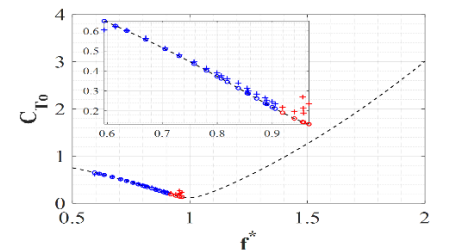


Fig. A5.h. Total force coefficient C_{T0} vs. f^*

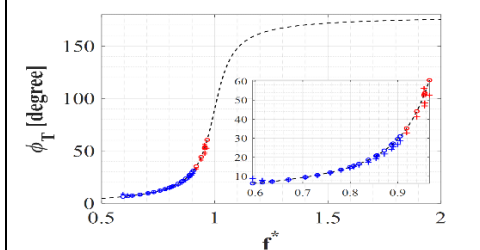
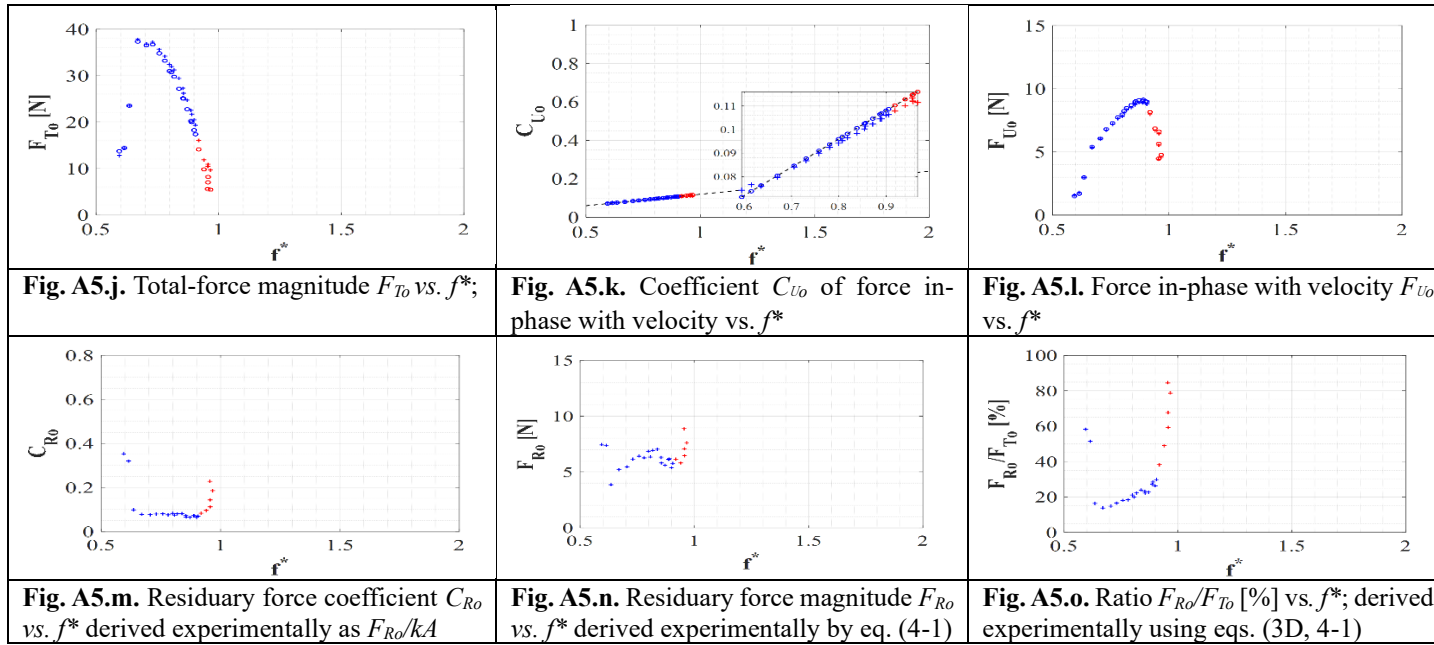
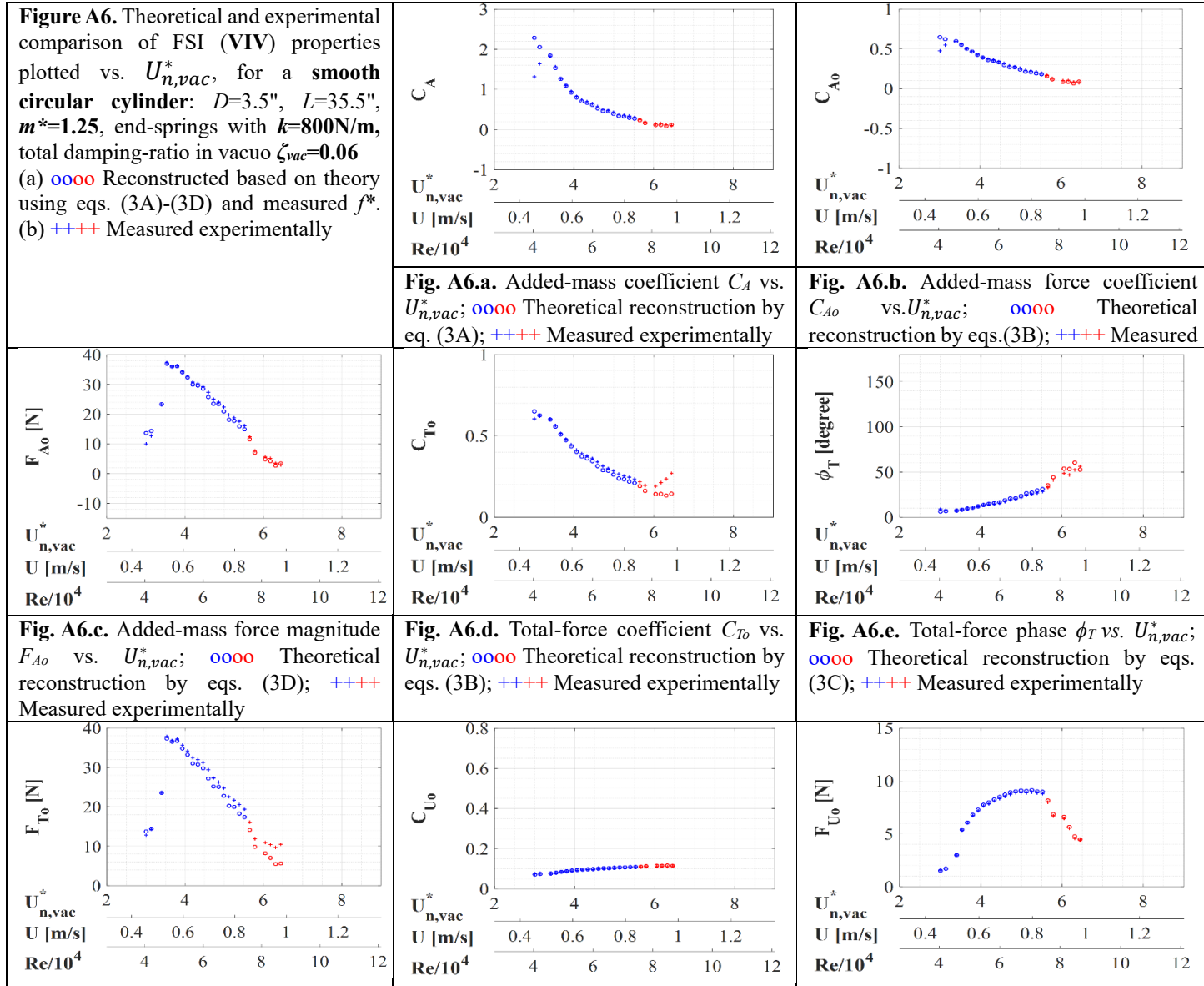


Fig. A5.i. Total-force phase ϕ_T vs. f^*





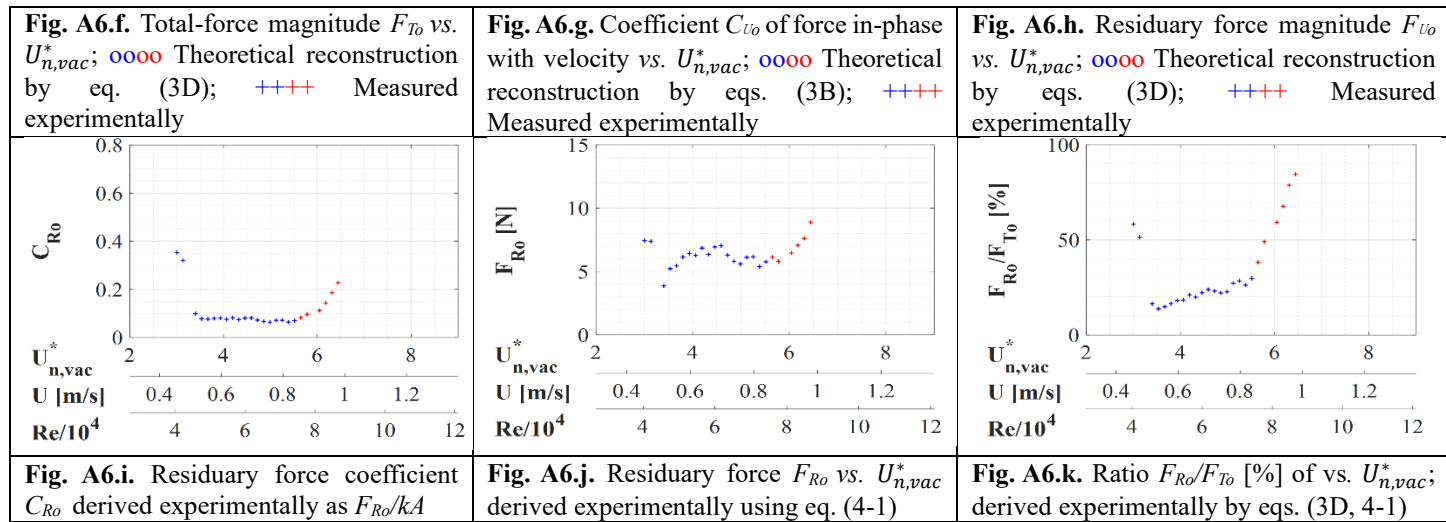
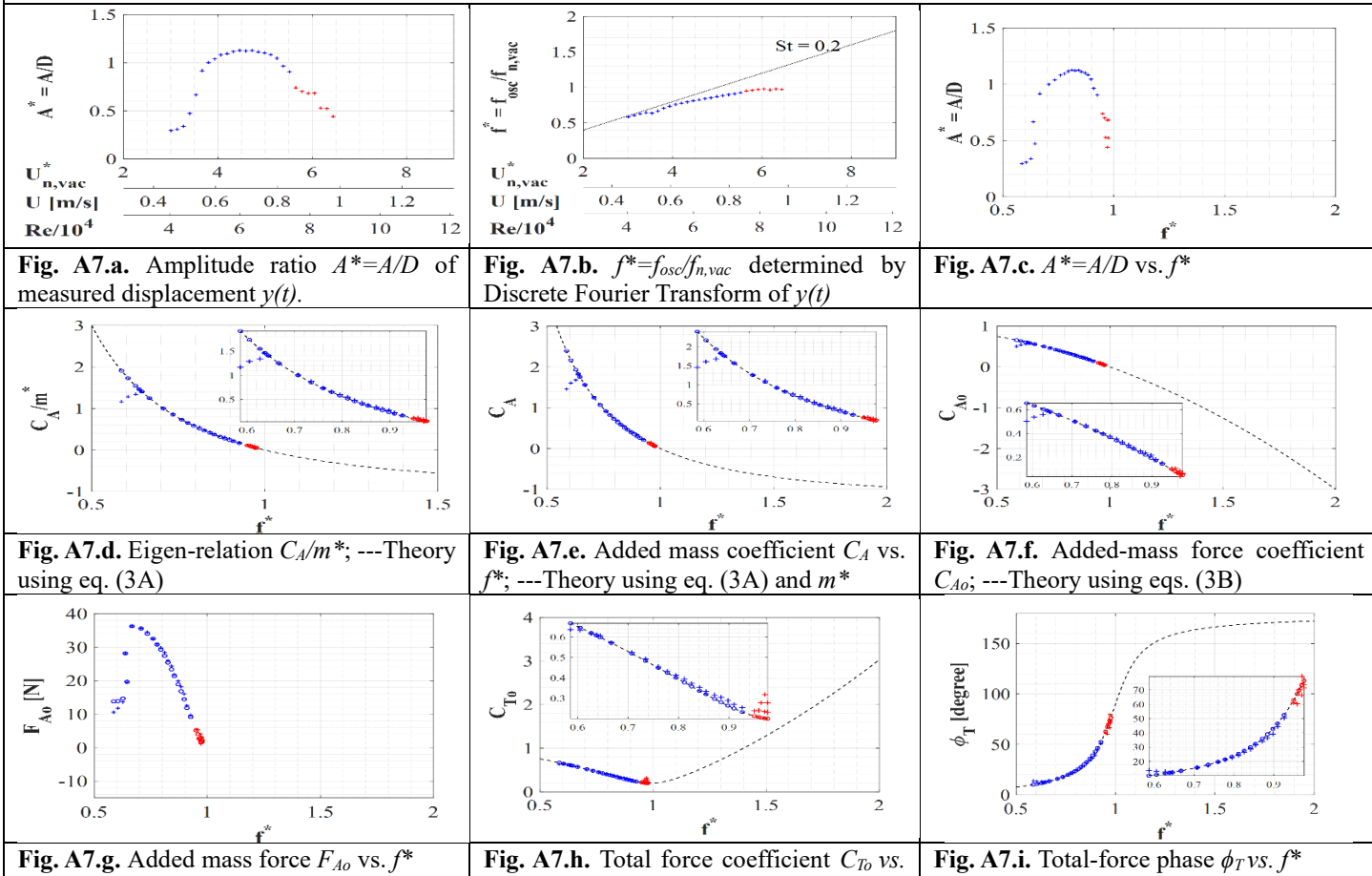
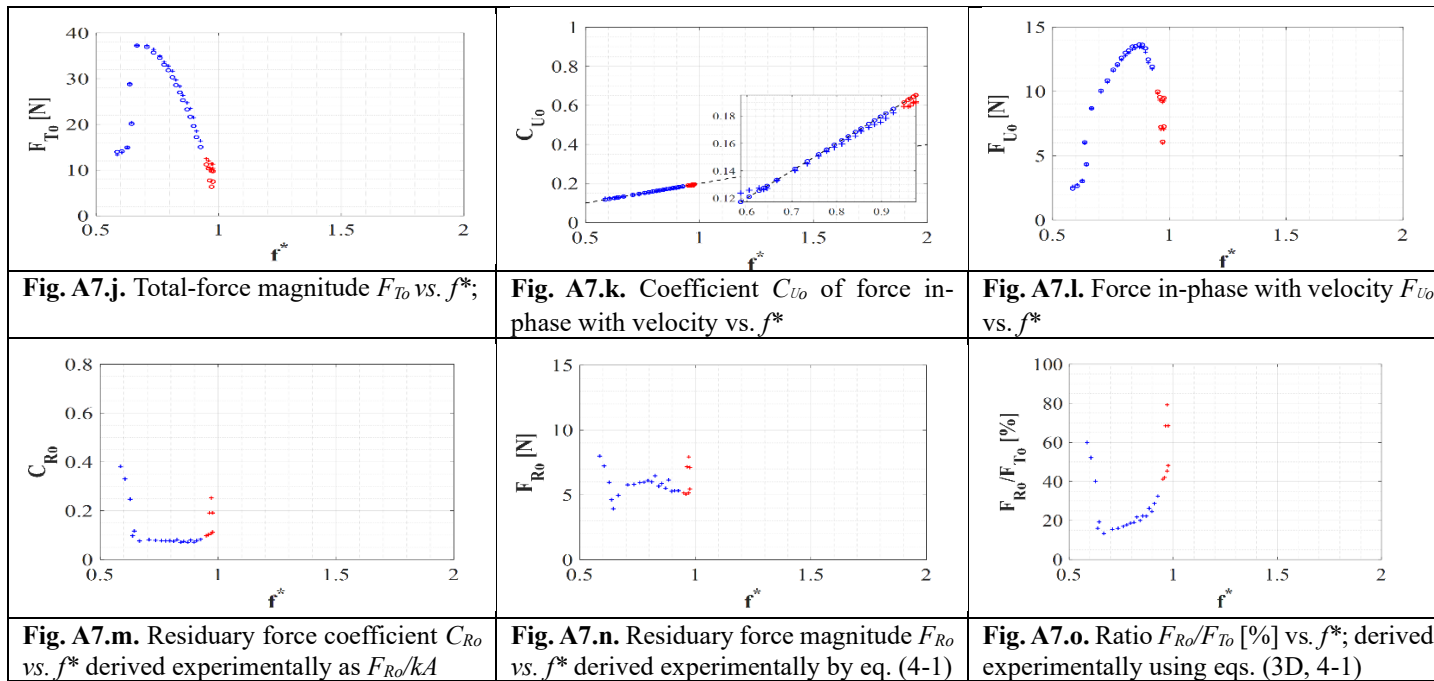
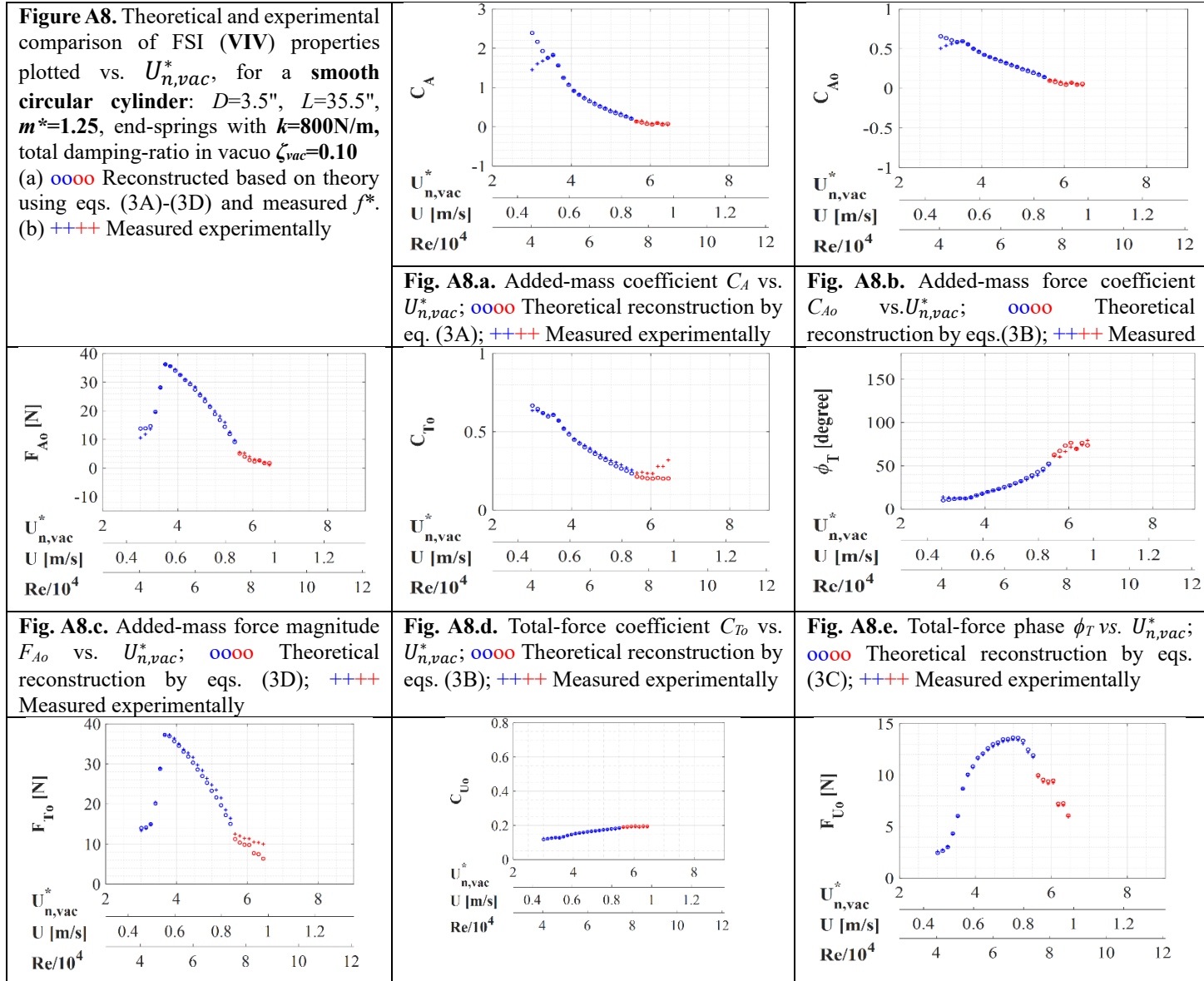


Figure A7. Theoretical and experimental comparison of FSI (VIV) properties plotted vs. f^* , for a smooth circular cylinder: $D=3.5''$, $L=35.5''$, $m^*=1.25$, end-springs with $k=800\text{N/m}$, total damping-ratio in vacuo $\zeta_{\text{vac}}=0.10$
 (a) ---- Theory using eqs. (3A)-(3D). (b) $\circ\circ\circ$ Reconstructed based on theory and measured f^* . (c) $+++$ Measured experimentally







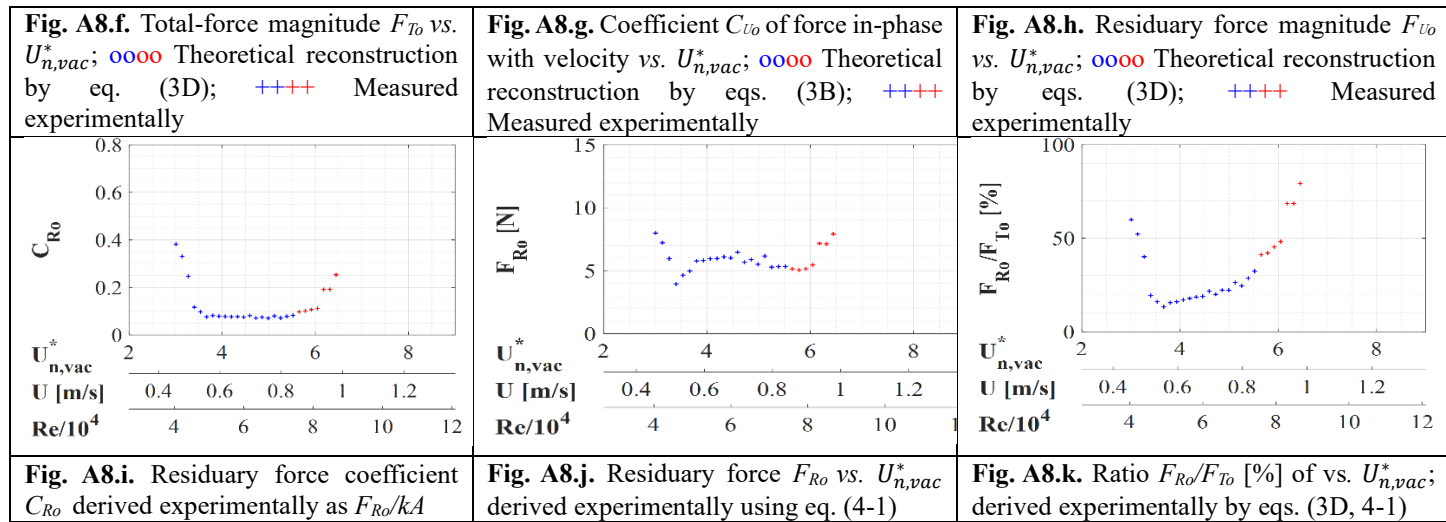
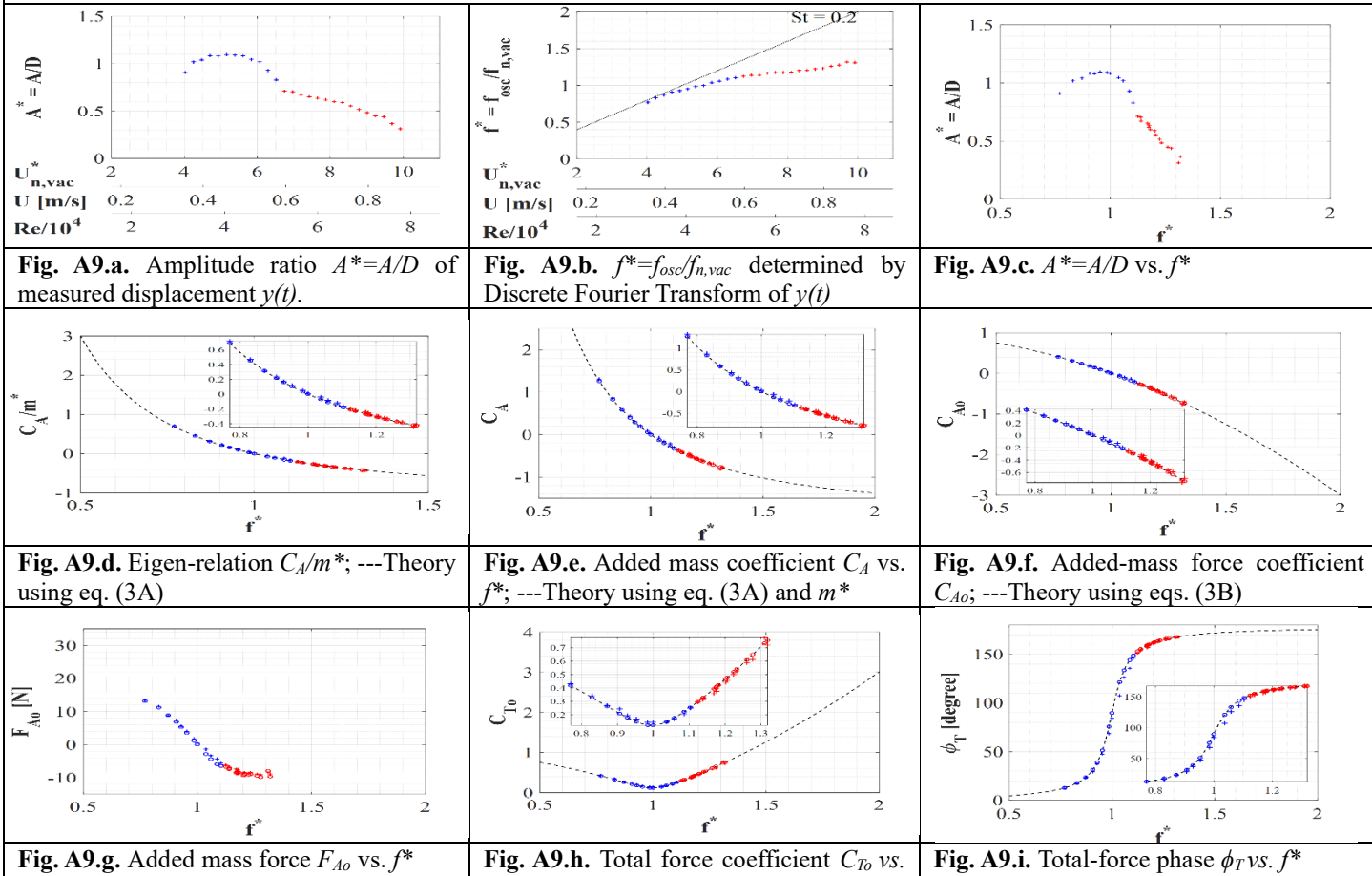
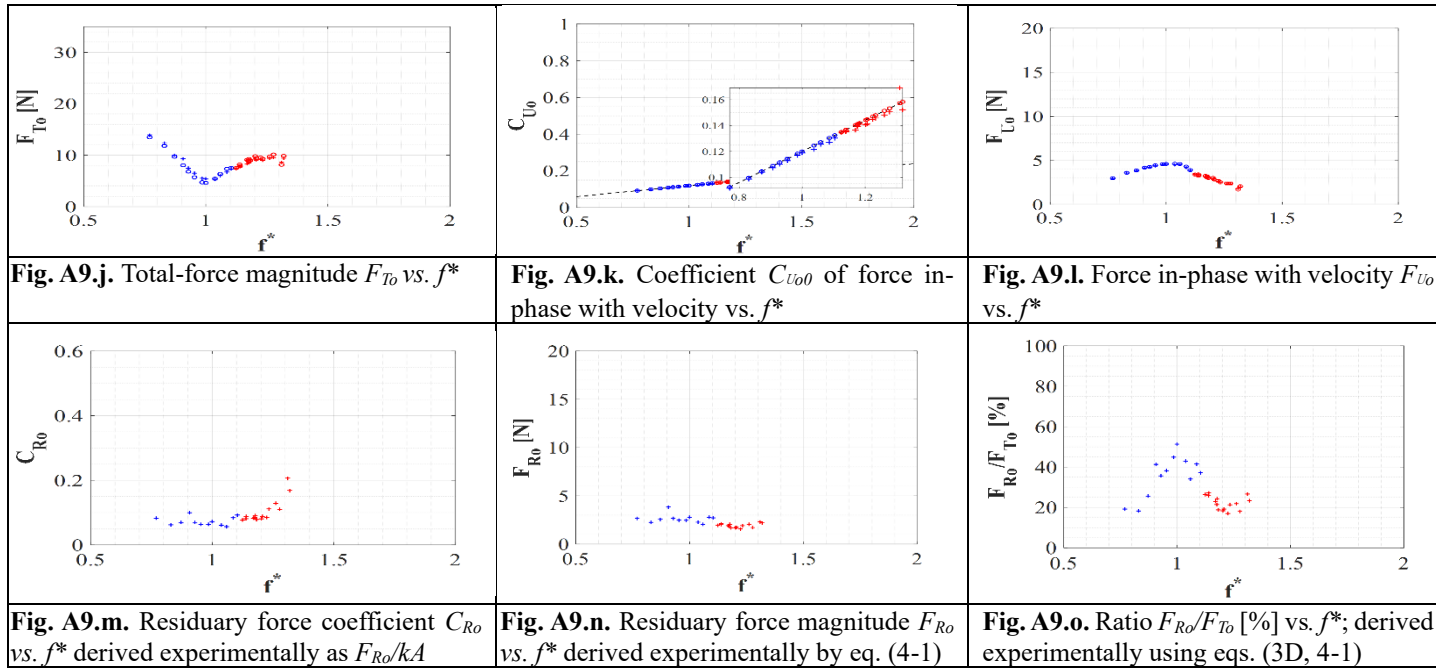
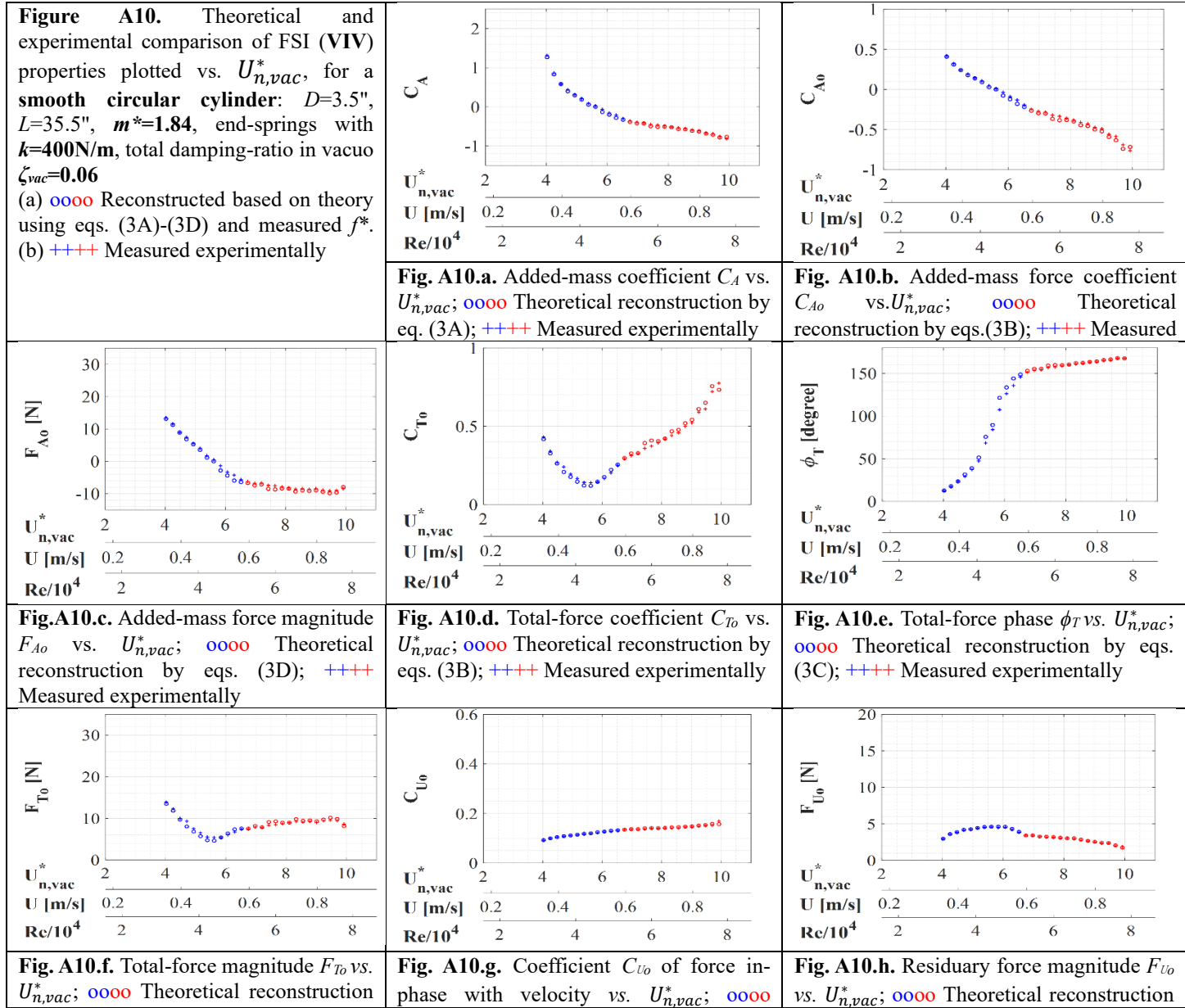


Figure A9. Theoretical and experimental comparison of FSI (VIV) properties plotted vs. f^* , for a smooth circular cylinder: $D=3.5''$, $L=35.5''$, $m^*=1.84$, end-springs with $k=400\text{N/m}$, total damping-ratio in vacuo $\zeta_{\text{vac}}=0.06$
 (a) ---- Theory using eqs. (3A)-(3D). (b) $\circ\circ\circ$ Reconstructed based on theory and measured f^* . (c) $+++$ Measured experimentally







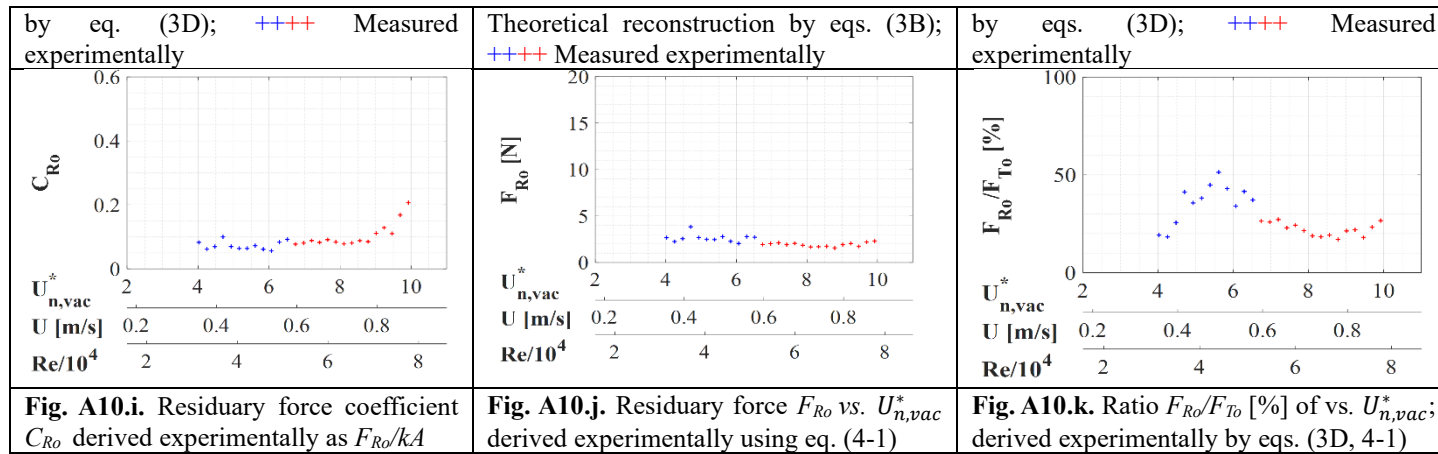
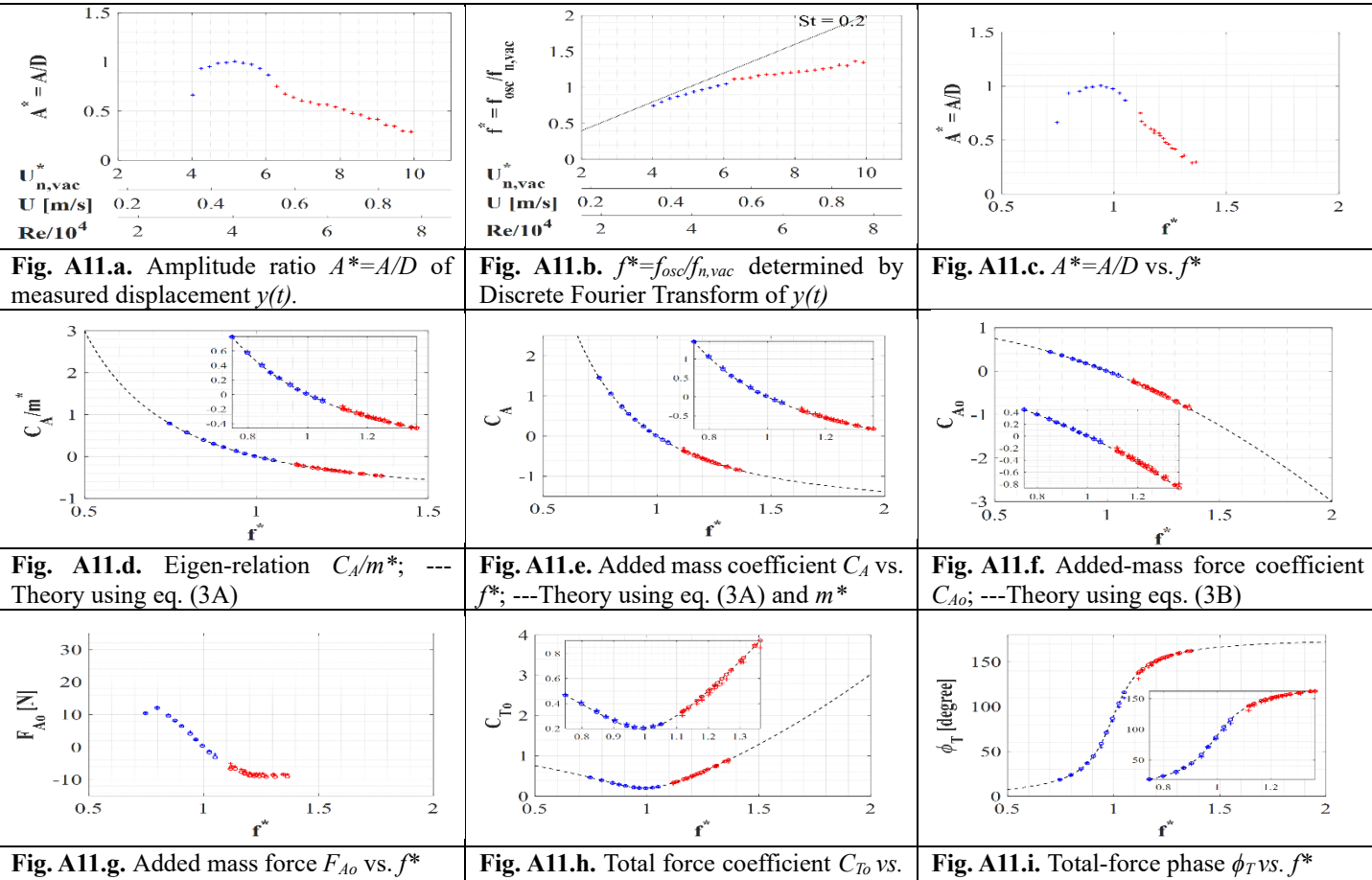
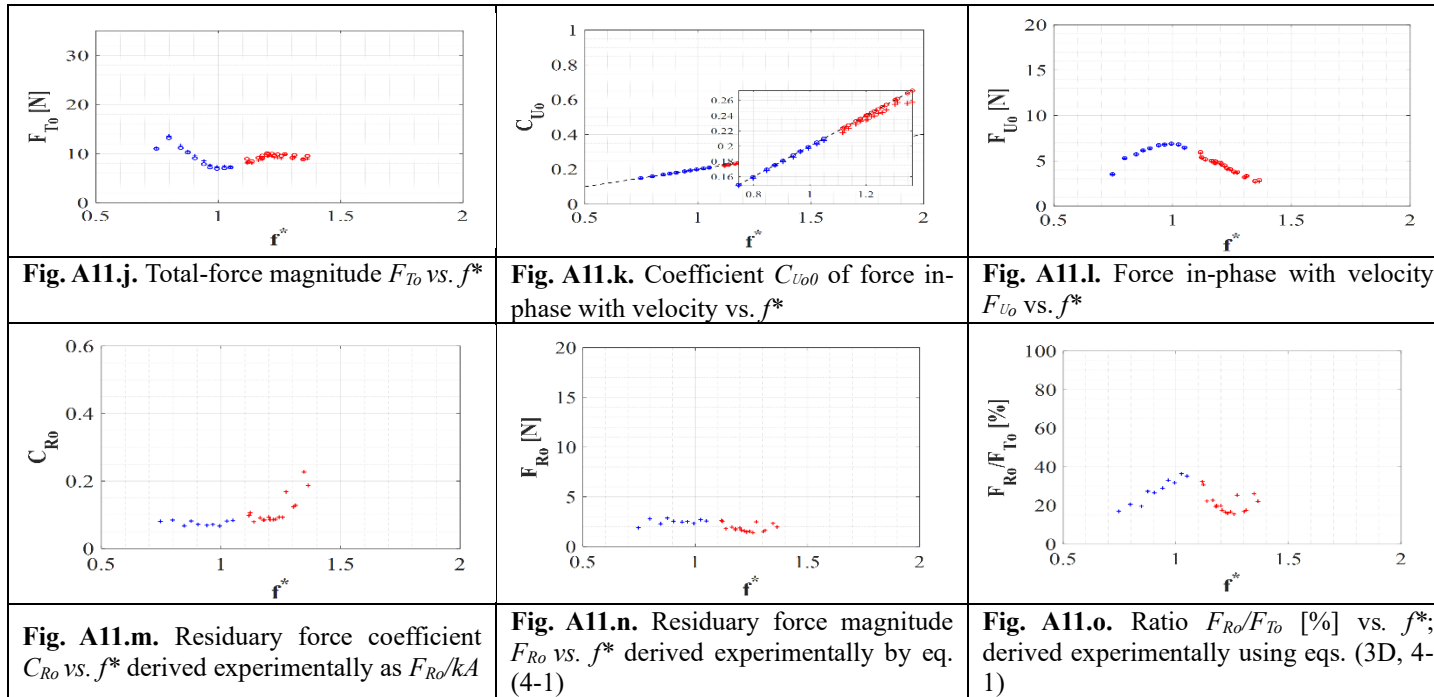
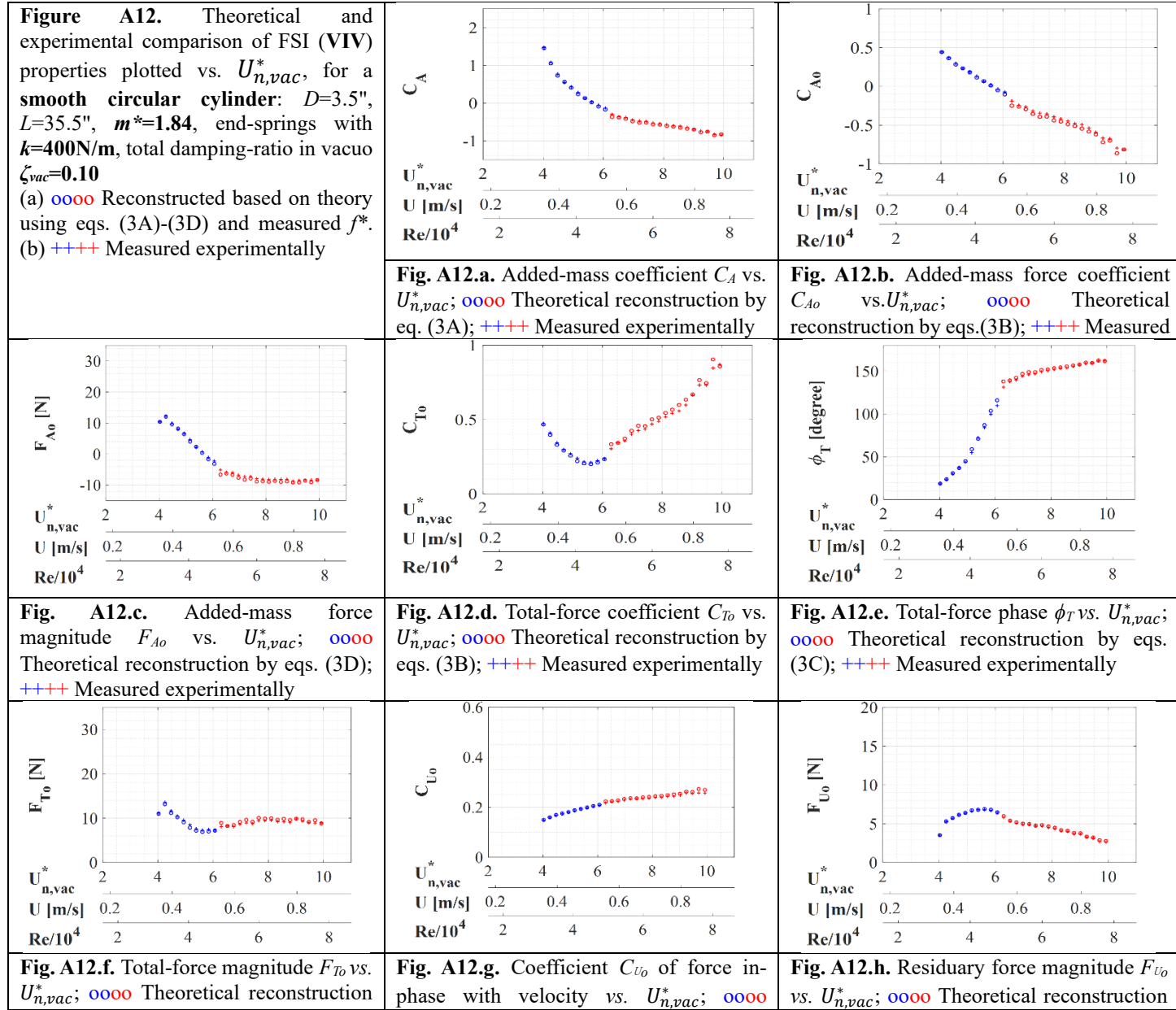


Figure A11. Theoretical and experimental comparison of FSI (VIV) properties plotted vs. f^* , for a smooth circular cylinder: $D=3.5"$, $L=35.5"$, $m^*=1.84$, end-springs with $k=400\text{N/m}$, total damping-ratio in vacuo $\zeta_{\text{vac}}=0.10$
 (a) ---- Theory using eqs. (3A)-(3D). (b) $\circ\circ\circ$ Reconstructed based on theory and measured f^* . (c) $+++$ Measured experimentally

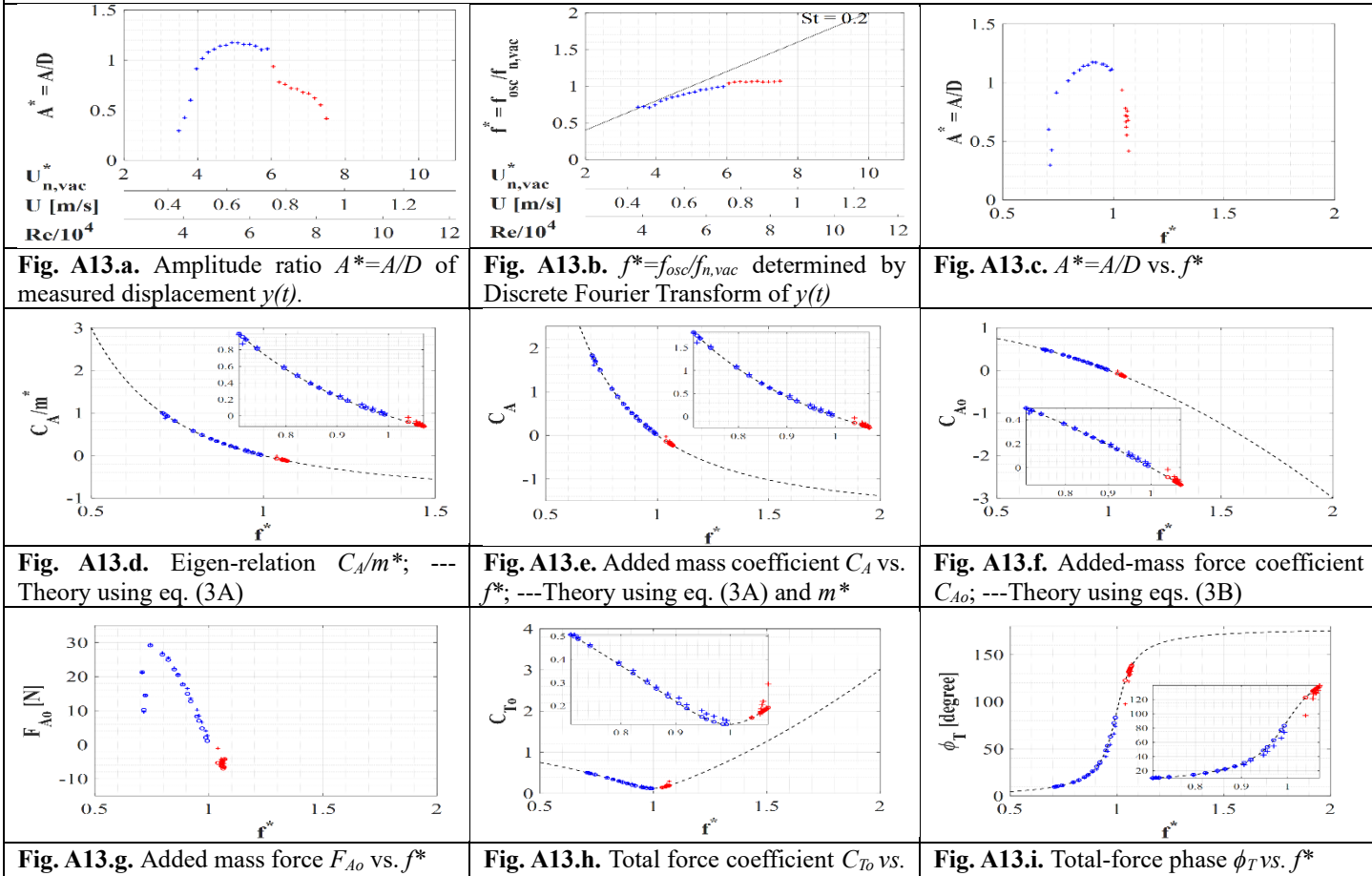


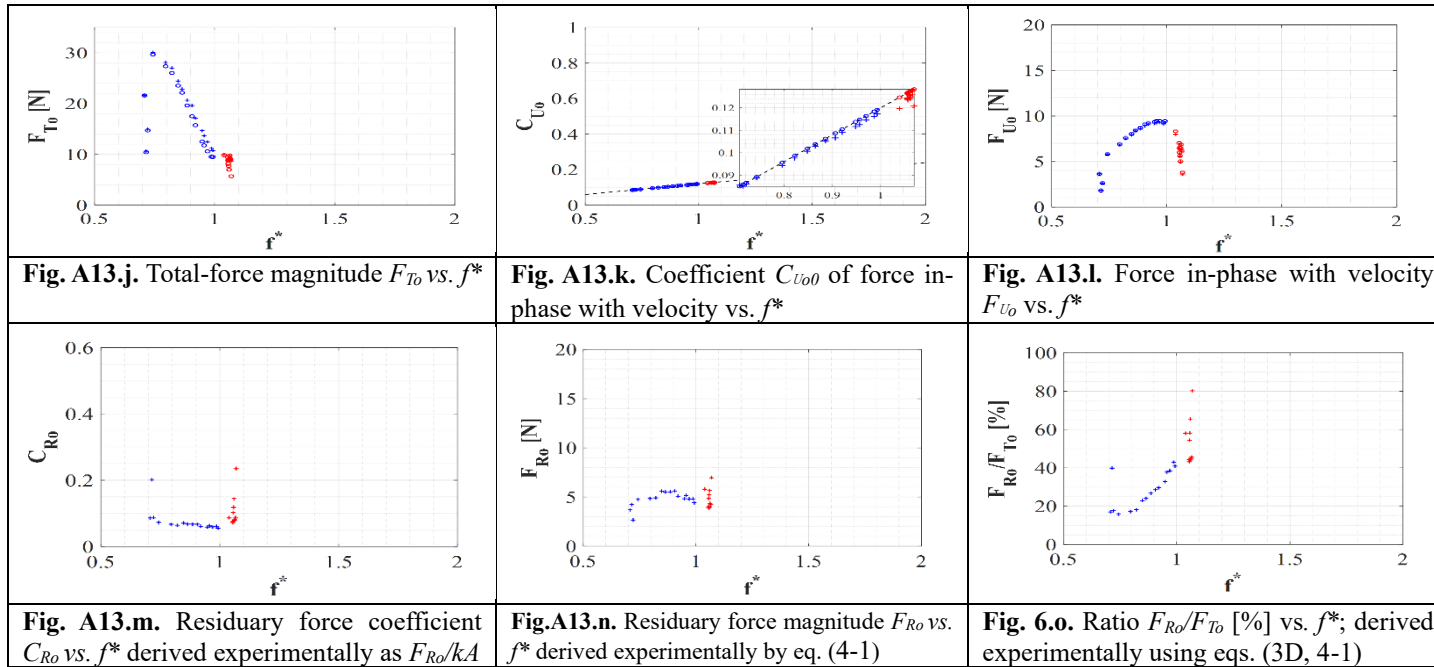


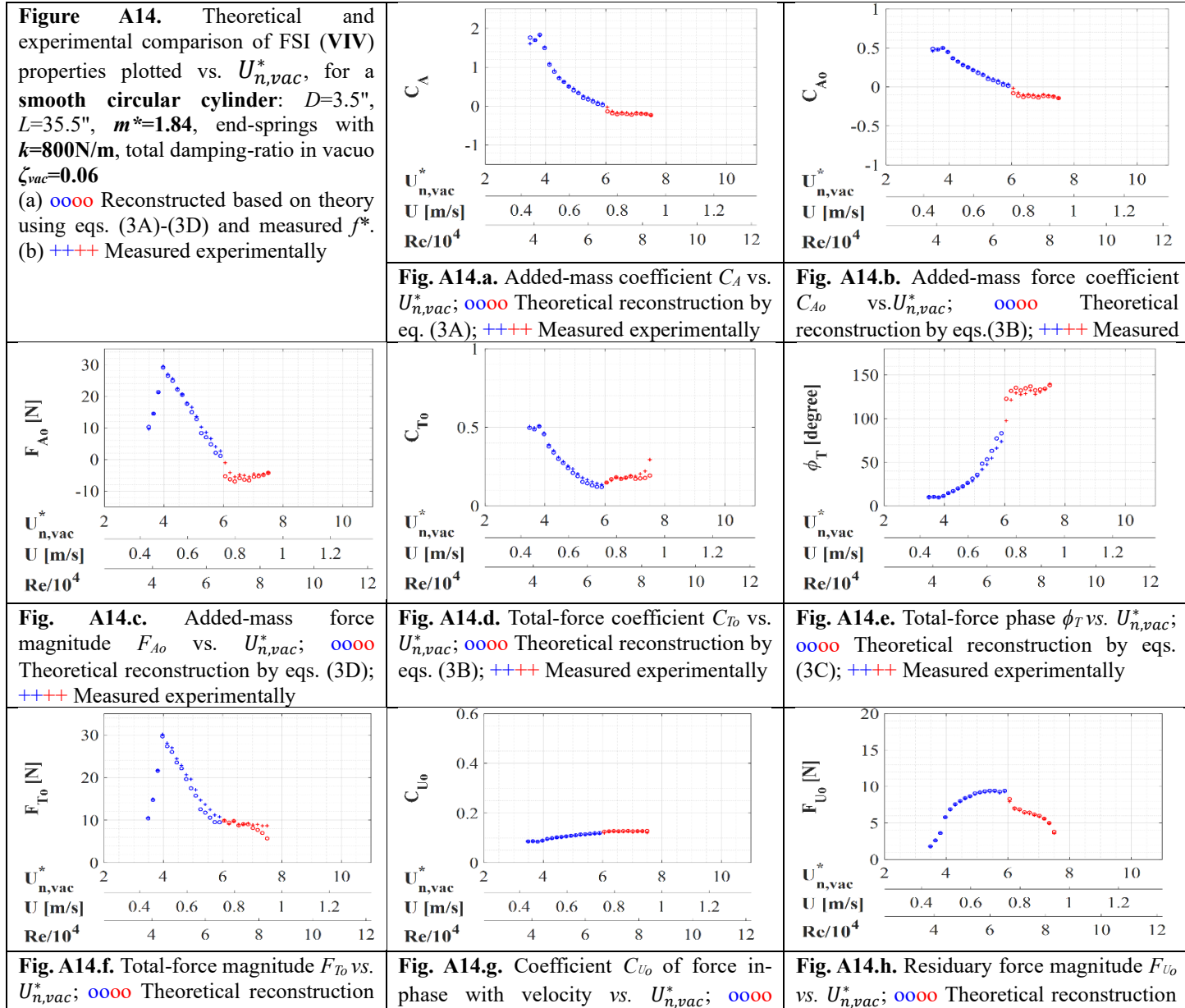


by eq. (3D); +++ Measured experimentally	Theoretical reconstruction by eqs. (3B); +++ Measured experimentally	by eqs. (3D); +++ Measured experimentally
Fig. A12.i. Residuary force coefficient C_{Ro} derived experimentally as F_{Ro}/kA	Fig. A12.j. Residuary force F_{Ro} vs. $U_{n,vac}^*$ derived experimentally using eq. (4-1)	Fig. A12.k. Ratio F_{Ro}/F_{To} [%] of vs. $U_{n,vac}^*$; derived experimentally by eqs. (3D, 4-1)

Figure A13. Theoretical and experimental comparison of FSI (VIV) properties plotted vs. f^* , for a smooth circular cylinder: $D=3.5''$, $L=35.5''$, $m^*=1.84$, end-springs with $k=800\text{N/m}$, total damping-ratio in vacuo $\zeta_{\text{vac}}=0.06$
 (a) ---- Theory using eqs. (3A)-(3D). (b) $\circ\circ\circ$ Reconstructed based on theory and measured f^* . (c) $+++$ Measured experimentally







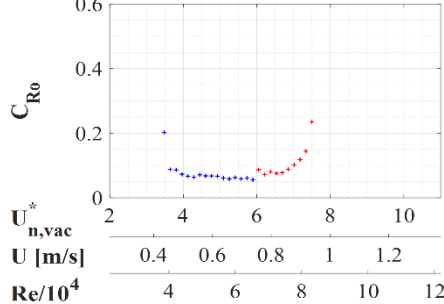
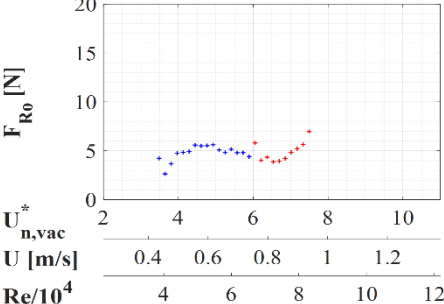
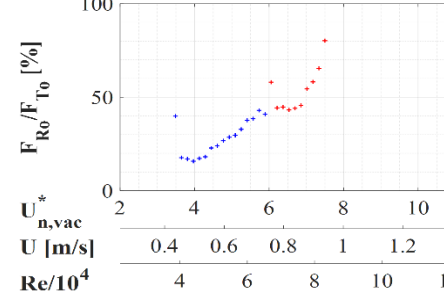
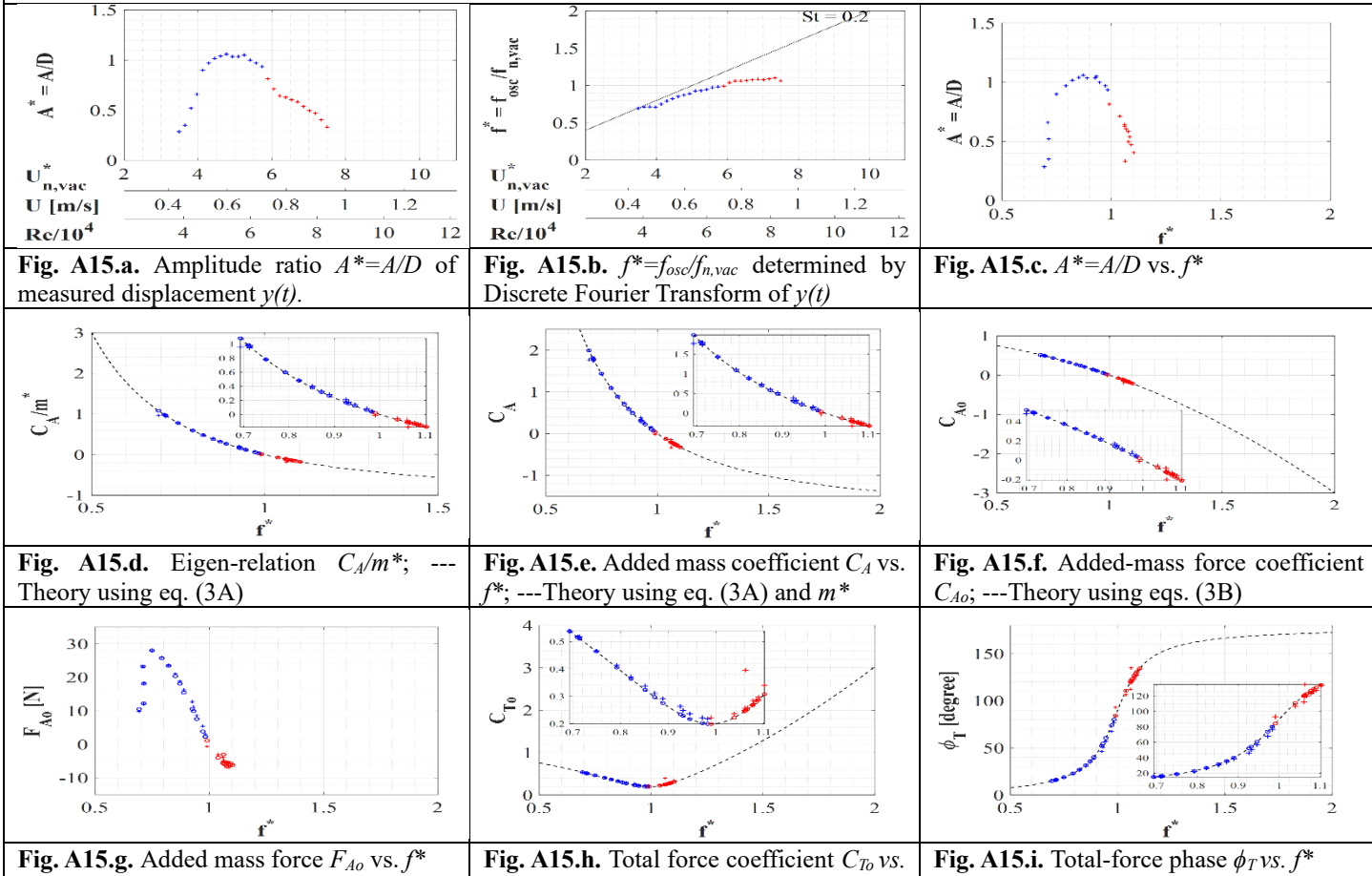
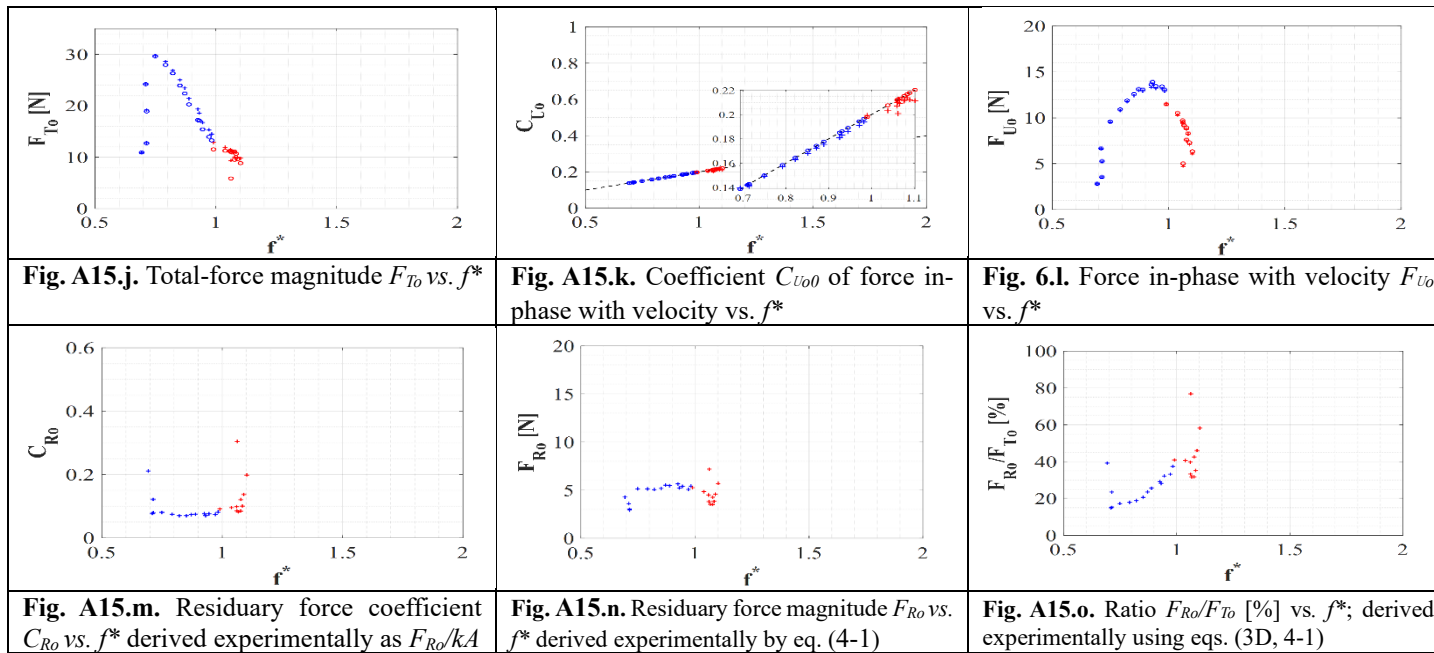
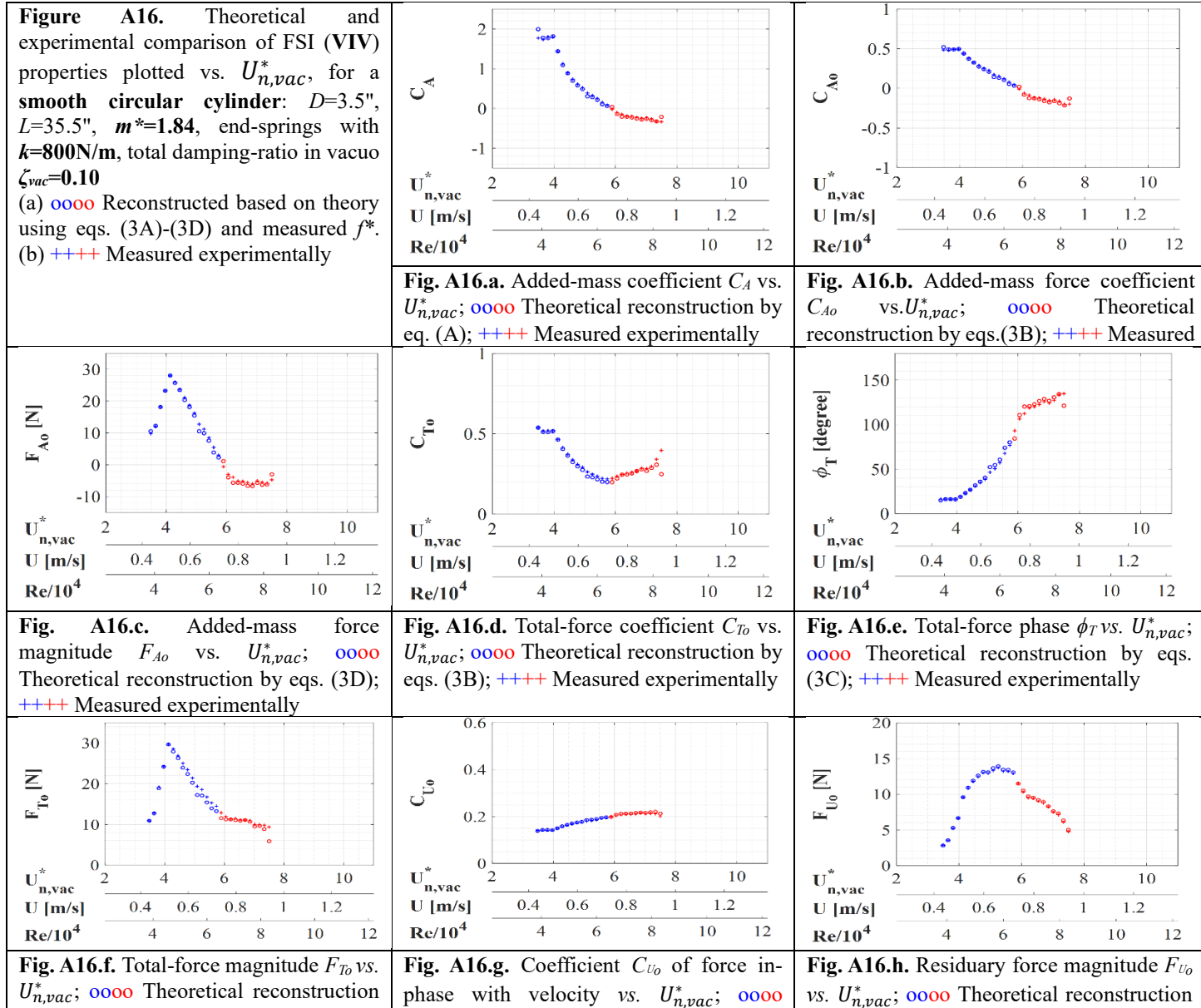
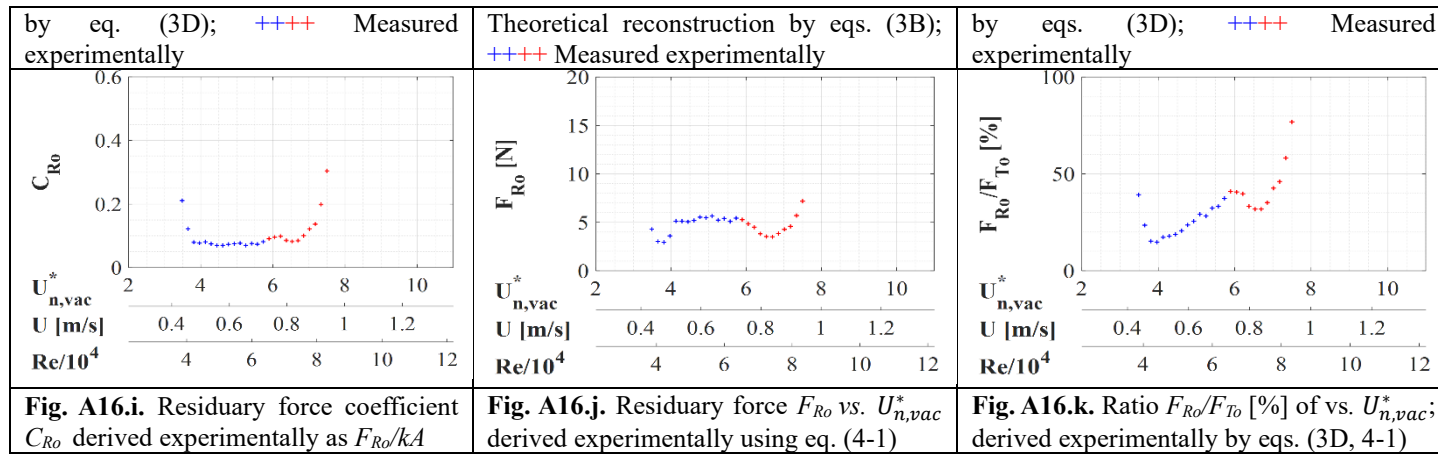
by eq. (3D); +++ Measured experimentally	Theoretical reconstruction by eqs. (3B); +++ Measured experimentally	by eqs. (3D); +++ Measured experimentally
 <p>C_{Ro}</p> <p>$U_{n,vac}^*$</p> <p>U [m/s]</p> <p>$Re/10^4$</p>	 <p>F_{Ro} [N]</p> <p>$U_{n,vac}^*$</p> <p>U [m/s]</p> <p>$Re/10^4$</p>	 <p>F_{Ro}/F_{To} [%]</p> <p>$U_{n,vac}^*$</p> <p>U [m/s]</p> <p>$Re/10^4$</p>
<p>Fig. A14.i. Residuary force coefficient C_{Ro} derived experimentally as F_{Ro}/kA</p>	<p>Fig. A14.j. Residuary force F_{Ro} vs. $U_{n,vac}^*$ derived experimentally using eq. (4-1)</p>	<p>Fig. A14.k. Ratio F_{Ro}/F_{To} [%] of vs. $U_{n,vac}^*$; derived experimentally by eqs. (3D, 4-1)</p>

Figure A15. Theoretical and experimental comparison of FSI (VIV) properties plotted vs. f^* , for a smooth circular cylinder: $D=3.5''$, $L=35.5''$, $m^*=1.84$, end-springs with $k=800\text{N/m}$, total damping-ratio in vacuo $\zeta_{\text{vac}}=0.10$
 (a) ---- Theory using eqs. (3A)-(3D). (b) $\circ\circ\circ$ Reconstructed based on theory and measured f^* . (c) $+++$ Measured experimentally









Appendix B

Post Processing Results for VIV and Galloping of Cylinder with Turbulence Stimulation

The figures in the next 32 pages show some of the results for data post processing for a cylinder with turbulence stimulation called passive stimulation control (PTC). Mass ratio ranging from 1.007 to 1.89. These results show how consistent the eigen-relation theory is with the experimental data just as it was shown in Sections 4.4 and 5.6.

For clarity and proper understanding of this appendix, the results are arranged in increasing stiffness, damping ratio, and mass ratio.

The arrangement is as follows:

$m^* = 1.007$ - pages 2-9 in this Appendix B

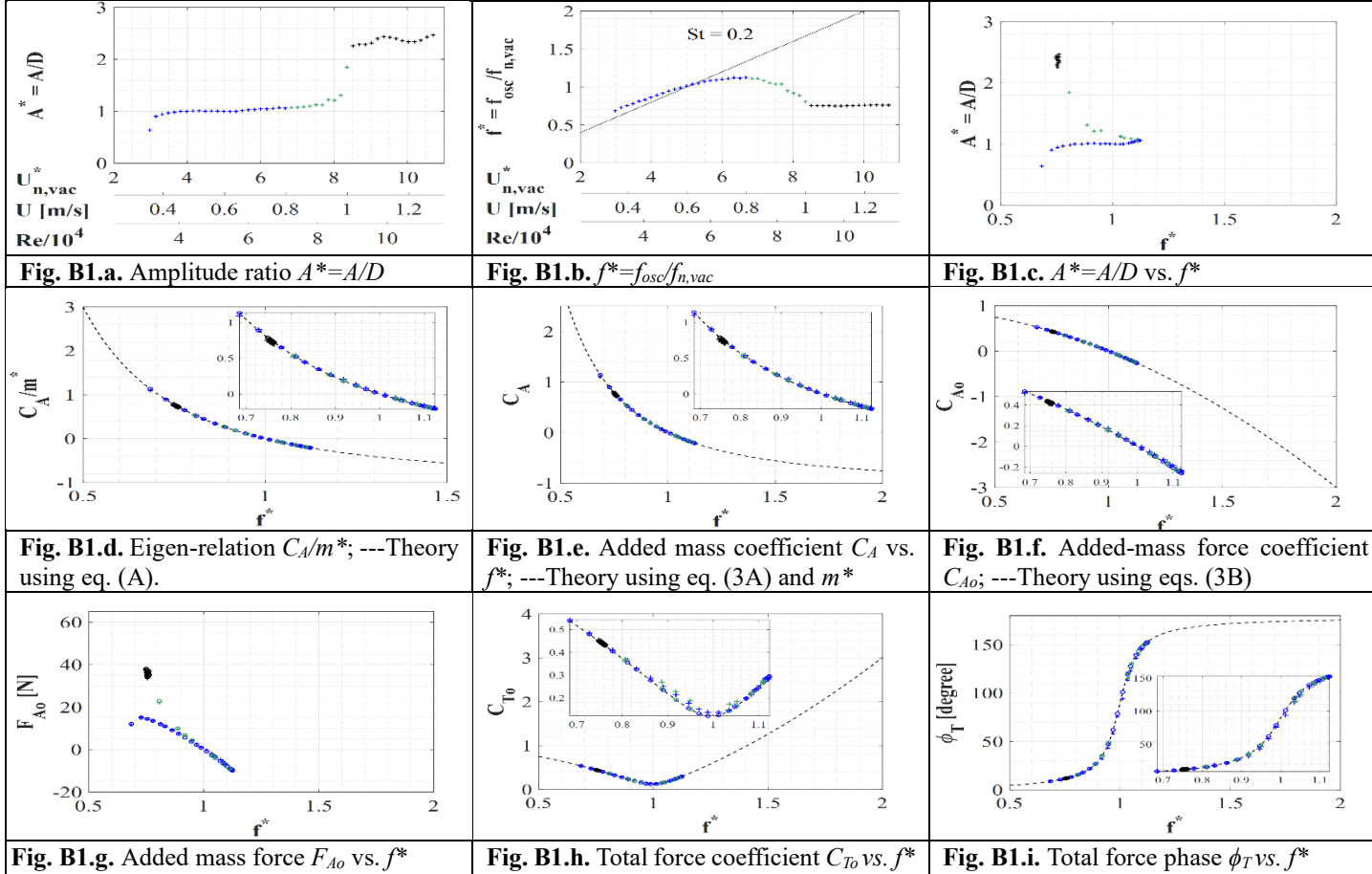
$m^* = 1.34$ - pages 10-17 in this Appendix B

$m^* = 1.685$ - pages 18-25 in this Appendix B

$m^* = 1.89$ - pages 26-33 in this Appendix B

Results in this appendix buttress further the claims in results presented in Sections 4.3 and 5.6. As in the first appendix, results for two stiffness values ($k = 400\text{N/m}$ and 800N/m) are presented here in order to conserve space. All other results are presented in the MRELab Report #13 and #14 [46,47] which has over 300 pages of figures including results for higher damping ratios up to 0.26.

Figure B1. Circular cylinder with turbulence stimulation, $m^*=1.007$, $k=400\text{N/m}$, $\zeta_{vac}=0.06$; $D=8.89\text{cm}$ (3.5"), $L=90.17\text{cm}$ (35.5") Theoretical and experimental comparison of FSI (VIV) properties plotted vs. f^*
 (a) ---- Theory using eqs. (3A)-(3D). (b) ooooo Reconstructed based on theory and measured f^* . (c) ++++ Measured experimentally



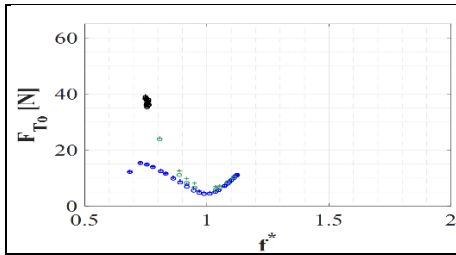


Fig. B1.j. Total force magnitude F_{T0} vs. f^*

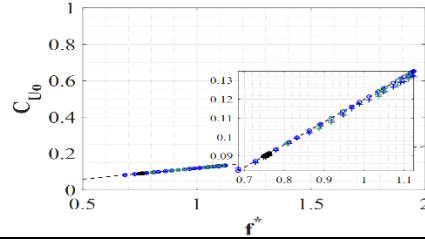


Fig. B1.k. Coefficient C_{U0} of force in-phase with velocity vs. f^*

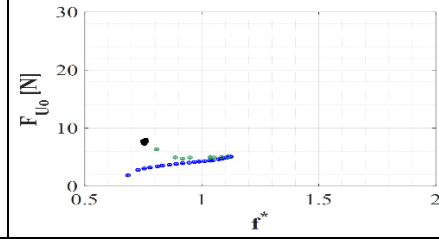


Fig. B1.l. Force in-phase with velocity F_{U0} vs. f^*

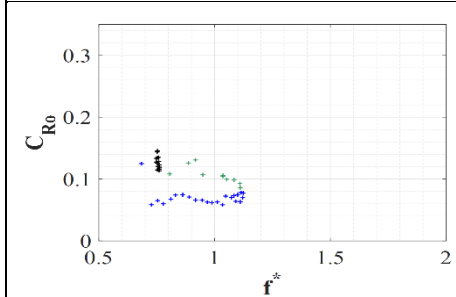


Fig. B1.m. Residuary force coefficient C_{R0} vs. f^* derived experimentally as F_{R0}/kA

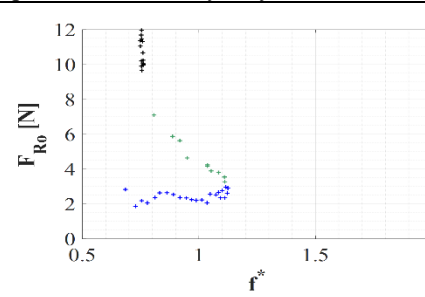


Fig. B1.n. Residuary force F_{R0} vs. f^* derived experimentally using eq. (4-1)

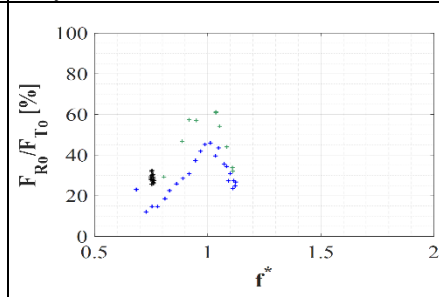
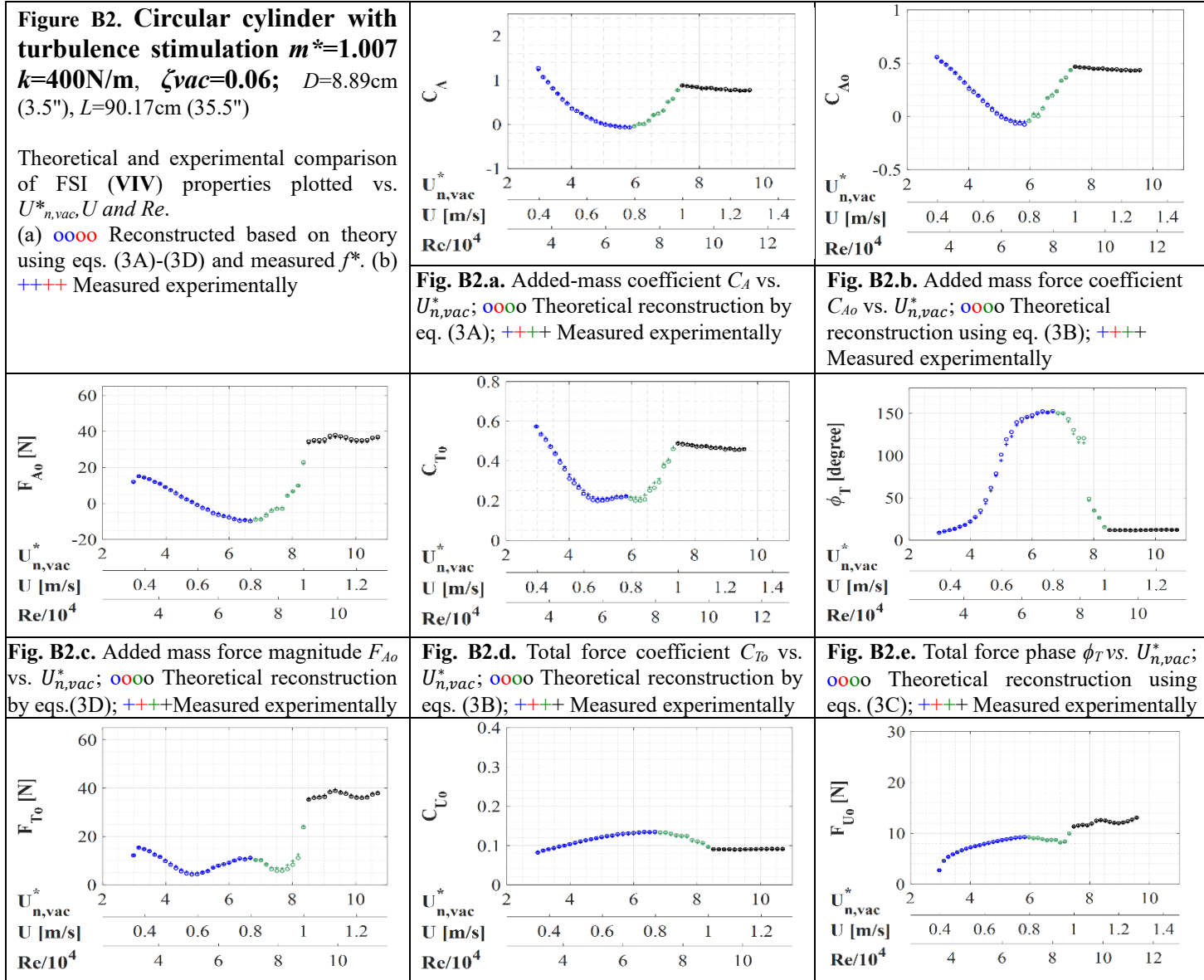


Fig. B1.o. Ratio F_{R0}/F_{T0} [%] of vs. f^* ; derived experimentally by eqs. (3D, 4-1)



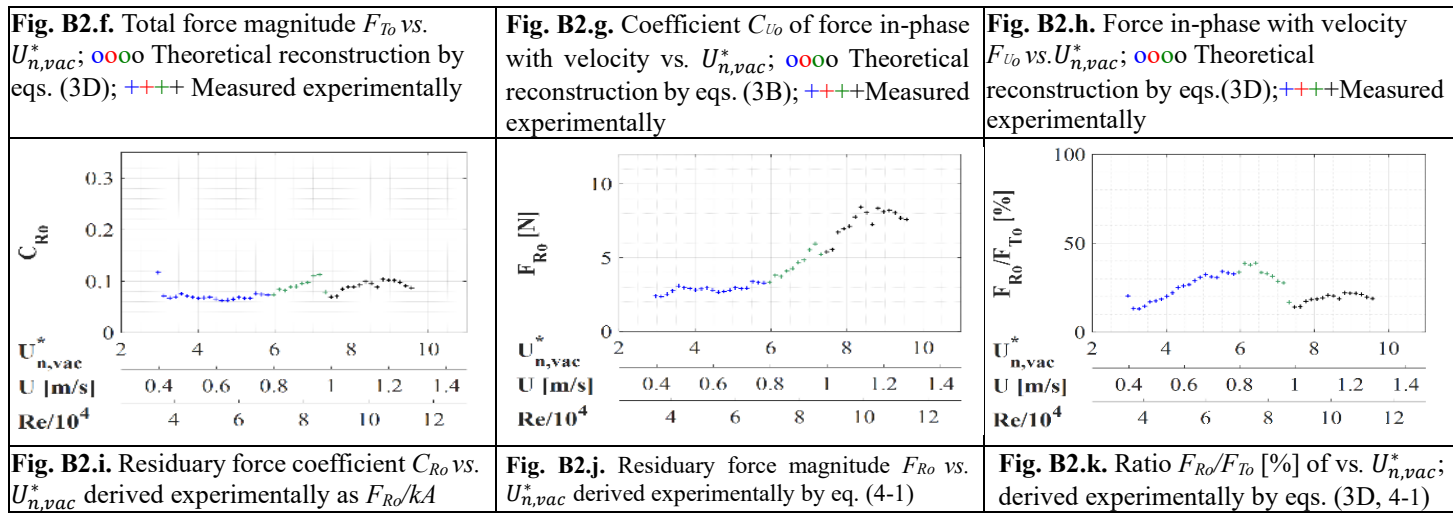
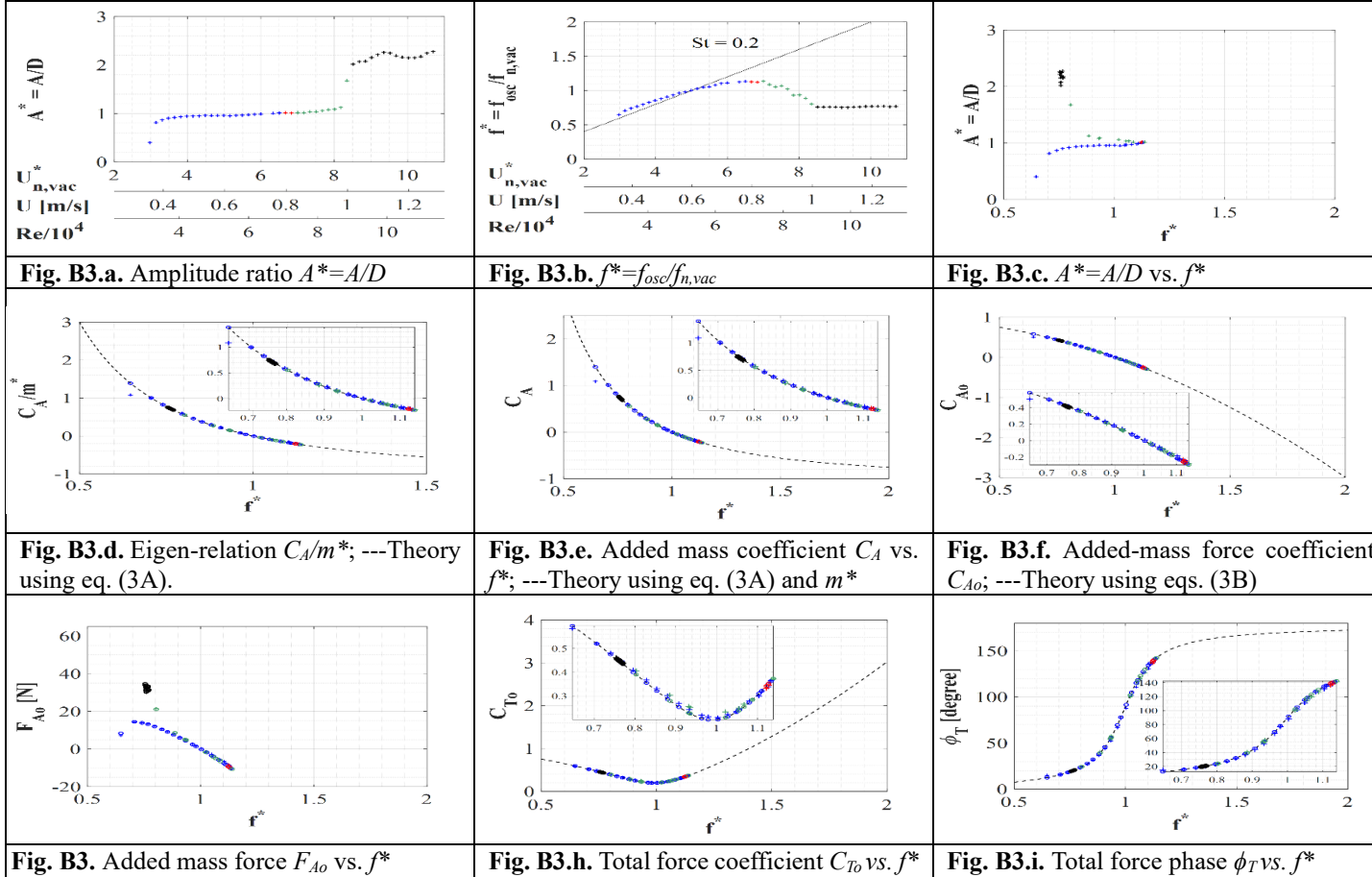
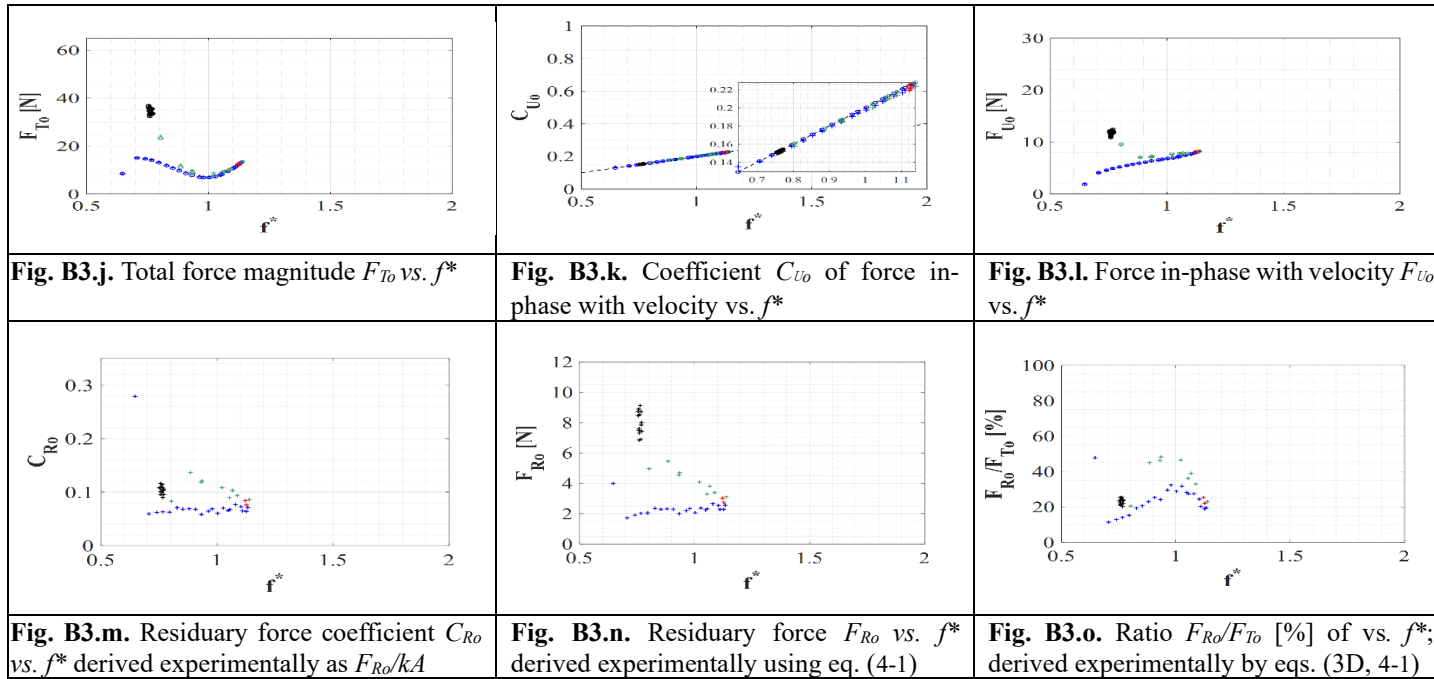
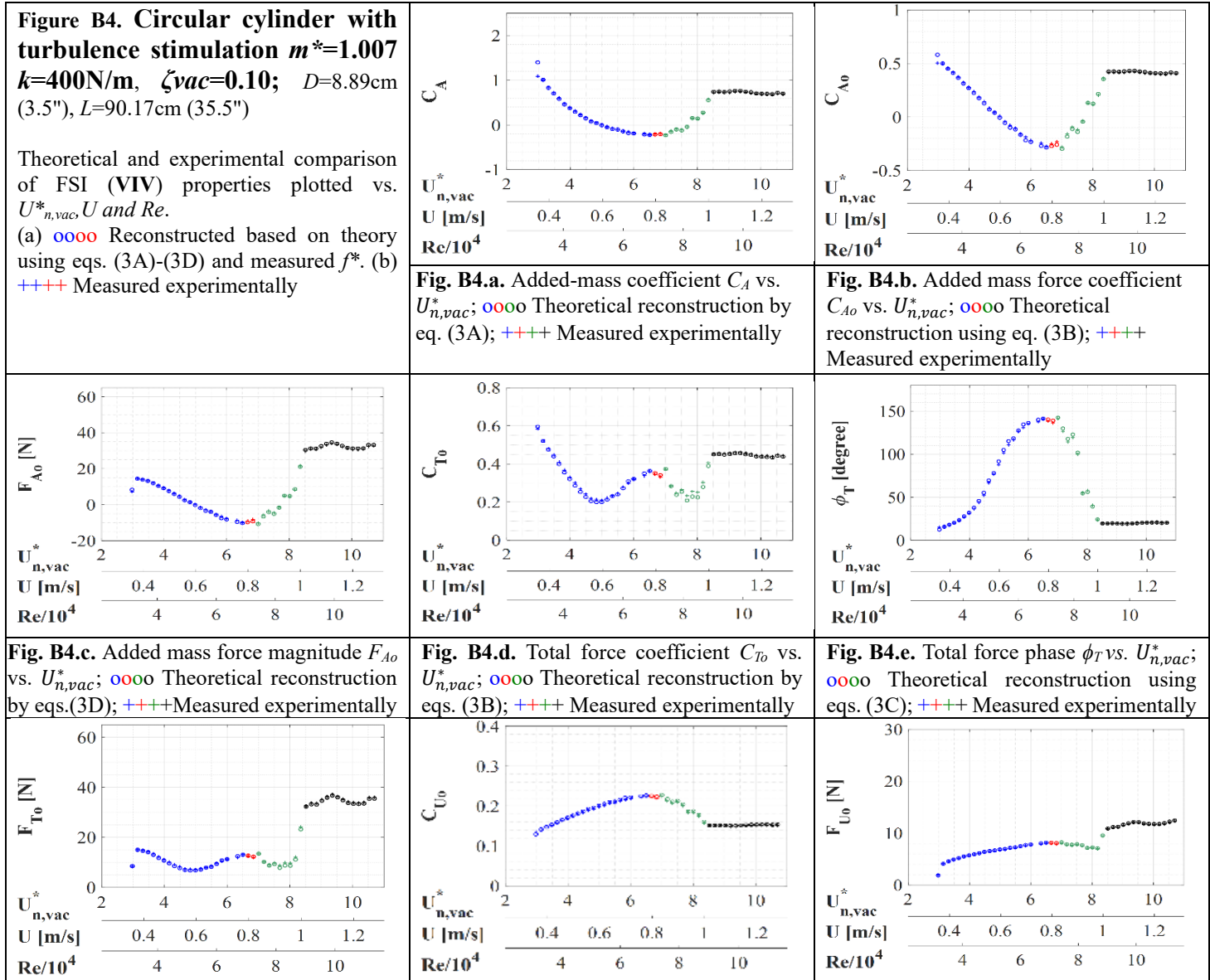


Figure B3. Circular cylinder with turbulence stimulation, $m^*=1.007$, $k=400\text{N/m}$, $\zeta_{vac}=0.10$; $D=8.89\text{cm}$ (3.5"), $L=90.17\text{cm}$ (35.5") Theoretical and experimental comparison of FSI (VIV) properties plotted vs. f^*
 (a) ---- Theory using eqs. (3A)-(3D). (b) ooooo Reconstructed based on theory and measured f^* . (c) ++++ Measured experimentally







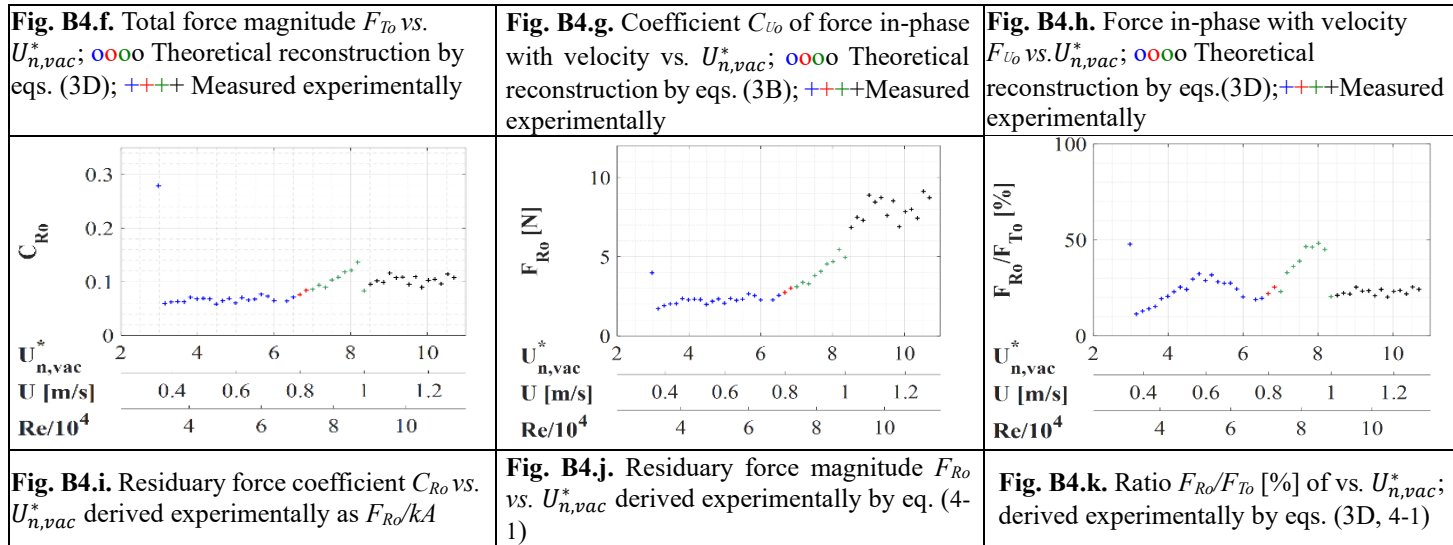


Figure B5. Circular cylinder with turbulence stimulation, $m^*=1.007$, $k=800\text{N/m}$, $\zeta_{vac}=0.06$; $D=8.89\text{cm}$ (3.5"), $L=90.17\text{cm}$ (35.5") Theoretical and experimental comparison of FSI (VIV) properties plotted vs. f^*
 (a) ---- Theory using eqs. (3A)-(3D). (b) ooooo Reconstructed based on theory and measured f^* . (c) ++++ Measured experimentally

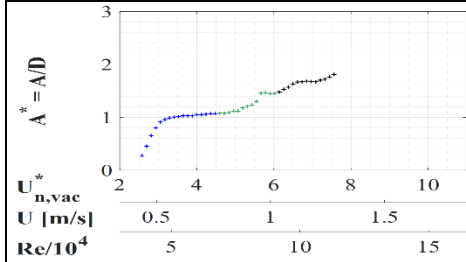


Fig. B5.a. Amplitude ratio $A^*=A/D$

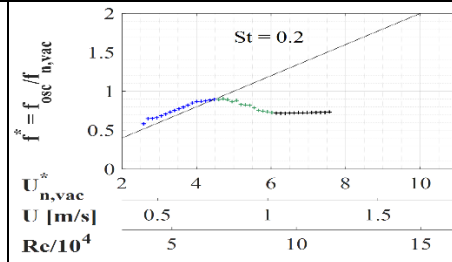


Fig. B5.b. $f^*=f_{osc}/f_{n,vac}$

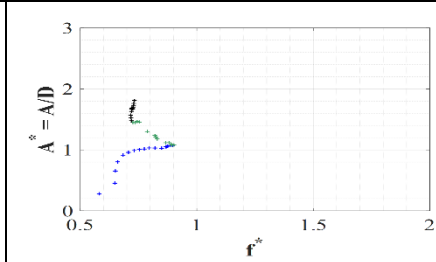


Fig. B5.c. $A^*=A/D$ vs. f^*

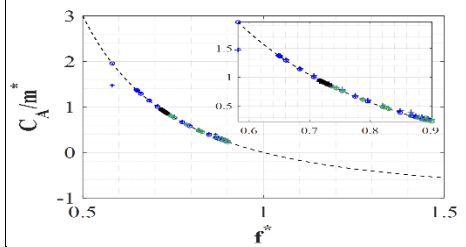


Fig. B5.d. Eigen-relation C_A/m^* ; ----Theory using eq. (3A).

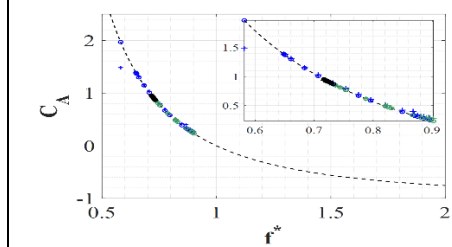


Fig. B5.e. Added mass coefficient C_A vs. f^* ; ----Theory using eq. (3A) and m^*

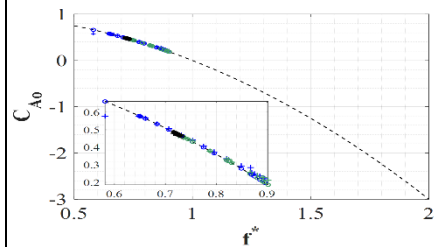


Fig. B5.f. Added-mass force coefficient C_{A0} ; ----Theory using eqs. (3B)

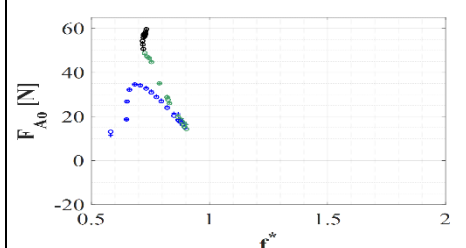


Fig. B5.g. Added mass force F_{A0} vs. f^*

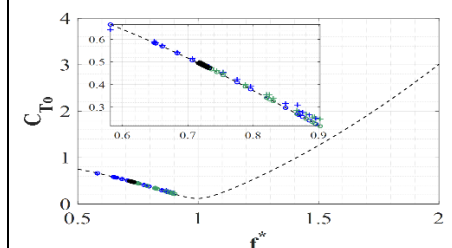


Fig. B5.h. Total force coefficient C_{T0} vs. f^*

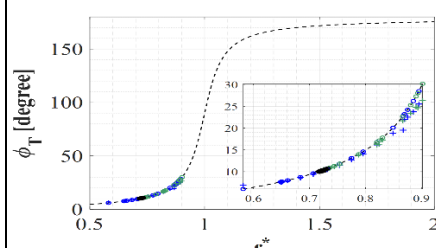
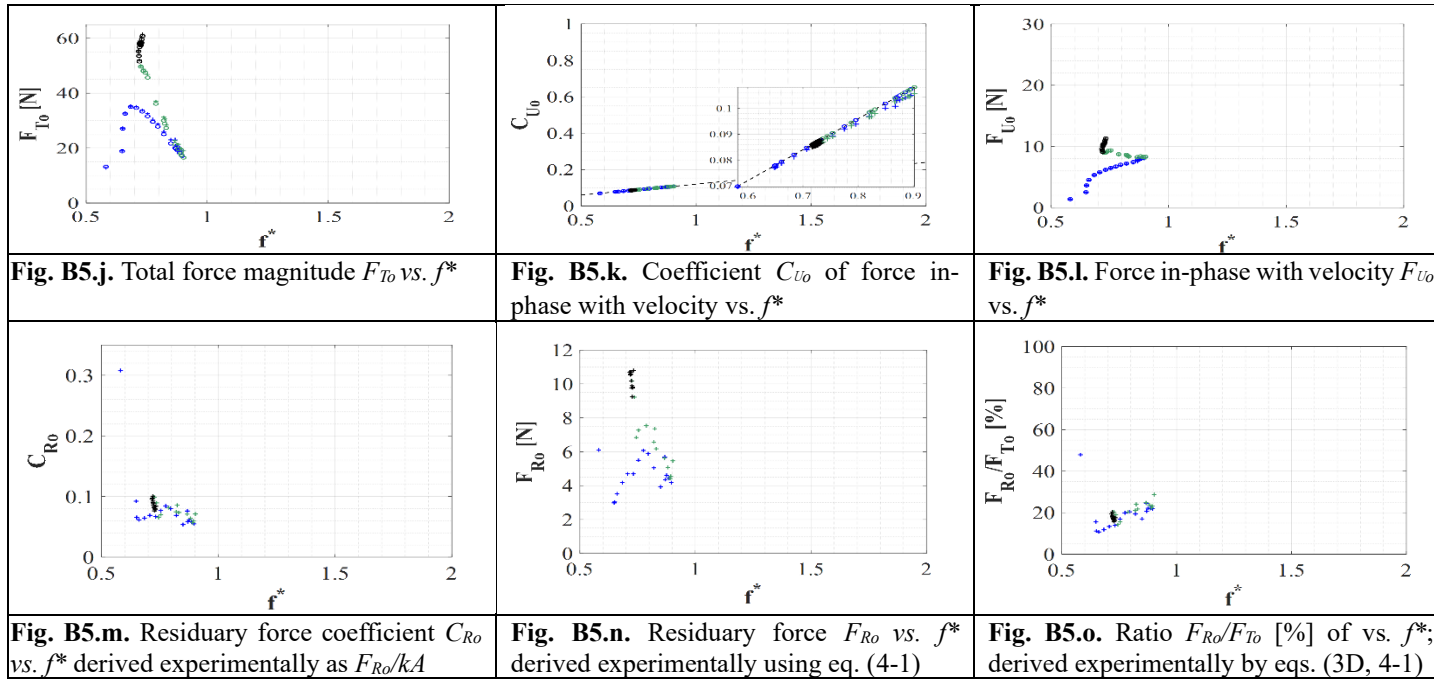
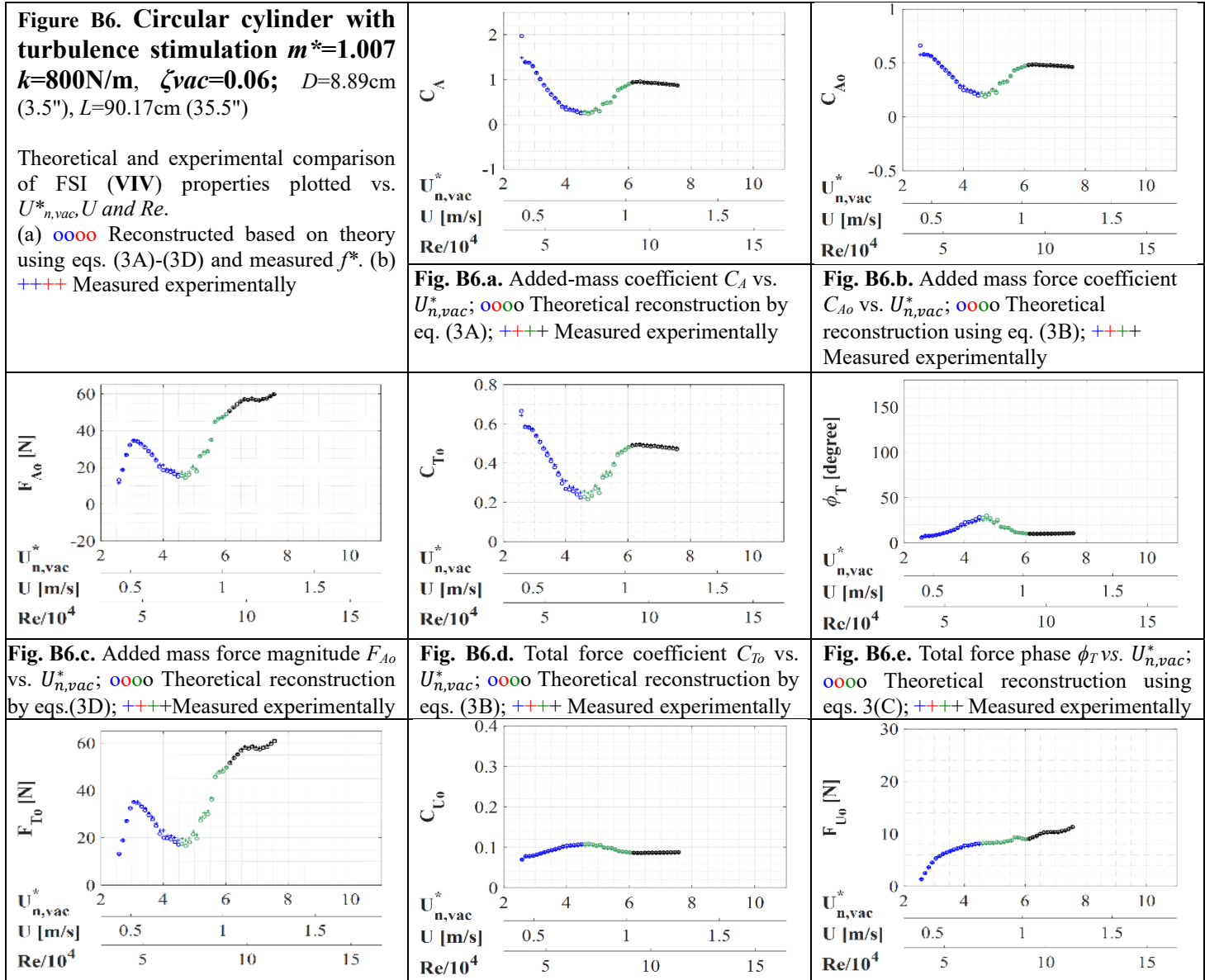


Fig. B5.i. Total force phase ϕ_T vs. f^*





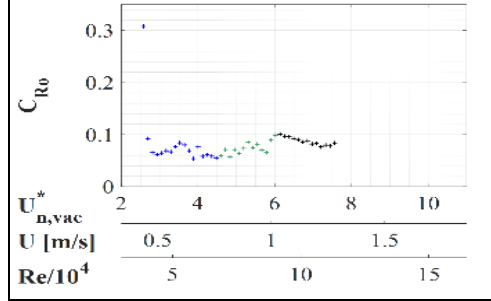
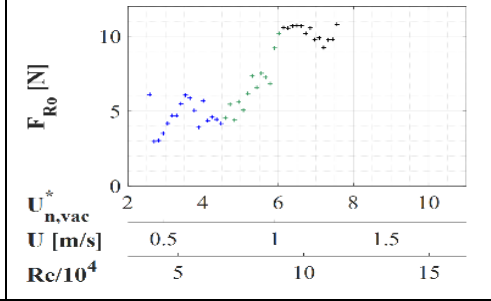
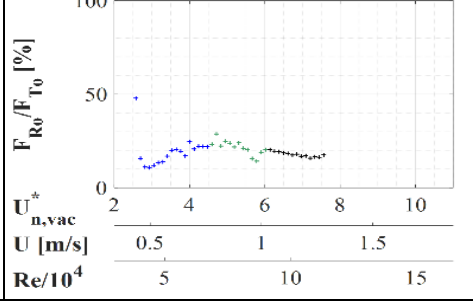
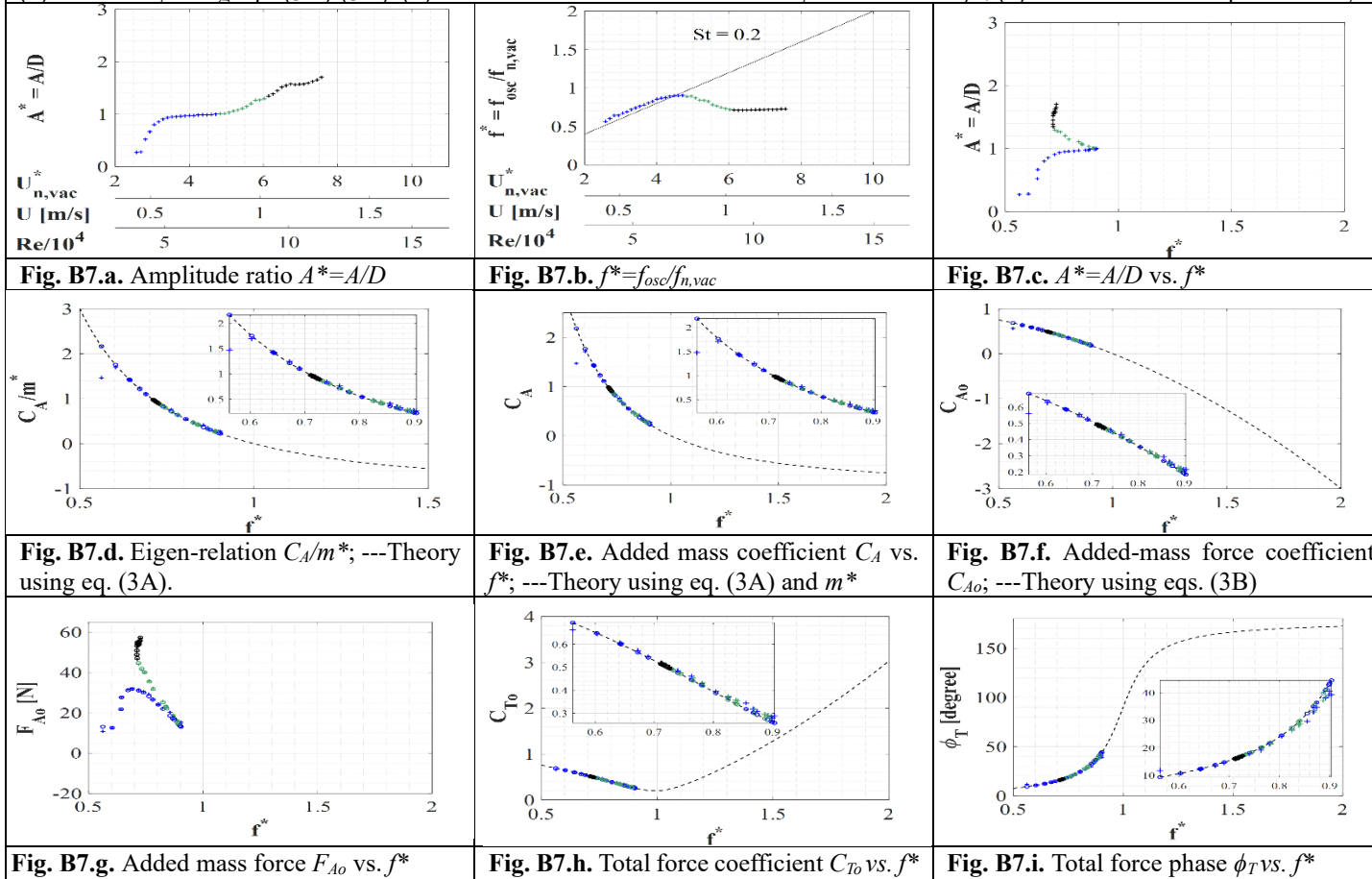
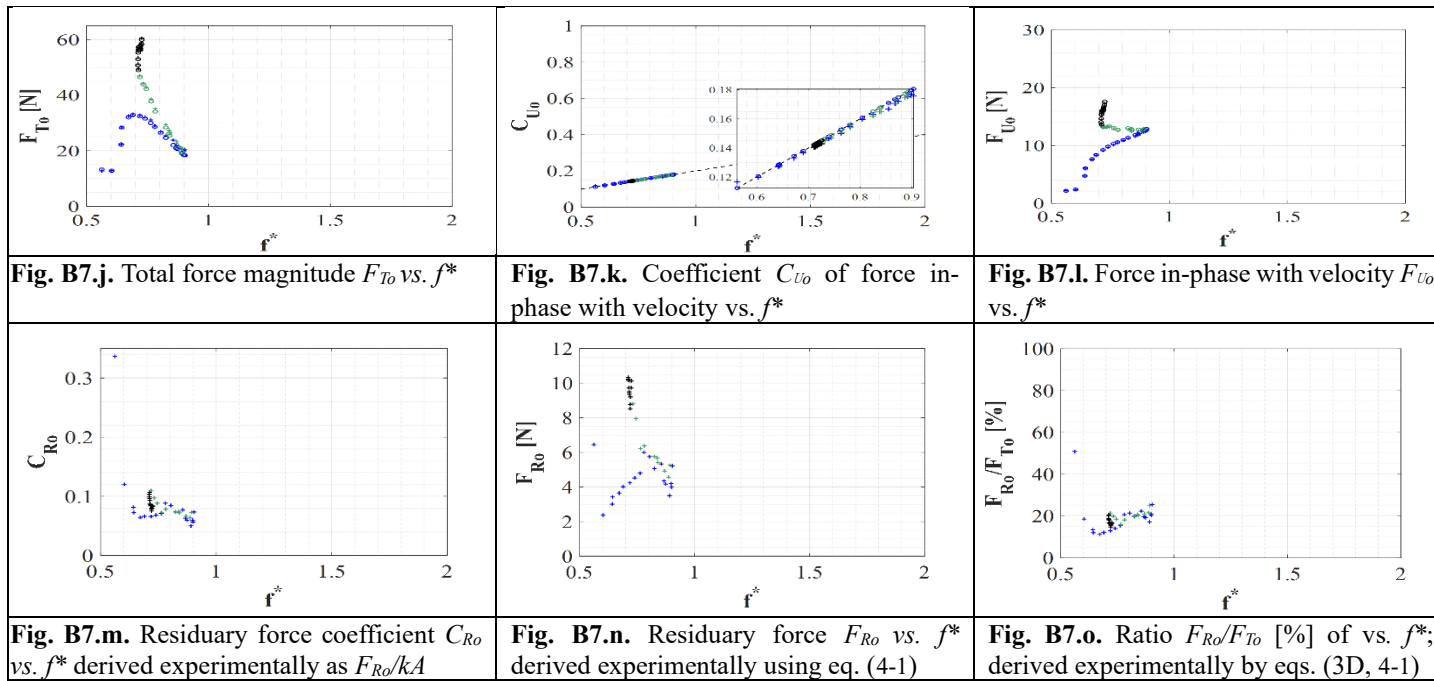
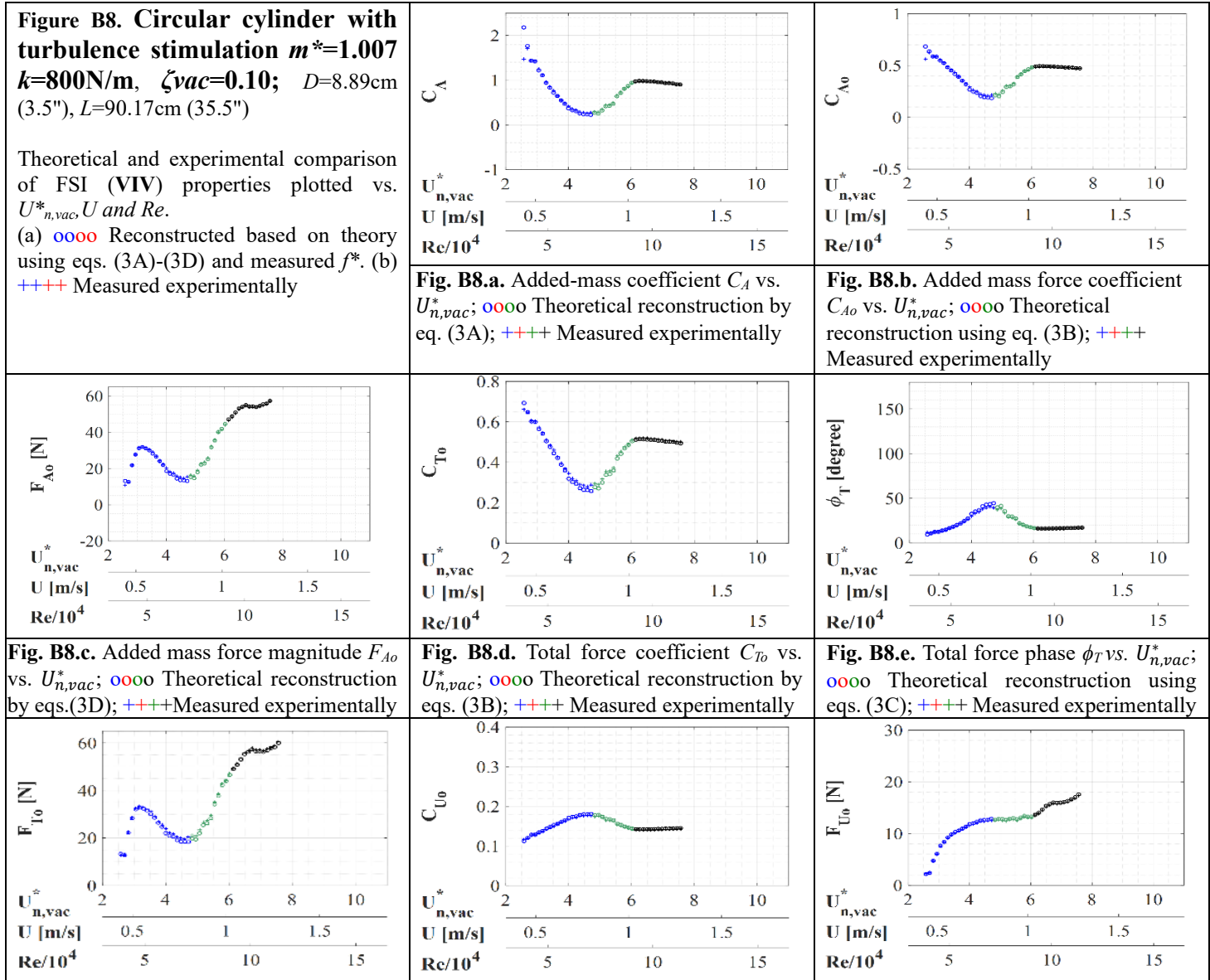
<p>Fig. B6.f. Total force magnitude F_{T0} vs. $U_{n,vac}^*$; $\circ\circ\circ\circ$ Theoretical reconstruction by eqs. (3D); $++++$ Measured experimentally</p>	<p>Fig. B6.g. Coefficient C_{v0} of force in-phase with velocity vs. $U_{n,vac}^*$; $\circ\circ\circ\circ$ Theoretical reconstruction by eqs. (3B); $++++$ Measured experimentally</p>	<p>Fig. B6.h. Force in-phase with velocity F_{v0} vs. $U_{n,vac}^*$; $\circ\circ\circ\circ$ Theoretical reconstruction by eqs.(3D); $++++$ Measured experimentally</p>
		
<p>Fig. B6.i. Residuary force coefficient C_{Ro} vs. $U_{n,vac}^*$ derived experimentally as F_{Ro}/kA</p>	<p>Fig. B6.j. Residuary force magnitude F_{Ro} vs. $U_{n,vac}^*$ derived experimentally by eq. (4-1)</p>	<p>Fig. B6.k. Ratio F_{Ro}/F_{T0} [%] of vs. $U_{n,vac}^*$; derived experimentally by eqs. (3D, 4-1)</p>

Figure B7. Circular cylinder with turbulence stimulation, $m^*=1.007$, $k=800\text{N/m}$, $\zeta_{vac}=0.10$; $D=8.89\text{cm}$ (3.5"), $L=90.17\text{cm}$ (35.5") Theoretical and experimental comparison of FSI (VIV) properties plotted vs. f^*
 (a) ---- Theory using eqs. (3A)-(3D). (b) ooooo Reconstructed based on theory and measured f^* . (c) ++++ Measured experimentally







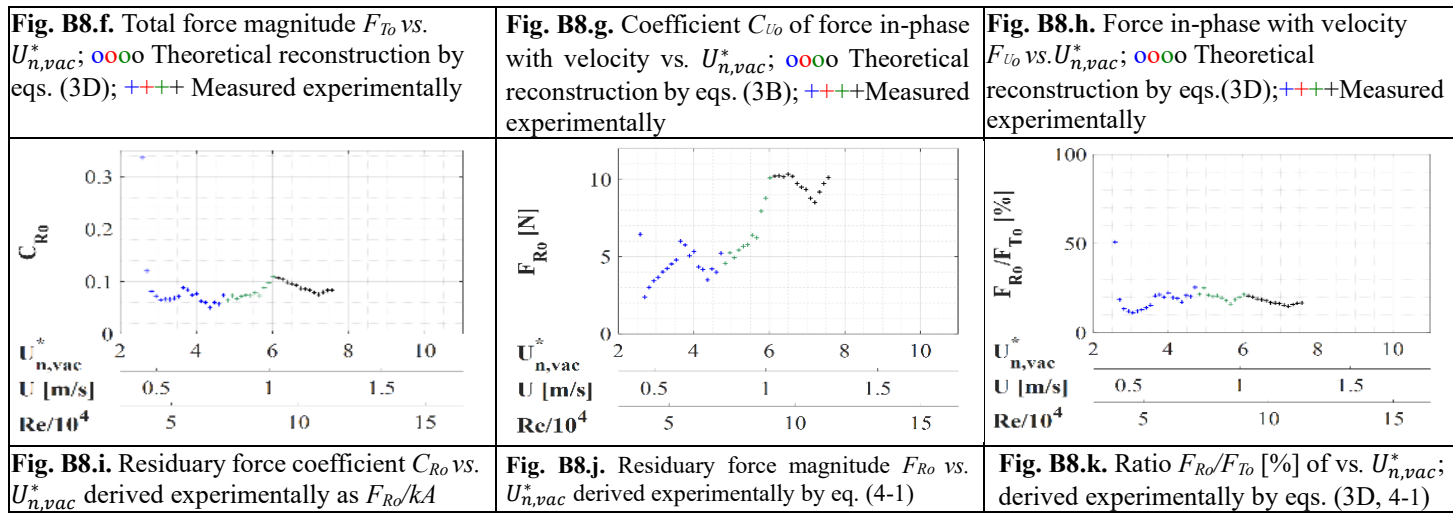
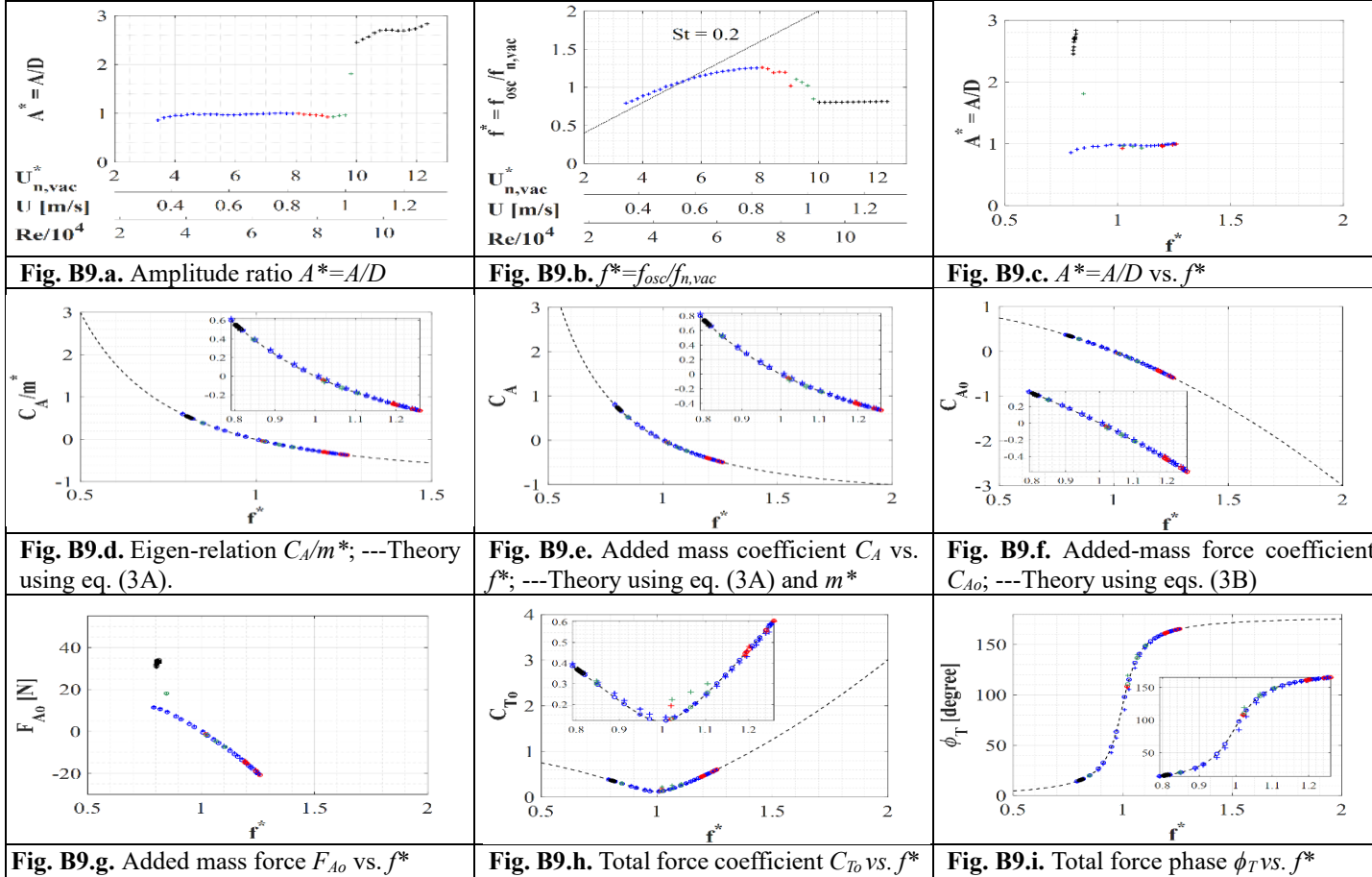
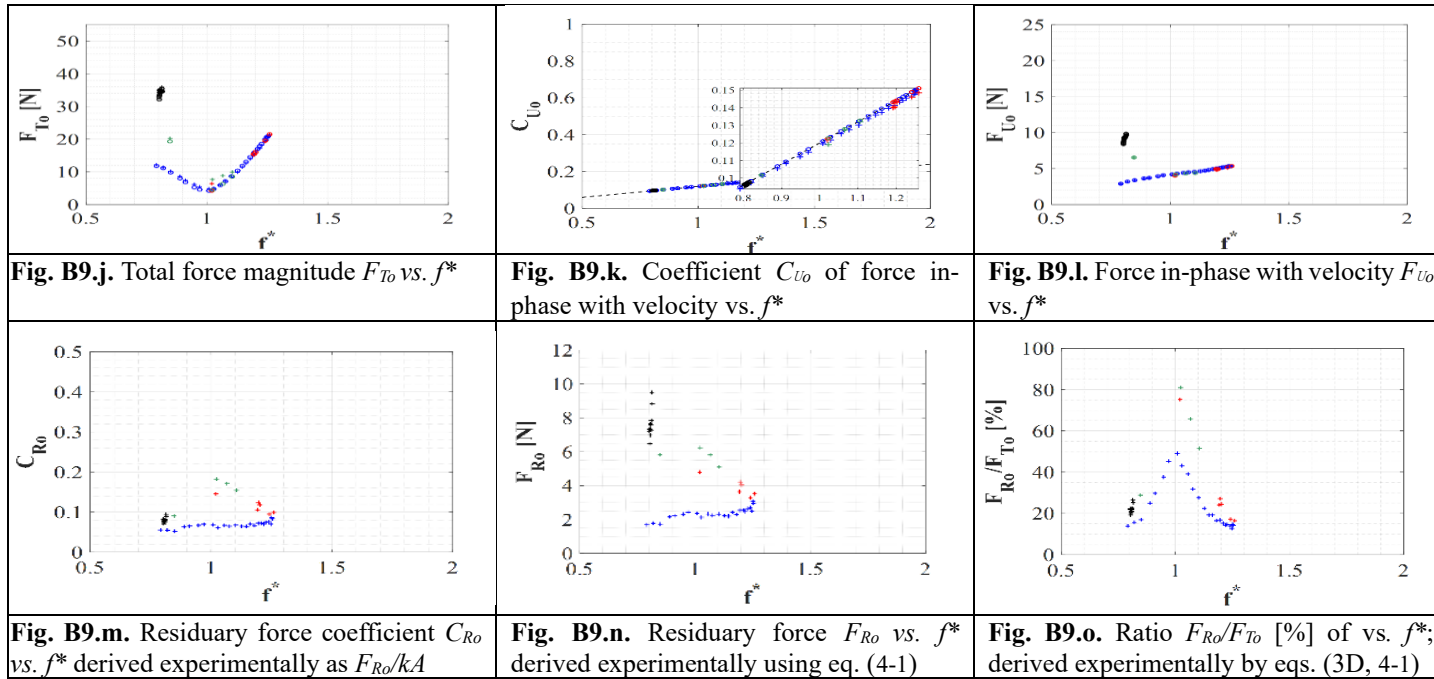
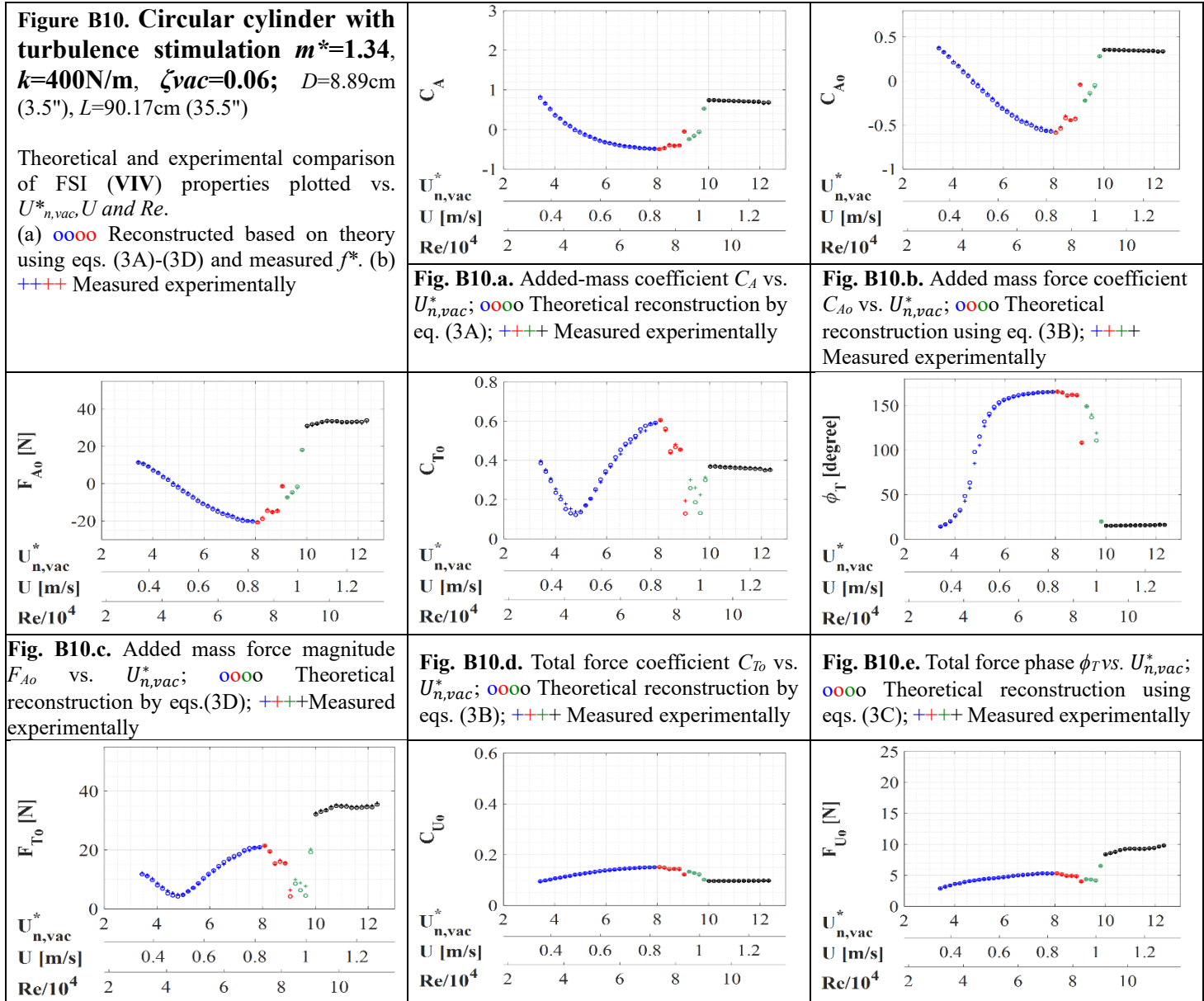


Figure B9. Circular cylinder with turbulence stimulation, $m^*=1.34$, $k=400\text{N/m}$, $\zeta_{vac}=0.06$; $D=8.89\text{cm}$ (3.5"), $L=90.17\text{cm}$ (35.5") Theoretical and experimental comparison of FSI (VIV) properties plotted vs. f^*
 (a) ---- Theory using eqs. (3A)-(3D). (b) ooooo Reconstructed based on theory and measured f^* . (c) ++++ Measured experimentally







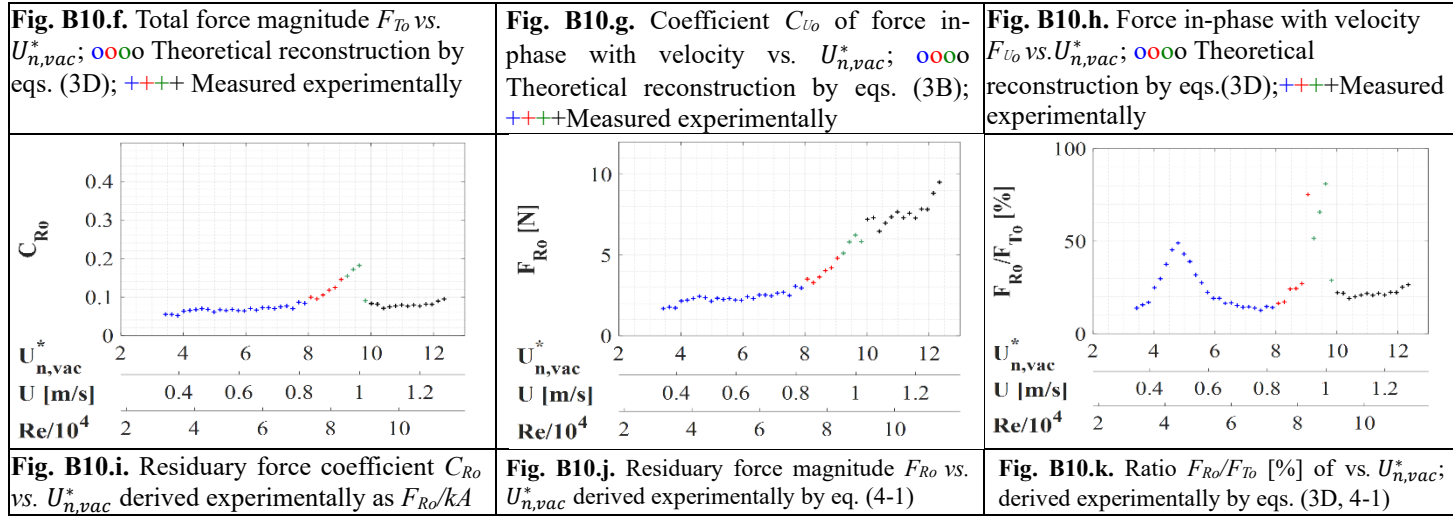
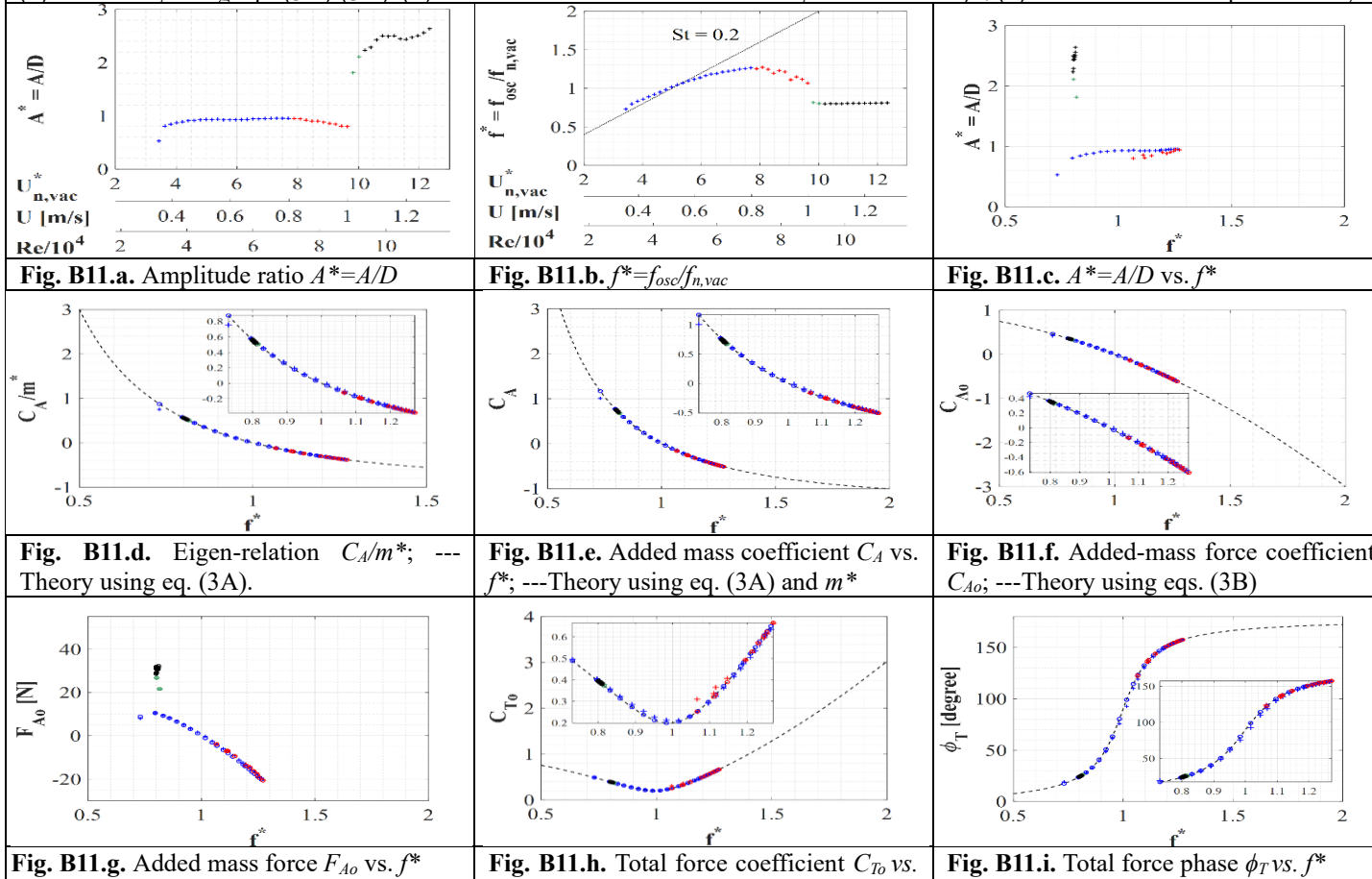
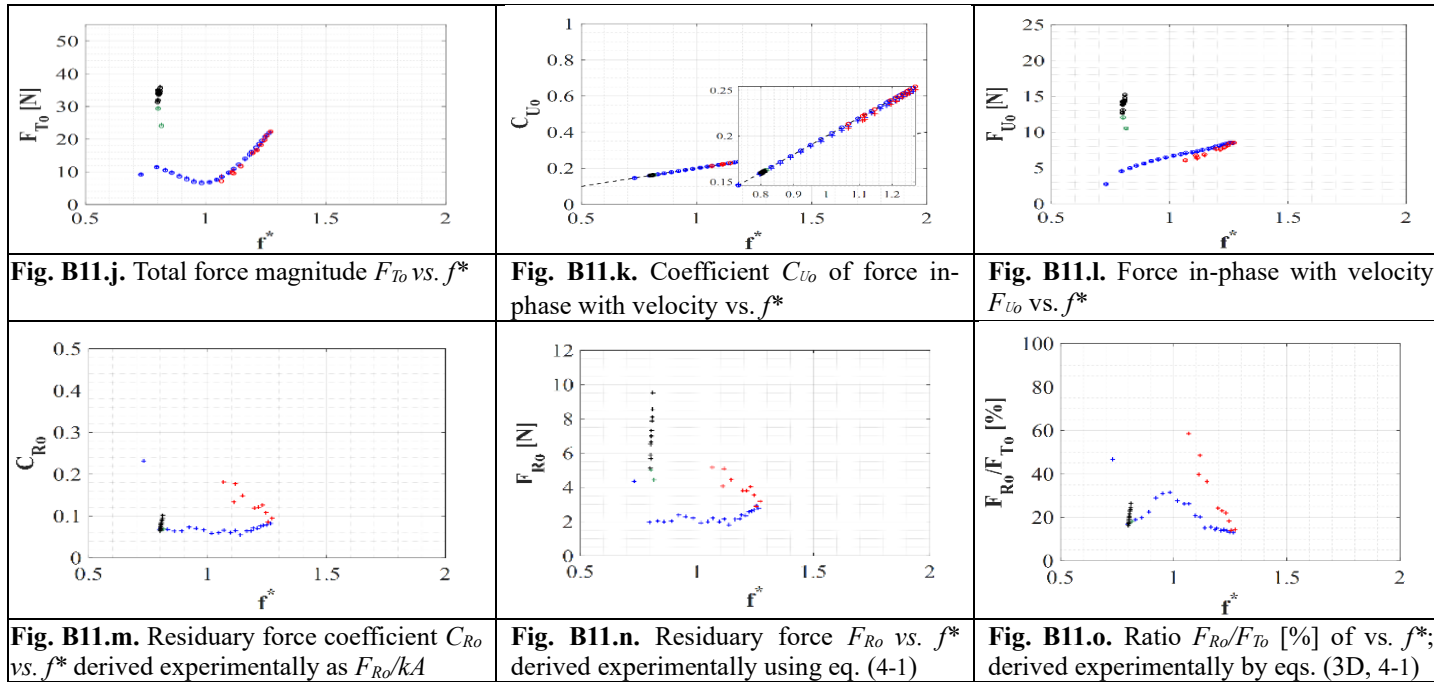
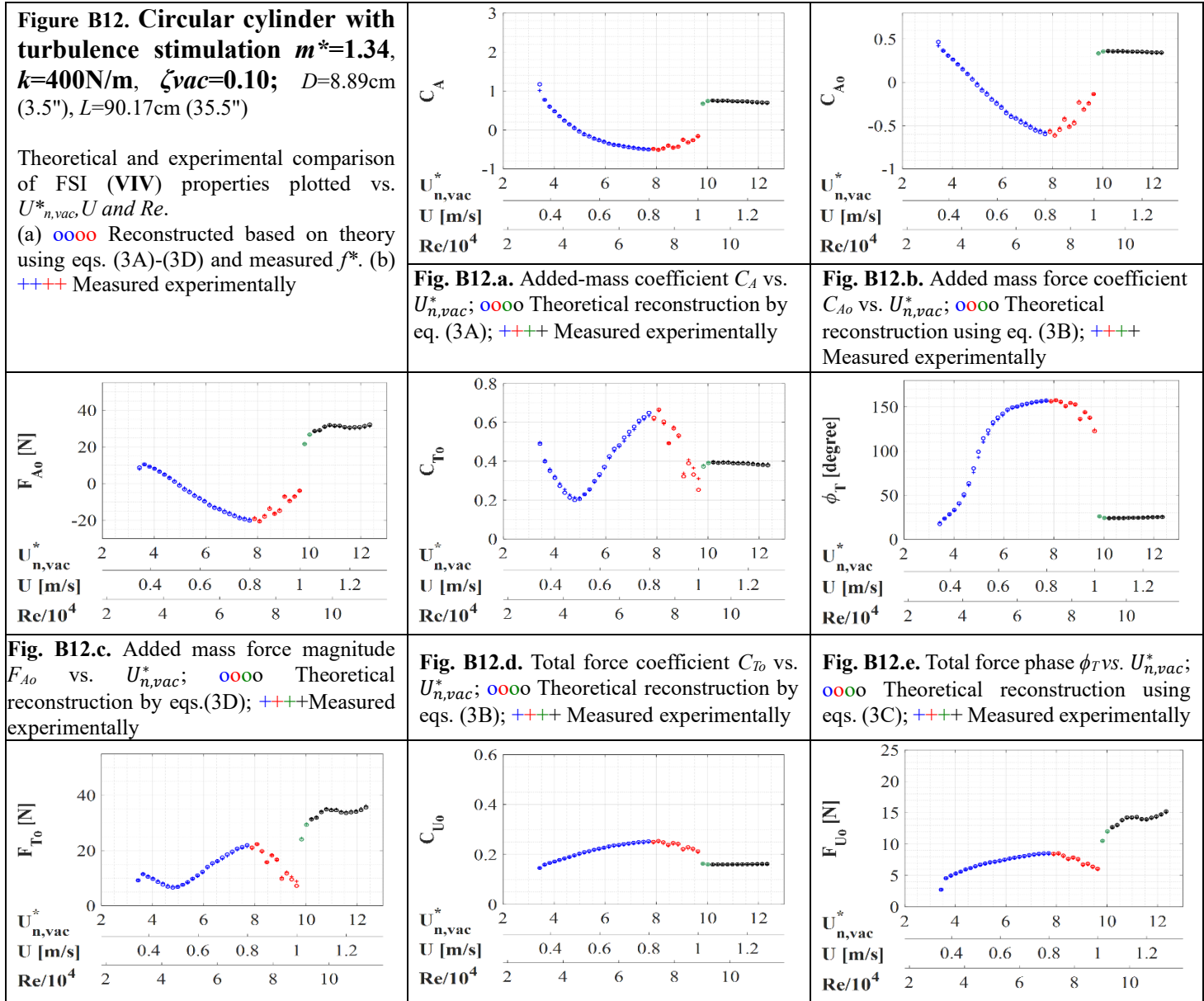


Figure B11. Circular cylinder with turbulence stimulation, $m^*=1.34$, $k=400\text{N/m}$, $\zeta_{vac}=0.10$; $D=8.89\text{cm}$ (3.5"), $L=90.17\text{cm}$ (35.5") Theoretical and experimental comparison of FSI (VIV) properties plotted vs. f^*
 (a) ---- Theory using eqs. (3A)-(3D). (b) ooooo Reconstructed based on theory and measured f^* . (c) ++++ Measured experimentally







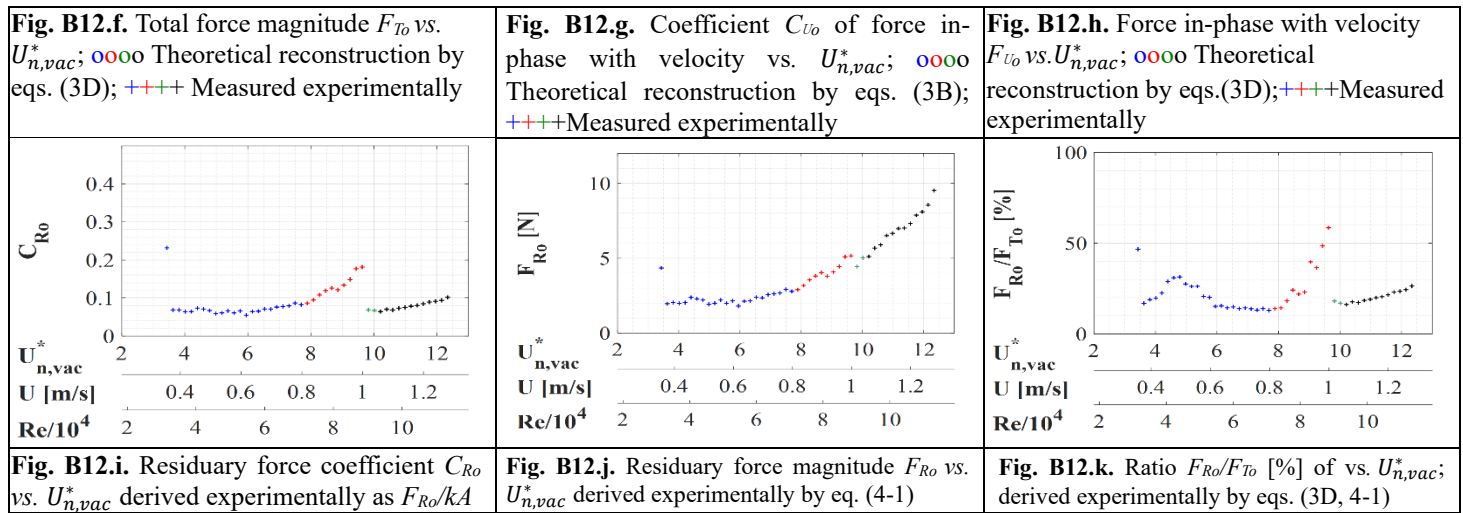


Figure B13. Circular cylinder with turbulence stimulation, $m^*=1.34$, $k=800\text{N/m}$, $\zeta_{vac}=0.06$; $D=8.89\text{cm}$ (3.5"), $L=90.17\text{cm}$ (35.5") Theoretical and experimental comparison of FSI (VIV) properties plotted vs. f^*
 (a) ---- Theory using eqs. (3A)-(3D). (b) ooooo Reconstructed based on theory and measured f^* . (c) ++++ Measured experimentally

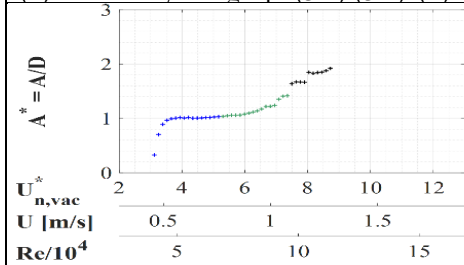


Fig. B13.a. Amplitude ratio $A^*=A/D$

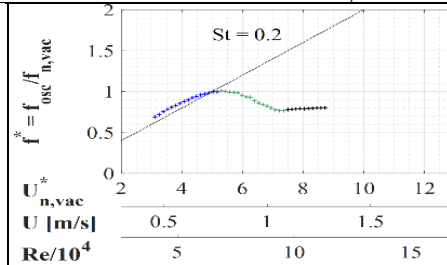


Fig. B13.b. $f^*=f_{osc}/f_{n,vac}$

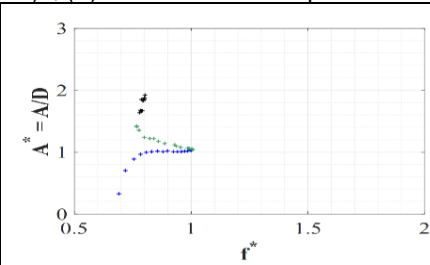


Fig. B13.c. $A^*=A/D$ vs. f^*

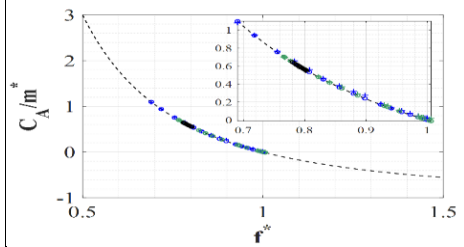


Fig. B13.d. Eigen-relation C_A/m^* ; --- Theory using eq. (3A).

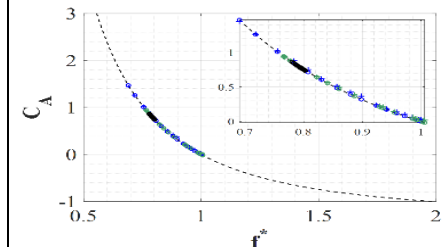


Fig. B13.e. Added mass coefficient C_A vs. f^* ; ---Theory using eq. (3A) and m^*

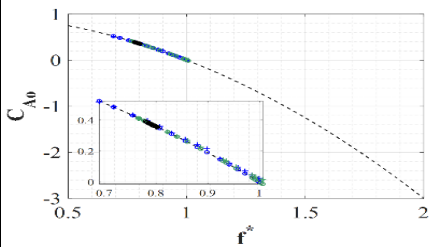


Fig. B13.f. Added-mass force coefficient C_{A0} ; ---Theory using eqs. (3B)

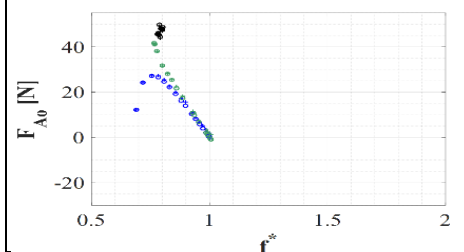


Fig. B13.g. Added mass force F_{A0} vs. f^*

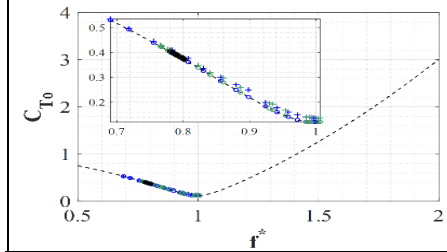


Fig. B13.h. Total force coefficient C_{T0} vs. f^*

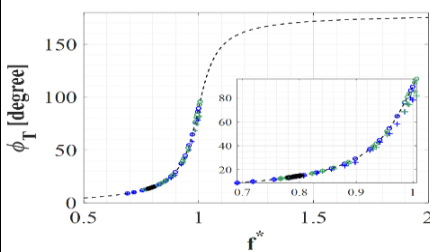
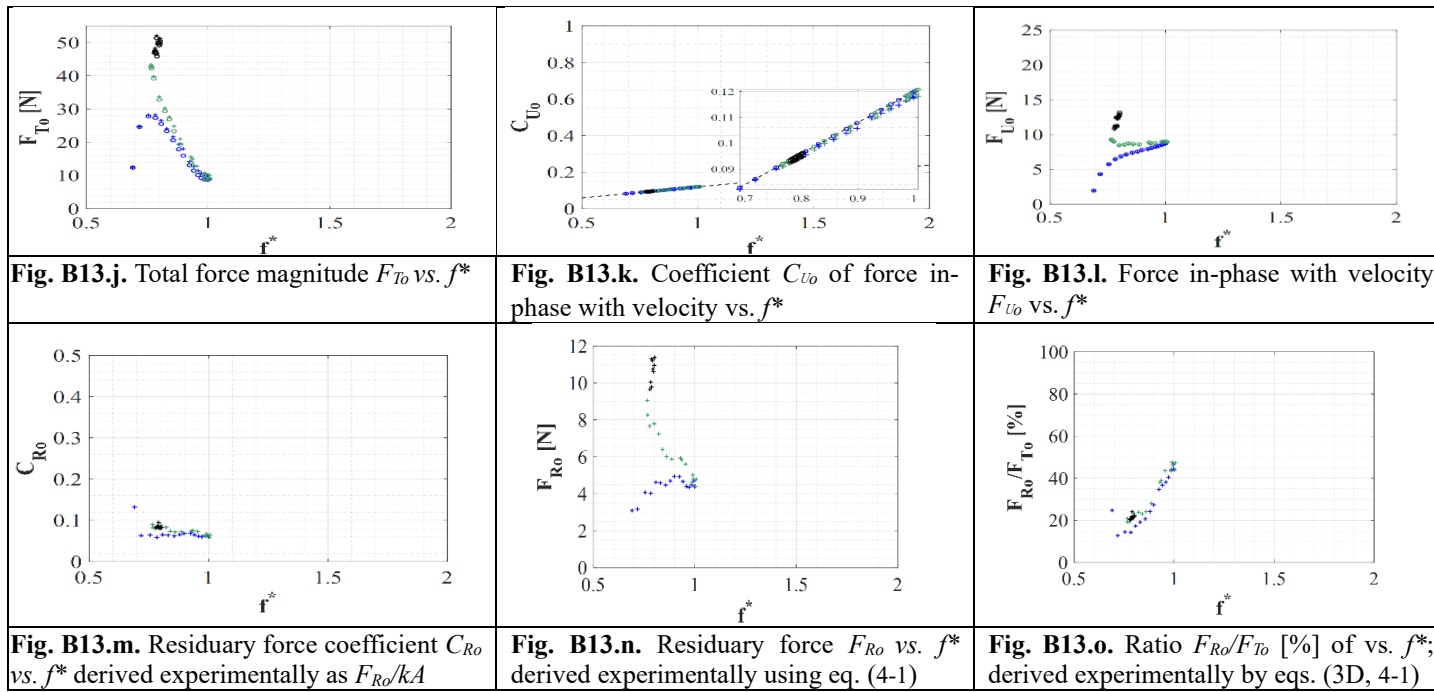
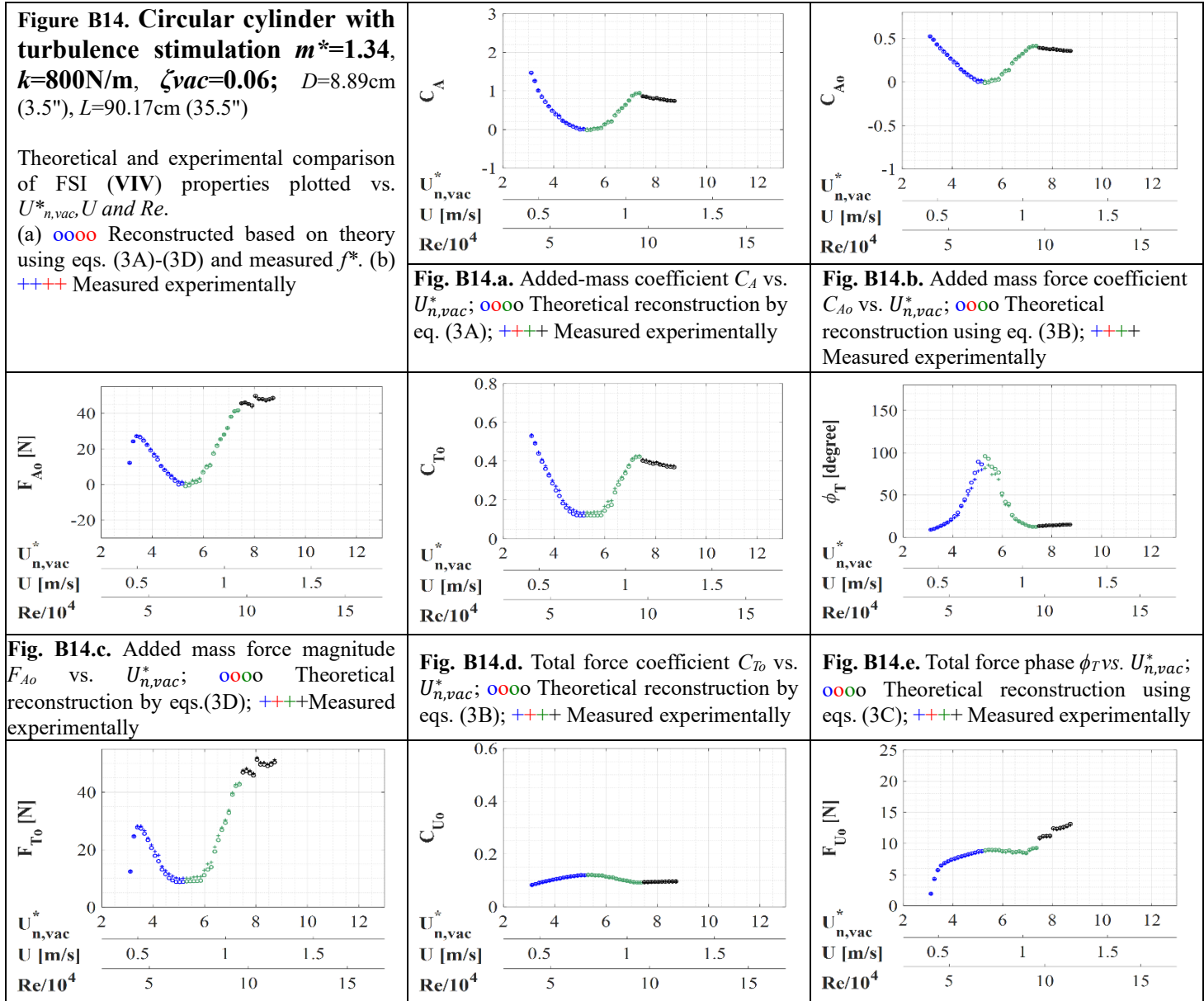


Fig. B13.i. Total force phase ϕ_T vs. f^*





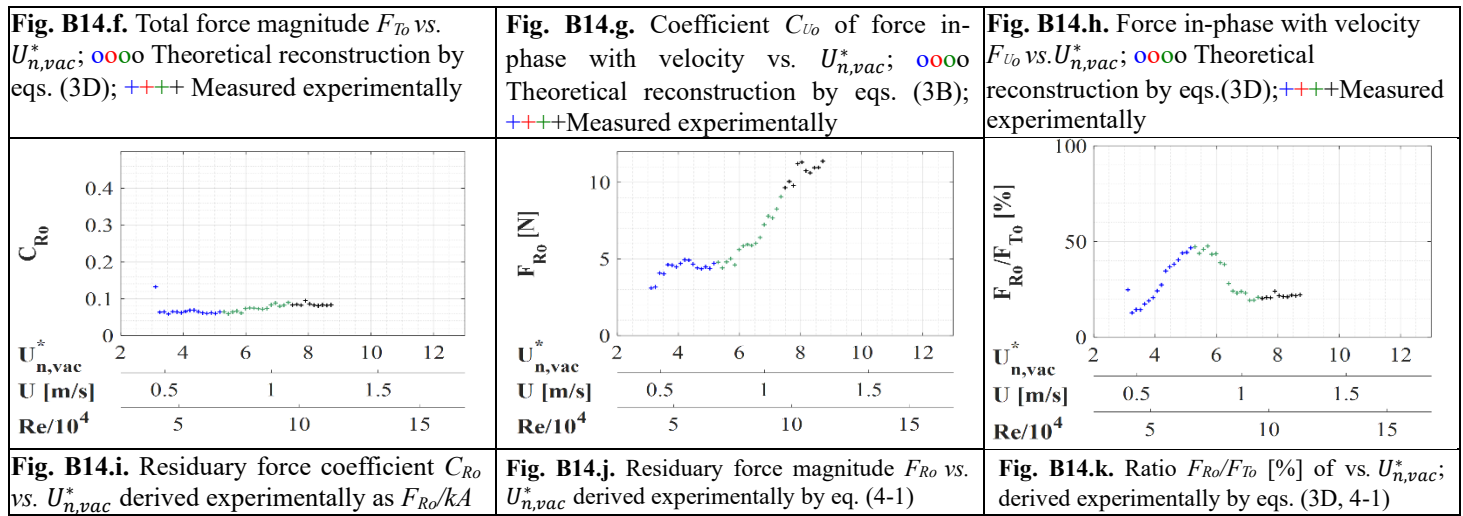


Figure B15. Circular cylinder with turbulence stimulation, $m^*=1.34$, $k=800\text{N/m}$, $\zeta_{vac}=0.10$; $D=8.89\text{cm}$ (3.5"), $L=90.17\text{cm}$ (35.5") Theoretical and experimental comparison of FSI (VIV) properties plotted vs. f^*

(a) ---- Theory using eqs. (A)-(D). (b) oooo Reconstructed based on theory and measured f^* . (c) ++++ Measured experimentally

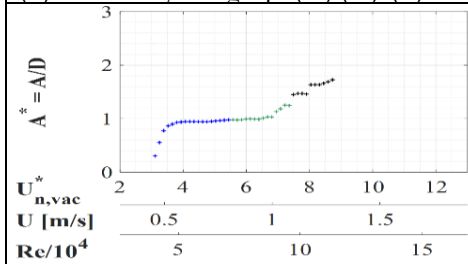


Fig. B15.a. Amplitude ratio $A^*=A/D$

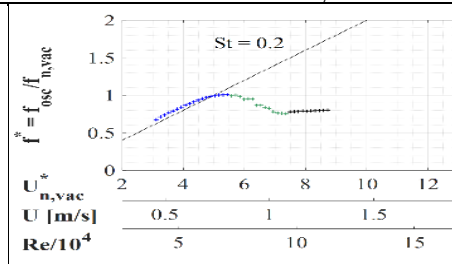


Fig. B15.b. $f^*=f_{osc}/f_{n,vac}$

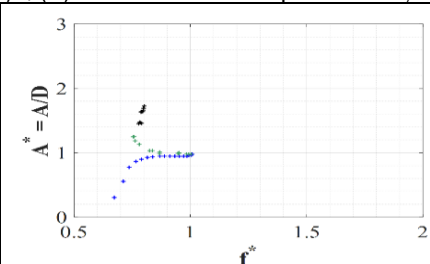


Fig. B15.c. $A^*=A/D$ vs. f^*

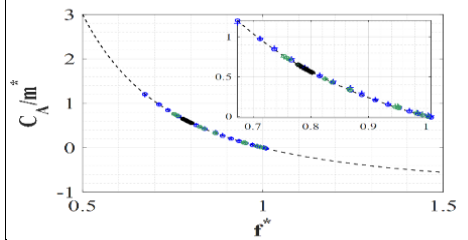


Fig. B15.d. Eigen-relation C_A/m^* ; ---- Theory using eq. (3A).

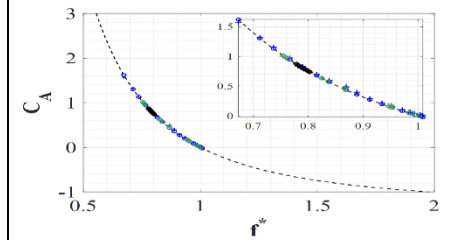


Fig. B15.e. Added mass coefficient C_A vs. f^* ; ---- Theory using eq. (3A) and m^*

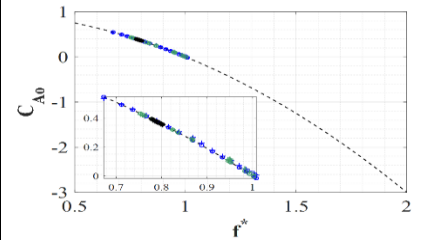


Fig. B15.f. Added-mass force coefficient C_{A0} ; ---- Theory using eqs. (3B)

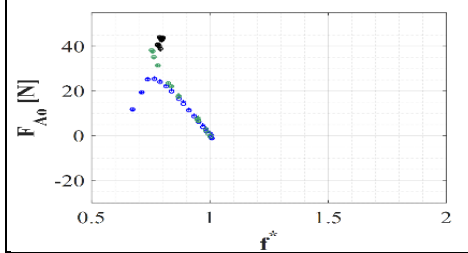


Fig. B15.g. Added mass force F_{A0} vs. f^*

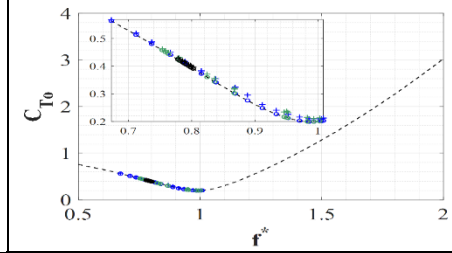


Fig. B15.h. Total force coefficient C_{T0} vs. f^*

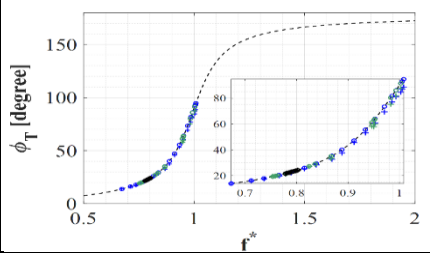
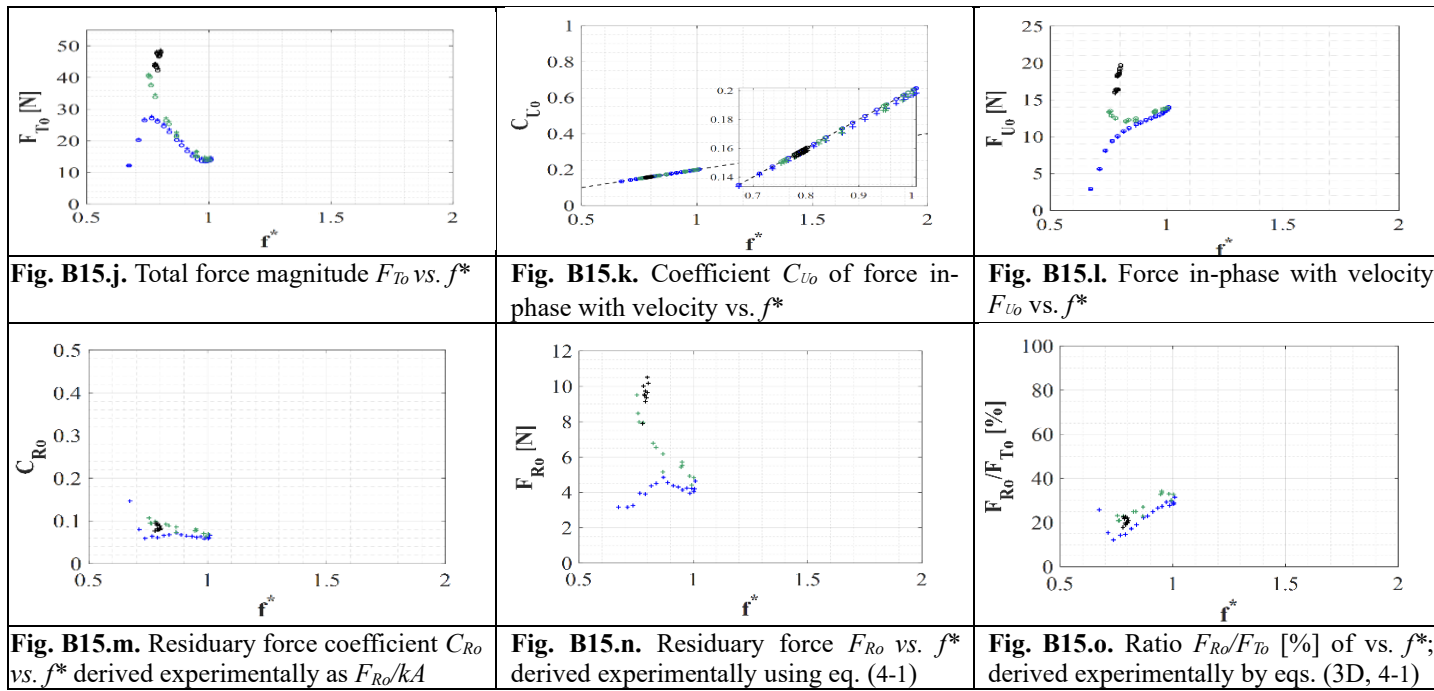
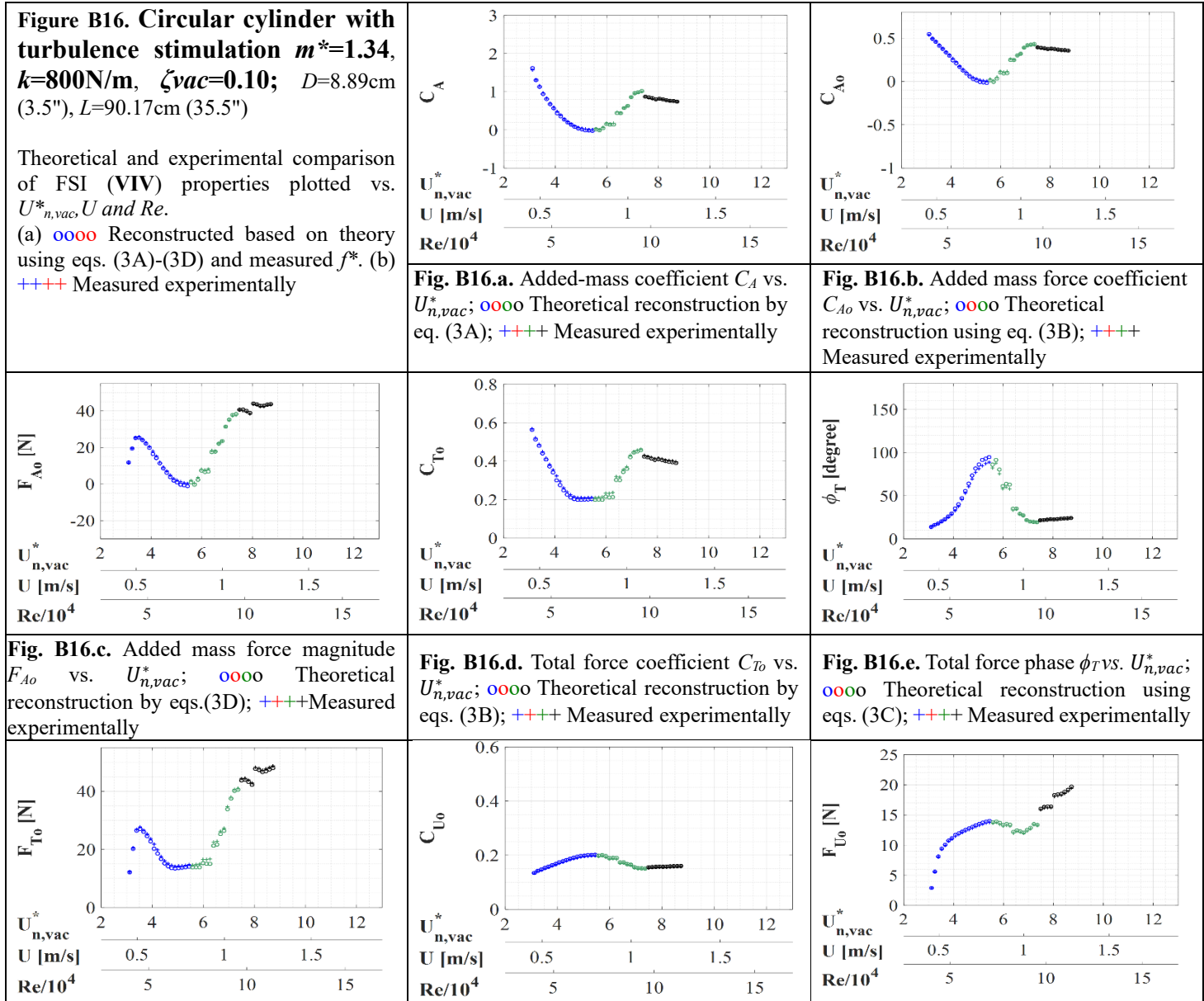


Fig. B15.i. Total force phase ϕ_T vs. f^*





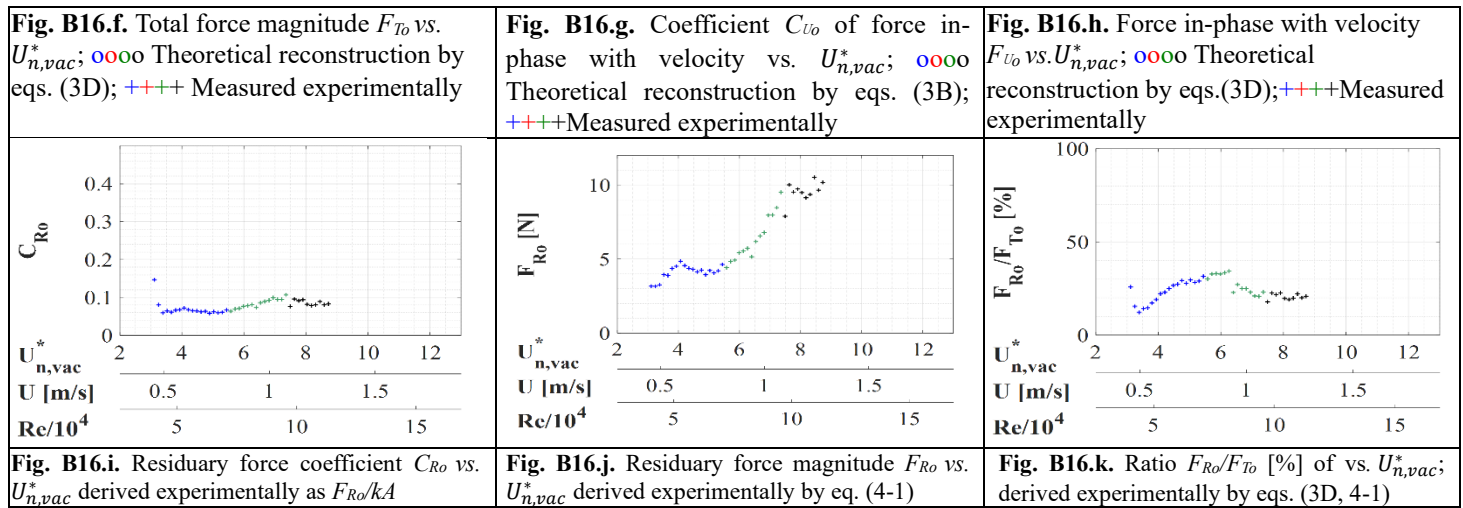
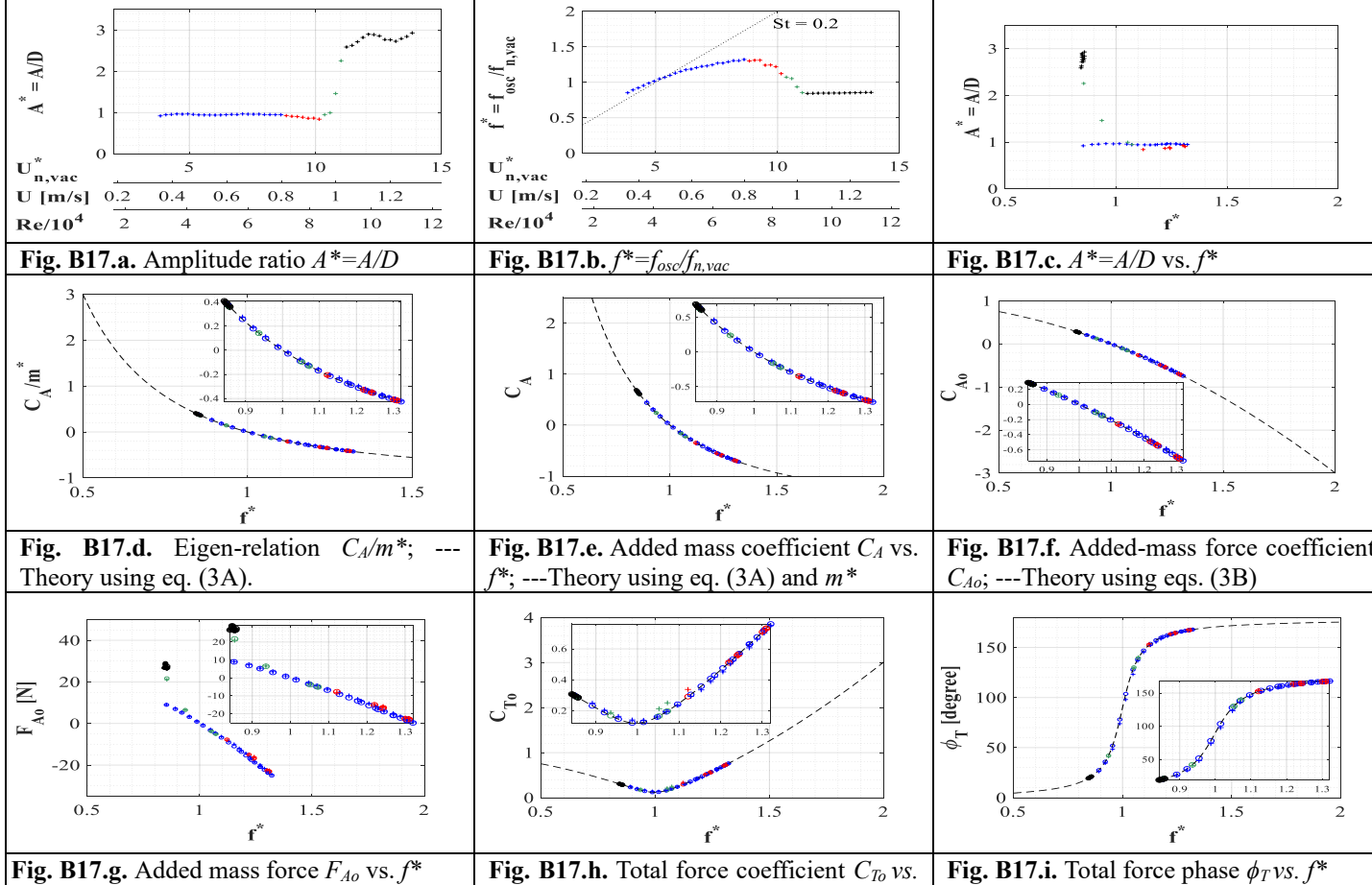
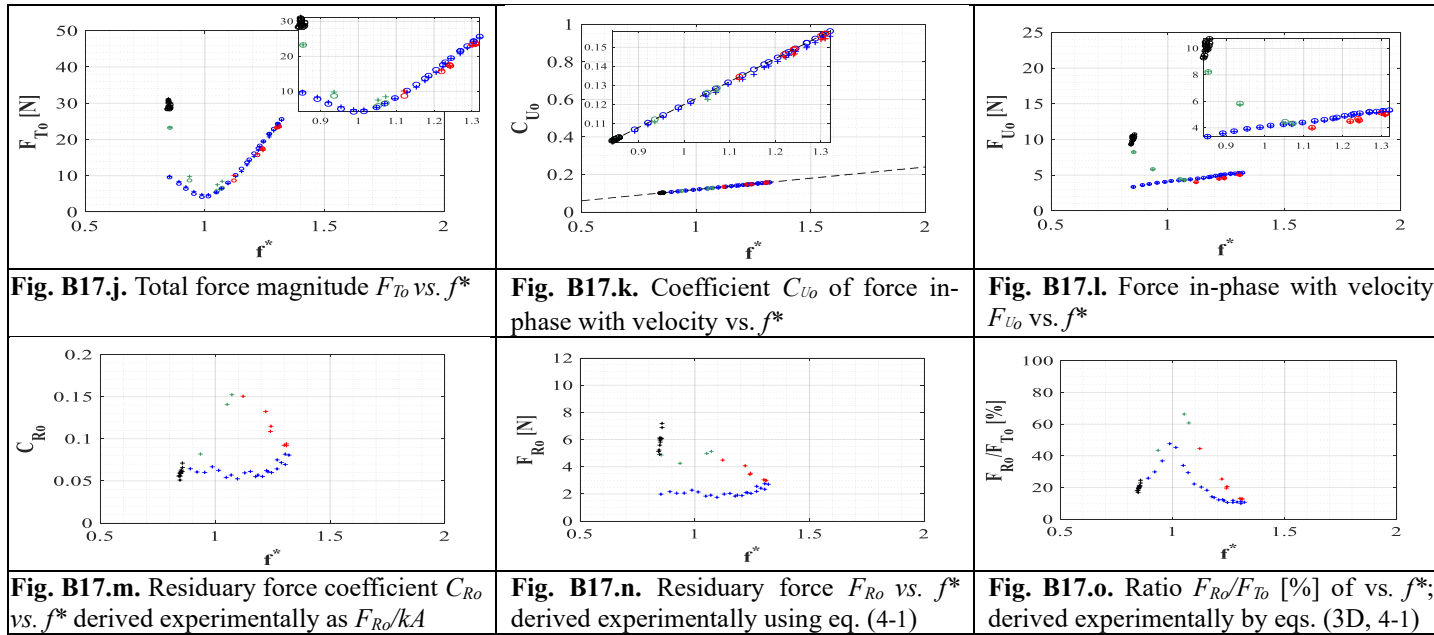
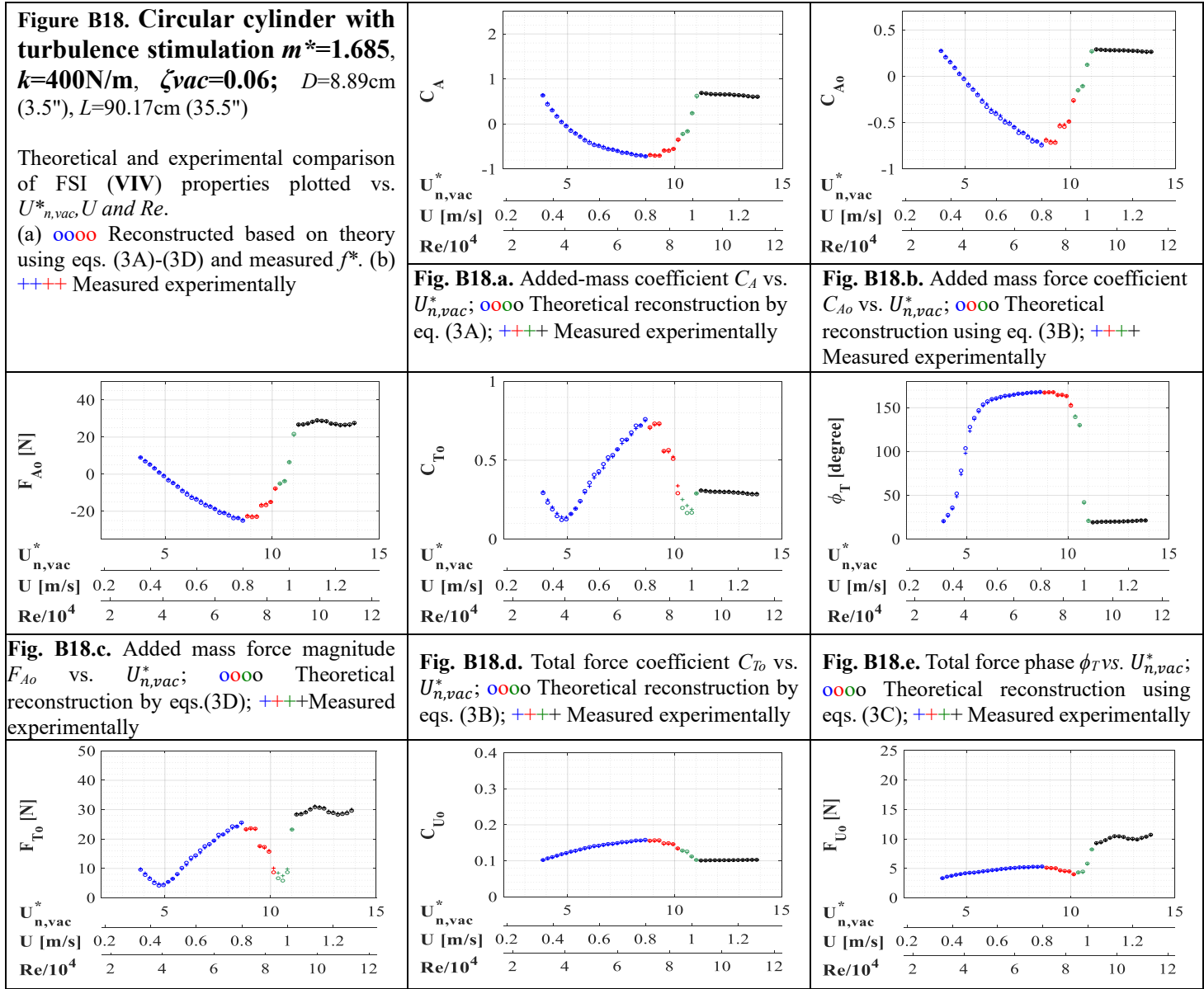


Figure B17. Circular cylinder with turbulence stimulation, $m^*=1.685$, $k=400\text{N/m}$, $\zeta_{vac}=0.06$; $D=8.89\text{cm}$ (3.5"), $L=90.17\text{cm}$ (35.5") Theoretical and experimental comparison of FSI (VIV) properties plotted vs. f^*
 (a) ---- Theory using eqs. (3A)-(3D). (b) ooooo Reconstructed based on theory and measured f^* . (c) ++++ Measured experimentally







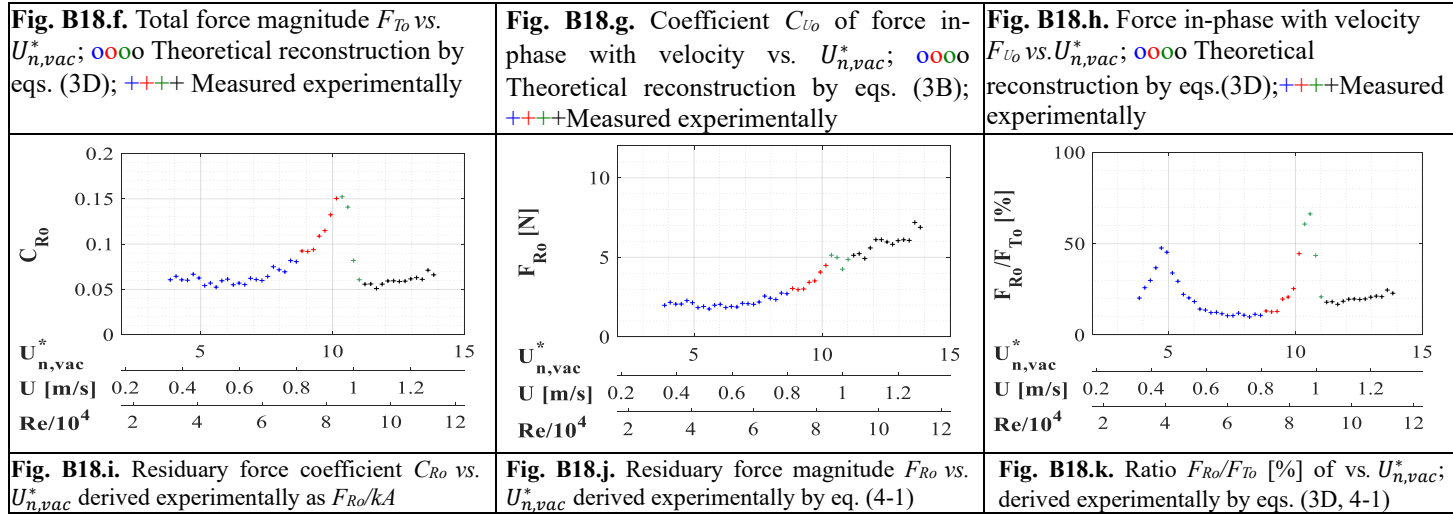


Figure B19. Circular cylinder with turbulence stimulation, $m^*=1.685$, $k=400\text{N/m}$, $\zeta_{vac}=0.10$; $D=8.89\text{cm}$ (3.5"), $L=90.17\text{cm}$ (35.5") Theoretical and experimental comparison of FSI (VIV) properties plotted vs. f^*
 (a) ---- Theory using eqs. (3A)-(3D). (b) ooooo Reconstructed based on theory and measured f^* . (c) ++++ Measured experimentally

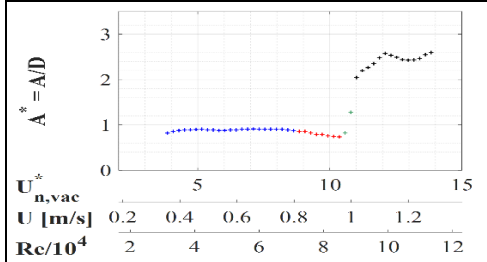


Fig. B19.a. Amplitude ratio $A^*=A/D$

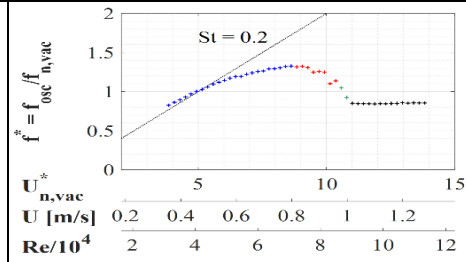


Fig. B19.b. $f^*=f_{osc}/f_{n,vac}$

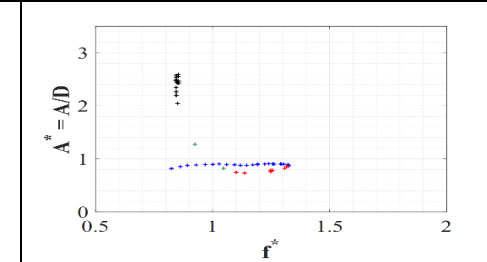


Fig. B19.c. $A^*=A/D$ vs. f^*

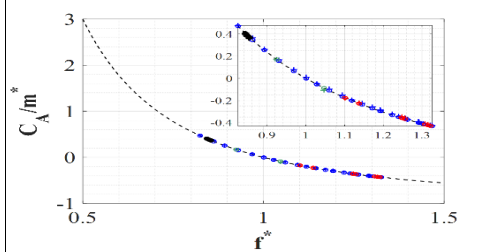


Fig. B19.d. Eigen-relation C_A/m^* ; --- Theory using eq. (3A).

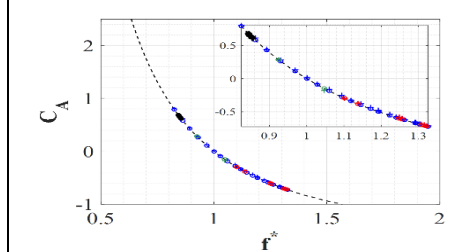


Fig. B19.e. Added mass coefficient C_A vs. f^* ; ---Theory using eq. (3A) and m^*

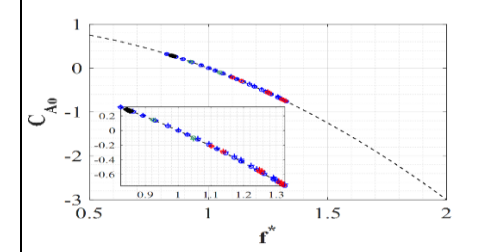


Fig. B19.f. Added-mass force coefficient C_{A0} ; ---Theory using eqs. (3B)

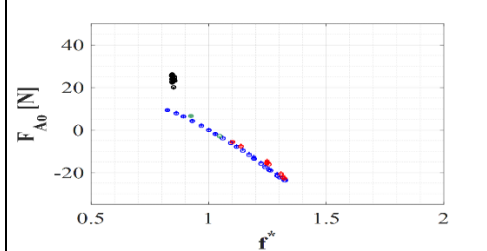


Fig. B19.g. Added mass force F_{A0} vs. f^*

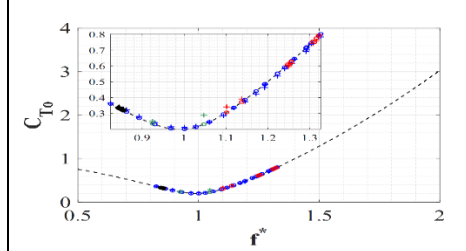


Fig. B19.h. Total force coefficient C_{T0} vs. f^*

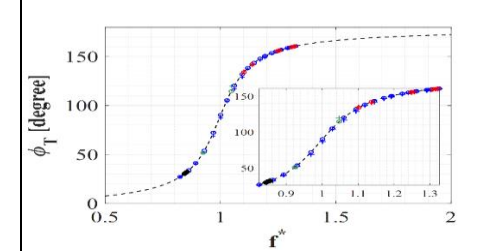
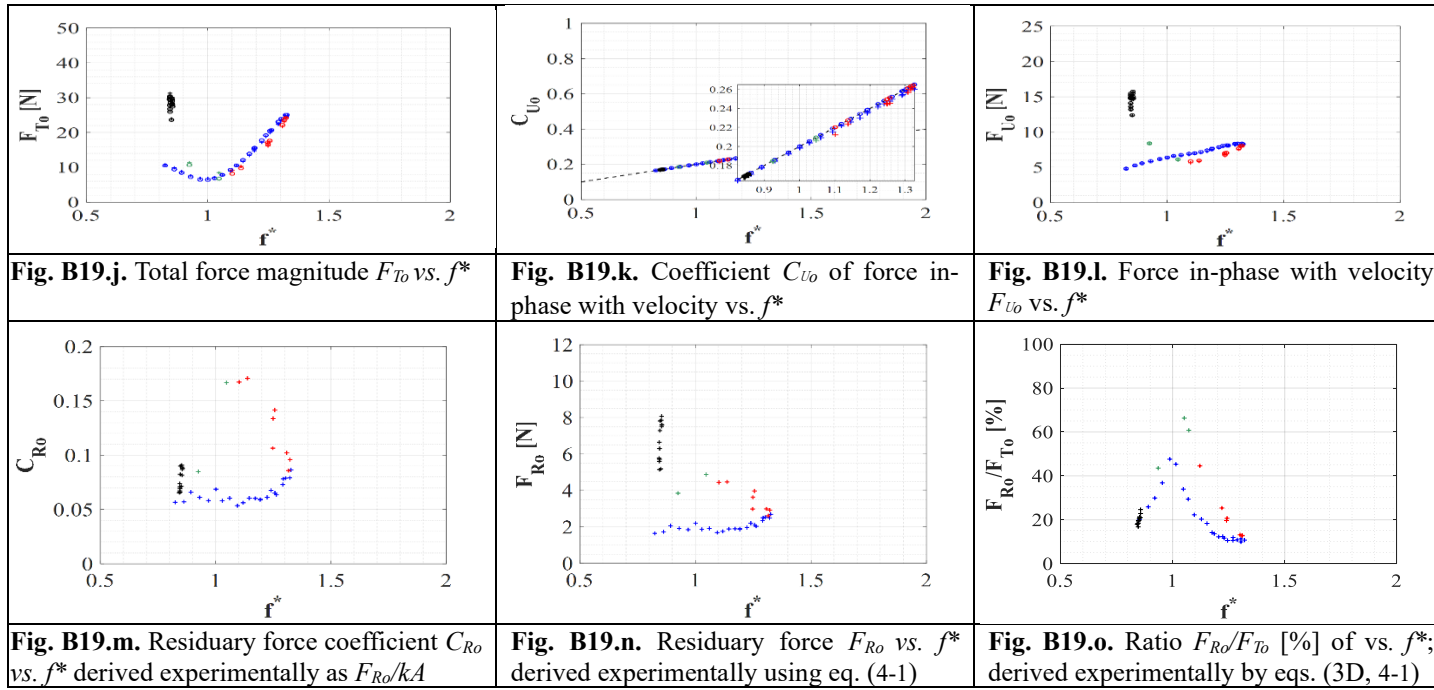
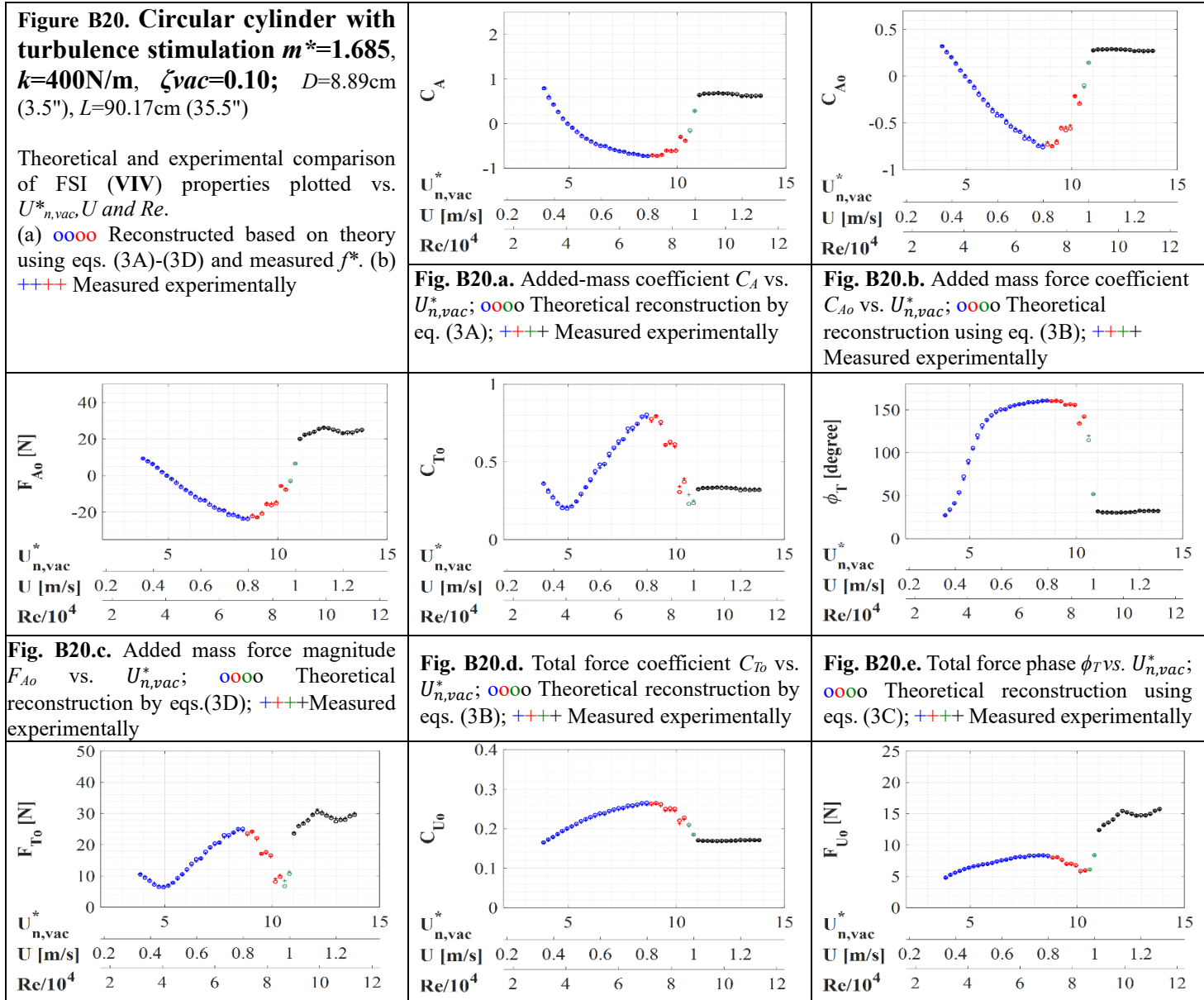


Fig. B19.i. Total force phase ϕ_T vs. f^*





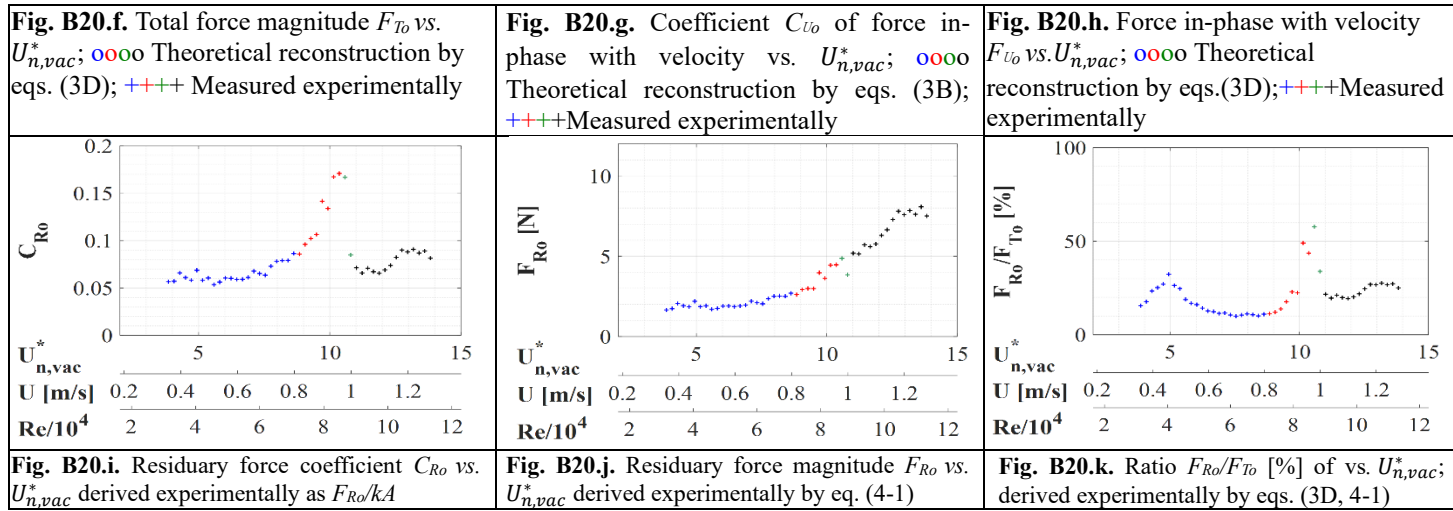


Figure B21. Circular cylinder with turbulence stimulation, $m^*=1.685$, $k=800\text{N/m}$, $\zeta_{vac}=0.06$; $D=8.89\text{cm}$ (3.5"), $L=90.17\text{cm}$ (35.5") Theoretical and experimental comparison of FSI (VIV) properties plotted vs. f^*
 (a) ---- Theory using eqs. (3A)-(3D). (b) ooooo Reconstructed based on theory and measured f^* . (c) ++++ Measured experimentally

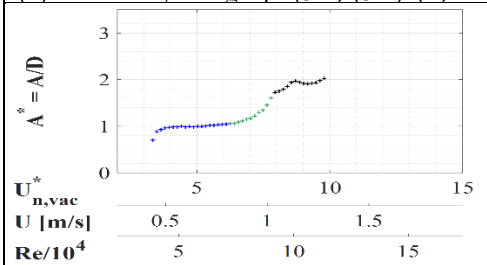


Fig. B21.a. Amplitude ratio $A^*=A/D$

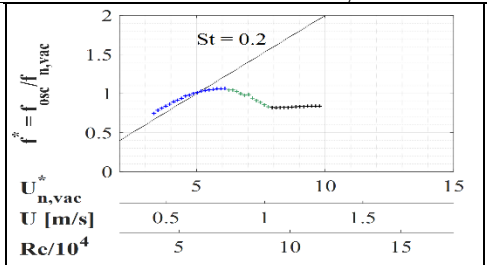


Fig. B21.b. $f^*=f_{osc}/f_{n,vac}$

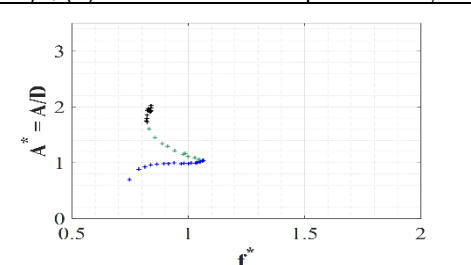


Fig. B21.c. $A^*=A/D$ vs. f^*

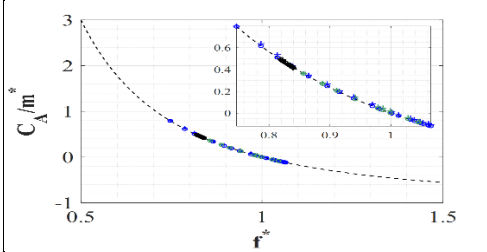


Fig. B21.d. Eigen-relation C_A/m^* ; --- Theory using eq. (3A).

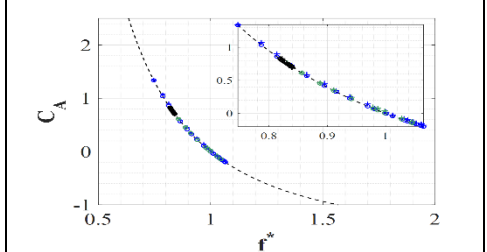


Fig. B21.e. Added mass coefficient C_A vs. f^* ; ---Theory using eq. (3A) and m^*

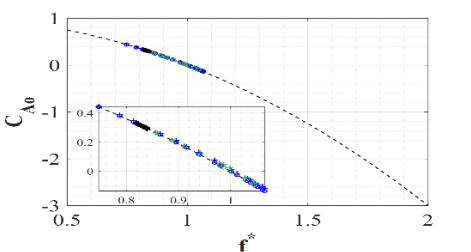


Fig. B21.f. Added-mass force coefficient C_{A0} ; ---Theory using eqs. (3B)

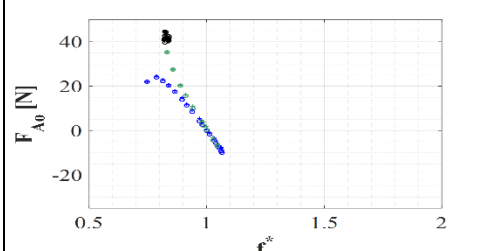


Fig. B21.g. Added mass force F_{A0} vs. f^*

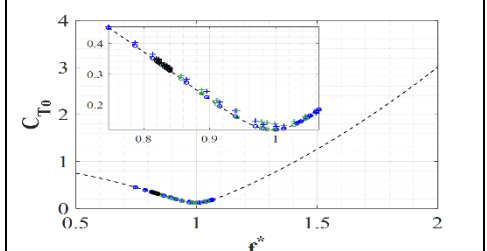


Fig. B21.h. Total force coefficient C_{T0} vs. f^*

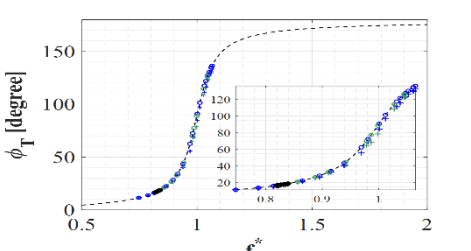
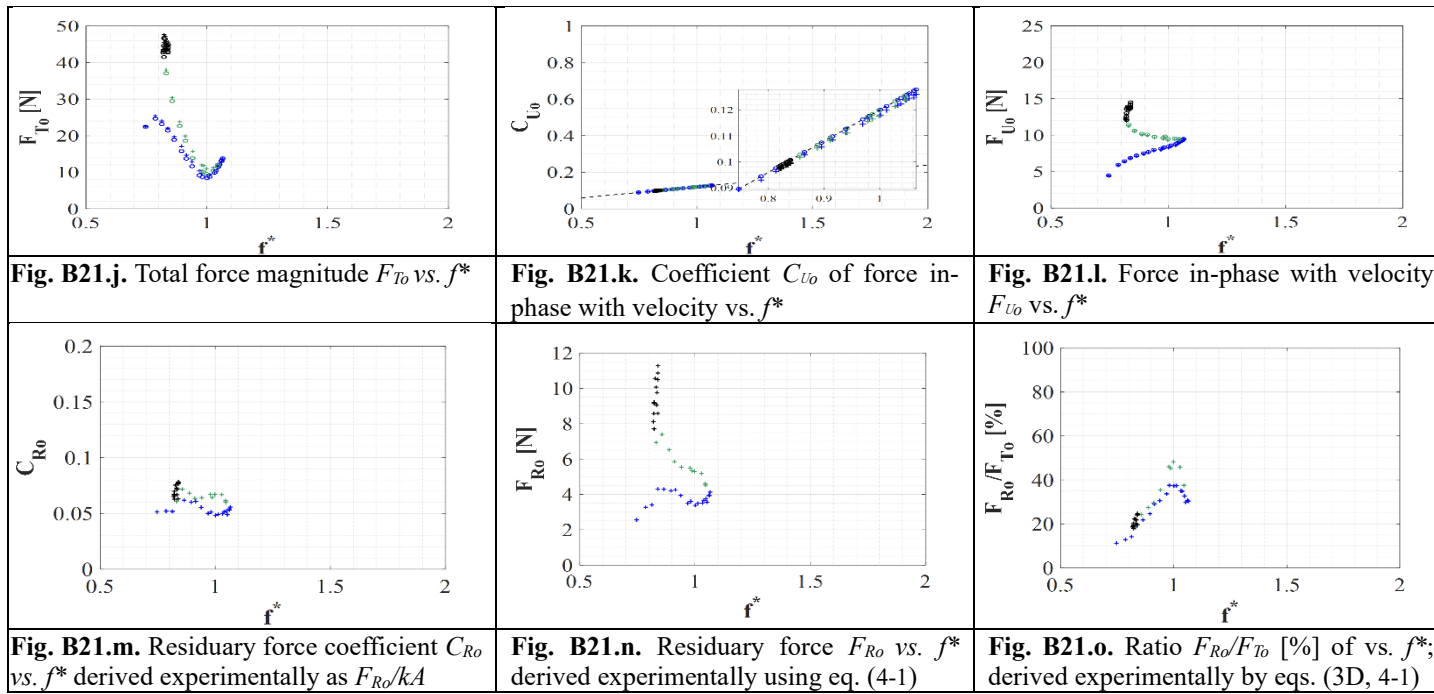
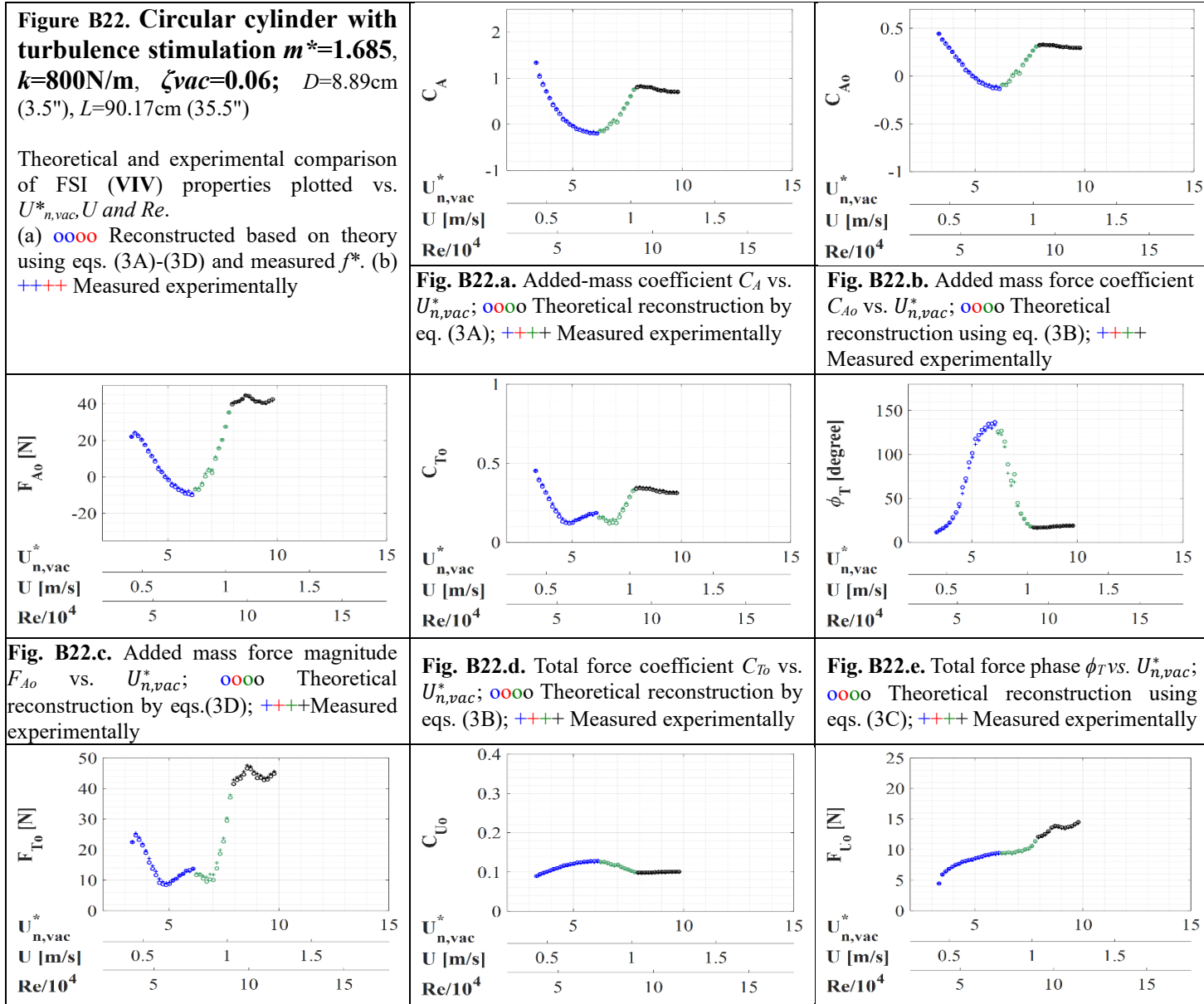


Fig. B21.i. Total force phase ϕ_T vs. f^*





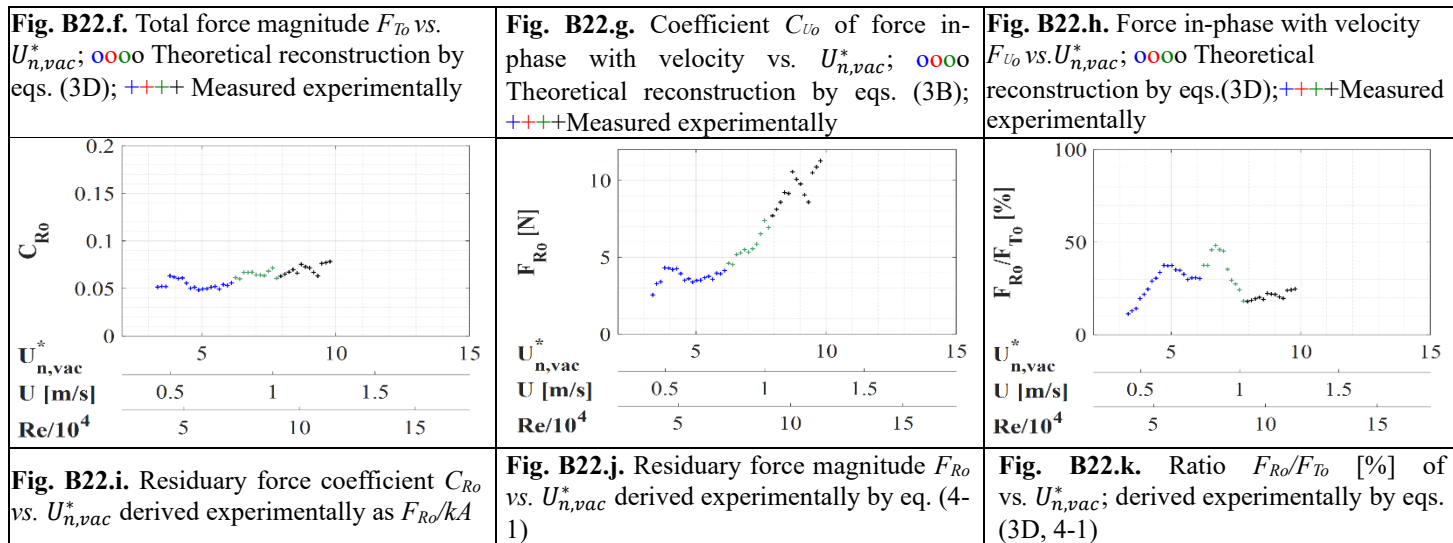


Figure B23. Circular cylinder with turbulence stimulation, $m^*=1.685$, $k=800\text{N/m}$, $\zeta_{vac}=0.10$; $D=8.89\text{cm}$ (3.5"), $L=90.17\text{cm}$ (35.5") Theoretical and experimental comparison of FSI (VIV) properties plotted vs. f^*
 (a) ---- Theory using eqs. (3A)-(3D). (b) ooooo Reconstructed based on theory and measured f^* . (c) ++++ Measured experimentally

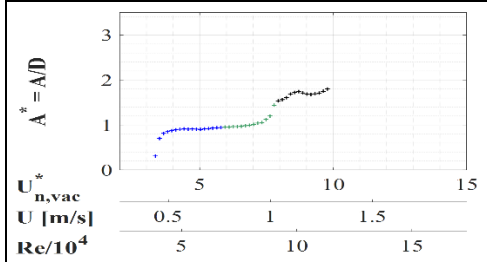


Fig. B23.a. Amplitude ratio $A^*=A/D$

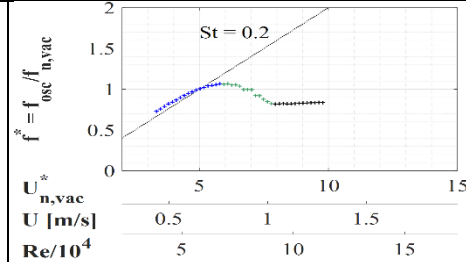


Fig. B23.b. $f^*=f_{osc}/f_{n,vac}$

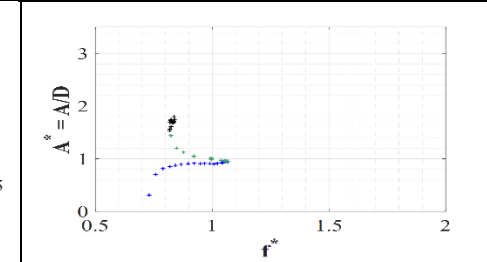


Fig. B23.c. $A^*=A/D$ vs. f^*

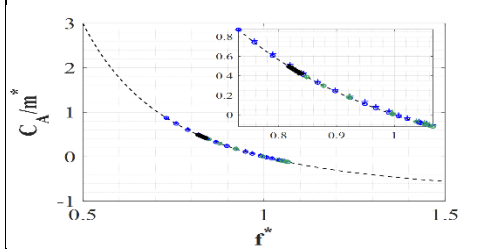


Fig. B23.d. Eigen-relation C_A/m^* ; ---- Theory using eq. (3A).

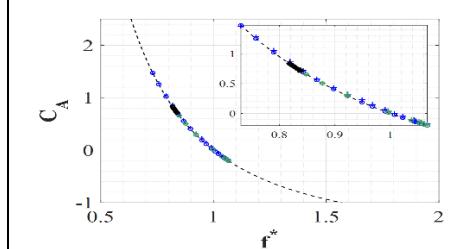


Fig. B23.e. Added mass coefficient C_A vs. f^* ; ---- Theory using eq. (3A) and m^*

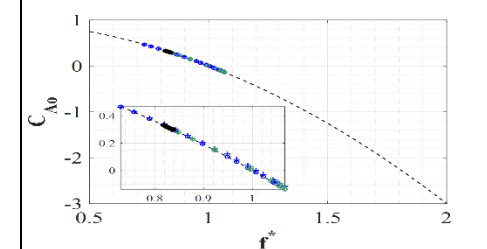


Fig. B23.f. Added-mass force coefficient C_{A0} ; ---- Theory using eqs. (3B)

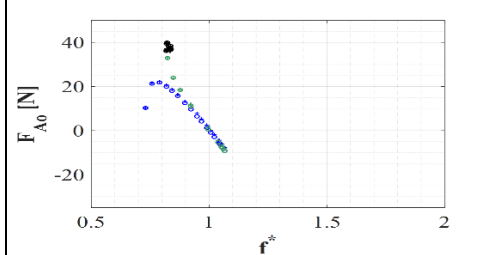


Fig. B23.g. Added mass force F_{A0} vs. f^*

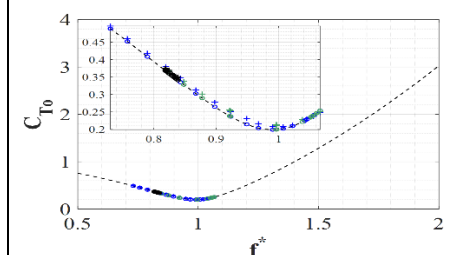


Fig. B23.h. Total force coefficient C_{T0} vs. f^*

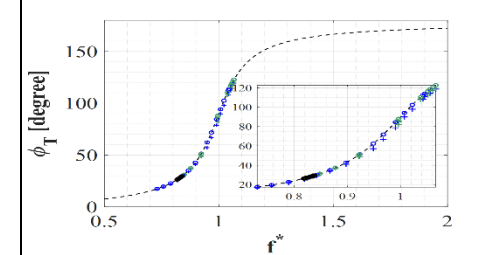
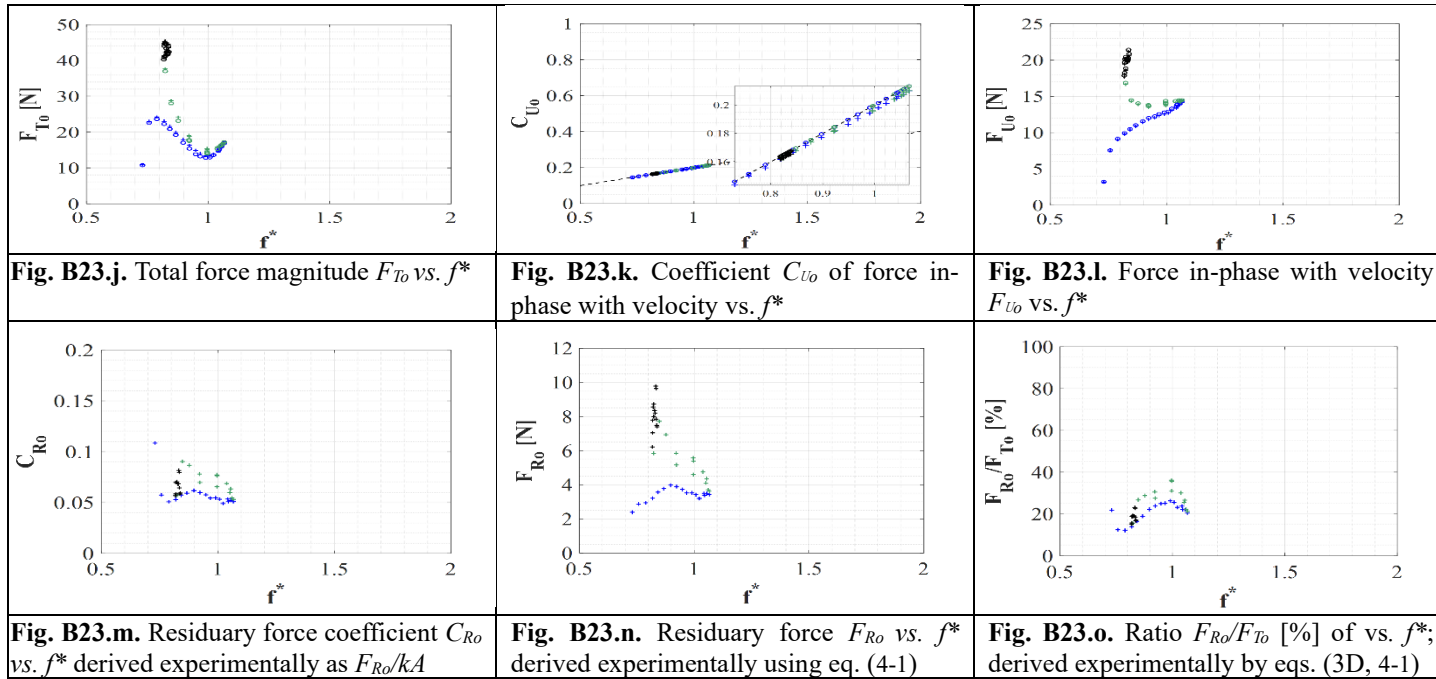
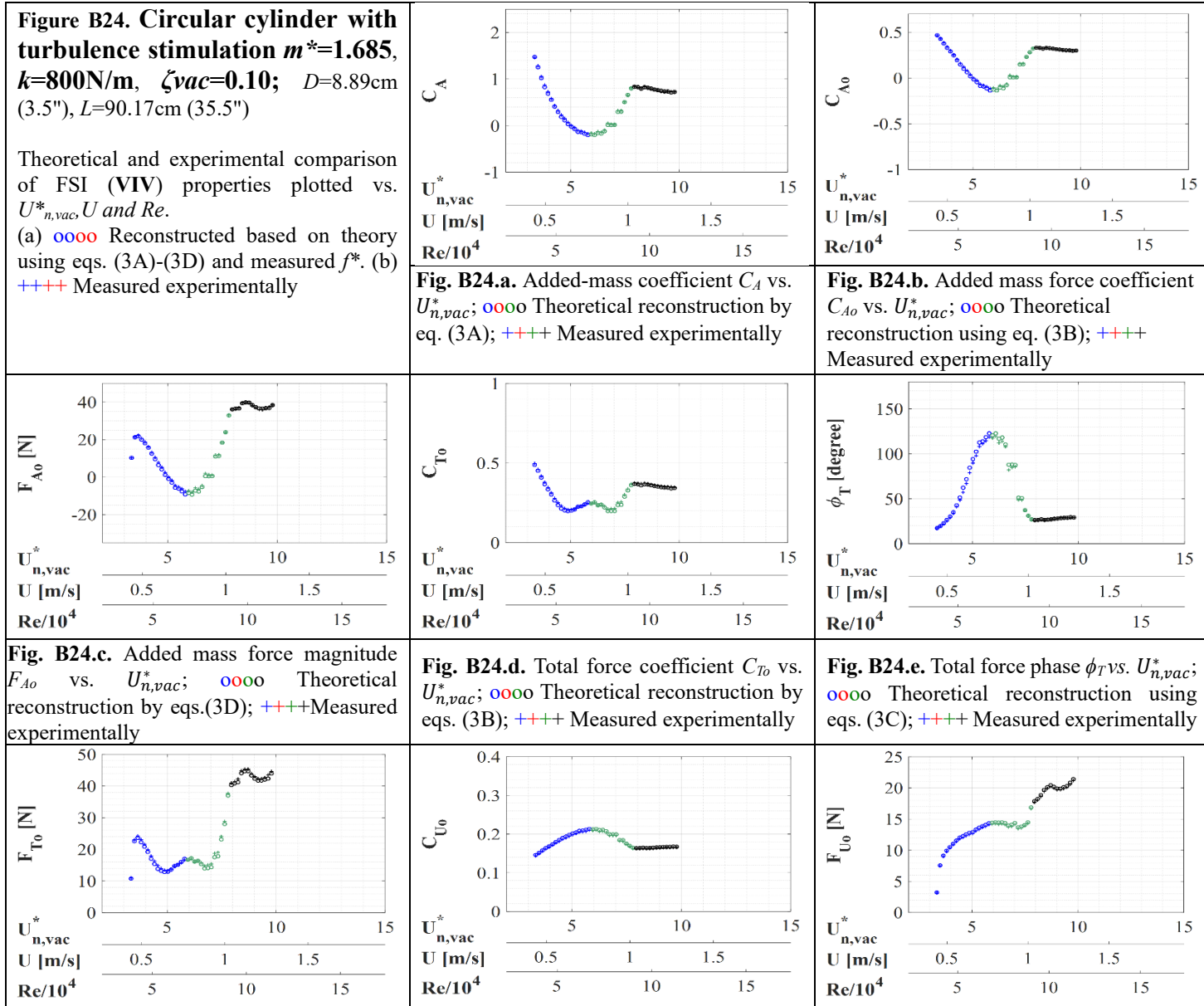


Fig. B23.i. Total force phase ϕ_T vs. f^*





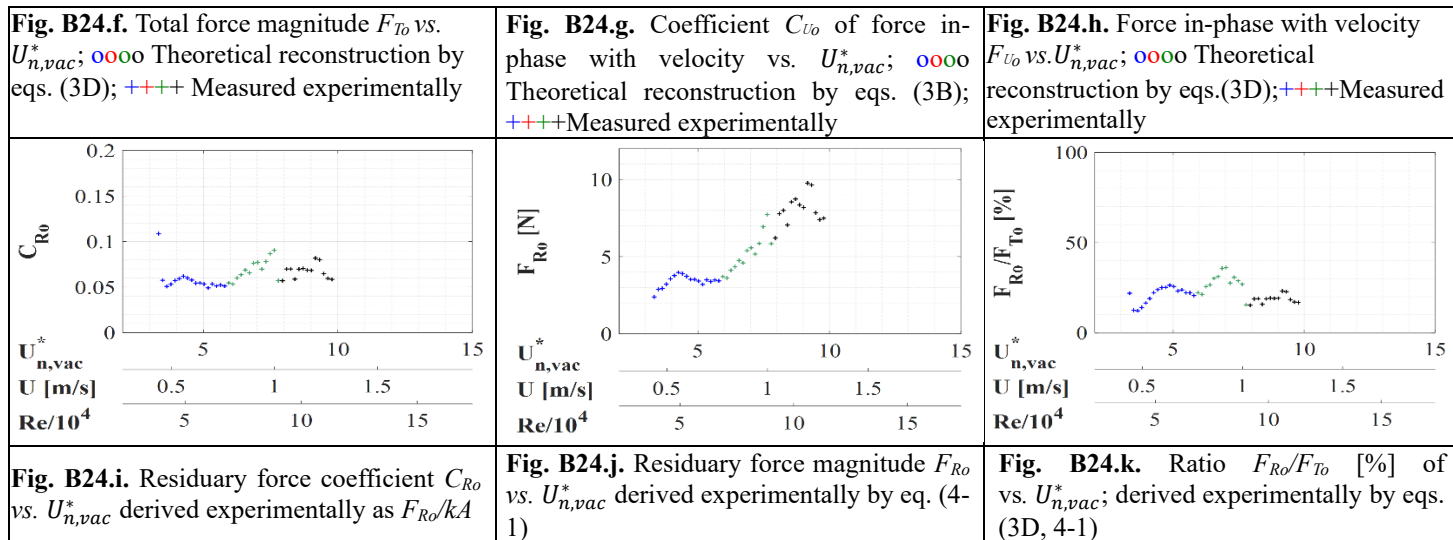


Figure B25. Circular cylinder with turbulence stimulation, $m^*=1.89$, $k=400\text{N/m}$, $\zeta_{vac}=0.06$; $D=8.89\text{cm}$ (3.5"), $L=90.17\text{cm}$ (35.5") Theoretical and experimental comparison of FSI (VIV) properties plotted vs. f^*
 (a) ---- Theory using eqs. (3A)-(3D). (b) ooooo Reconstructed based on theory and measured f^* . (c) ++++ Measured experimentally

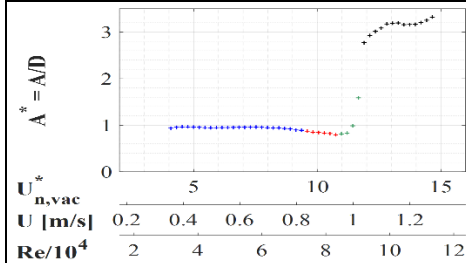


Fig. B25.a. Amplitude ratio $A^*=A/D$

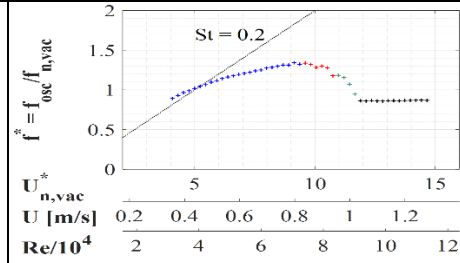


Fig. B25.b. $f^*=f_{osc}/f_{n,vac}$

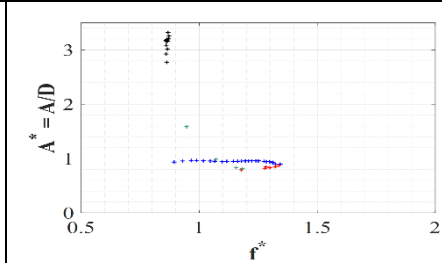


Fig. B25.c. $A^*=A/D$ vs. f^*

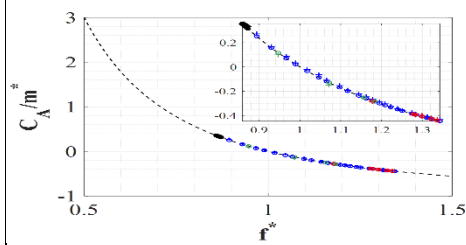


Fig. B25.d. Eigen-relation C_A/m^* ; ---- Theory using eq. (3A).

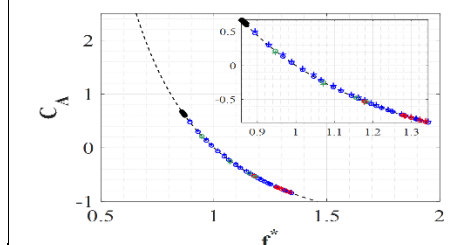


Fig. B25.e. Added mass coefficient C_A vs. f^* ; ---- Theory using eq. (3A) and m^*

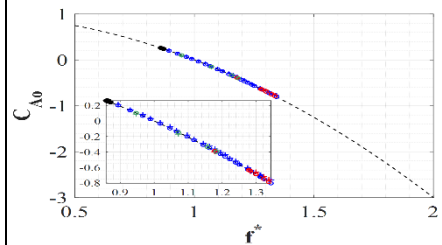


Fig. B25.f. Added-mass force coefficient C_{A0} ; ---- Theory using eqs. (3B)

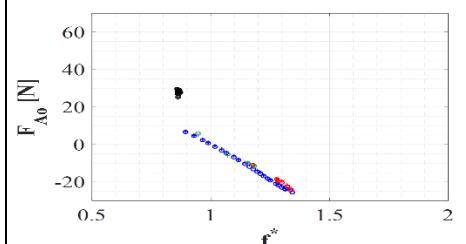


Fig. B25.g. Added mass force F_{A0} vs. f^*

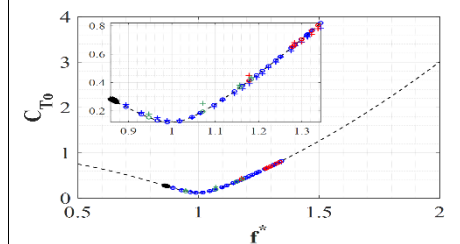


Fig. B25.h. Total force coefficient C_{T0} vs. f^*

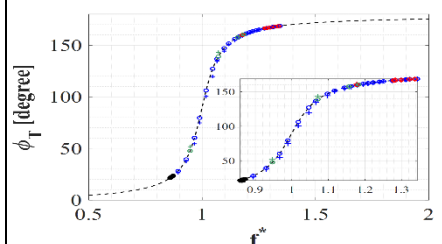
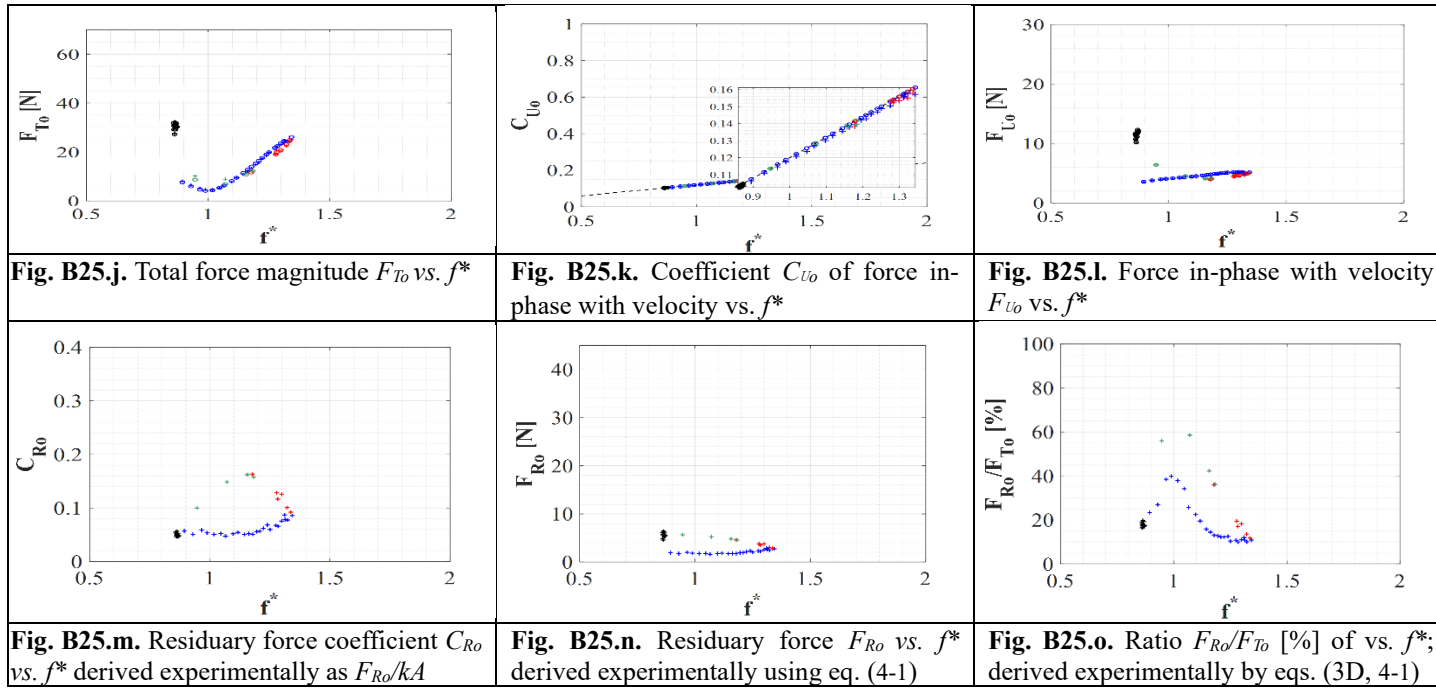
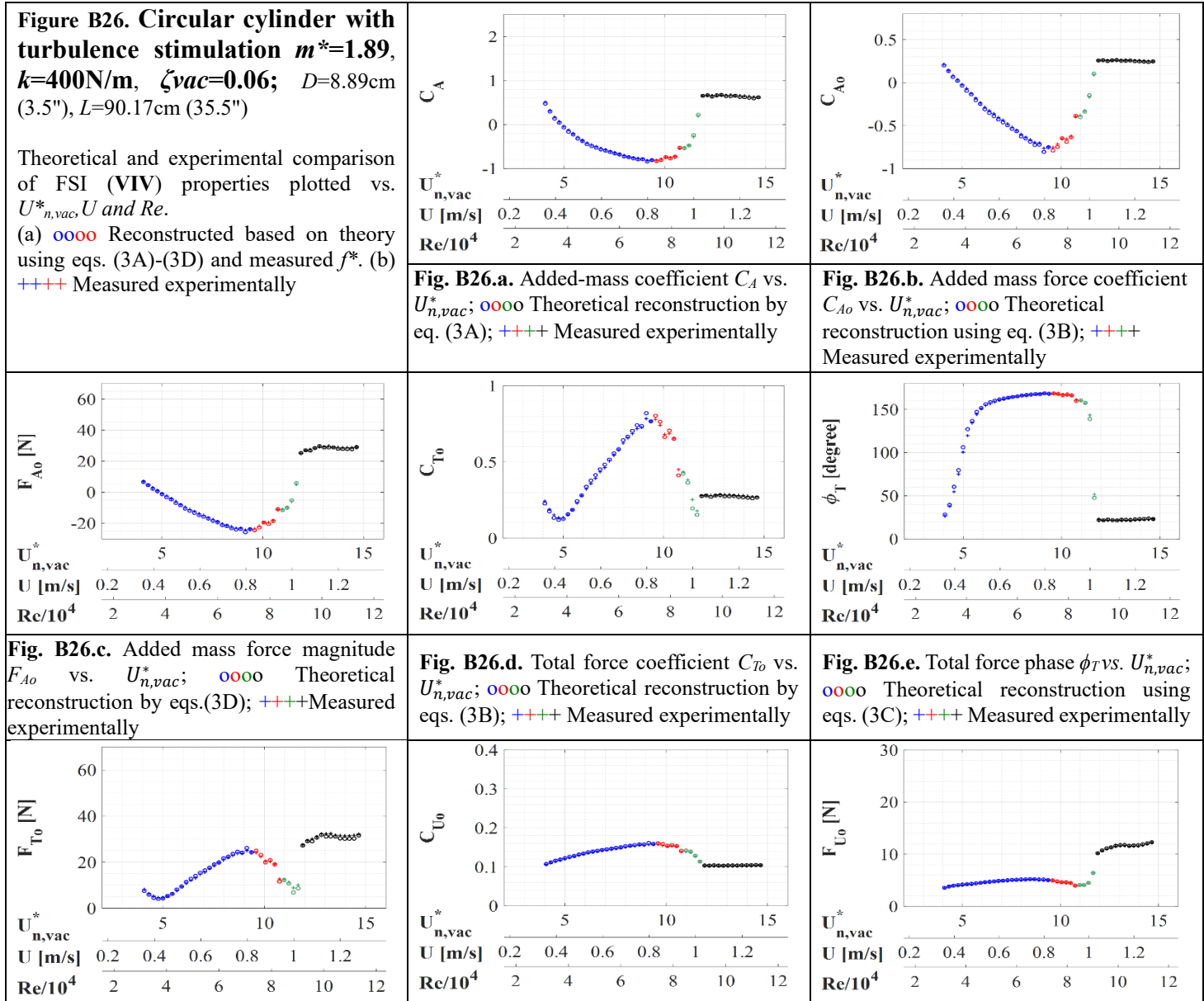


Fig. B25.i. Total force phase ϕ_T vs. f^*





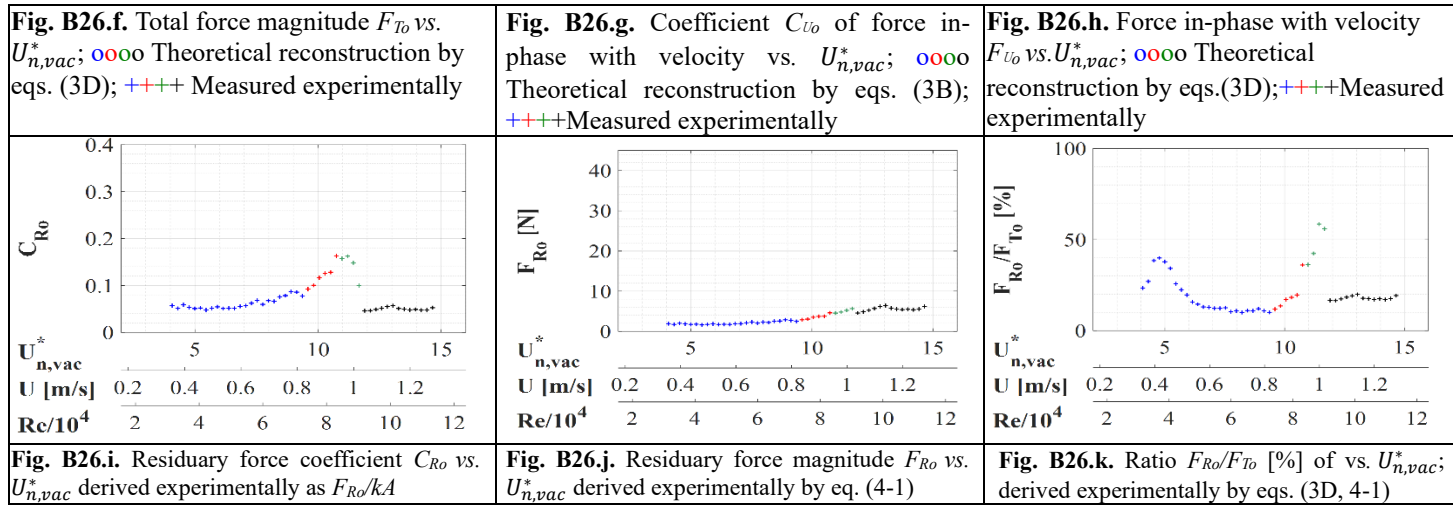


Figure B27. Circular cylinder with turbulence stimulation, $m^*=1.89$, $k=400\text{N/m}$, $\zeta_{vac}=0.10$; $D=8.89\text{cm}$ (3.5"), $L=90.17\text{cm}$ (35.5") Theoretical and experimental comparison of FSI (VIV) properties plotted vs. f^*
 (a) ---- Theory using eqs. (3A)-(3D). (b) ooooo Reconstructed based on theory and measured f^* . (c) ++++ Measured experimentally

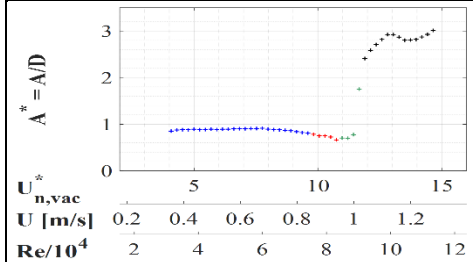


Fig. B27.a. Amplitude ratio $A^*=A/D$

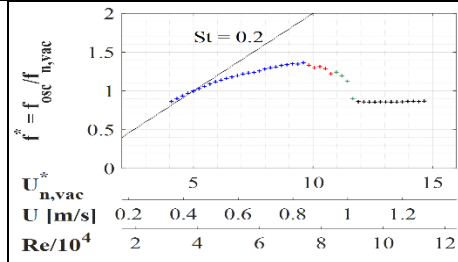


Fig. B27.b. $f^*=f_{osc}/f_{n,vac}$

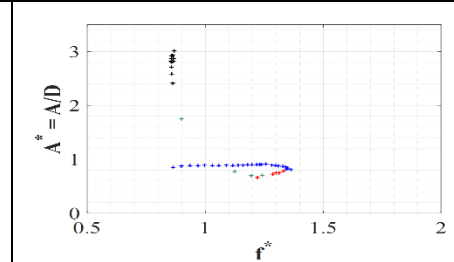


Fig. B27.c. $A^*=A/D$ vs. f^*

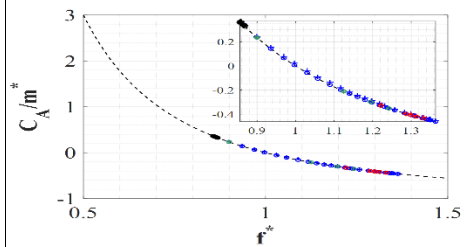


Fig. B27.d. Eigen-relation C_A/m^* ; ---- Theory using eq. (3A).

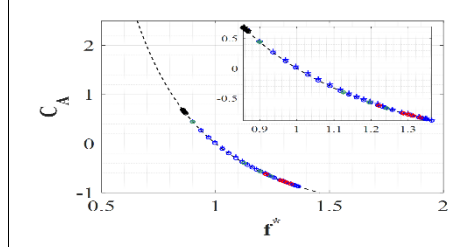


Fig. B27.e. Added mass coefficient C_A vs. f^* ; ---- Theory using eq. (3A) and m^*

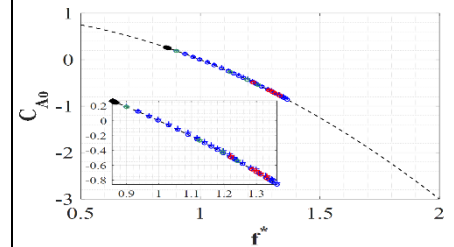


Fig. B27.f. Added-mass force coefficient C_{A0} ; ---- Theory using eqs. (3B)

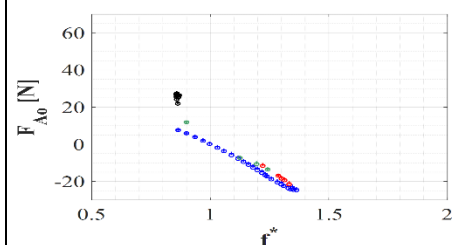


Fig. B27.g. Added mass force F_{A0} vs. f^*

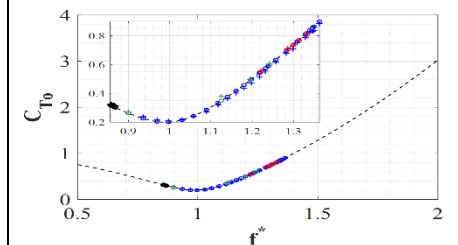


Fig. B27.h. Total force coefficient C_{T0} vs. f^*

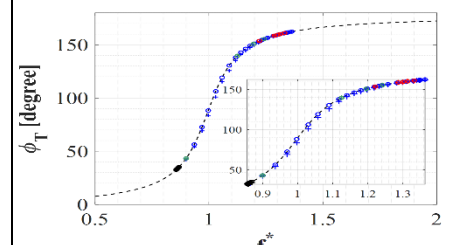
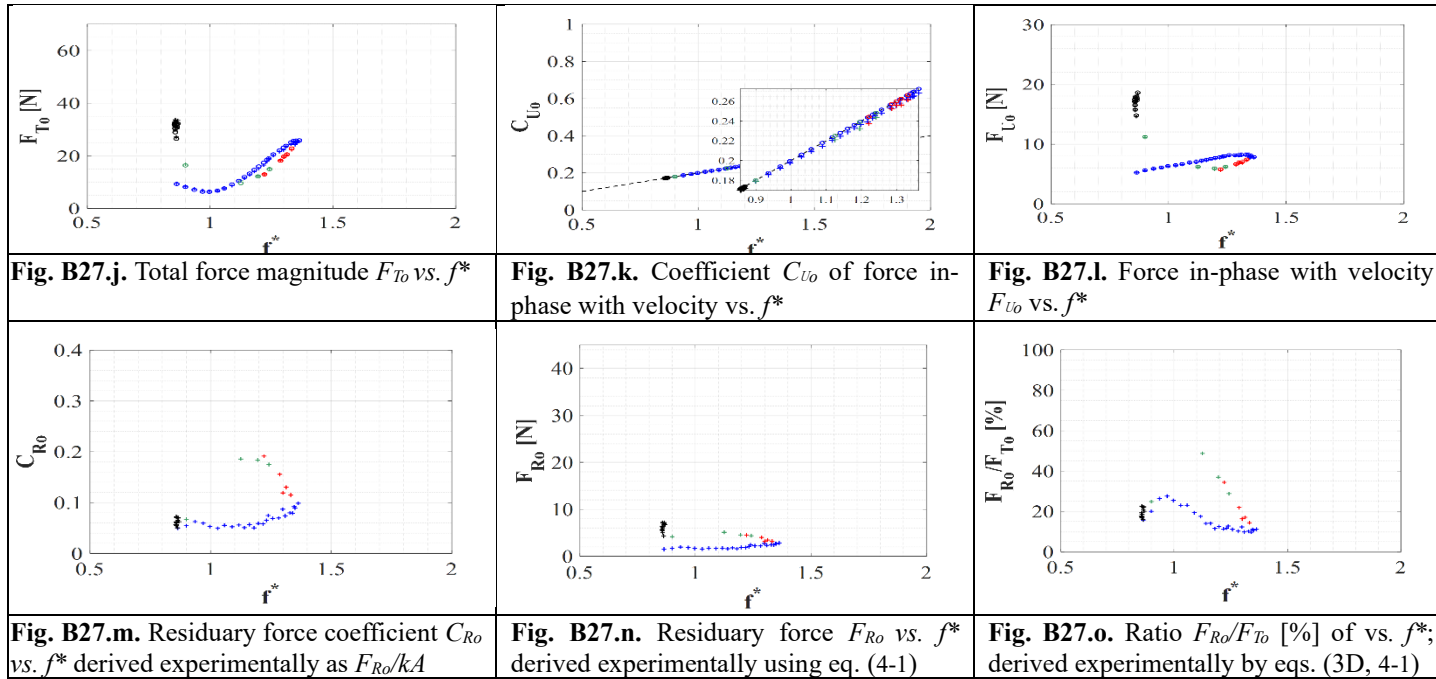
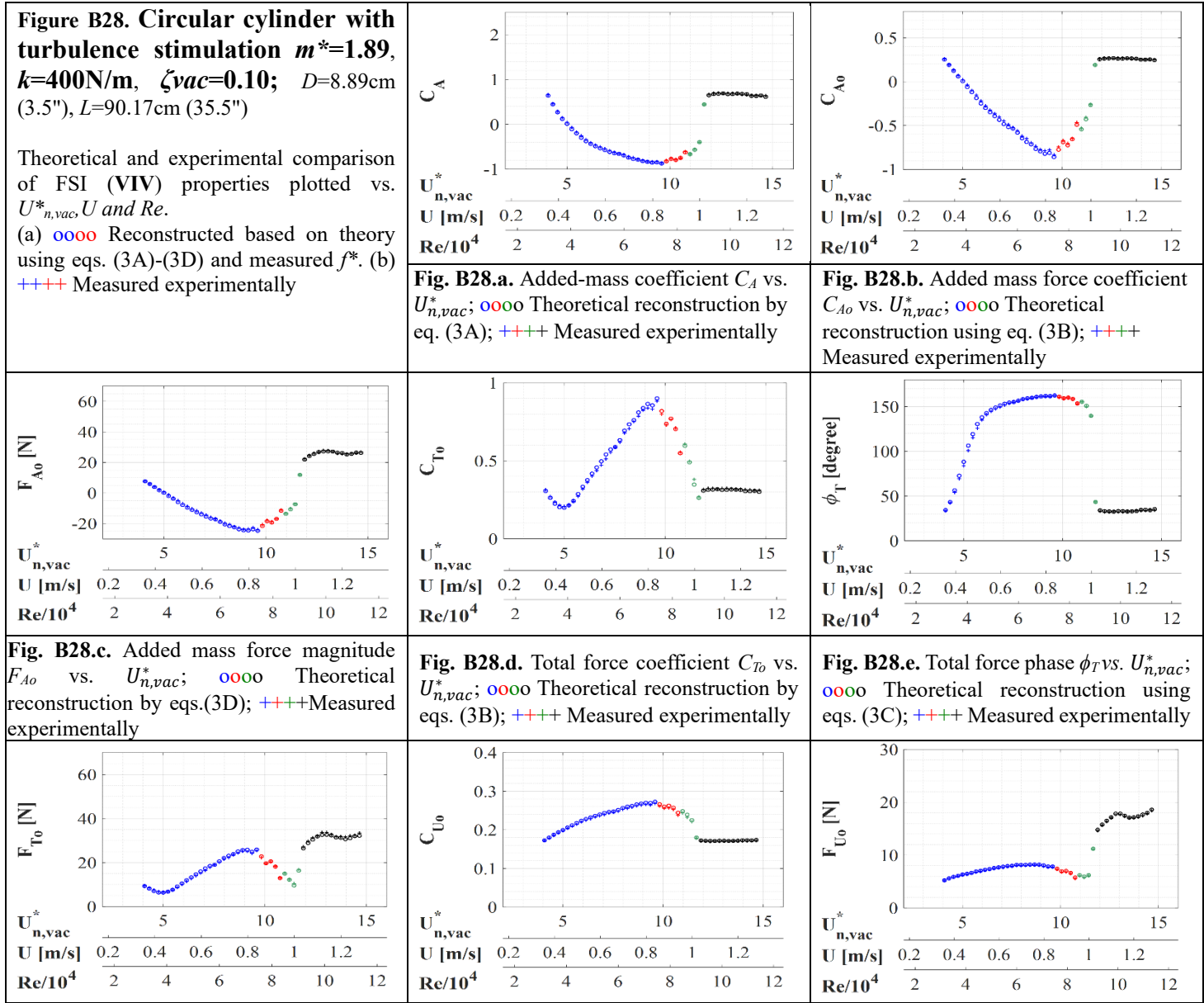


Fig. B27.i. Total force phase ϕ_T vs. f^*





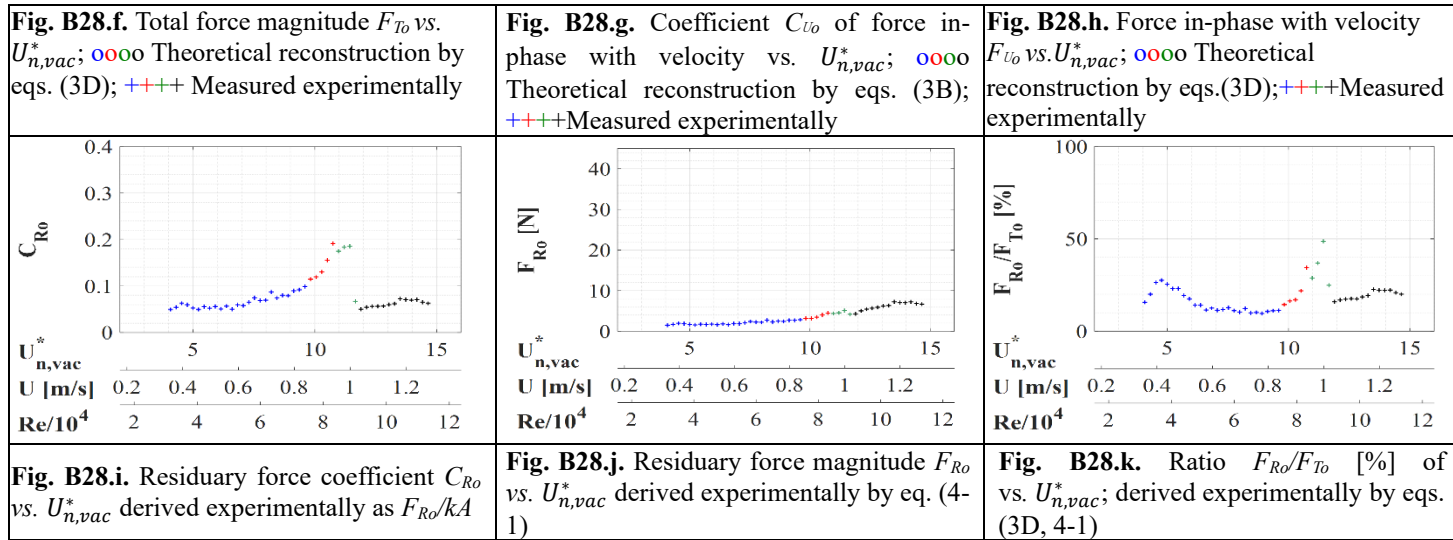


Figure B29. Circular cylinder with turbulence stimulation, $m^*=1.89$, $k=800\text{N/m}$, $\zeta_{vac}=0.06$; $D=8.89\text{cm}$ (3.5"), $L=90.17\text{cm}$ (35.5") Theoretical and experimental comparison of FSI (VIV) properties plotted vs. f^*
 (a) ---- Theory using eqs. (3A)-(3D). (b) ooooo Reconstructed based on theory and measured f^* . (c) ++++ Measured experimentally

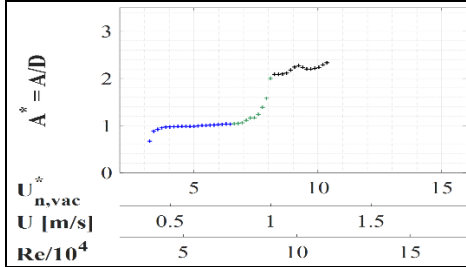


Fig. B29.a. Amplitude ratio $A^*=A/D$

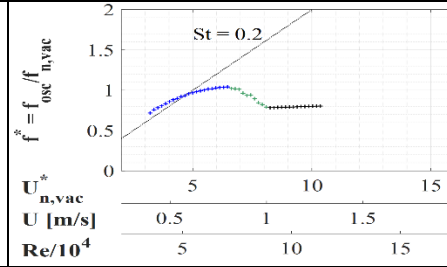


Fig. B29.b. $f^*=f_{osc}/f_{n,vac}$

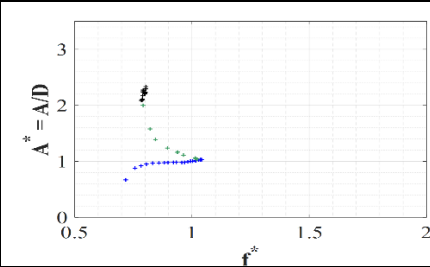


Fig. B29.c. $A^*=A/D$ vs. f^*

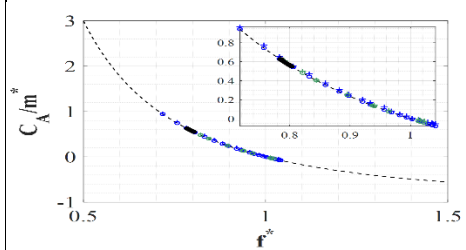


Fig. B29.d. Eigen-relation C_A/m^* ; ---- Theory using eq. (3A).

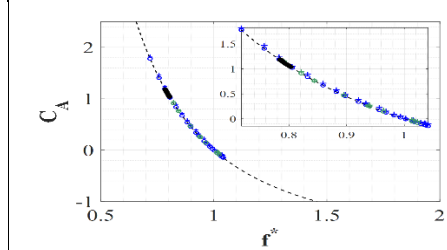


Fig. B29.e. Added mass coefficient C_A vs. f^* ; ----Theory using eq. (3A) and m^*

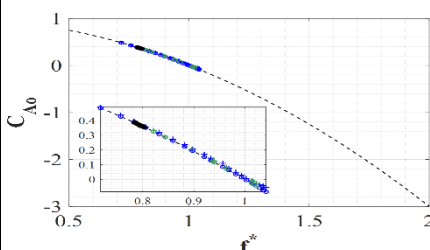


Fig. B29.f. Added-mass force coefficient C_{A0} ; ----Theory using eqs. (3B)

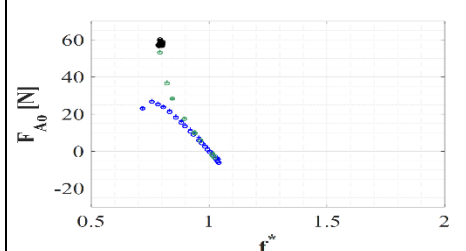


Fig. B29.g. Added mass force F_{A0} vs. f^*

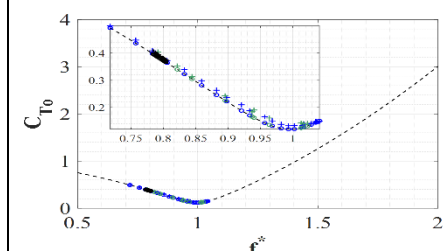


Fig. B29.h. Total force coefficient C_{T0} vs. f^*

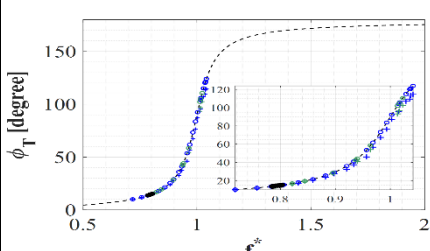
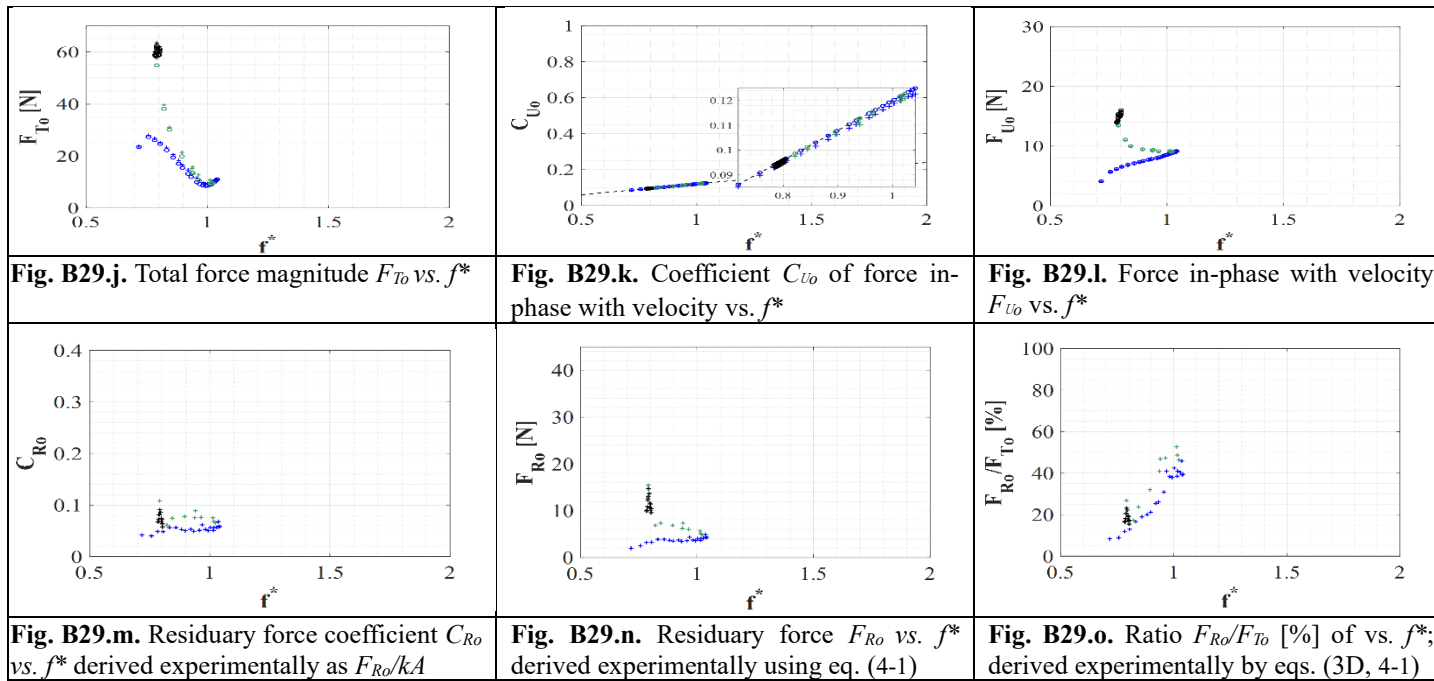
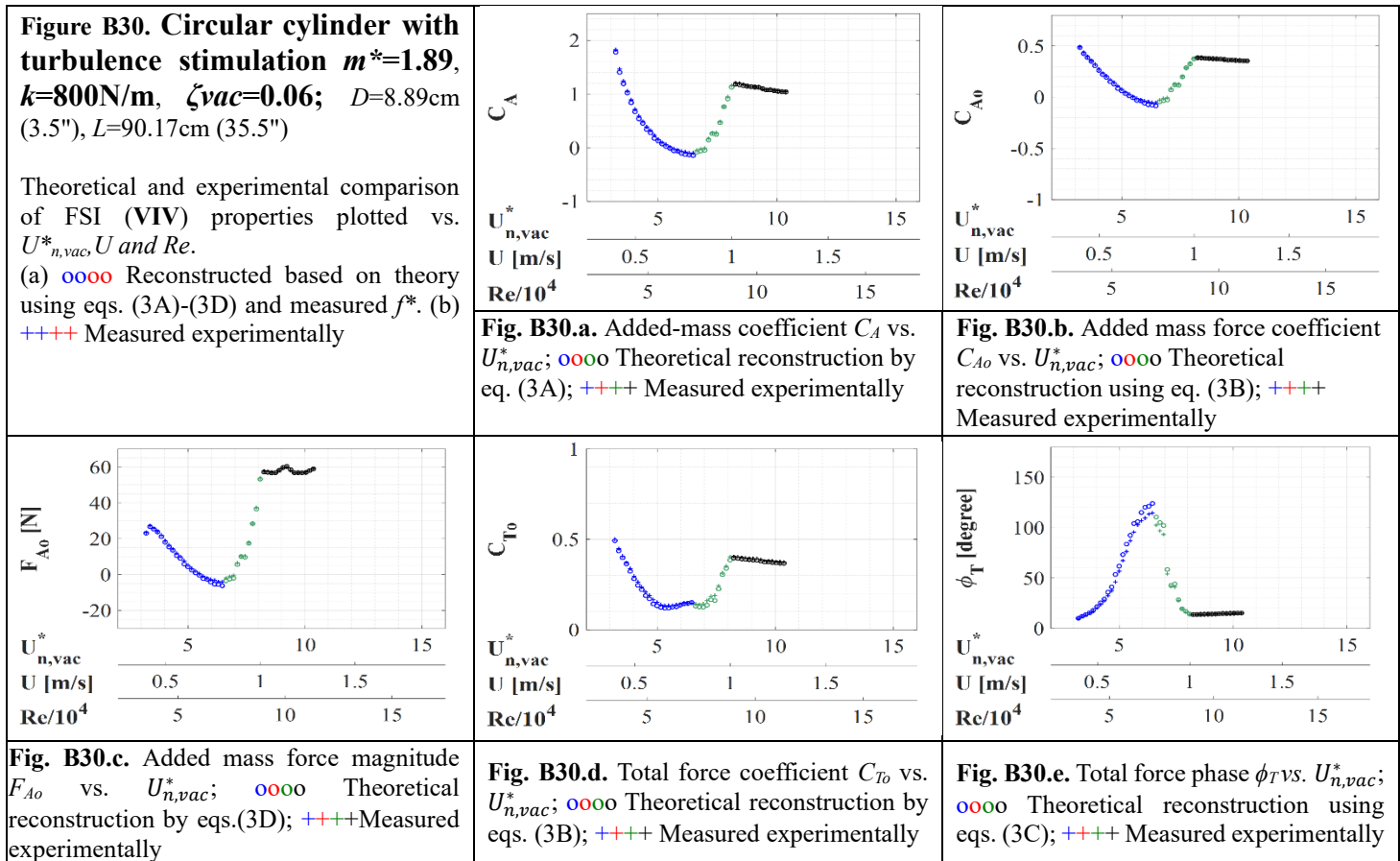


Fig. B29.i. Total force phase ϕ_T vs. f^*





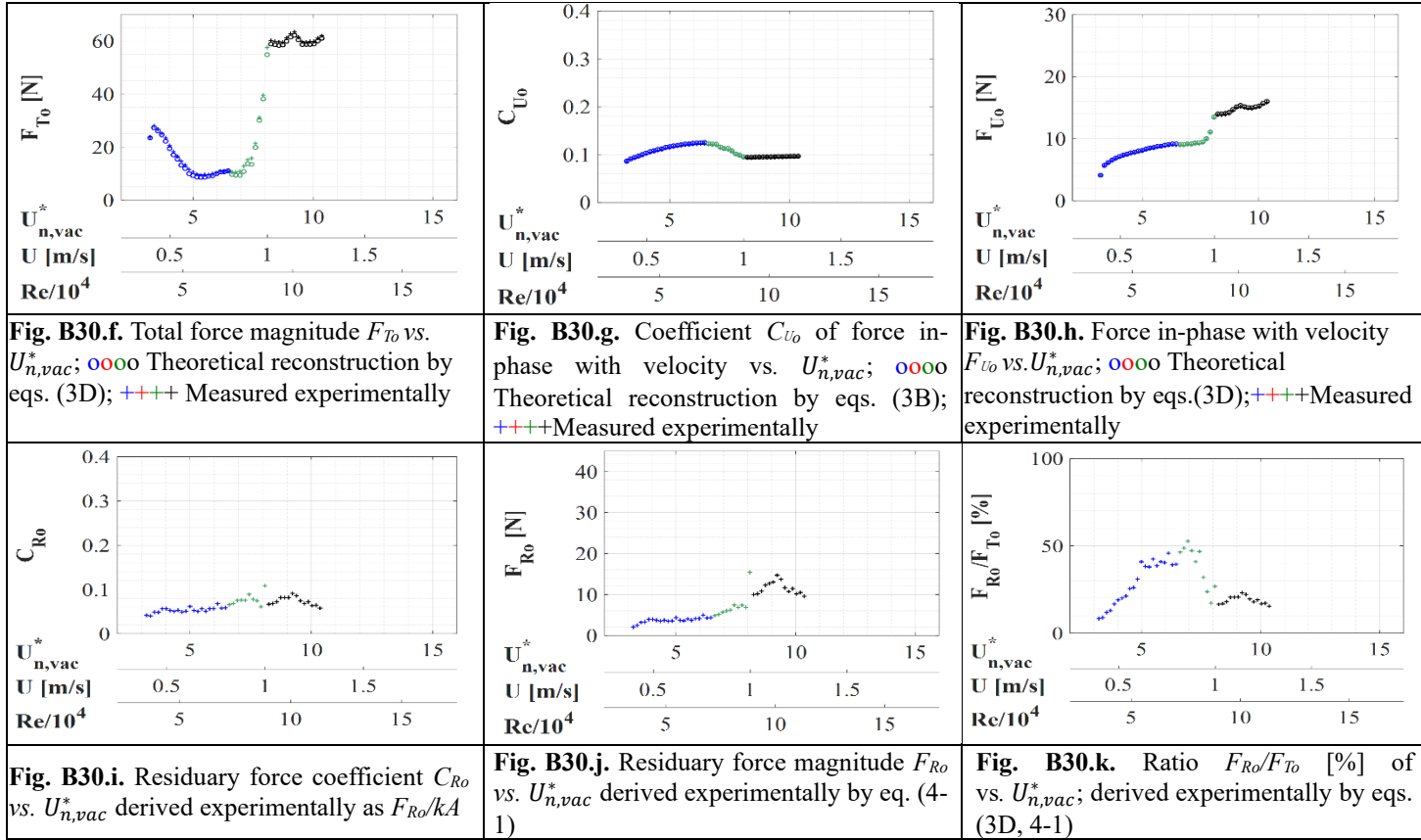


Figure B31. Circular cylinder with turbulence stimulation, $m^*=1.89$, $k=800\text{N/m}$, $\zeta_{vac}=0.10$; $D=8.89\text{cm}$ (3.5"), $L=90.17\text{cm}$ (35.5") Theoretical and experimental comparison of FSI (VIV) properties plotted vs. f^*
 (a) ---- Theory using eqs. (A)-(D). (b) oooo Reconstructed based on theory and measured f^* . (c) ++++ Measured experimentally

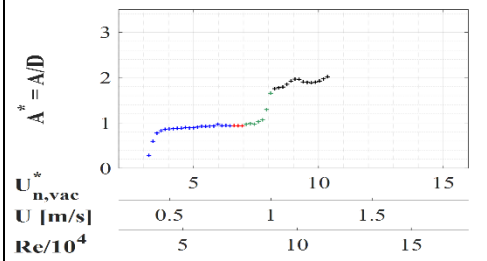


Fig. B31.a. Amplitude ratio $A^*=A/D$

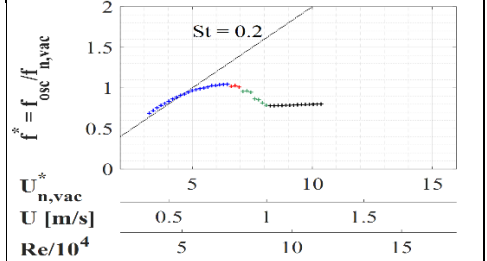


Fig. B31.b. $f^*=f_{osc}/f_{n,vac}$

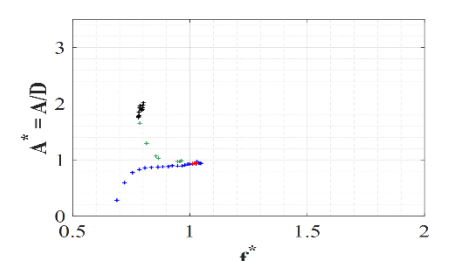


Fig. B31.c. $A^*=A/D$ vs. f^*

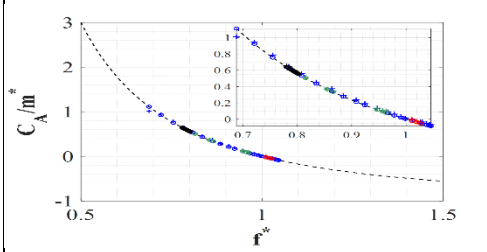


Fig. B31.d. Eigen-relation C_A/m^* ; --- Theory using eq. (3A).

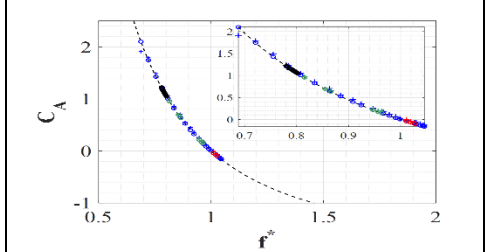


Fig. B31.e. Added mass coefficient C_A vs. f^* ; ---Theory using eq. (3A) and m^*

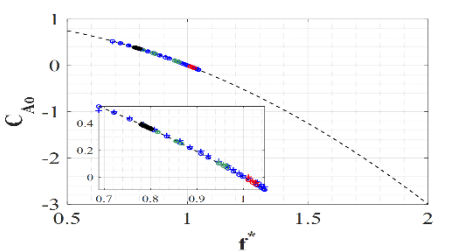


Fig. B31.f. Added-mass force coefficient C_{A0} ; ---Theory using eqs. (3B)

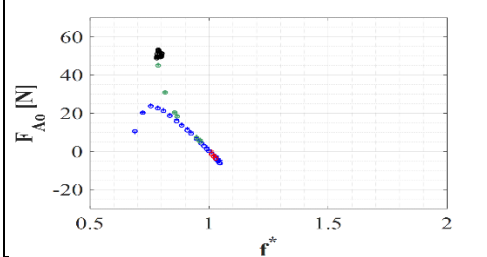


Fig. B31.g. Added mass force F_{A0} vs. f^*

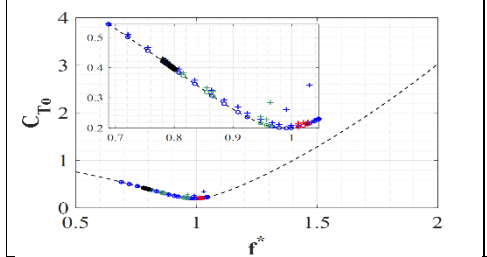


Fig. B31.h. Total force coefficient C_{T0} vs. f^*

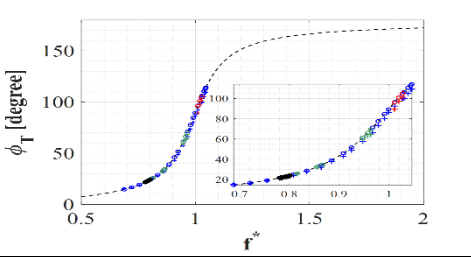


Fig. B31.i. Total force phase ϕ_T vs. f^*

